TESIS DE LA UNIVERSIDAD
DE ZARAGOZA

2013

63

María José Ramón Ortiga

Flexural unfolding of complex geometries in fold and thrust belts using paleomagnetic vectors

Departamento
Ciencias de la Tierra

Director/es
Pueyo Morer, Emilio L.
Pocoví Juan, Andrés
Briz Velasco, José Luis

ISSN 2254-7606

Prensas de la Universidad
Universidad Zaragoza

Tesis Doctoral

FLEXURAL UNFOLDING OF COMPLEX GEOMETRIES IN FOLD AND THRUST BELTS USING PALEOMAGNETIC VECTORS

Autor

María José Ramón Ortiga

Director/es

Pueyo Morer, Emilio L.
Pocoví Juan, Andrés
Briz Velasco, José Luis

UNIVERSIDAD DE ZARAGOZA

Ciencias de la Tierra

2013

Tesis Doctoral. Julio 2013

Flexural unfolding of complex geometries in fold and thrust belts using paleomagnetic vectors

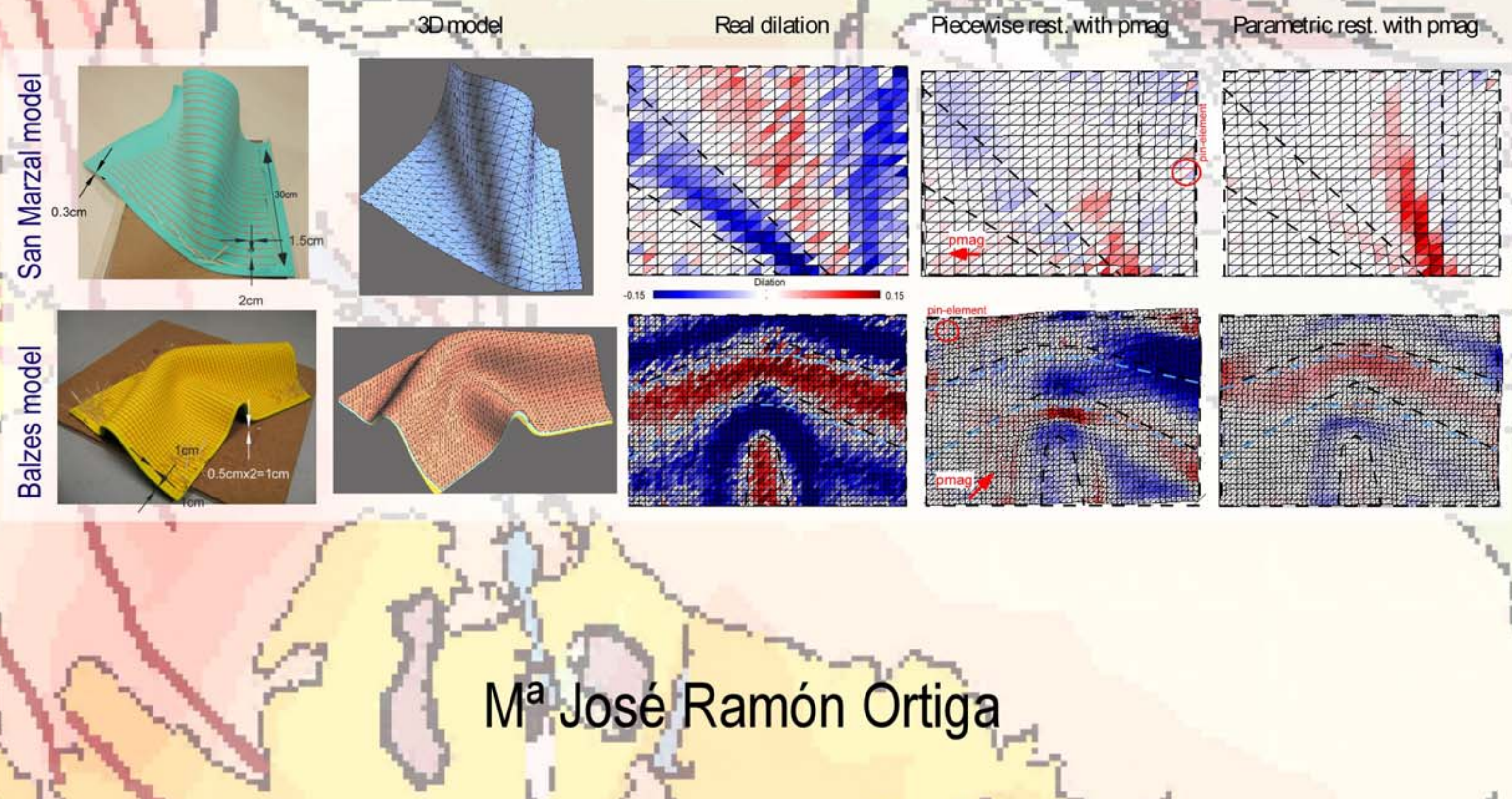

Mª José Ramón Ortiga

Instituto Geológico y Minero de España- Unidad de Zaragoza
Departamento de Ciencias de la Tierra. Universidad de Zaragoza

Instituto Geológico y Minero de España

MINISTERIO
DE ECONOMÍA Y
COMPETITIVIDAD

Instituto Geológico
y Minero de España

Zaragoza a 13 de Mayo de 2013

Emilio L. Pueyo Morer, Científico Titular del Instituto Geológico y Minero de España en la Unidad de Zaragoza y en su calidad de director de la Tesis Doctoral de María José Ramón Ortiga, certifica que la Memoria de dicha Tesis titulada "**Flexural unfolding of complex geometries in fold and thrust belts using paleomagnetic vectors**" se ajusta a los objetivos propuestos en el Proyecto de Tesis Doctoral aprobado por el Departamento de Ciencias de la Tierra de la Universidad de Zaragoza (18-04-2013).

Atentamente

Fdo. Emilio L. Pueyo Morer

Instituto Geológico y Minero de España-Unidad de Zaragoza.
c/ Manuel Lasala 44, 9º, 50006 Zaragoza
+34 976 55 51 53, unaim@igme.es,
http://www.igme.es/internet/zaragoza/

Departamento de Informática e Ingeniería de Sistemas
Universidad Zaragoza

Zaragoza a 13 de Mayo de 2013

José Luiz Briz Morer, Profesor Titular del Departamento de Informática e Ingeniería de Sistemas de la Universidad de Zaragoza y en su calidad de codirector de la Tesis Doctoral de María José Ramón Ortiga, certifica que la Memoria de dicha Tesis titulada "**Flexural unfolding of complex geometries in fold and thrust belts using paleomagnetic vectors**" se ajusta a los objetivos propuestos en el Proyecto de Tesis Doctoral aprobado por el Departamento de Ciencias de la Tierra de la Universidad de Zaragoza (18-04-2013).

Atentamente

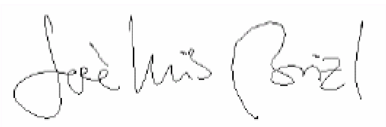

Fdo. José Luis Briz Morer

Departamento de Informática e Ingeniería de Sistemas, Universidad de Zaragoza
Pedro Cerbuna 12, 50009 Zaragoza, briz@unizar.es
http://diis.unizar.es

Zaragoza a 13 de Mayo de 2013

Andrés Pocoví Juan, Profesor Titular del Departamento de Ciencias de la Tierra de la Universidad de Zaragoza y en su calidad de codirector de la Tesis Doctoral de María José Ramón Ortiga, certifica que la Memoria de dicha Tesis titulada "**Flexural unfolding of complex geometries in fold and thrust belts using paleomagnetic vectors**" se ajusta a los objetivos propuestos en el Proyecto de Tesis Doctoral aprobado por el Departamento de Ciencias de la Tierra de la Universidad de Zaragoza (18-04-2013).

Atentamente

Fdo. Andrés Pocoví Juan

Departamento de Ciencias de la Tierra, Universidad de Zaragoza
Pedro Cerbuna 12, 50009 Zaragoza, apocovi@unizar.es,
http://www.igme.es/internet/zaragoza/

Agradecimientos

Esta tesis doctoral ha sido realizada gracias a la financiación de un Contrato del Programa de Personal Técnico de Apoyo (PTAC2007-0282) del Ministerio de Educación y Ciencia (MEC), a una Beca de la OTRI de la Universidad de Zaragoza financiada desde el IGME ("Desarrollo de modelos 3D de estructuras Pirenaicas") con un proyecto del Gob. De Aragón (3DR3- PI165/09) y un año adicional de contrato financiado en el marco de un Proyecto del Plan Nacional de Investigación (CGL2009-14214) del Ministerio de Ciencia e Innovación (MICINN). Los gastos de investigación han corrido a cargo de los proyectos del Instituto Geológico y Minero de España (Unidad de Zaragoza): Pmag3Drest (CGL-2006-2289-BTE MEC, CGL2009-14214 MICINN del Plan Nacional de Investigación) y 3DR3 & GeoPyrDatabases (PI165/09 & CTPP01/07-INTTERREGIII del Dpto. de Ciencia Tecnología y Universidad del Gobierno de Aragón). También se agradece el apoyo mostrado a dichos proyectos, ya fuera en el seguimiento o ejecución; Midland Valley Exploration Ltd., BP Exploration, Repsol, Statoil, SAMCA, Gessal, Compañía General de Sondeos, Z-Amaltea, GeoSpatium Lab. Geoparque del Sobrarbe.

Agradecer de forma muy especial a los directores de tesis como parte artífice de este trabajo. Particularmente a Emilio Pueyo que ha motivado esta tesis, por su continuo ánimo e impulso en los momentos de decaimiento y por su gran implicación y trabajo continuo. A José Luis Briz que siempre ha estado presente y tomado parte activa en todo. A Andrés Pocoví, que desde el principio ha compartido sus conocimientos y habilidades.

A todas las personas e instituciones que han colaborado en el desarrollo de esta tesis. Especialmente a los compañeros de los centros donde se ha desarrollado esta tesis; la Unidad de Zaragoza del IGME y el Area de Geodinámica Interna (Estructural) de la Universidad de Zaragoza. A José Carlos Ciria por todo su apoyo en el área matemática. A Gelu López y Adriana Rodríguez por la ayuda prestada en el desarrollo de los modelos análogos. A Luis H. Ros y el equipo de radiología del Hospital Royo Villanova que han puesto a nuestra disposición los equipos y conocimientos para hacer posible el escáner de los modelos. A Alfredo Serreta que se brindó con el láser escáner (aunque finalmente no diera buen resultado). Juanjo Villalaín (UBU) y Alberto Carrión (UZ) nos asesoraron sobre materiales con contraste radiológico. A los hermanos Chueca (serigrafía Chueca) por escuchar nuestras batallas y ayudarnos a conseguir lo que queríamos en el desarrollo de análogos. Agradecer a Guillaume Caumon por facilitarme la estancia en el *Institut National Polytechnique de Lorraine* y darme pleno acceso para trabajar con el grupo de Gocad. A Óscar Fernández por implicarse con este trabajo. Al grupo Geomodels de Barcelona (Jordi Bausa y Oskar Vidal) por su apoyo y formación con el software de reconstrucción geológica. A María de los Ángeles Pérez y al depto. de Ing. Mecánica y a José María Montiel del depto. de Informática e Ingeniería de Sistemas que nos facilitaron el software Mimmics y Photomodeller. A Midland Valley Exploration, por la cesión gratuita del software Move (aunque finalmente no lo hayamos empleado mucho). A Javier Ramajo por el apoyo con el GIS y a Antonio Barnolas por facilitarnos el acceso al mapa 1:400.000 del Pirineo. Especial mención para Antonio Azcón por su altura de miras. Coautores de artículos: Belén Oliva y Juan Cruz Larrasoaña. Finalmente agradecer revisores y editores de los artículos enviados (aunque no todos se hayan publicado): Richard Lisle, Fabrizio Storti, Pauline Durand-Riard, Peter Cobbold, Andrew P. Roberts, Randy Enkin, Cor Langerais, Graham Borradaile, Phil McFadden, etc...

A Dios y mi familia que siempre han estado ahí apoyando y animando.

Index

Resumen

1 Introducción

La reconstrucción geológica del subsuelo es de vital importancia en muchos ámbitos como la exploración y extracción de recursos naturales (minería, hidrocarburos, recursos hídricos…) y por tanto tiene fuertes implicaciones socio-económicas. La reconstrucción en 3D consiste en la integración de todo tipo de datos geológicos provenientes de la exploración geofísica (fundamentalmente sísmica), de datos de sondeos (litología y diagrafías) y por supuesto de datos de superficie como la cartografía (Groshong, 1999). Los datos son normalmente escasos y provienen de fuentes heterogéneas por lo que es muy importante validar la reconstrucción.

Los métodos de restitución son una herramienta de gran utilidad en la búsqueda de coherencia de una reconstrucción geológica. Restituir significa pasar del estado deformado al estado no deformado. Los métodos de restitución se basan en un conjunto de reglas geométricas, cinemáticas y/o mecánicas que se apoyan en una serie de supuestos sobre el proceso de deformación. El principio básico de restitución en 3D es la conservación de volúmenes durante el plegamiento (Goguel, 1952), así como la horizontalidad de las capas en el estado no deformado. Con ello se busca que los horizontes estratigráficos reconstruidos tengan consistencia geológica con un estado inicial y un proceso de deformación concreto. Así mismo, los procesos de restitución pueden ser de ayuda a la hora de predecir la deformación sufrida por una estructura.

Existe un gran abanico de métodos de restitución que se aplican en 2D y 3D y que se desarrollaron inicialmente para cortes geológicos “compensados” (Dahlstrom, 1969; Hossack, 1979; etc.), evolucionaron a superficies plegadas y falladas (Gratier et al., 1991; Rouby et al., 2000; Massot, 2002; etc.) y actualmente se aplican ya a volúmenes (Moretti, 2005; Maerten and Maerten, 2006; etc.). Sin embargo, vemos que la mayoría de ellos presentan importantes limitaciones a la hora de restituir estructuras plegadas complejas (no cilíndricas y/o no coaxiales) y/o afectadas por gradientes laterales de acortamiento (rotaciones). Son estructuras que podemos encontrar habitualmente en sistemas de pliegues y cabalgamientos y que han sufrido movimiento fuera de plano (asumido como nulo en los métodos 2D) durante el proceso de plegamiento.

2 Objetivos

El objetivo fundamental de esta tesis es añadir el paleomagnetismo a métodos de restitución existentes para mejorar su eficacia. El paleomagnetismo es el estudio del campo magnético terrestre del pasado a partir del estudio de la magnetización registrada en las rocas. Es la única técnica que permite describir movimientos respecto a un sistema de referencia absoluto, externo y global: el campo magnético terrestre. El paleomagnetismo ha sido utilizado con gran éxito desde los años 60 para la caracterización de rotaciones en zonas cinturones de cabalgamientos (Allerton, 1998; Sussman et al., 2012; etc.) y por tanto puede ser utilizado en los métodos de restitución para determinar el valor de la rotación y reducir así el número de incertidumbres. El uso del paleomagnetismo en técnicas de restitución fue recomendado a principios de los años 90 (McCaig and McClelland, 1992) y sin embargo sólo se ha utilizado hasta la fecha como criterio de corrección (Bonhommet et al., 1981; Bourgeois et al., 1997; Arriagada, 2004; Pueyo, 2000).

Por tanto, la propuesta es utilizar en métodos de restitución el paleomagnetismo junto con el plano estratigráfico, puesto que ambos son una referencia conocida en los estados inicial y plegado. El plano estratigráfico determina la rotación de eje horizontal mientras que el paleomagnetismo determina la rotación de eje vertical, aportando así información complementaria. Por supuesto, los datos paleomagnéticos incorporados en el método de restitución deberán cumplir una serie de criterios de fiabilidad a los que también prestamos atención (Van der Voo, 1990; Pueyo, 2010).

Concretamente, vamos a incorporar la información paleomagnética a dos métodos de restitución de superficie válidos para *superficies globalmente desarrollables*. No se trata propiamente de restitución 3D, pero creemos que desplegar superficies (horizontes estratigráficos) de forma correcta es el mejor punto de partida para una certera reconstrucción volumétrica. Superficies desarrollables son aquellas con curvatura gaussiana nula en todos sus puntos, superficies que han sido plegadas de forma isométrica (conservación de ángulos y longitudes) y por tanto podemos desplegarlas sin que sea necesario deformarlas (Lisle, 1992); son las que llamamos superficies *flexurales*. Del mismo modo, entendemos por superficies globalmente desarrollables aquellas que cumplen este supuesto de forma global a pesar de que hayan podido sufrir deformación en algunos puntos.

El primer método de restitución está basado en la triangulación de la superficie y parte del método desarrollado por Gratier et al. (1991). La superficie plegada está discretizada por una malla de triángulos en los que incorporamos el vector paleomagnético. Cada uno de los triángulos es abatido a la horizontal para después ser trasladado y rotado de forma que se minimice la distancia entre los vértices comunes. El dato paleomagnético nos determinará el valor de la rotación disminuyendo así el número de variables.

El segundo método está basado en la parametrización de la superficie y parte del método desarrollado para gOcad por Massot (2002). La idea de la representación paramétrica es poder proyectar una superficie definida en 3D (estado plegado o deformado) a un plano en 2D (estado inicial o no deformado). Hay infinidad de posibilidades, pero por simplicidad y puesto que suponemos un plegamiento isométrico, se eligen unas coordenadas para el estado no deformado que sean rectilíneas y ortonormales. Este método está muy condicionado por la solución inicial y es aquí donde el paleomagnetismo viene en nuestra ayuda porque nos permite determinarla.

Finalmente, extenderemos los métodos desarrollados a la restitución cartográfica en planta, válido tanto a escala regional cómo tectónica. No se trata de “desplegar” superficies sino de “des-rotar” la cartografía según el valor de las rotaciones verticales (VARs) obtenidas a partir de datos paleomagnéticos.

3 Metodología

Para evaluar la bondad de los métodos desarrollados nos vamos a apoyar en modelos a escala. Los análogos han sido siempre de gran utilidad para tratar de comprender y explicar comportamientos y estructuras geológicas. En nuestro caso son cruciales ya que nos permiten conocer al detalle el estado deformado y no deformado y de esta forma poder compararlos con la restitución obtenida.

Los modelos análogos desarrollados están basados en estructuras complejas reales que nos parecen significativas. En concreto modelizamos un pliegue cónico basado en Santo Domingo con el cierre periclinal de San Marzal y un pliegue curvo basado en el anticlinal del Balzes, ambas estructuras localizadas en Sierras Exteriores (Pirineos). Los modelos se han construido utilizando planchas de goma EVA y se han digitalizado por medio de dos técnicas: 1) la fotogrametría, únicamente válida para la reconstrucción de la superficie superior y 2) la reconstrucción de volúmenes a partir de secciones obtenidas mediante un escáner de rayos X (TAC).

Con la reconstrucción de estos modelos se realizan un gran número de pruebas para evaluar los diferentes métodos de restitución y los diferentes parámetros en juego. Analizamos la importancia del uso del paleomagnetismo, la sensibilidad de los diferentes métodos al mallado de la superficie, al punto de inicio y a la orientación del vector paleomagnético. Del mismo modo, se evalúan los resultados cuando el paleomagnetismo no se conoce en todos los puntos y viene definido con un cierto grado de error, tratando así de simular un caso real.

4 Línea argumental

La primera parte de la tesis centra el problema. Después de la introducción (Capítulo 1) hacemos un pequeño recorrido de todo lo que se ha hecho hasta ahora (Capítulo 2). Se describen los métodos de restitución existentes para cortes compensados, superficies y volúmenes prestando atención a los supuestos sobre el proceso de plegamiento de los que parten (Sección 2.1). A continuación nos centramos en el paleomagnetismo: qué es, cómo se adquiere y qué requisitos de fiabilidad es necesario cumplir para su correcto uso (Sección 2.2). Introducimos también el uso de los modelos análogos en aplicaciones geológicas y su digitalización mediante fotogrametría, escáner de rayos X y láser escáner (aunque este último ha sido finalmente descartado) (Sección 2.3). Por último, nos centramos en el marco geológico sobre el que hemos basado el desarrollo de los modelos análogos: el cierre periclinal de San Marzal y el anticlinal curvado del Balzes situados en Sierras Exteriores (Sección 2.4).

En la segunda parte pasamos a describir el trabajo desarrollado. En el capítulo 3 explicamos la metodología de los modelos análogos y los modelos concretos desarrollados. Tras una serie de pruebas, los modelos a escala finalmente utilizados han sido construidos con planchas de goma EVA sobre las que se ha serigrafiado una cuadrícula con minio a modo de sistema de referencia (Sección 3.1.3). Con el escáner de rayos X se obtienen una serie de secciones a partir de las cuales se reconstruyen las distintas superficies y su sistema de referencia utilizando gOcad, un programa de reconstrucción geológica (Sección 3.1.4). Una vez reconstruido el modelo es posible calcular los tensores de deformación gracias al sistema de referencia conocido antes y después de la deformación (Sección 3.1.5). Para el modelo concreto del Bazles hacemos un análisis completo de las potencialidades de la metodología descrita haciendo un estudio de la deformación tras el proceso de plegamiento (Sección 3.2.3).

El capítulo 4 es la descripción de los métodos de restitución de superficie en los que hemos incorporado el paleomagnetismo como nueva variable de entrada. El primero (Sección 4.1) es un método iterativo que trata de encajar los triángulos abatidos mediante mínimos cuadrados. El paleomagnetismo determina el valor de la rotación individual de cada triángulo, restringiendo así el número de variables y disminuyendo la incertidumbre. El segundo método está basado en la parametrización de la superficie (Sección 4.2) y el paleomagnetismo sirve para determinar la solución inicial que condiciona severamente el resultado. Finalmente se describen los parámetros de dilatación y deformación que nos ayudarán a valorar la credibilidad del método (Sección 4.3).

En el capítulo 5 y 6 se llevan a cabo una serie de simulaciones para tratar de evaluar los métodos de restitución descritos junto con los distintos parámetros en juego; la sensibilidad del método en un primer lugar y la sensibilidad del paleomagnetismo en un segundo lugar. Los resultados obtenidos con la restitución se comparan con la superficie inicial y la deformación real sufrida durante la deformación (Sección 5.1). En primer lugar, se muestran la diferencia en los resultados al desplegar las superficies con o sin paleomagnetismo (Sección 5.2). Del mismo modo se evalúa si el tipo de malla que define la superficie y su densidad (Sección 5.3), así como el punto de inicio por el que se empieza a desplegar la superficie (Sección 5.4) tienen efecto sobre el resultado final. Para completar el estudio, se muestran los resultados de una restitución multi-superficie como punto de partida para una restitución volumétrica; además se comparan los resultados con una restitución 3D real exponiendo las limitaciones adicionales que ésta presenta (Sección 5.5).

Adicionalmente se lleva a cabo el estudio sobre el efecto que tienen en la restitución los datos iniciales de paleomagnetismo. Se evalúa en primer lugar el efecto de la orientación inicial del vector paleomagnético con respecto a la estructura principal (Sección 6.1). No perdemos de vista que el paleomagnetismo viene definido con un cierto grado de error y se analiza su influencia (Sección 6.2). Además, es fundamental el análisis de la restitución con datos de paleomagnetismo aislados y no definidos en toda la superficie (Sección 6.3). Para poder utilizar con mayor fiabilidad los métodos de restitución en un caso real donde el paleomagnetismo es conocido únicamente en estaciones puntuales, se desarrolla un método de interpolación que se basa en la suposición de partida de que las superficies son desarrollables (Sección 6.4). Se aplica de esta forma el método a un escenario más realista (Sección 6.5).

En el capítulo 7 aplicamos la idea de restitución con paleomagnetismo a una restitución cartográfica en planta. Definimos las bases de este nuevo método (Sección 7.1) y mostramos los resultados para dos casos de estudio: el anticlinal del Balzes (Sección 7.2.1) y el sistema sur-pirenaico central (Sección 7.2.2).

Los resultados obtenidos se evalúan en el apartado de las conclusiones proponiendo al mismo tiempo futuras líneas de investigación.

En los apéndices se trata un tema de igual importancia pero un poco más alejado de la línea principal de la tesis y que está relacionado con la fiabilidad de los datos paleomangéticos. En el apéndice 1 proponemos una técnica para el procesado de los datos paleomagnéticos basada en el cálculo de direcciones virtuales como apoyo a las herramientas tradicionales. Para ello se desarrolla el programa “Virtual Paleomagnetic Directions” (VPD). En el apéndice 2 se describen matemáticamente tres posibles fuentes de error de los datos paleomagnéticos: el solapamiento de una componente secundaria, la deformación interna por cizalla y un mal control estructural del plegamiento producido en dos etapas.

1 Introduction

1.1 Focus

Three-dimensional reconstructions of the subsurface are an important field in Earth Sciences due to their considerable socio-economic implications as exploration of natural resources (mining, oil, water, etc.). 3D reconstructions aim at providing a plausible image of the underground, which entails the integration of discrete and heterogeneous datasets: field observation (stratigraphic contacts and orientations, fault planes, etc.), interpretative map and cross-sections, seismic sections, borehole data… (e.g. Caumon et al., 2009 and references therein). Reconstruction techniques are based on geometric/mechanic laws and are designed to tackle areas with scarce and heterogeneous data.

Restoration algorithms are an important tool to validate these 3D geological reconstructions of the subsurface. Each step of reconstruction must be checked and validated with geological criteria (e.g. Groshong 2006). Restoration is the way back from the deformed to the undeformed state (retro-deformation). Undoing the deformation and achieving an initial surface with geological meaning (*balanced structure*) is useful to validate the reconstruction of the folded structure and the deformation processes assumed. The main postulate in most restoration methods is the horizontality of the initial layers while restoration algorithms are based in several deformation processes as flexural slip or simple shear. At regional scales and crustal levels, we can assume that deformation does not change the total rock volume, at least overall (Goguel, 1952). These and other rules based on geological criteria are applied in restoration as well as in forward modeling. We deepen in restoration techniques in next chapter but we want to emphasize here the importance of a continuous feedback between reconstruction and restoration. This becomes especially important when complex deformation processes are implied and limited data is available. In addition, restoration tools may also be useful to predict deformation patterns for well characterized structures because the knowledge of deformed and undeformed states allows calculation dilation and strain tensors.

However, existing restoration methods do not always succeed for complex structures like non-cylindrical, non-coaxial and/or areas undergoing vertical axis rotations (*out-of-plane motions*). We suggest using paleomagnetic information, which is known in both the undeformed (horizontal) and deformed state, as an additional and powerful constraint to improve restoration methods and to reduce the uncertainty of the results. The use of paleomagnetism in restoration tools was recommended in the early 90's (McCaig and McClelland, 1992). So far, however, relatively few researchers have tried using paleomagnetic information to double-check the rotation inferred from restoration methods, and hardly ever paleomagnetism is used as primary information of these tools.

1.2 Objectives

In this PhD we want to show how paleomagnetism can reduce the uncertainty in restoration tools when it is used as a constraint, particularly for structures with out-of-plane motions. The bedding plane is the basic 2D reference to relate the undeformed and deformed states, but never could be a real 3D indicator. Our proposal is the usage of paleomagnetism together with the bedding plane as references known in both states. The bedding plane determines the horizontal rotation and paleomagnetism the vertical axis rotation (Fig. 1.1).

Paleomagnetic vectors are the record of the ancient magnetic field at the time of the rock formation and we assume that they behave as a passive marker during the deformation process. Its original orientation can be known in the undeformed surface, and it is represented by the *paleomagnetic reference vector*. If we see the deformation mechanisms (Fig. 1.2), paleomagnetism allows reducing the number of variables, since it is a passive marker that may record the internal deformation and provides us with information on vertical axis rotation. Because accurate paleomagnetic data is necessary to improve results we also work on a good data acquisition.

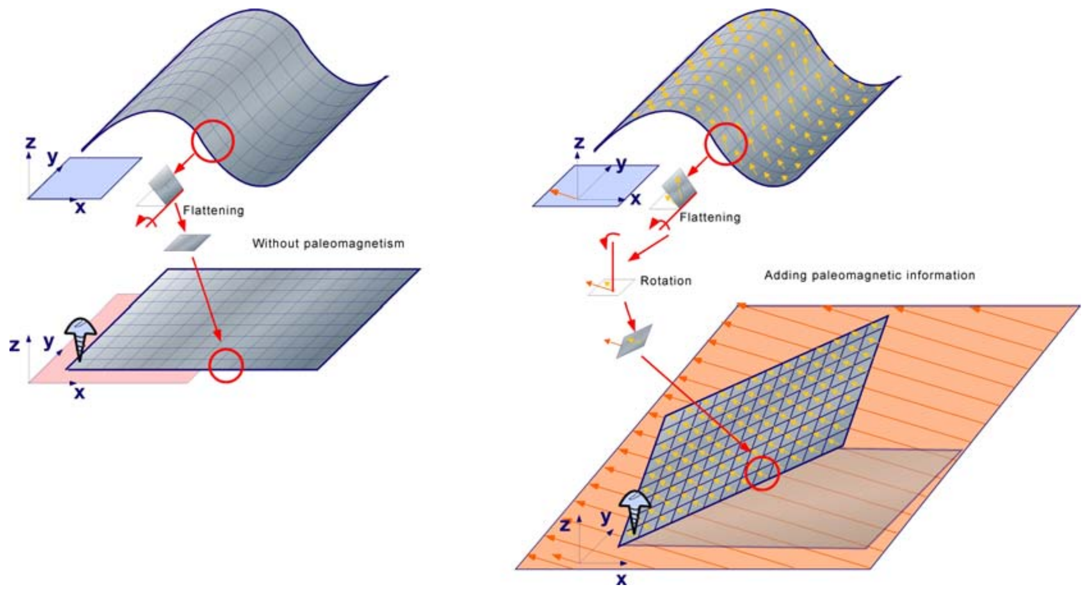

Figure 1.1: Conceptual model of 3D restoration by integrating paleomagnetic data.

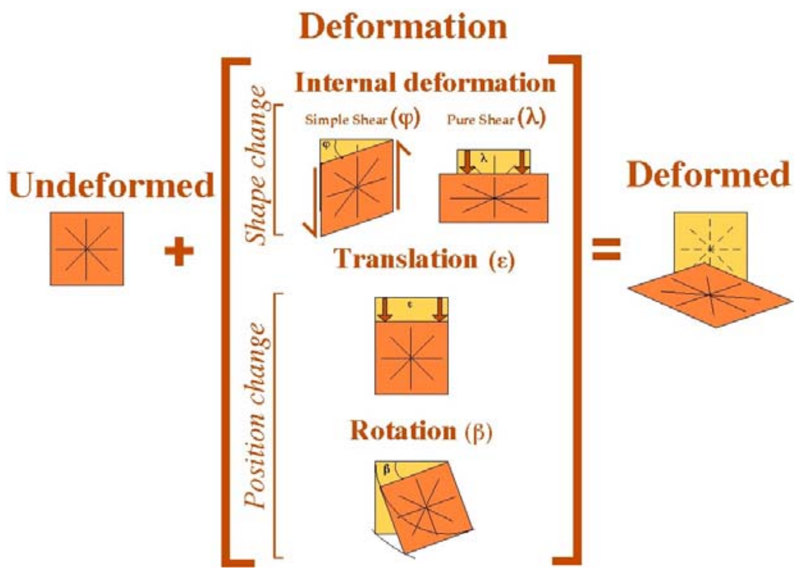

Figure 1.2: Deformation mechanisms. Paleomagnetism helps determining the rotation.

Paleomagnetism may be incorporated in many restoration tools. Particularly we center our study in geometrical surface unfolding algorithms valid for globally developable surfaces. *Developable surfaces* are those with Gaussian curvature equal to zero everywhere (Lisle, 1992). These surfaces in geology are stratigraphic horizons folded under *flexural conditions* that have minimum internal deformation. That implies surfaces isometrically folded with preservation of lengths and angles and consequently with preservation of area. By *globally* we mean that these constraints are valid almost everywhere but there are areas where internal deformation is possible. We can find this kind of structures in the fold and thrust belts (FATs) of competent layers at upper crustal levels.

In order to test the restoration methods we develop analog models of complex structures. Laboratory-scale models are based on non-coaxial structures of External Sierras (Pyrenees). These analogs are digitalized with photogrametry and X-Ray CT scanner techniques. In this way, models are completely characterized before and after deformation. This allows the calculus of strain ellipsoid of the folded surface and the comparison of the restored surface with the initial one.

Additionally to the unfolding algorithms, we propose the usage of paleomagnetism in a map-view restoration technique. With this restoration we undo the vertical axis rotations (VARs) occurred during a narrow period of time. We do not pretend to do a rigorous restoration but help the location of deformation areas in the cartographic map.

Premises	Objectives
Paleomagnetism (pmag) is reliable data known before and after deformation	Incorporation of paleomagnetism in restoration techniques
Pmag + bedding plane are complementary indicators in surface restoration	The new constraint may help to locate the deformation
FATs usually lead to globally developable surfaces	Development of flexural unfolding algorithms (piecewise and parametric)
Analog models are completely characterized before and after deformation	Usage of analog models to test restoration algorithms
VARs occur in a narrow period of time at tectonic scale	Development of map-view restoration to unravel VARs

1.3 Outline

We summarize in this section the main points of this PhD. In the background chapter we want to synthesize the relevant pervious knowledge. In the first section (2.1) we go trough and compare the main restoration algorithms, their strengths and limits. The second section (2.2) details the proper usage of paleomagnetism, paying special attention to its resolution and possible errors. The section on analog models (2.3) describes the usage of this kind of models in several areas, focusing on the techniques set forth here: photogrametry and X-Ray CT scanner; although we also describe laser scan techniques. Next section (2.4) relates the geological background of the particular models selected to develop the analogs: San Marzal Pericline (a conical fold) and Balzes Anticline (a curved fold) from External Sierras.

The following chapters explain the main core of the PhD. The chapter on analog models introduces the methodology developed for the two techniques (3.1) and the particularities of the analogs based on the geological structures explained before (3.2). The particular models are used in next chapters and the technique itself may be used in several areas for further research.

The next chapter is the main part of this PhD, in which we develop the restoration methods including the paleomagnetic constraint. *Pmag3Drest* is an unfolding algorithm based on a piecewise approximation (Gratier et al., 1991) (4.1) while the other is the equivalent based on a parametric approximation (Massot, 2002) (4.2). In order to evaluate the restoration results we define several control parameters to quantify the deformation (4.3).

Chapter 5 presents the results of the restoration methods applied to the two analog models developed. We perform a sensitivity analysis on the meshing and the pin-element and compare results with the same methods without using the paleomagnetic constraint. We also introduce the multi-surface restoration and compare results with a method of real 3D restoration. Chapter 6 analyzes the effects of paleomagnetism accuracy and resolution. In this chapter, we introduce an interpolation technique to be able to use the developed methods in real scenarios with scarce data.

Next chapter (7) presents a map-view restoration algorithm that only uses rotational data as initial data. We apply this technique to two study cases to evaluate its utility.Finally we conclude this work discussing the results and pointing its strengths and weaknesses (Chapter 8). We also propose further developments: might include faults and extend the idea to volume restoration, among others.

Appendices deal with the calculus of paleomagnetic data. The first appendix proposes a new tool and software (VPD) to help determining paleomagnetic vectors. The second presents the possible sources of errors and theoretically quantify the error: overlapping, shear errors and superposed folds.

2 Background

Understanding the methods and postulates of the thesis requires some knowledge about restoration methods, paleomagnetism, the regional geology of the Southern Pyrenees and model building techniques. While providing this background, we are also laying the foundations of our postulates about paleomagnetism as a useful tool to improve the results in restoration, and about computer and analog models as promising avenues to understand and evaluate restoration methods. More specifically, we set down the requirements needed to use paleomagnetism in restoration methods, we show the importance of using analog models for validation and we explain the geological background of the selected models.

2.1 Restoration methods

Restoration consists of returning a structure to its original pre-deformation state. A restorable structure is internally consistent and has a plausible initial geometry, usually assumed to be horizontal. That validates the interpretation of the reconstruction and helps finding strain patterns. In this section, we provide an historical review of main restoration methods from cross-section to 3D, from purely geometrical techniques to geomechanical ones. The first methods were developed along the 70's, although the technological developments over the last two decades have facilitated new tools and software packages with higher processing capabilities (e.g. Move by Midland Valley Exploration [Griffiths et al., 2002], gOcad with Kine3D by Paradigm [Moretti et al., 2005]; and Dinel3D by iGeoss [Maerten and Maerten, 2006]). Given this wide variety of methods the point is to know when to use each of them, depending on the assumptions taken for each scenario (e.g. extensional vs. compressional) and the available data. Last, we review the scarce usage of paleomagnetism in restoration.

2.1.1 Cross-section restoration

The term of balanced cross-section was first introduced by Chamberlin (1910) who assumed plane strain and constant area before and after deformation in cross-sections.

This idea was first applied in restoration techniques by Dahlstrom (1969), assuming that bed length and bed thickness remained constant during the deformation process, which is valid for post-depositional concentric deformation that produces no significant change in rock volume. This is the *flexural slip* method (Fig. 2.1A) mainly valid for fold and thrust belts (FAT belts) where internal deformation is assumed to occur mostly by layer-parallel simple shear located either in the fold hinges (tangential-longitudinal strain) or in the fold limbs (simple-shear). With the same assumptions Hossack (1979) uses balanced cross-sections to calculate the orogenic shortening, suggesting that the margins of orogenic belts have contracted by 35–54%. For oblique and inclined cross-sections Cooper (1983) proposes a conversion to calculate the real strain.

Analysis on lateral terminations of FAT systems, and derived problems related to gradients of shortening, displacement fields, cross section balancing, etc. have been extensively tackled as well (Wilkerson, 1992; Marshak et al., 1992; Hindle and Burkhard, 1999; Wilkerson and Dickens, 2001; Wilkerson et al. 2002; Soto et al., 2006)

Later on, cross-section restoration has been applied in extensional tectonics (Gibss, 1983). The typical method valid in these cases, in particular for hanging wall rollovers associated with half grabens, is the *simple shear* (Fig. 2.1B), which assumes the preservation of distances in the shear direction (not the bed length neither the thickness). The shear direction is specified as having a dip α with respect to a regional that does not change during deformation. This angle is usually around 60º but can vary along the fault.

In cases where no internal deformation is observed the method applied is the *rigid body displacement* (also called *domino style*) (Fig. 2.1C) in which everything is preserved: bed lengths, thicknesses, areas and even cut-off angles between faults and horizons. Only rigid body translations and rotations are allowed.

For structures in which deformation has produced significant changes in the original bed lengths and thicknesses (e.g. for decollement levels such as shale or salt) the method applied is *area balance* or *ductile flow* (Fig. 2.1D) where only global area is preserved (Miltra and Namson, 1989). These methods do not depend on specific kinematic models (independent on the evolution of geometry through time) and in that sense represent the most general approaches.

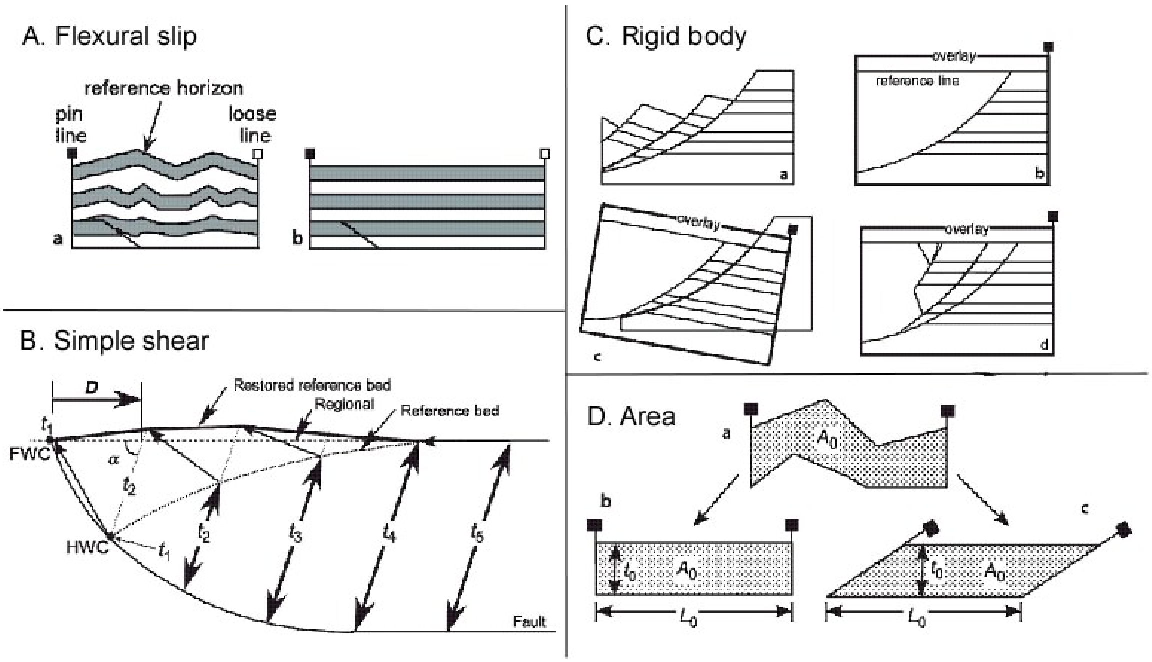

Figure 2.1: Geometrical cross-section restoration based on main kinematic models (Groshong, 2006). A) Flexural slip method. *Pin line*, solid-head; *loose line*, open-head. **a** Deformed-state cross section. **b** Restored section: equal bed lengths and a *straight loose line* indicate a satisfactory restoration. B) Simple shear oblique to bending, restoration of the hangingwall of a fault. *FWC:* footwall cutoff of reference bed; *HWC:* hangingwall cutoff of reference bed; *t*i: distance between reference bed and fault, measured along shear direction; α *:* shear angle; *D:* block displacement. C) Restoration of rigid-body displacement by the overlay method. **a** Section to be restored. **b** Preparation of the overlay. **c** Restoration of the first block. **d** Complete restoration. D) Area restoration. *A*0: Original area; *t*0: original bed thickness; *L*0: original bed length. Shape of the restored area depends on assumed original orientations of the pin lines. **a** Deformed-state cross section. **b** Section restored to vertical pin lines. **c** Section restored to tilted pin lines.

Commercial software helps to apply these methods (Geosec_2D, Locace, 2D_Move; Kligfield et al., 1986; Moretti and Larrère, 1989). Moreover, all these geometric rules described here can also be used in kinematic forward modeling (Elliott, 1983) to infer the geometry of structures. Furthermore, they are the starting point for 3D restoration methods. Many algorithms have been developed since then, but the simplest ones are still in use. 2D balance is used extensively to validate concepts as well as individual interpretations, and to build workflow templates that are then used in 3D interpretation or to guide 3D balancing (Groshong et al., 2012).

The methods described so far assume homogeneous strain that produces affine transformations (rigid-body translation and rotation plus internal deformation). However, these linear transformations cannot, in general, preserve both area and continuity (gaps and overlaps may appear). Non-linear algorithms based on strain-minimization have been developed trying to solve that (Wickham & Moeckel, 1997). Moreover, strain measurements and fault discontinuities can be incorporated. On the other hand, these methods are too sensitive to boundary conditions (as pin-line and reference surface).

2.1.2 Map-view restoration

Map-view restoration methods are also two dimensional techniques. They are mainly geometrical methods based on finite-element techniques and least-square fitting which were first applied in geology for ductile deformation (Schwerdtner, 1977; Cobbold and Percevaut, 1983). Audibert (1991) developed a method of rigid blocks for dominantly strike-slip deformation and Rouby et al. (1993) for normal faulting regions (Fig. 2.2). Both divide the initial region into rigid horizontal blocks bounded by faults and heaves (real or artificial respectively) and use an iterative algorithm to minimize the sum of the squares of the distances across cut-off lenses.

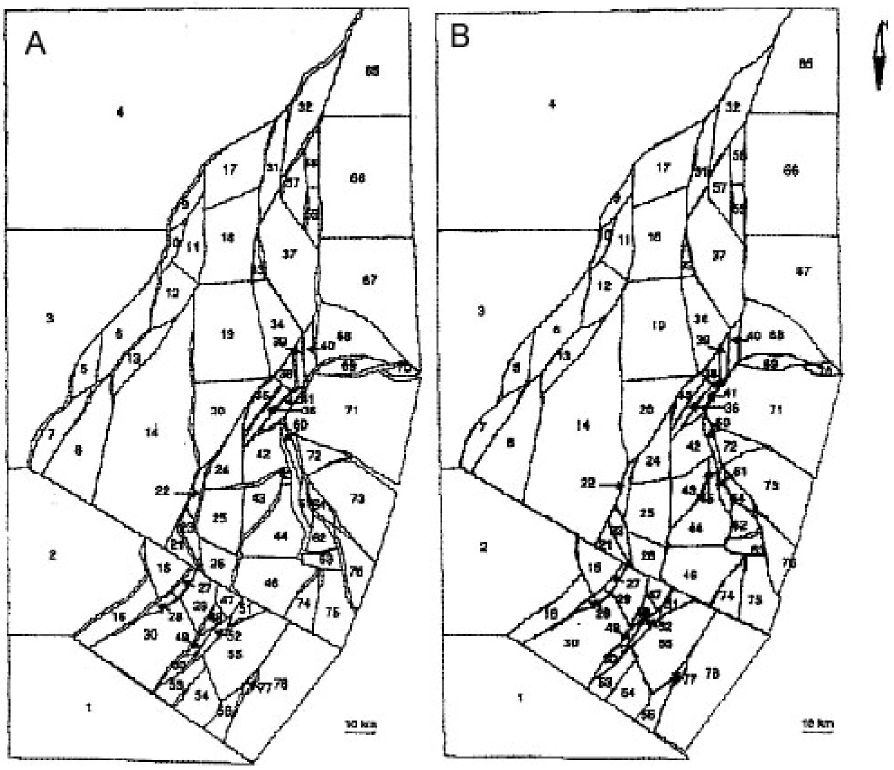

Figure 2.2: Map-view restoration of Campos area in Brazil (Rouby et al., 1993). A) Fault block map of Campos area in deformed state. Fault blocks are sequentially numbered. Cut-off lenses appear as gaps. Artificial faults appear as straight lines without gaps. B) Fault block map of Campos area in restored state. Between the blocks are some remaining gaps and some overlaps (black).

2.1.3 Surface restoration

Here, stratigraphic horizons are represented with triangular meshed surfaces. Surface restoration is usually called 2.5D because only the top of the horizon is considered and not its thickness. They are usually extended to multi-surface restoration by assuming that the thickness of the layers is constant or varies in a controlled way. Rouby et al. (2000) break the process down into two separate steps: *unfolding* and *unfaulting*. In turn, unfolding algorithms are based on the two main deformation mechanisms extended from cross-sections: *simple shear* (Kerr et al., 1993; Buddin et al., 1997) and *flexural slip* (Gratier et al., 1991; Gratier and Guillier, 1993; Williams et al., 1997; Léger et al., 1997; Griffiths et al., 2002; Massot, 2002, Thibert et al., 2005). Simple shear assumes folds have internal deformation, whereas flexural slip assumes surfaces are globally developable (area and lengths are preserved) (Fig. 2.3). The unfaulting step involves dividing the region into blocks bounded by faults that can be solved with the techniques described in map-view restoration (Audibert, 1991; Rouby et al., 1993; Arriagada, 2004; Arriagada et al., 2008). Surface restoration can also be performed in one single step, using, for instance, finite elements (Dunbar and Cook, 2003) or parameterization of the surface (Massot, 2002).

Concerning flexural unfolding, first methods developed were based on the triangulation of the surface (piecewise) while last methods are based on the parameterization of the surface. Gratier et al. (1991) and Gratier and Guillier (1993) divide the surface in zones defined by a network of rigid triangular elements that are rotated to the horizontal and then fitted with its neighbors by translation and rotation minimizing the sum of distances (Fig. 2.4A). Williams et al. (1997) follows the same process with a different fitting, they minimize the finite strain preserving the total area of each finite element (Fig. 2.4B). On the other hand, Griffiths et al. (2002) define a slip system (composed by a template surface, target surface, pin surface and unfolding plane) and the surface is systematically restored preserving the connectivity of the nodes (Fig. 2.4C). This technique is the one implemented in 3DMove software; unfortunately, it is not valid for structures that have suffered rotation during folding because a plane of movement is assumed and therefore, out-of-plane movements invalidate the method.

Later on, several parametric approaches became to appear. Léger et al. (1997) define the unfolding process for a multi-surface in terms of parameterizations and solve it by a least-squares method assuming: initial horizontality, bed-length and volume conservation (Fig. 2.4D). Massot (2002) uses a different parameterization with isometric constraints, curvilinear coordinates are orthogonal in the undeformed state (Fig. 2.4E). The commercial module Kine2D for gOcad is based on this technique (Moretti et al., 2006, Moretti, 2008). In any case, all these algorithms are designed for developable surfaces (flexural slip assumption) and when surfaces are unfoldable, the algorithm searches for the best solution although the result is never deterministic.

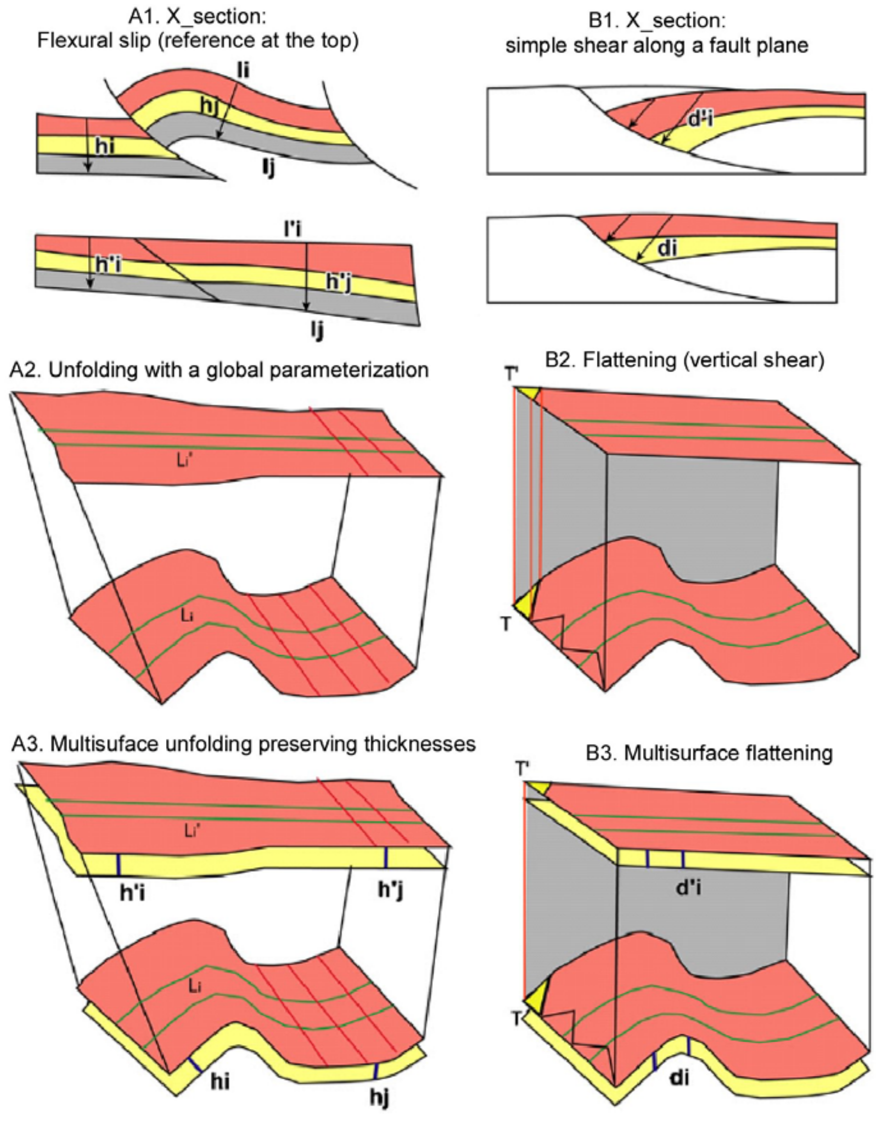

Figure 2.3: Simple shear versus flexural slip in cross-section, surface and multi-surface restorations (Moretti, 2008). A) Flexural slip: lengths, thicknesses and area preserved. B) Simple shear: distances in the shear direction (*di*) are preserved, thickness, lengths and areas change.

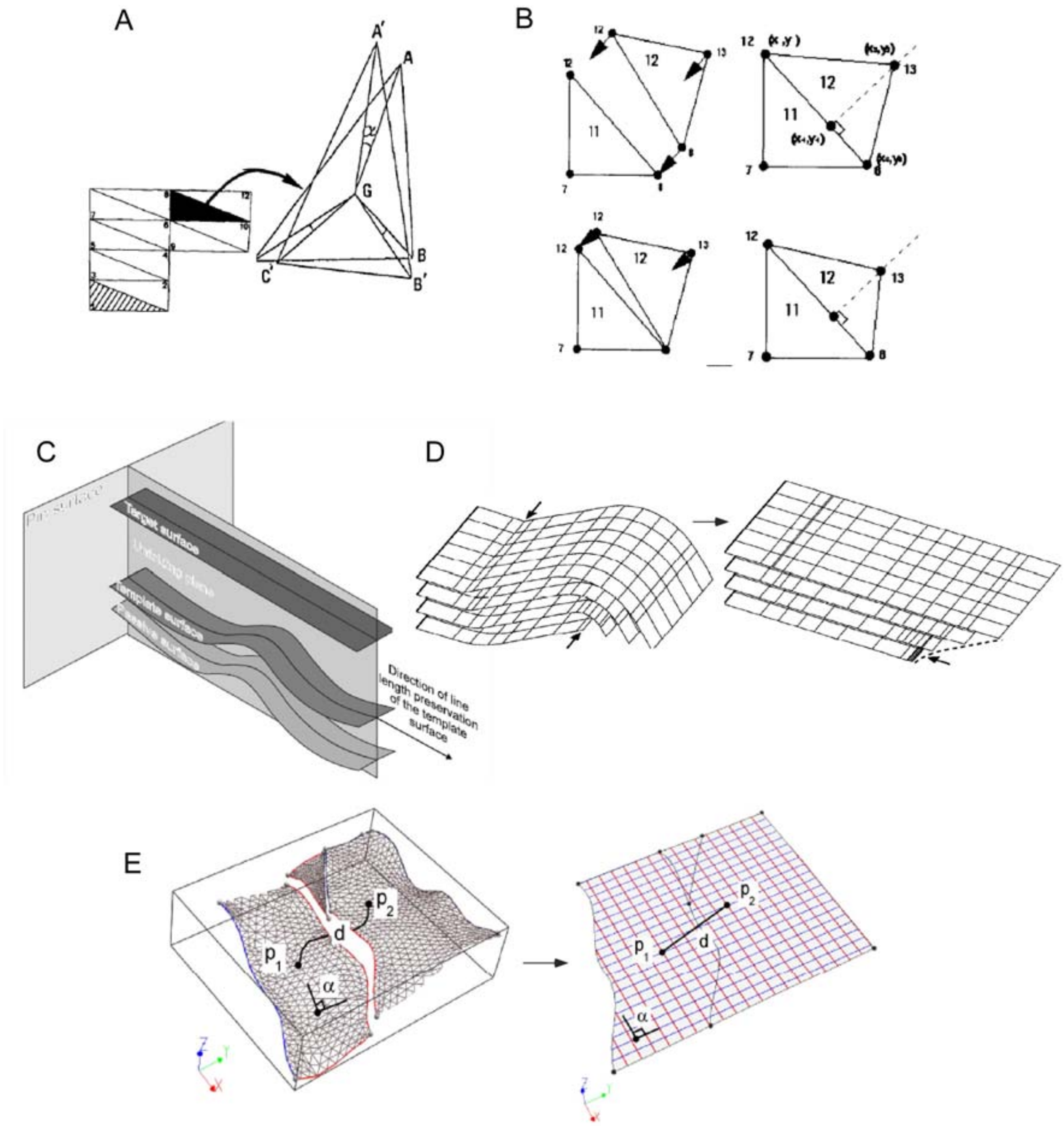

Figure 2.4: Flexural unfolding algorithms with piecewise (A, B & C) and parametric (D & E) approximations. A) After flattening to the horizontal, triangles are fitted with rigid translation and rotations to minimize distances between common vertices (gaps and overlaps remain) (Gratier et al., 1991). B) After flattening, triangles are sewed together preserving its area and minimizing the strain (Willliams, 1997). C) Line length is preserved in a given unfolding direction. Node connectivity is preserved. (Griffiths et al., 2002) D) Folded and restored structure least-square minimization as defined by Léger (1997). E) Folded and restored surface using isometric constraints (Massot, 2002).

2.1.4 Volume restoration

Real 3D restoration considers layers with thickness. The volume is represented with a grid or tetrahedral mesh. Lately, implicit approaches with relaxed meshed have been proposed (Durand-Riard et al., 2010). Last efforts leverage geomechanical approaches that meld the retrodeformational merits of kinematic balancing with principles of continuum mechanics (mass preservation and strain minimization; usually an elastic finite element model is used), without assumptions of plane strain and allowing heterogeneous fault interaction (Muron, 2005; Maerten and Maerten, 2006; Griffiths and Maerten, 2007; Guzofski et al., 2009). The drawback is that they are too dependant on boundary conditions apart from the computational requirements needed. There are also combined geometrical and geomechanical approaches (Moretti et al., 2005) and the usage of several techniques is also recommended (Lovely et al. 2012).

2.1.5 Paleomagnetism in restoration

The use of paleomagnetism in restoration tools was recommended in the early 1990's (McCaig and McClelland, 1992) as a way to tackle the restoration problem in 3D. So far, however, relatively few researchers have tried using paleomagnetic information to double-check the rotation inferred from restoration methods (Bonhommet et al., 1981; Bourgeois et al., 1997; Arriagada, 2004). These authors contrast the rotation data obtained with the restoration methods with real paleomagnetic datasets.

Recently, Arriagada et al. (2008) have modified the map-view restoration method, developed by Audibert (1991) and Rouby et al. (1993), to include paleomagnetic data as primary information during the restoration process (Fig. 2.5). Although their approach is the first we are aware of that incorporates paleomagnetic data, it is still a 2D restoration method, as are two map-view methods that have been proposed involving paleomagnetic vectors (Millán et al., 1996; Pueyo, 2000 and Pueyo et al., 2004). These map-view methods (Fig. 2.5), which correct shortening estimated from cross-sections and calculate realistic shortening (using trigonometric calculus), have recently been applied in the Pyrenees (Oliva and Pueyo, 2007) and in the Rocky Mountains (Sussman et al., 2012).

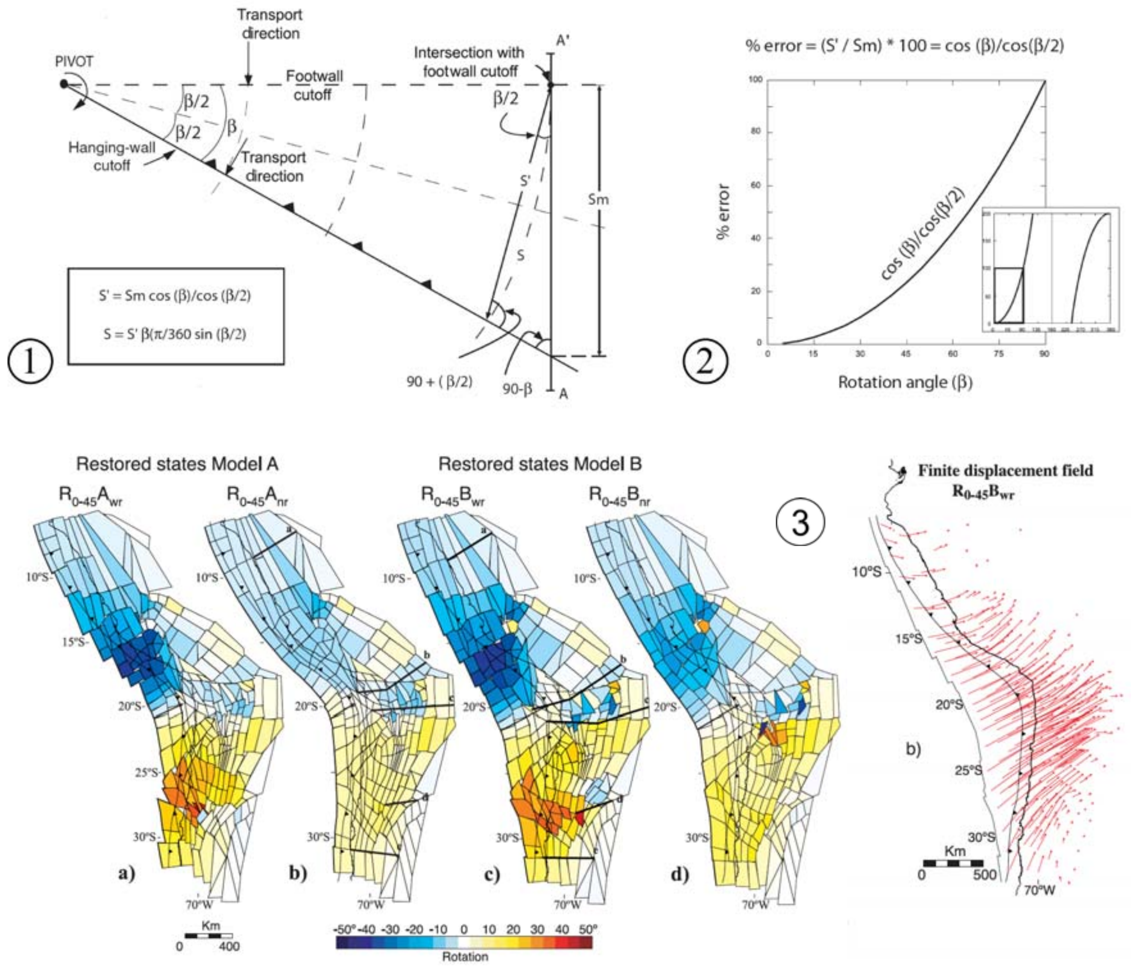

Figure 2.5: Applications of paleomagnetism in restoration techniques. 1) Map-view concept for correction of shortening estimates in cross-sections (Pueyo et al., 2004). 2) Shortening errors as a function of the vertical axis rotations (Sussman et al., 2012). 3) Map-view applications. Two-dimensional restorations of the central Andes using two shortening models (A and B) by Arriagada et al. (2008). Colors indicate rotations of each block during restoration. A) Restored map for model with constrained block rotations (R0–15Awr). B) without rotation constraints (R0–45Anr). Arrow illustrates total displacement of 210 km in the center of the orocline. C) Restored map for model with constrained block rotations (R0–45Bwr). D) Blocks are allowed to freely rotate during the last stages of the restoration (R0–45Bnr). Arrow illustrates total displacement of 430 km in the center of the orocline. Total (Paleogene to present) displacement vectors for restoration R0–45Bwr.

Paleomagnetism can be of great aid for structures with out-of-plane motions as it is the most reliable way to estimate vertical axis rotations (VARs). Of course, paleomagnetic data must be a proven and reliable record of the ancient magnetic field; the next chapter is devoted to this particular issue.

2.2 Paleomagnetism

Paleomagnetism is the study of the ancient Earth magnetic field (EMF) recorded by ferromagnetic minerals present in most rocks of the crust. Igneous and sedimentary rocks acquire an initial, or primary, magnetization shortly after formation, which is usually aligned along the Earth's field direction. This component may be unstable over time because of physical or chemical processes. Moreover, it can coexist with later, secondary, magnetizations and also register the ambient field direction. Thus, laboratory work is important to unravel the natural remanent magnetizations. The basic assumption to use paleomagnetism in many geological applications (e.g. detect absolute magnitudes of rotation) is that we can isolate the primary acquisition which is stable over time (Park, 1983) and it is a reliable record of the ancient field. Besides, the magnetic field is assumed to be generated by a Geocentric Axial Dipole (GAD) (Meert, 2009). Paleomagnetism is a good kinematic indicator to understand the processes of lateral transference of deformation.

Following the pioneering works on plate tectonic reconstructions (see overview by Van der Voo, 1993), paleomagnetism has been increasingly used as a fundamental tool to assess the tectonic evolution of deformed areas all over the world because of its great and exclusive potential in quantifying vertical axis-rotations in an absolute way. In the last 50 years (Norris and Black, 1961) paleomagnetic data have been extensively applied to tackle tectonic problems at different scales in several orogenic systems (see overviews at McCaig and McClelland, 1992; Allerton, 1998; Sussman et al., 2012). In particular, paleomagnetism has been increasingly used as key quantitative information for unraveling tectonic deformation in fold and thrust belts and for defining the timing of the bending by its ability to determine the distribution and magnitude of vertical axis rotations (Elredge et al., 1985; Weil and Sussman, 2004; Yonkee and Weil, 2010). Together with classic structural geology analysis, reliable paleomagnetic vectors allow a spatial and temporal understanding of fold and thrust belts, including complex case-studies of non-cylindrical and non-coaxial structures. All orogenic regions have been or still are under study; Pyrenees (Oliva et al., 2010 and 2012) Alps-Carpathian system (e.g. Pueyo et al., 2007; Marton et al., 2011), Eastern Mediterranean (Mattei et al., 2007; Speranza et al., 2011), Zagros (Aubourg et al., 2008), Himalayas (e.g. Antolín et al., 2010), Andes (Roperch et al., 2011), Rockies (Wawrzyniec et al., 2007), Appalachians (Stamatakos et al., 1996; Hnat et al., 2008 and 2009), Andes (Barke et al., 2007; Maffione et al., 2010), Rockies (Weil et al., 2010), the Cantabrian mountains (Weil, 2006), etc.

For deformed areas it has been suggested that the remanent paleomagnetic vector might be treated as a strain marker, assuming that the magnetization is entirely pre-tectonic. These means that deformation has not taken place only by rigid-body rotations but by internal strain and, accordingly, paleomagnetic orientation may be modified during the deformation process. As a first approximation, it is assumed that the remanent vector behaves as a passive linear marker, rotation toward the direction of maximum extension (Facer, 1983; Cogné and Perround, 1985; Lowrie et al., 1986; van der Pluijm, 1987; Kodama et al., 1988; Stamatakos and Kodama, 1991). However, the experiments do not always confirm this simple passive-rotational behaviour of magnetic vector (Borradaile and Mothersill, 1989). Therefore, to ensure the credibility of paleomagnetic data we better consider only samples from undeformed areas or where rock internal strain can be ruled out (or assumed as lineal).

2.2.1 Characteristic remanent magnetization direction

Calculation of a characteristic remanent magnetization (ChRM), as mentioned before, is a key step during paleomagnetic data processing. ChRMs are stable directions that can be effectively isolated from a given demagnetization procedure (thermal or alterning fields); subsequent application of stability tests is necessary to provide information on their geological significance. “Ideally, analytical methods (...) should be based on as much of the original magnetic information as possible, with minimal assumptions” (Kirschvink, 1980). Though, the best interpretation should always incorporate all available information (magnetic, geological, etc.).

The most common technique used to separate different paleomagnetic components is to eye-ball select the relevant demagnetization interval observed in an orthogonal projection of demagnetization data (Zijderveld, 1967). Once the demagnetization interval has been selected for each specimen, directions are fitted by principal component analysis (PCA) (Kirschvink, 1980). PCA is a least-squares method to determine the linear and planar orientations of the data. Collinear points indicate the progressive removal of one magnetic vector and determine the paleomagnetic direction.

Coplanar points exist when two simultaneous components define a demagnetization circle[1] (DC) (Jones et al., 1975; Halls, 1976). When a demagnetization routine completely demagnetizes a sample, the origin is the end-point of line through the demagnetization data; it is possible to calculate the resultant direction (R), while the other possibility is to calculate the difference direction (D) excluding the origin (Roy and Park, 1974; Hoffman and Day, 1978). Working with DCs, the paleomagnetic vector will be the intersection point between the demagnetization circles derived from different samples (Jones et al., 1975; Halls, 1976; Bailey and Halls, 1984). When multiple samples are analyzed, and where some samples provide clear end-point magnetizations and others give rise to DCs, some studies have focused on the problem of combining direct observations and intersections of demagnetization circles (McFadden and McElhinny, 1988).

After obtaining an individual ChRM for each specimen, the Fisher (1953), Bingham (1974) or *bootstrap* (Tauxe et al., 1991) statistics are applied to determine the paleomagnetic mean vector of the site and its precision. Fisher's parameters (α and k) are standard in most paleomagnetic studies (Van der Voo, 1990). Other preliminary or auxiliary methods such as the *Stacking Routine* (SR) (Scheepers and Zijderveld, 1992) are more objective and automatic. In the SR approach, an individual mean is calculated from specimen vectors for each demagnetization step for a given site and builds a stacked demagnetization diagram for the site. Other approaches have been used to automatically fit the ChRM; linearity spectrum analysis (LSA) (Schmidt, 1982) seeks to objectively establish the demagnetization interval by means of the quality of the directions (linearity is related to the maximum angular deviation or MAD from PCA). On the other hand, the *Line Find* method (Kent et al., 1983) is a statistical analysis of linearity and planarity that takes into account measurement errors. So far, there is no software integrating all these methods and the transference of data between them is usually intricate. In Appendix I, we propose a new program developed based on the virtual directions to help finding the ChRM: *Virtual Paleomagnetic Directions* (VPD), which also integrates other methods.

[1] A plane defines a great circle on an equal area projection

2.2.2 Reliability of paleomagnetic data in FAT belts

Following the philosophy of the reliability criteria established by Van der Voo (1990) to evaluate the quality of paleopoles, Pueyo (2010) proposed some specific criteria of a paleomagnetic investigation focused on the characterization of vertical axis rotations (VAR) in an individual thrust sheet:

1) Rock, deformation and magnetization ages are known.

2) A minimum of five sites (ten is desirable) per thrust unit (10-15 specimens per site) is available. Site mean is characterized by $\alpha_{95} \leq 10°$ (never > 15°) and k > 20 (never < 10).

3) There is a detailed demagnetization procedure isolating all magnetization components which should be fitted by PCA (Kirschvink, 1980) in which more than four steps should be involved in the calculation and MAD < 10° (never > 15°).

4) Field tests and error-control techniques (conglomerate, reversal, fold test and the small-circle intersection method) have to be performed to support the magnetization age.

5) Structural control is needed; fold and thrust geometry and kinematics should be known to avoid restoration errors.

6) The origin of the inclination error has to be identified among compaction, internal deformation and overlapping of directions by means of geometric techniques.

7) Rotations have to be contrasted to an appropriate reference in the undeformed foreland (absolute VAR) or in the nearest footwall (relative VAR).

For the surface restoration methods proposed in this PhD we do not intend to calculate a VAR but only use the paleomagnetic vector in restoration techniques. Among the former criteria only points 1 and 5 do not need to be fulfilled: only pre-deformation acquisition must be ensured (specific age is not necessary) and paleomagnetic vector is used *in situ* (before any bedding correction).

Table 2.1 summarizes possible sources of errors in the calculus of VARs that come from neglecting inherent assumptions about paleomagnetism in FAT belts (Pueyo, 2010). Note that, for the usage of paleomagnetism in surface restoration techniques, point 4 is not applicable because we use the vector before any correction.

Inclination errors, due to differential lithostatic load, are the most studied; corrections are proposed in (Tauxe, 2005). The other three possible sources of error with intrinsic structural (geometric) control are described in Appendix 2: overlapped paleomagnetic directions (C), rock volume deformation passively recorded by the paleomagnetic vector (D) and incorrect restoration of beds in non-coaxial structures (E).

Assumption	Source of error
1) For a given period of time, the EMF behaves as a geocentric axial dipole.	A) Insufficient averaged out of the secular variations.
2) Natural mechanisms of magnetic field acquisition may be efficient to allow the ferromagnetic minerals for an accurate field orientation recording.	B) Inclination flattening (shallowing). C) Overlapped directions.
3) The EMF memory may remain stable along the geological time.	D) Internal deformation of the rock volume.
4) A paleomagnetic vector restored to the ancient reference system (paleo-horizontal) allows quantifying the vertical axis rotations in this point (declination difference with the expected direction).	E) Wrong bedding correction in complex areas where a reverse sequential restoration should be performed.

Table 2.1: Error sources in the calculus of VARs.

2.3 Analog models

In order to evaluate the restoration methods developed in this PhD we are going to use analog models. Analog models are really useful because they let us know the simulations (based on paper, cardboard, fabric or plasticine models) have long been performed by geologists to conceptually illustrate and understand complex structures at the laboratory scale. In particular, scaled analog models as sand-box experiments (Hubbert, 1937; Ramberg, 1981; McClay, 1990) have played an important role in establishing key variables controlling the 3D geometry and kinematics of oblique structures in FAT belts (Colletta et al., 1991; Schreurs et al., 2001; Soto et al., 2002 and 2006; Reiter et al., 2011). To digitalize the analog models we summarize here three possible techniques, although we have finally used only the first two: X-ray computer tomography for volumes, photogrammetry and laser scan for surfaces.

2.3.1 X-ray computer tomography

X-ray computer tomography (CT) is a technique that uses X-rays to obtain cross-section images. The object to be scanned is illuminated with X-rays that interact with electrons, and the contrast in the image is generated by local differences in mass density and mean atomic number. Effectively, the intensity in slice images of the scanned volume is related to the photoelectric absorption property of the material. The sensitivity of CT to material properties like density and composition makes it very versatile.

X-ray CT, since its development in the 1970s, has been applied in many non-medical fields, among them geology. Specifically, it has been used for understanding the internal 3D geometry of a wide range of earth and planetary materials (see overview by Carlson, 2006). Within this field, the application of CT scanning techniques to reconstruct the 3D geometry of analog models deserves special attention (Colleta et al., 1991; Schreurs et al., 2001 and 2003; Adam et al., 2008). Reconstructions in 3D of a series of images obtained at different times during the experiment makes possible to obtain an overall 4D image. Current technological improvements allow virtually limitless and closely spaced serial cross-sections to be obtained and processed. Existing approaches do not, however, enable us to monitor the strain patterns within the model volume during the deformation.

2.3.2 Photogrammetry

Photogrammetry is a simple image-based modeling technique that assembles the 3D reconstruction using only photographs taken from different angles. This technique is an inexpensive, high-resolution, noninvasive, and efficient method that only needs standard commercial software (e.g. *PhotoModeler*[2]) and a digital camera to determine the x, y, z positions of high-contrast markers placed on the model surface. It has been used in geology by Fischer and Keating (2005) among others.

2.3.3 Laser scan techniques

Georeferenced laser-scan techniques have multiple applications in Earth Sciences; outcrop and topographic reconstructions, hazard surveying and others since they allow for 3D and 4D control of surfaces. For this reason they are very useful to reconstruct the topography of analog models at laboratory scale (Nilforoushan et al., 2008; Donnadieu et al., 2003). Even complex refolded structures can be tackled with the double-scan technique (Grujic et al., 2002) to avoid shadows and occlusion areas during the scanning. Looking to obtain a detailed topography of our complex geometries, we performed some trials at the Department of Design and Manufacturing Engineering (Area of Engineering Graphic Expression) of the University of Zaragoza in collaboration with Alfredo Serreta.

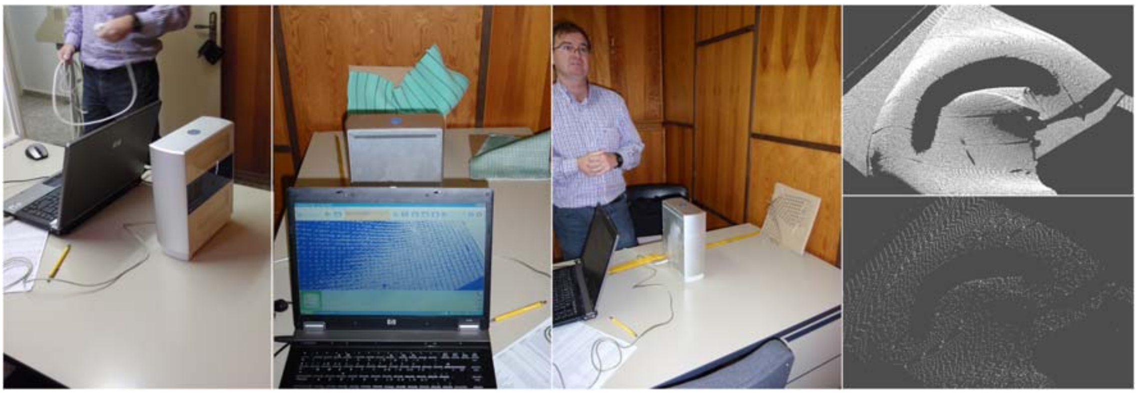

Figure 2.6: Laser scan digitalization with a very high-resolution scanner. It gives extremely dense point-clouds of the scanned surface. The use of only one scanner source impedes the total reconstructions of the complex model (shadows in figure).

Unfortunately, we had only access to either, very high-resolution scanner (for engineering design) or medium-resolution ones for topographic reconstructions. The use of the high-resolution scanners (Fig. 2.6) gave extremely dense point-clouds of the scanned surface that required a time-consuming and demanding post-processing. Besides, the use of only one scanner source impeded the total reconstructions of some

[2] www.photomodeler.com

of our complex models (see shadows in figure 2.6). These results motivated us to use the aforementioned photogrammetric techniques. Moreover, we finally discarded the usage of laser scan because it was unsuccessful to digitalize the reference system we required.

2.4 Geological background of analog models

The restoration methods proposed in this work are specially designed for fold and thrust belt structures (FATs), which have undergone out-of-plane motions and thus, may present different amounts of vertical axis rotation and tilting. The analog models developed to check the restoration methods are based on complex structures found in External Sierras (Southwesterern Pyrenees). Particularly, we have selected two type-structures: the conical fold of the Santo Domingo termination (San Marzal pericline) and the curved fold of Balzes Anticline. These are well-studied structures with much geological and paleomagnetic information. In this section we first and briefly introduce the geology of the Southwestern Pyrenees and the External Sierras and then explain in more detail the two complex structures that have inspired our geometric analogue models.

2.4.1 Geological setting

2.4.1.A The Southwestern Pyrenees

The Pyrenean orogen is an asymmetric, double-vergent fold-thrust wedge resulting from Alpine continental collision and partial subduction of the Iberian plate beneath the European plate (ECORS Pyrenees Team, 1988; Choukroune et al., 1989; Roure et al., 1989; Muñoz, 1992; Teixell, 1996). Tectonic compression occurred between the Late Cretaceous and Early Miocene (e.g. Puigdefàbregas and Souquet, 1986), giving raise to the North Pyrenean and the South Pyrenean thrust systems and their corresponding foreland basins (Aquitania and Ebro respectively). While the North Pyrenean thrust system verges to the north and developed over the European plate, the South Pyrenean thrust system developed on top of the Iberian plate and is characterized by south-directed thrust-sheets. It is the South Pyrenean thrust system, which has taken up most of the shortening within the tectonic wedge (Seguret, 1972; Muñoz, 1992; Teixell, 1998). Several units can be recognized in the Southwestern sector: the Axial Zone in the core of the mountains is followed by the Internal Sierras, the Jaca turbiditic and molassic basin and the southernmost thrust front; the External Sierras (e.g. Mallada, 1878; Almera y Ríos, 1951) (Fig. 2.7).

The structural evolution can be described in terms of the relation of basement and cover thrust systems (Fig. 2.8). The oldest Lakora thrust to the North is responsible for the development of the Larra-Monte Perdido cover thrust system during Paleocene-Eocene times (Teixel, 1998). The diachronic Gavarnie system broke the southern foreland and yielded the External Sierras thrust system during Lutetian to Rupelian times (Teixel, 1996; Millán et al., 2000; Huyghe et al., 2009). At that time, still under marine conditions, the foreland basin was very thin, a key factor to understand the number and wavelength of the imbricate thrusts. The younger basement thrusting (Guarga) took place during Oligocene-Miocene times (Millán et al., 2000) and it is responsible for the present-day elevation of the Western Pyrenees. The progression to the cover of the Guarga deformation reactivated the External Sierras sole thrust. At thas time, the cover rocks thicknesses were much higher, and heavily condition a new style of the deformation.

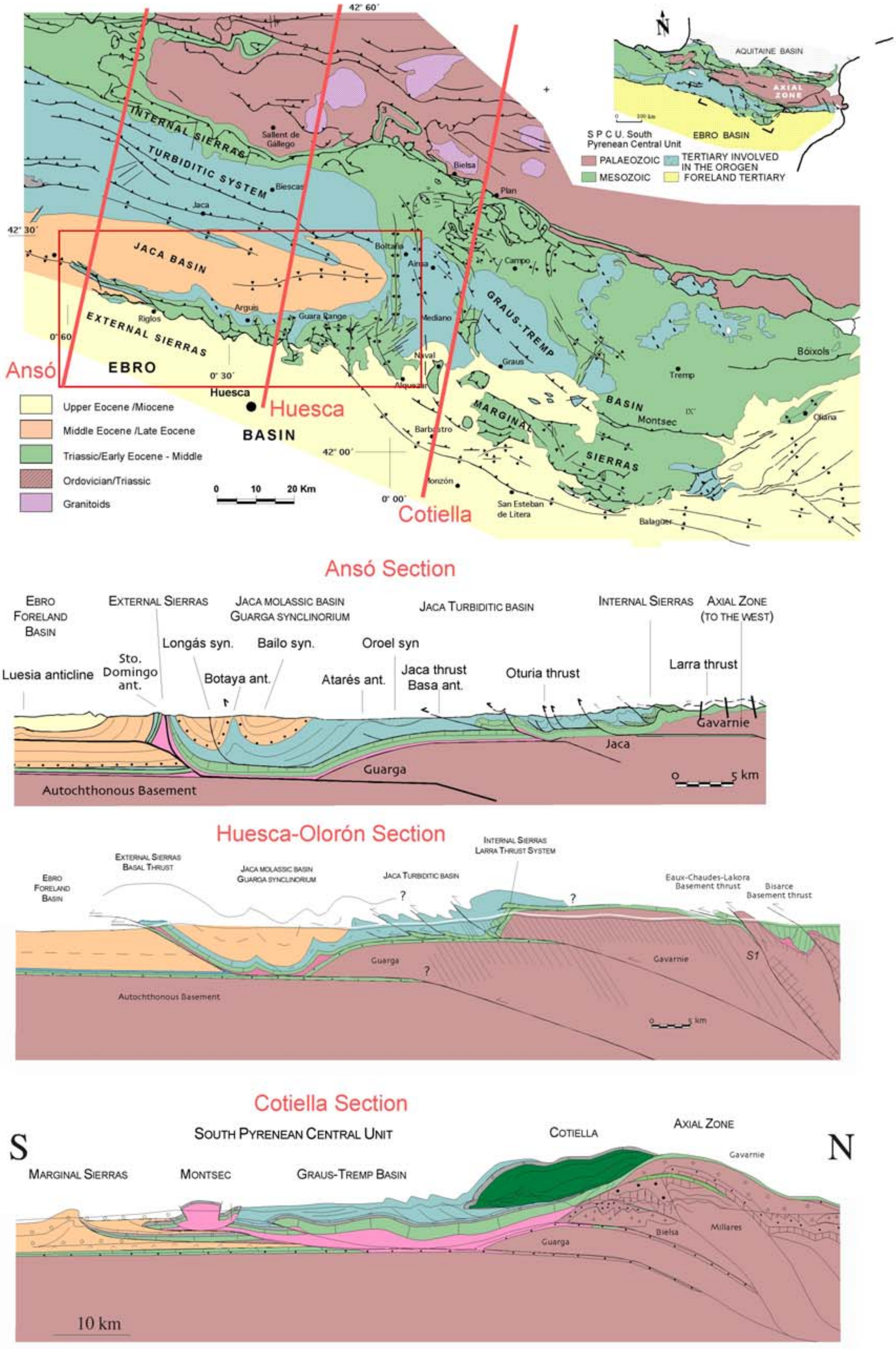

Figure 2.7: Geologic sketch map (Millán et al., 2000) and cross-sections from the Southwestern Pyrenees (Ansó by Teixell, 1996, Huesca-Olorón by Casas and Pardo, 2004 and Cotiella by Martínez-Peña and Casas, 2003).

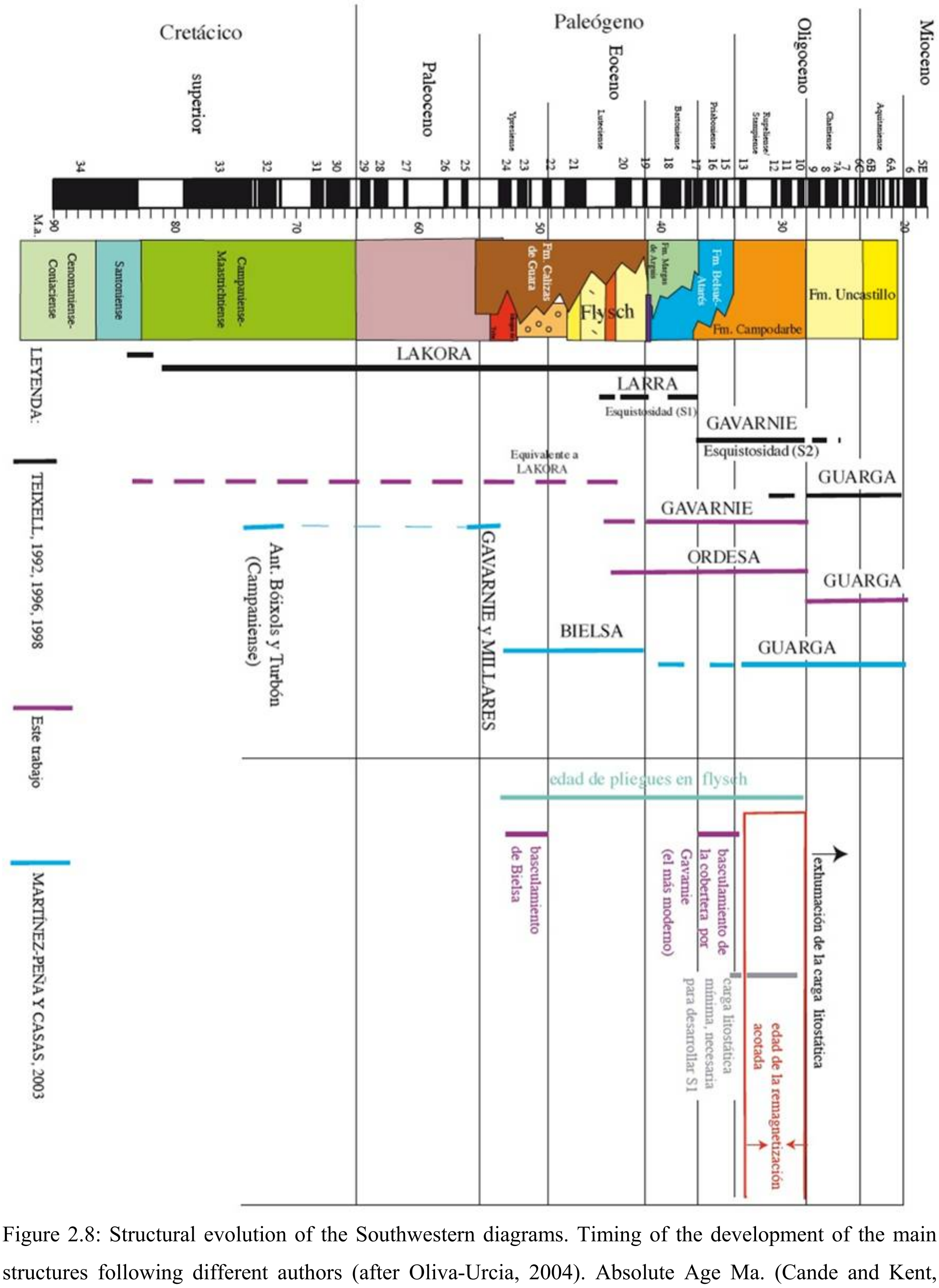

Figure 2.8: Structural evolution of the Southwestern diagrams. Timing of the development of the main structures following different authors (after Oliva-Urcia, 2004). Absolute Age Ma. (Cande and Kent, 1995). Black lines; ages deduced by Teixell (1992). Purple lines, those derived by Oliva-Urcia (2004). Blue lines by Martínez-Peña and Casas (2003).

2.4.1.B The External Sierras

The External Sierras (Fig. 2.9) are placed in the South Pyrenean sole thrust system, WNW-ESE trending and 100km long. They developed from Late Lutetian to Early Miocene (Puigdefàbregas, 1975; Arenas, 1993; Millán et al., 2000; Arenas et al., 2001), and caused the separation of the Jaca piggy-back basin to the North, from the main part of the Ebro foreland basin to the South (e.g. Puigdefàbregas y Soler, 1973; Ori and Friend, 1984; McElroy, 1990; Anastasio, 1992; Millán et al., 1995; Teixell y García Sansegundo 1995; Anastasio and Holl, 2001; Millán et al., 2000). The deformation of the Middle-Late Triassic to Early Miocene sediments were heavily influenced by the weak rheology of the Triassic evaporite deposits that served as a regional detachment horizon. The External Sierras display remarkable interference patterns between transverse (N-S to NW-SE) structures and the N-S trending Pyrenean folds and thrusts (e.g. Mallada 1878, Almera y Ríos, 1951). Millán et al. (1994 and 1995) suggests that the oblique structures were genetically related to the WNW-ESE thrust front, and also postulates that early in the structural evolution (Lutetian-Chattian), the External Sierras thrust system simultaneously developed to the south and west. Following the Chattian deformation, the kinematics changed significantly in the western and central segments of the South Pyrenean thrust system, as the development of the Santo Domingo Anticline (a regional scale detachment fold related to the emplacement of the Guarga basement thrust) and its associated south-directed thrust system progressively folded and/or truncated the earlier thrust structures. The evolution of the External Sierras involved a general clockwise rotation (e.g. Puigdefábregas, 1975; Burbank et al., 1987; Hogan and Burbank, 1996; Pueyo et al., 2002, 2003a, 2003b, 2004; Oliva et al., 2012a; Pueyo-Anchuela et al., 2012) that manifested itself in greater shortening towards the east (e.g. Soler, 1970; McElroy, 1990; Millán et al., 1995, 2000; Pueyo et al., 2004; Oliva and Pueyo, 2007a).

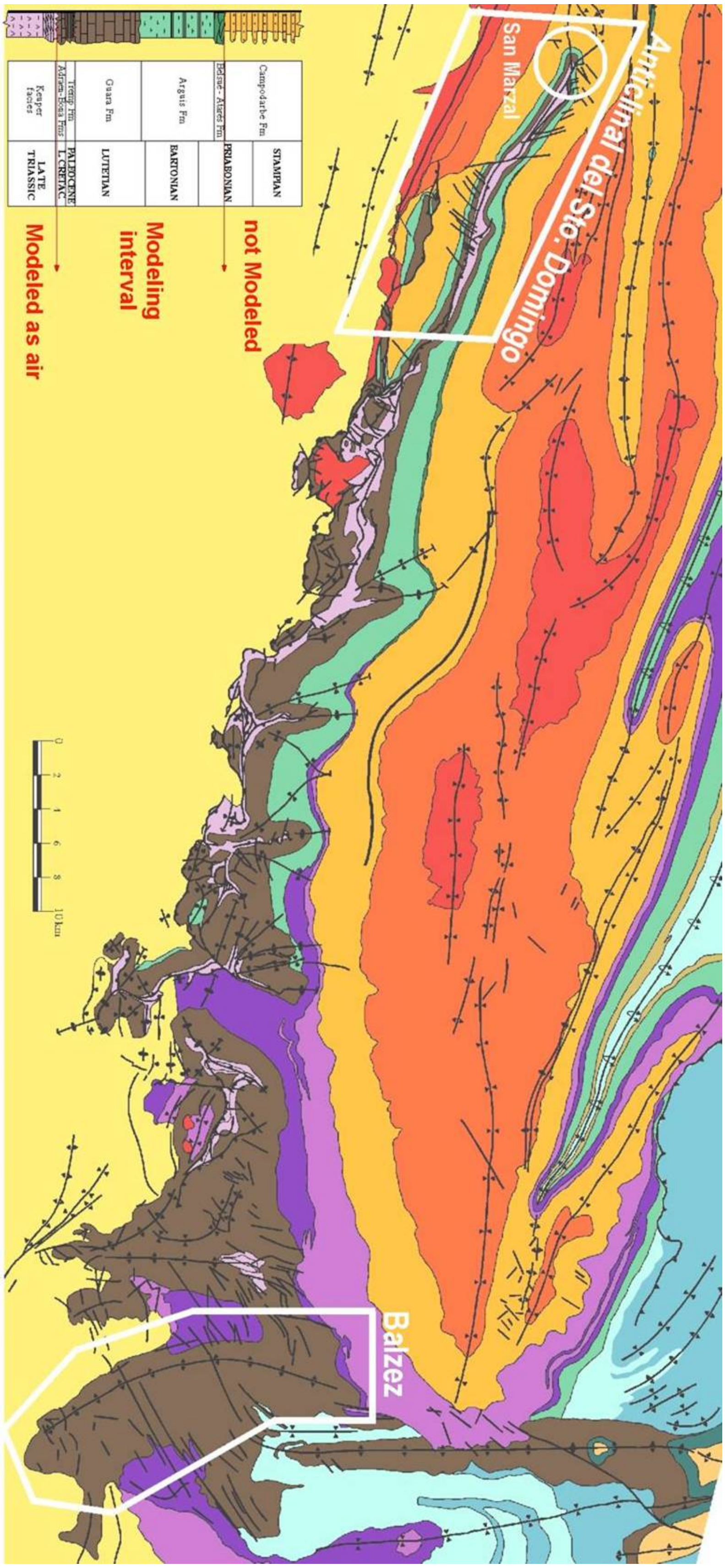

Figure 2.9: Geological setting of the External Sierras in the Southwestern Pyrenees displaying the location of the San Marzal Pericline and Balzes Anticline (mapping by Pueyo, 2000 integrating data by Puigdefábregas, 1975 and Millán, 1996).

Concerning the stratigraphy of the External Sierras, the lowest part of the well-exposed stratigraphic section is comprised of Upper Triassic evaporites (serving as the detachment horizon), marls and dolomites that are uncomformably overlain by Upper Cretaceous sandstones and limestones and Garumnian fluvial lacustrine facies. The shallow carbonate series of the Boltaña and Guara Fms. represent the Eocene platform that covers a great part of the south Pyrenean basin (Barnolas y Gil-Peña, 2001). In the western and central portions of the External Sierras, these Eocene carbonate deposits grade into the deposits of the Arguis Fm., consisting of azoic blue marls from outer ramp areas as well as shallow siliciclastic and carbonate facies from middle and inner ramp areas. The synorogenic deltaic sequences of the Belsué-Atarés Fm. span the Latest Lutetian to the Early Priabonian, and thin significantly to the west. Continental synorogenic strata, known as the Campodarbe Fm., is a 3000 to 4000 m thick fluvial sediment package which ranges in age from Late Priabonian to Stampian through the whole External Sierras, but is exclusively Oligocene in its western sector. Finally, the conglomerates, sandstones and siltstones of the Uncastillo Fm. span Late Eocene to Early Miocene. These strata border the southern edge of the External Sierras and lay uncomformably over the former lithostratigraphic units, recording the last compressive stages of deformation in the region.

2.4.2 Structural evolution of the External Sierras

Chronology of deformation. The emplacement of the cover thrust system coetaneous with the Gavarnie basement thrust displays a remarkable diachronic character (Millán et al., 2000). This diachronism is very well-established all along the External Sierras and Marginal Ranges (South Pyrenean Central Unit) as attested by numerous syntectonic deposits. In the External Sierras, this time gap spans from Lutetian deformation (Balzes Anticline) to the onset of folding during Rupelian (Sto. Domingo Anticline). Conversely, the reactivation of cover structures simultaneous to the Guarga basement thrust affects the entire South Pyrenean basal thrust in a more isochronic fashion (Fig. 2.10). Regarding our examples, the Sto Domingo Anticline continued the recently initiated folding (with a faster pace; Oliva et al., 2012c) and the Balzes Anticline was passively (piggyback) relocated over a basal ramp-flat setting.

This situation is responsible for the present day plunging to the North observed in the northern sector of the anticline.

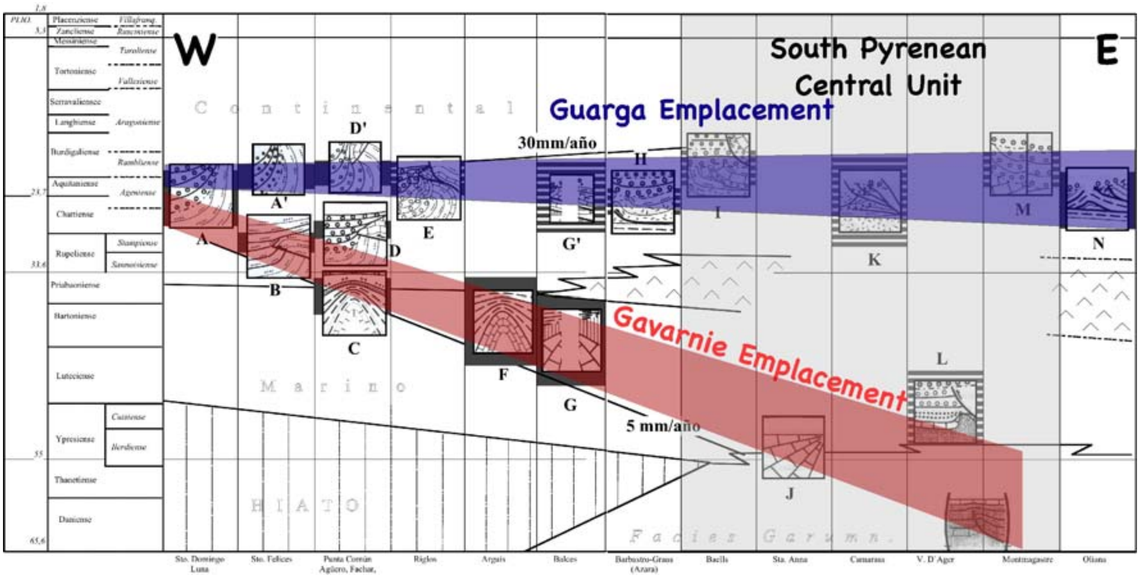

Figure 2.10: Chronostratigraphic chart of deformation evidences deduced from syntectonic materials all along the South Pyrenean Front in relation to the main basement events (modified from Millán et al., 2000).

4D evolution of the External Sierras front. The existence of abundant paleomagnetic and magnetostratigraphic data has permitted to accurately control the rotation magnitude, age and even velocity in some sectors and allows for an integrative analysis of the 4D evolution of the thrust front. The diachronic emplacement of the basal thrust during the Gavarnie activity together with the very thin marine sedimentary thickness is responsible for the structuring of the first imbricate thrust system, the low wavelength and the high density of oblique anticlines in the External Sierras (Balzes, Nasarre, Tozal, Gabardiella, Lusera, Pico del Aguila, Bentué de Rasal, Rasal, La Peña, Fachar and Peña Ronquillo).

The rotation activity of these formerly oblique structures, displaying systematic N-S present-day orientation, is normally coetaneous with the diachronic folding and thrusting events responsible for their genesis during the Gavarnie period (Fig. 2.11). This is demonstrated in those structures where synrotational sediments have been studied in full detail: Pico del Aguila (Pueyo et al., 2002; Rodríguez-Pintó et al., 2008), Boltaña (Mochales et al., 2012a), Balzes (Rodríguez-Pintó et al., 2013c), Mediano (Muñoz et al., 2013). Despite the onset of rotation is only partially established, a well-defined diachronism has been demonstrated for the end of the rotational movement. The rotation laterally vanishes at an averaged rate of ≈ 5 km/M.a. although this velocity may be faster if a non-steady scenario is considered. Comparable values could be expected for the rotation onset as regards of the remarkable similarities found with the lateral migration of the deformation along the External Sierras front (Millán et al., 2000) or the westwards onlap of the turbiditic trough (Labaume et al., 1985). Younger rotational activity (related to the Guarga emplacement) cannot be completely ruled out but, if exists, is expected to be very small. This observation, apart from the existent paleomagnetic data, is supported by the very quick lateral expansion of the Guarga thrust front (≈ 30 mm /year), which, in turn, implies a very small lateral gradient of shortening (and equivalent associated rotations of the thrust front).

Due to this complex deformation pattern (imbrication, obliquity, diachronity and two main deformation events), the External Sierras are an excellent natural laboratory to study the 3D geometry and kinematics of complex structures caused by non-coaxial axis of deformation and vertical axis rotations.

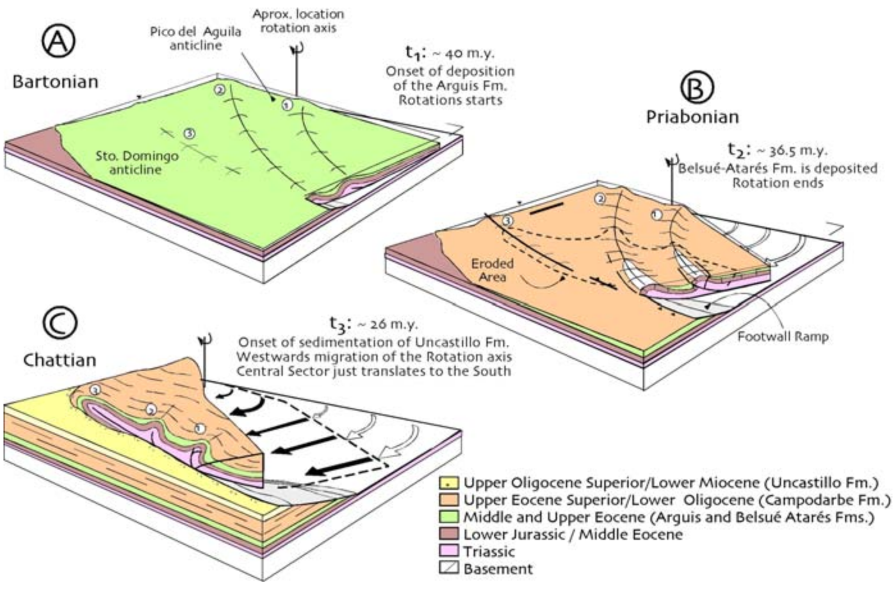

Figure 2.11: 3D diagrams (not to scale) showing a schematic rotation model of the evolution of the Western and Central sectors of the External Sierras front (Pueyo et al., 2002). A) t1 (40 Ma); at the beginning of the deposit of the marl sediments (Arguis Fm.), illustrating the effect of the onset of rotation in the hanging wall of the South Pyrenean basal thrust. B) t2 (36.5 Ma); until the end of the deposit of the transitional sediments (Belsué-Atarés Fm.), which also represents the end of the rotation of the basal thrust in the Central sector. C) t3 (26 Ma); during this period, the studied area did not show any significant rotations but experimented important translation towards the south, while for the same time span, the western sector of the External Sierras suffered important rotations.

2.4.3 San Marzal Pericline

The San Marzal Pericline is the lateral termination of the Santo Domingo Anticline, located at the westernmost sector of the External Sierras (South Pyrenean sole thrust). This deca-kilometric and apparently cylindrical anticline accommodated most of the shortening in that area. It strikes WNW-ESE, detaches along the incompetent Keuper facies and depicts parallel near-vertical limbs (Millán et al., 1995). It was active during Late Oligocene-Early Miocene (last stage of the structural evolution of South Pyrenean thrust front). Recent magnetostratigraphic studies (Oliva et al., 2012c and in prep.) in the southern flank of the anticline as well as and the reinterpretation of previous sections (Hogan 1993; Arenas et al., 2001) identify two distinct folding periods in relation to the Gavarnie and Guarga emplacements. These two periods display very contrasted folding velocities (Fig. 2.12).

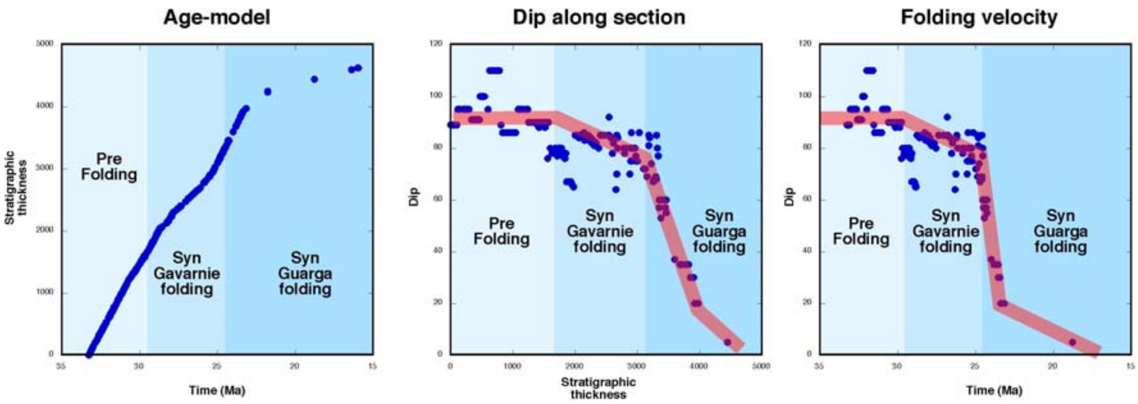

Figure 2.12: Kinematics of the Sto. Domingo Anticline deduced from the magnetostratigraphic studies in its southern flank (Luesia section by Oliva et al., 2012c and 2013 in prep)

The Mesozoic beds as well as the marine and lowermost continental strata of Tertiary age involved in the Santo Domingo Anticline describe a cylindrical closure at the western termination of the External Sierras: the, so-called, San Marzal Pericline which folds axis orientation is 305º, 67º (Fig. 2.13). The underground western geometry of the fold reflects a quick diminishing of the plunge of the axis (Oliva, 2000; Oliva et al., 2012a).

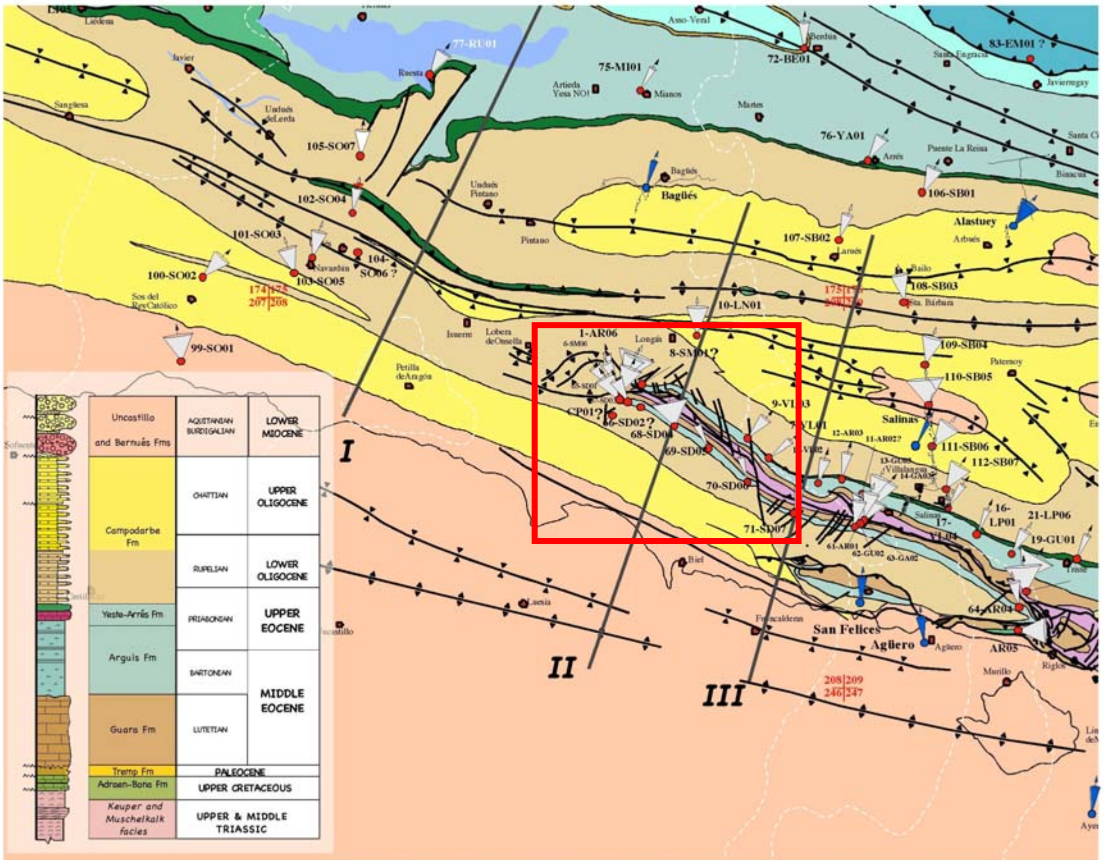

Figure 2.13A: Geological setting of the Sto. Domingo Anticline (red rectangle) at the western end of the south Pyrenean sole thrust. Geological sketch map displaying the location of paleomagnetic data and cross-sections (modified from Puigdefábregas, 1975, Millán, 1996 and Pueyo, 2000). Paleomagnetic rotations by Hogan (1993-blue) and Pueyo (2000-white) are also displayed; cone axis is the mean paleomagnetic declination and its semi-apical angle represents the confidence angle (α_{95}).

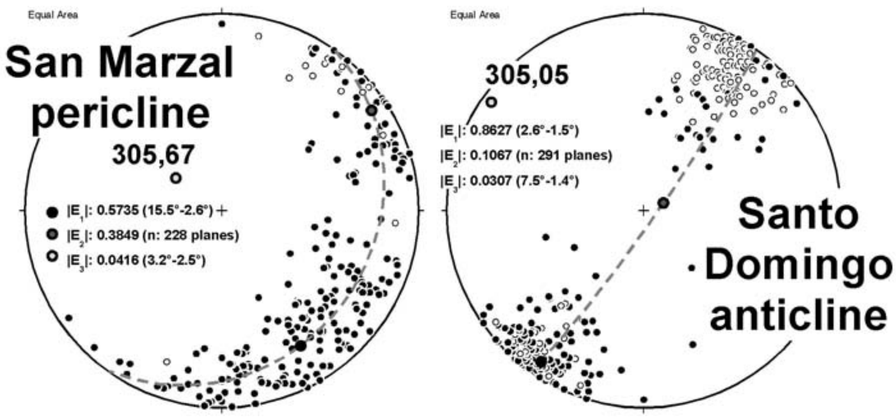

Figure 2.13B: Stereographic projection of bedding poles; San Marzal Pericline and Sto Domingo Anticline. A cylindrical best-fit (Bingham's [1974] statistics) performed with the Stereonet program characterizes the fold trend and plunge. Stereographic projections using *Stereonet* (Allmendinger et al., 2012 and Cardozo and Allmendinger, 2013).

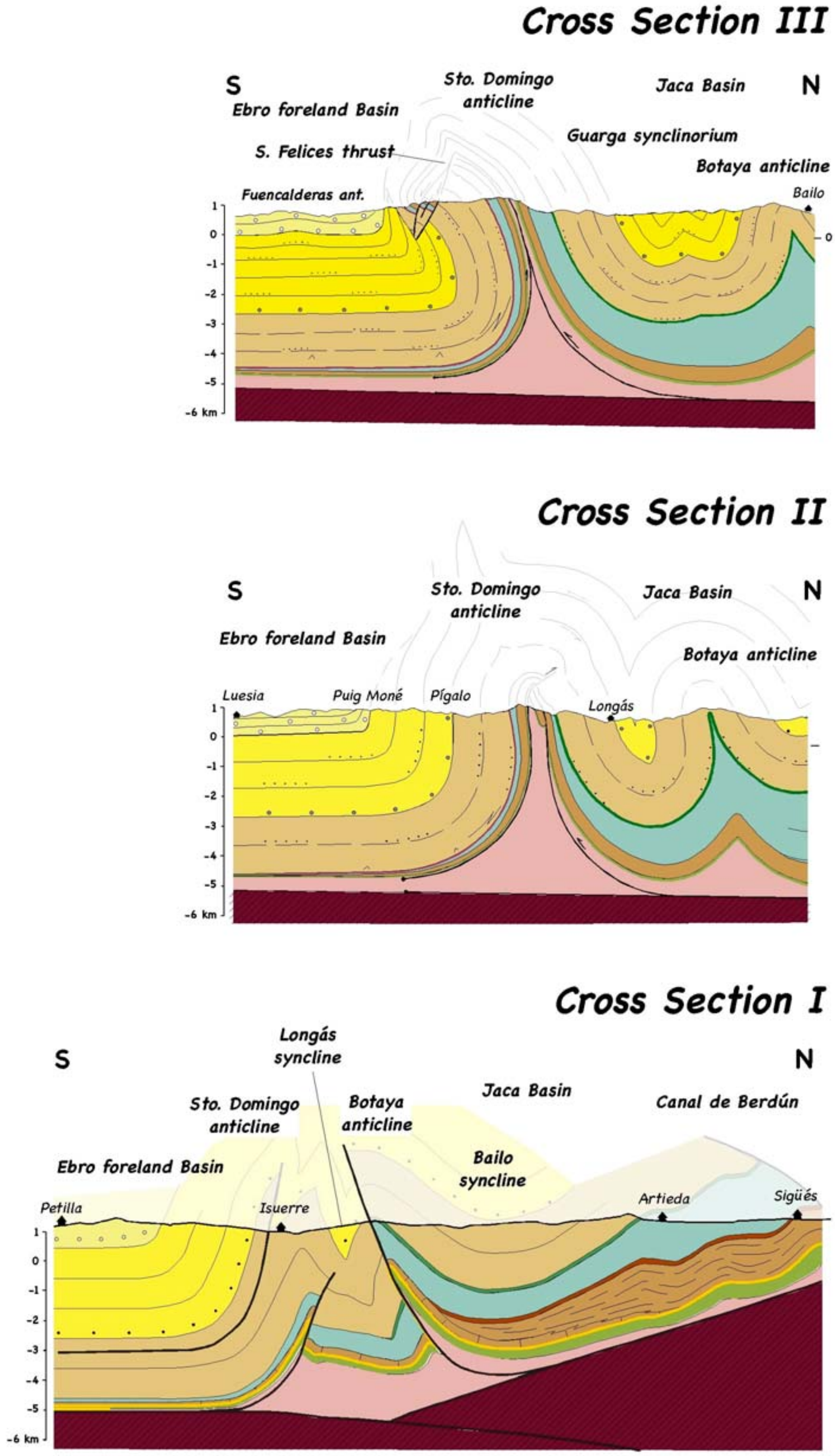

Figure 2.13C: Balanced sections in the western termination of the External Sierras; Cross section-I: Isuerre (Oliva et al., 1996 and 2012a) and cross section-II: San Marzal and III: San Felices (Millán, 1996). Note the effect of the fold axis plunge (cone generator trend) on the geometry of the pre-Campodarbe sequence.

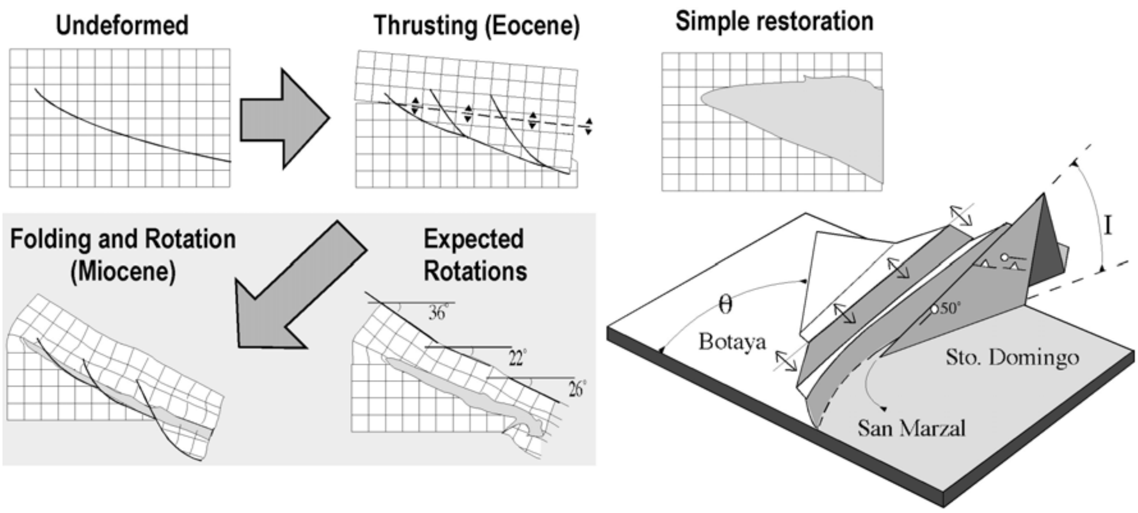

Figure 2.13D: Conceptual model for the Sto. Domingo anticline at the western end of the south Pyrenean sole thrust (Millán et al., 1992 and 1995).

The interest of this conical structure underlies in the large rotation magnitudes associated to its genesis, as originally proposed by simple analog modeling (Millán et al., 1992). Paleomagnetic analysis, carried out in fourteen marly sites (Arguis Fm.) at both flanks of the anticline as well as in the fold termination, attests a significant clockwise rotations (CW ≈ 45°) at the northern flank and almost 20° counter clockwise rotation (CCW) at the southern one (Pueyo, 2000; Oliva et al., 2012a; Pueyo-Anchuela et al., 2012). The sites located around the fold hinge (San Marzal area) display variable and gradual rotations between both extreme terms.

This particular geometry is probably due to three combined mechanisms: 1) The general lateral gradient of shortening associated to the emplacement of the External Sierras thrust system responsible for the about 30° CW rotation in average (McElroy, 1990; Millan, 1996; Pueyo et al., 1996 and 2004: Oliva and Pueyo, 2007a). 2) The lateral disappearance of the detachment level (Keuper facies) to the West, as demonstrated by the borehole records (Aoiz, Roncal and Sangüesa wells; Lanaja, 1987 and balanced cross sections by Oliva et al., 2012a) that would have produced a pinning effect and the conical geometry of the fold. 3) The southern flank CCW rotation seems to be local and it dies out to the Southeast of the Santa Engracia fault (Pueyo et al., 2003). Consequently this rotation looks to be a local effect probably caused by the pinning of the fold and the impossibility of the northern flank in accommodating more rotation.

Therefore the Santo Domingo anticline and the San Marzal lateral termination seems to be a pivot-point conical fold (in terms of Allerton, 1994) and it is a perfect paradigm of a complex-structure that can be used to test the reliability of our restoration method.

2.4.4 Balzes Anticline

The Balzes Anticline (BA) (Figs. 2.9 & 2.14) represents the southeasternmost structure of the External Sierras in the Southern Pyrenees. It is a 17 km-long curved structure with a fold hinge trending N011E in the northern sector passing to N152E in the southernmost sector, therefore, in map view, it displays an apparent bending of about 40° (southwestwards convex). Another interesting aspect is its connection with the N-S Boltaña anticline to the N, which partially overlaps the Balzes fold axis to the East.

In contrast to the western sector, the particular stratigraphy involved in the BA comprises three main marine platform sequences during the Eocene (de Federico, 1981; Barnolas and Teixell, 1994): the Ypresian Alveoline limestones of the first platform outcrop in the core of the structure; the Boltaña Formation (late Ypresian, locally Cuisian), the second platform, represented by ≈300 m of shallow limestones and siliciclastic input; and the third platform, the Guara Formation, made of up to 650 m of Lutetian limestones. The sedimentation of the Guara Formation was determined by the growing of the Balzes Anticline as attested by an angular unconformity (Fig. 2.15) observed in its western flank (Millán et al., 2000; Barnolas and Gil-Peña, 2001; Rodríguez-Pintó et al., 2012b). On top of the Lutetian, in the northern part of the anticline, the Sobrarbe deltaic formation (Bartonian) marks the transition to continental conditions, the onset of which is clearly indicated by the thick Campodarbe Group (Puigdefàbregas, 1975) cropping out in the core of the vast Guarga Syncline (Jaca Basin).

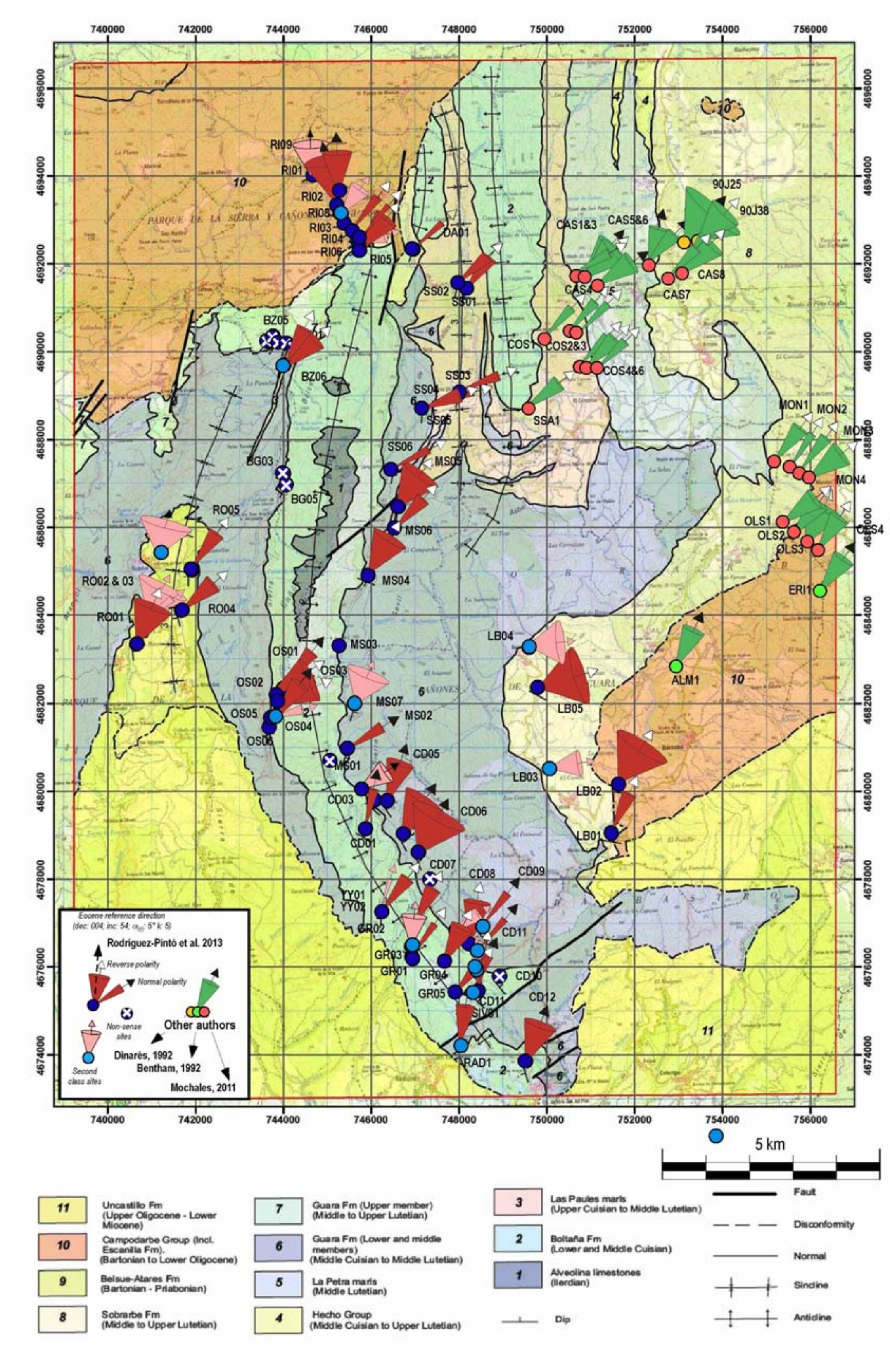

Figure 2.14: Geological map of the Balzes Anticline (Barnolas et al., in press) displaying paleomagnetically derivedvertical axis rotations. Data by Dinarès-Turell (1992), Bentham (1992), Mochales (2011), Rodríguez-Pintó (2013) compiled by (Rodríguez-Pintó et al., 2013c)

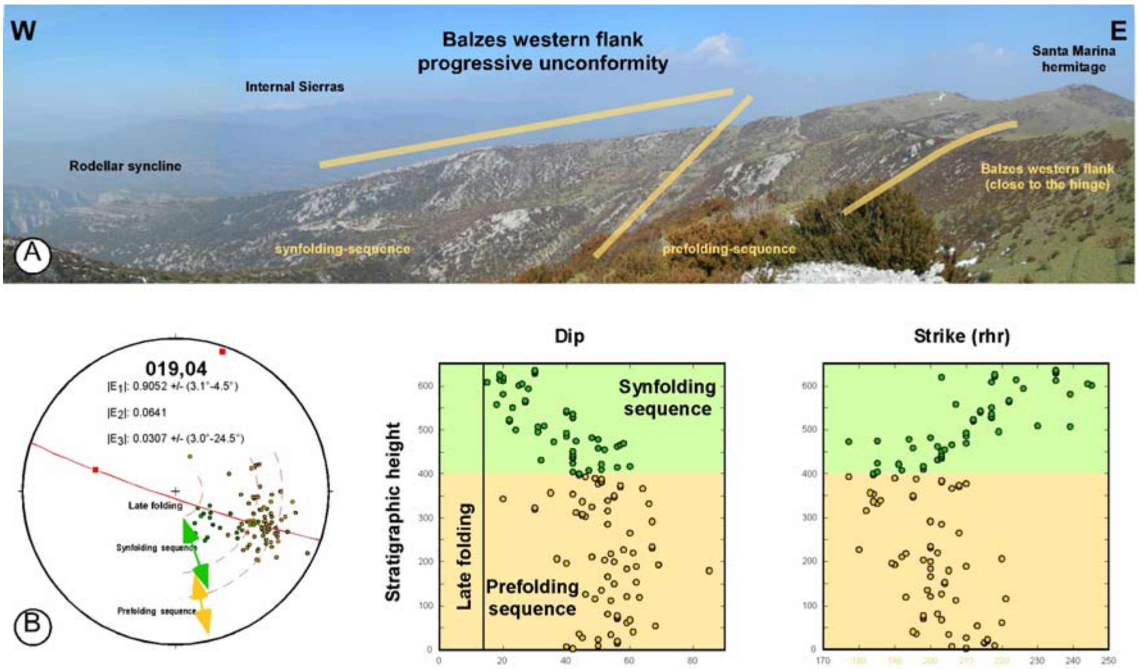

Figure 2.15: Folding kinematics of the Balzes Anticline based on the analysis of the Santa Marina progressive unconformity (Rodríguez-Pintó et al., 2013c). Picture taken near the Santa María de Bagüeste hermitage. B) Stereoplot of bedding poles along the Sta Marina magnetostartigraphic profile (Rodríguez-Pintó et al., 2012b). Strike and Dip versus stratigraphic height are also displayed (data by Rodríguez-Pintó, 2013).

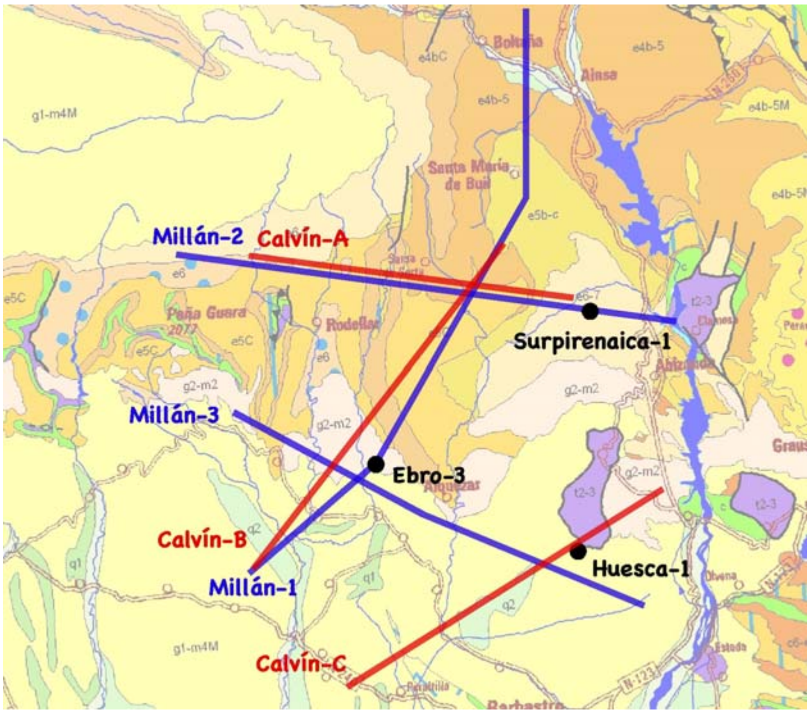

Figure 2.16: Selected cross-sections in the Balzes region, eastern External Sierras (Millán 1996; Calvín et al., 2013). Oil-exploration wells are also displayed (Lanaja 1987). Geological map by Barnolas et al. (2008).

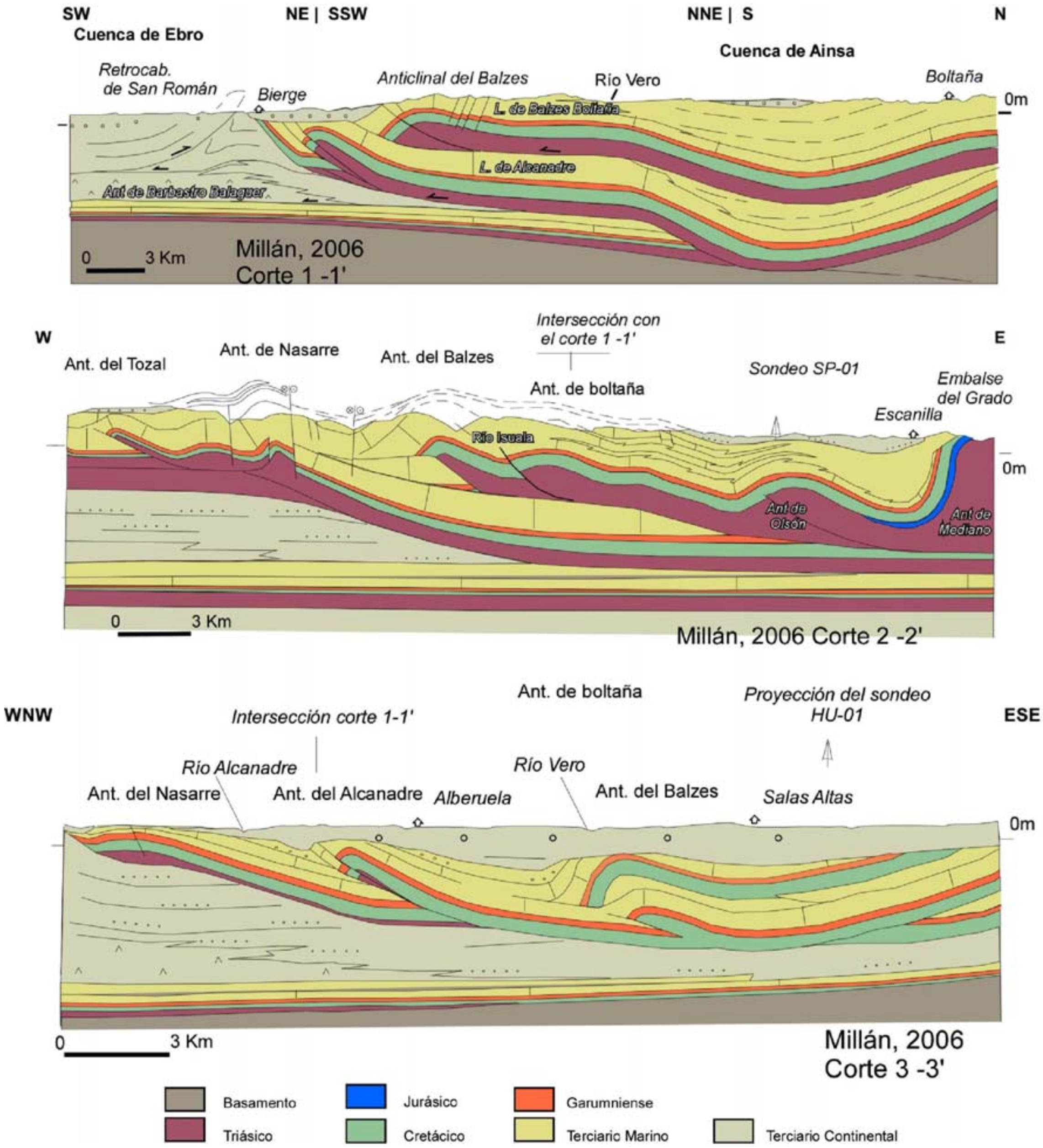

Figure 2.17: Cross-sections from the Eastern External Sierras (Millán, 1996; 2006)

Several cross sections are available in the region (Séguret, 1972; Cámara and Klimovitz 1985; Martínez-Peña, 1991; Gil & Jurado 1998; Soto and Casas, 2001; Santolaria, 2010) as well as borehole information (Lanaja 1987) but they diverge from a unique interpretation (Fig. 2.16). We have adopted the sections performed by Millán (1996) and Calvín et al., (2013) since they are serial cross-sections based on seismic interpretation, laterally consistent and built with a regional perspective. Despite the lack of agreement between them (Figs. 2.17 & 2.18), some considerations can be established.

The Mesozoic-Tertiary cover in this sector is thrusting over a sedimentary wedge belonging to the foreland Ebro Basin, with several imbricated thrust sheets striking between N-S and E-W. This imbricated thrust system shows a highdensity of thrust sheets in this region (Millán et al., 2000). The Balzes-Boltaña structure is located in the footwall of the Mediano-Olsón thrust sheet (to the Northeast) and over the Tozal-Alcanadre sheet (to the Southwest). The emplacement of these thrust sheets follows a piggyback sequence, and is diachronous, progressively younging to the west (Millán, 1996).

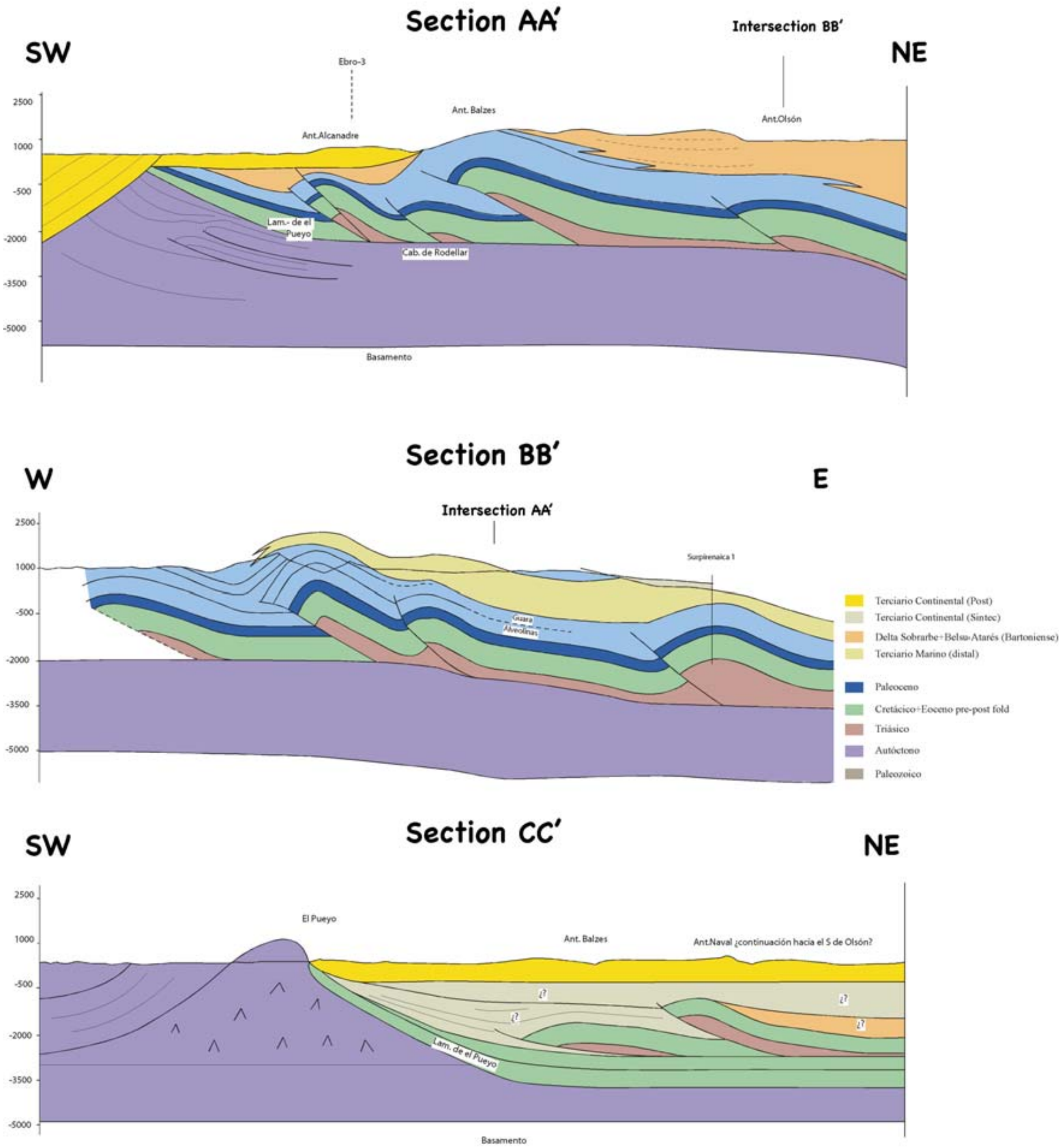

Figure 2.18: Cross-sections from the Eastern External Sierras (Calvín et al., 2013)

On the other hand, the geometry of the autochthonous footwall ramp, and the degree of superposition (i.e. displacement) between individual thrust sheets are still controversial (Rodrígez-Pintó et al., 2013c; Calvín et al., 2013); while some authors considered a major oblique ramp underneath the target structure (Millán, 1996; Fig. 2.17), others (Calvín et al., 2013; Fig. 2.18) considered that the complete thrust sheet system is directly located on a footwall flat, defined by the autochthonous Eocene evaporitic materials of the Ebro foreland Basin (Barbastro Fm.). In this case, a minor superposition of thrust sheets exists. In the northern sector, different structures (i.e. Olsón and Balzes anticlines) appear as detachment anticlines without significant displacements of the underlying thrusts. Conversely, in the southern sector there is a slight overlap defining a small footwall flat (a few kilometers) associated with the Balzes and Naval thrust sheets. This particular geometry in the south can be related with the thinning of the pre-tectonic stratigraphic series involved in thrusting and folding. Furthermore and for the same reason, in this sector the vertical development of structures is lower than in the northern sector and unconformable Tertiary materials of Ebro foreland Basin (Uncastillo Fm.) unconfomably cover the top of the thrust sequence.

Regional structural and paleogeographic studies in the area suggest a substantial increasing of the shortening eastwards (Puigdefàbregas, 1975; McElroy, 1990; Millán, 1996; Millán et al., 2000; Pueyo et al., 2002). This gradient, related to the vertical axis rotation, multiplies by a factor of 3 the shortening of the westernmost sector (≈ 10 km) in comparison to the easternmost sections (≈ 30km). Paleomagnetically derived vertical axis rotations of 40 to 60° have been observed in the Boltaña Anticline, to the north of the BA (Mochales et al., 2012; and references therein), while there are moderate CW rotations of 15 to 20° and non-significant rotations in the Bartonian-Priabonian deltaic and continental sediments to the east and south (Sta. Maria de Buil syncline) (Bentham, 1992; Bentham and Burbank, 1996; Pueyo, 2000; Mochales, 2011), pointing to a Bartonian-Priabonian age of the rotational emplacement of the underneath thrust sheets (Mochales et al., 2012).

Reliable paleomagnetic directions derived from 75 new sites in the Balzes anticline (>500 specimens from more than thousand) from Ypresian to Priabonian rocks have been recently obtained (Rodríguez-Pintó et al., 2013c) (Fig. 2.19). The ChRM is a single component direction, displays two polarities and passes the fold test. After comparing with the expected Eocene reference, individual sites display from negligible up to > 80° clockwise rotations. This variability is related to the fold curvature (Fig. 2.20) as attested by the strike vs. rotation diagram where a good-quality regression (VAR= - 46° + 0,511 * TREND [R = 0.9724]). It reveals the addition of primary and secondary curvatures (Fig. 2.20A) and then, the original (primary) curvature of this thrust sheet can be reconstructed. Synfolding materials attest a Middle-Late Lutetian major folding event recorded in a progressive unconformity (Santa Marina) (Fig. 2.15). The detailed analysis of the syn-rotational sedimentary record together with an accurate temporal calibration based on previous magnetostratigraphies has allowed us to obtain the rotation velocity for the Balzes anticline (5.2°/M.a.) as well as the rotation period (Lutetian-Bartonian) (Fig. 2.20B). These rate and ages are in agreement with previously published from the South Pyrenean front.

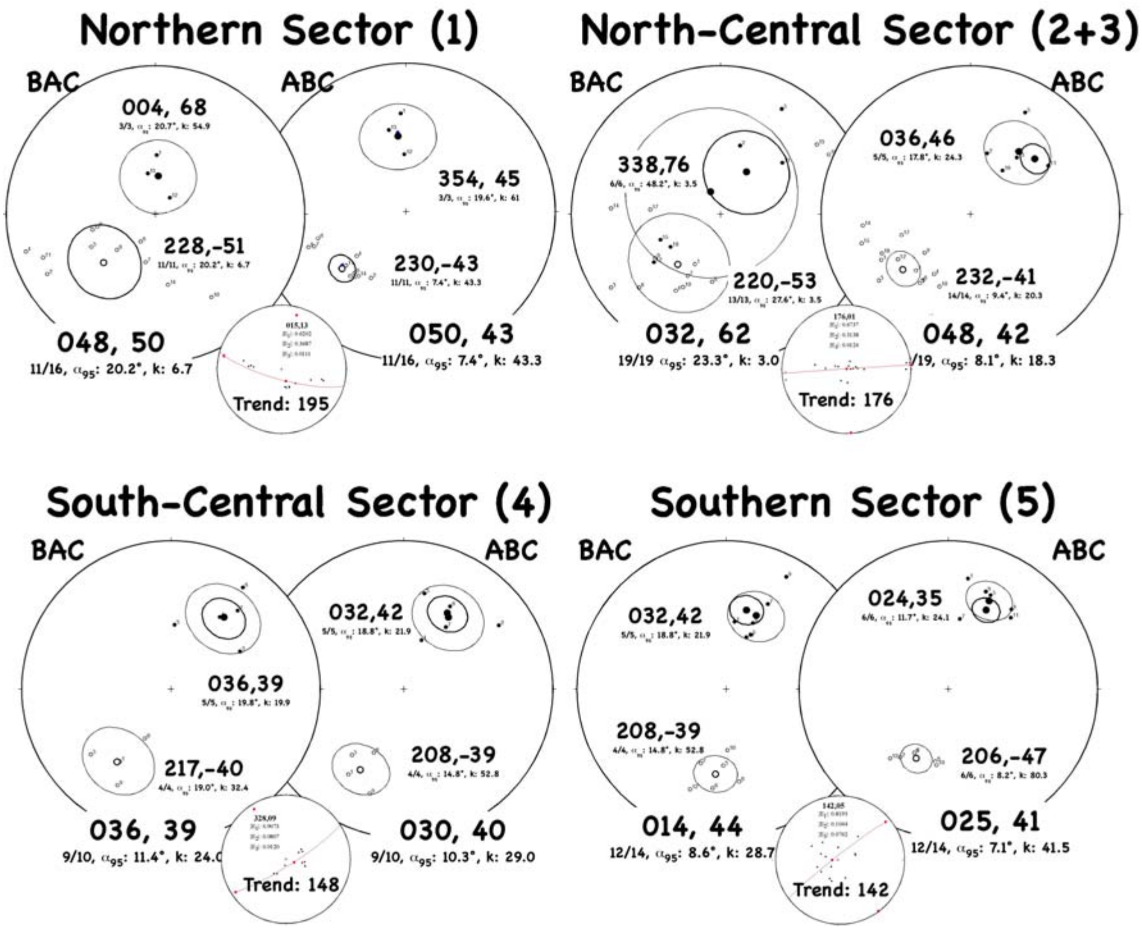

Figure 2.19: Paleomagnetic rotations in different sectors of the Balzes anticline (Rodríguez-Pintó et al., 2013c). Site means are projected before (BAC) and after (ABC) bedding correction. Normal and reverse polarities are treated separately and a global mean for every sector is only referred to the lower hemisphere. Fold axes trends are also displayed with their Bingham's (1974) distribution.

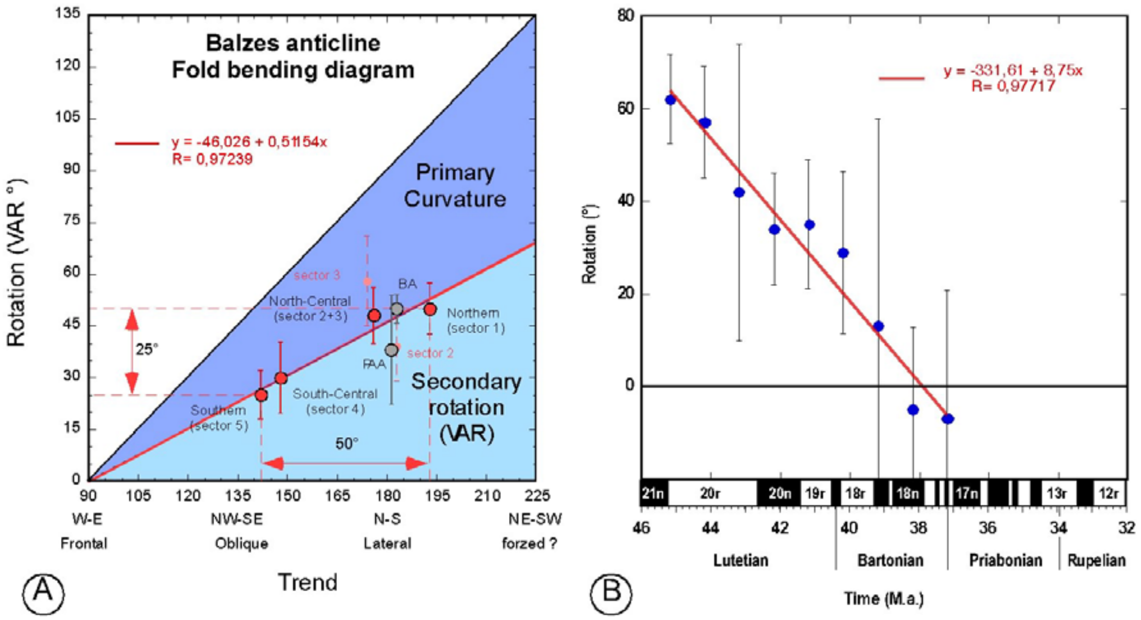

Figure 2.20: Balzes Anticline geometry and kinematics constraints (Rodríguez-Pintó et al., 2013c). A) Balzes curvature. Bending diagram (VAR versus structural trend) in the anticline, data from Boltaña (BA) and from Pico del Aguila (PAA) anticlines are also shown. B) Rotation velocity in the Balzes anticline. Paleomagnetic rotations derived from mean (robust) values obtained for discrete temporal gaps (2-3 Ma).

3 Analog models

Laboratory scale models are designed to evaluate the goodness of the restoration method. So far, we have developed static models in which only initial and final states are detailed. With these experiments we can fully characterize the geometry of any structure before and after deformation. Thus, they are perfect tools to compare the restored surface obtained with the restoration method with the initial and expected one.

The analogs we want to simulate are complex structures from fold and thrust belts (FAT belts) at upper crustal levels. In this work we have only modeled folded layers without considering the faults; the whole structure is divided by regions bounded by faults and each block is treated individually. In the upper crustal levels (within the first 5-6 km depth), competent layers such as limestones or sandstones behave more typically with a flexural slip mode (Ramsay and Huber, 1983). The preservation of lengths and angles (and consequently also areas) during folding is called in differential geometry as isometric bending. A remarkable property of isometric bending is that Gaussian curvature (the product of the two principal curvatures) is invariant and equal to zero everywhere; the surfaces are developable (Lisle, 1992). However, there may be some localized deformation in specific areas, i.e. flexural flow on the flanks or tangential longitudinal strain at the hinges (Ramsay, 1967). Therefore, we can speak about globally developable surfaces.

The other important property we want to simulate is paleomagnetism. We are going to plot lines on the surfaces to represent paleomagnetic vectors (declination component). The initial paleomagnetic vectors in a real scenario are not contained in the surface as those simulated, but we can simply rotate them to have null inclination and then be embedded in the surface. Only the declination is relevant. It is worth saying that, we assumed a perfect primary record of a GAD magnetic field.

Additionally, an interesting aspect that analog models may offer is the possibility to quantitatively measure the internal deformation, and not only qualitatively evaluate the results. An appropriate reference system allows the quantification of displacement, area or volume change and strain. The reference system proposed is an orthogonal grid drawn on each surface. The comparison of nodes location of two adjacent will allow us to reconstruct the strain ellipsoid (see more details later).

Otherwise, to digitalize or reconstruct the analog models we use two techniques already introduced: X-ray computer tomography scanner for volumes (built from a dense set of serial cross-sections) and photogrammetry for surfaces (built from a set of referenced nodes). The first technique requires materials with radiological contrast.

The restoration methods developed in this work are for single surfaces and do not for the whole volume. In that sense, only reconstruction with photogrammetry would be enough. However, the technique of CT scanner allows evaluating inner surfaces and opens a wide range of possibilities for future researches, like understanding complex structures and characterizing its 3D deformation patterns, as well as validating others 3D reconstruction and restoration methods and software. We show its potentiality with the example of the Balzes Anticline.

3.1 Methodology

In this section we describe the particularities of the analog models developed. These models are valid for flexural folds, they incorporate paleomagnetic data and an orthogonal reference system, and are appropriate for X-ray CT and photogrammetry reconstruction. We first describe the principles of photogrammetry because it is a technique with few requirements, and we focus later on the needs for the X-ray computer tomography (Ramón et al., 2013). The upper surface of models built for CT reconstruction can be also reconstructed using photogrammetry. In the last subsection we explain how to calculate the strain ellipsoid to quantify deformation using the orthogonal reference system.

3.1.1 Photogrammetry: principles and settings

Photogrammetry is a technique that only requires a few photographs taken from different angles to reconstruct a 3D model. Any conventional camera is valid as long as all photos are taken with the same focal length. The software used for the reconstruction is PhotoModeler. This program uses the description of the camera (including data on the focal length, imaging scale, image center and lens distortion) to build a proper geometrical relationship between points on the photograph and points in 3D space. This information is obtained by the camera calibration, performed by taking a minimum of six photographs of a reference grid provided by de program.

Once the camera is calibrated we take photographs of the model from different angles, in order to see all points from at least two views, and recommended from at least three. Then, we proceed with the referencing process, marking on two or more different photographs points that represent the same physical object in space. We mark all points that define the grid (the reference system that we have drawn on our model). From these set of *xyz* points we build the triangular mesh that defines the surface.

Accuracy depends heavily on the precise marking (or not) of locations on the images. A normal relative accuracy of 1:5,000 means that for an object with a 1 m largest dimension, PhotoModeler can produce 3D coordinates with 0.2 mm accuracy at 68% (one standard deviation) probability.

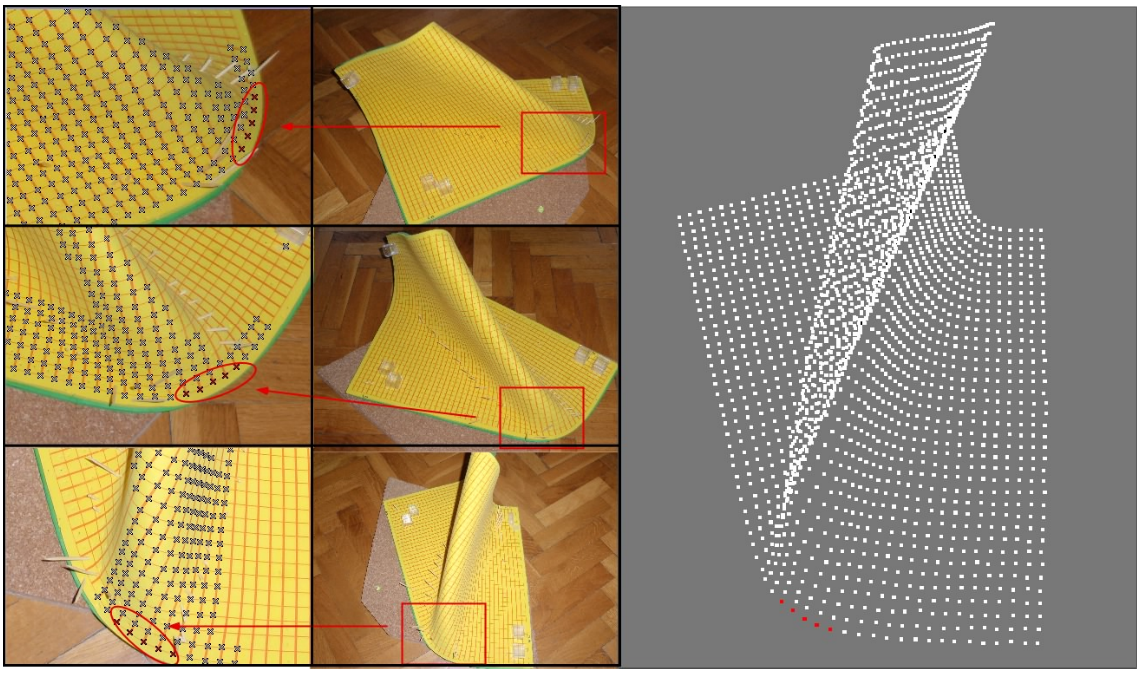

Figure 3.1: Analog model reconstruction with photogrammetry. Reference points are marked from several photos to build the 3D model (right). All photos must be referenced between them and all points must be seen at least in two photos taken from different angles.

3.1.2 X-ray CT: principles and settings

Conventional CT scanners used in medicine usually have millimeter-scale resolution based on using low-energy X-rays (below 125 kV). A scanner with these characteristics is sufficiently powerful for our purpose. If the object scanned has a low radiological density, it is possible to increase the intensity of the emission source. This should, however, be avoided when possible because of the risk of gantry overheating (in particular, the X-ray tube). Apart from the reological considerations, the proper selection of the materials to build the model is an important factor in achieving clear CT images.

We used a General Electric HiSpeed FX/i CT scanner at the Royo Villanova Hospital in Zaragoza (Aragon Health Service, SALUD) (Fig. 3.2) in collaboration with L.H. Ros and the Radiology Service technicians. For the current study, the settings selected to optimize the digital reconstruction were (Fig. 3.2): 1) axial scans, rather than helical, because they generate a sharper image, with the minimum slice thickness allowed (1 mm); 2) slices spaced 0.5 to 1 cm apart, which is close enough for the required resolution; 3) a high resolution chest CT protocol with a beam energy of 120 kV and low current of 180 mA to avoid gantry overheating; 4) the lung window to properly view the images on the CT system; and 5) the DICOM format to export the data to the 3D reconstruction software.

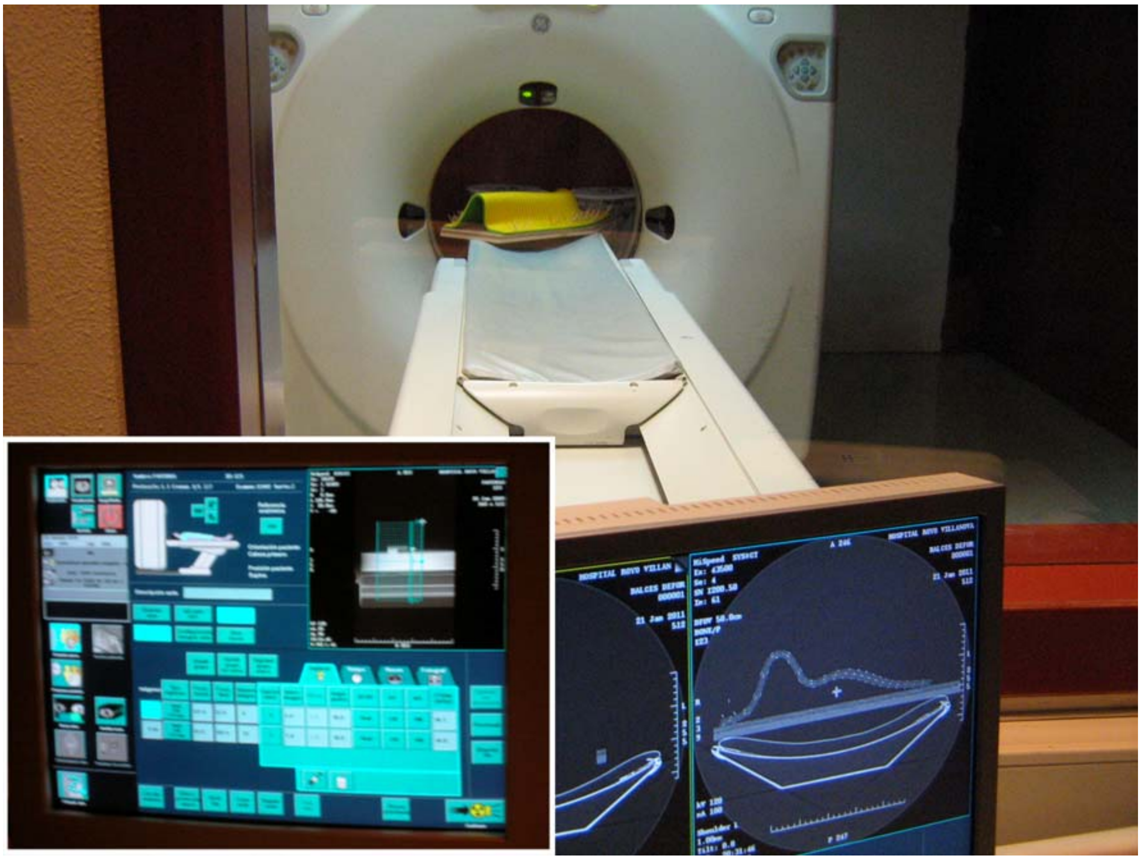

Figure 3.2: General Electric HiSpeed FX/I CT scanner at Royo Villanova Hospital in Zaragoza. Left bottom inlet. Scanner settings in the main menu.

3.1.3 Materials and rheology

Many of textile fabrics accomplish the basic geometric principles of isometric folding. They can be complexly folded but they will always be (globally) developable. Therefore, simple fabric simulations can be a very useful basis for realistic 3D models (Fig.3.3).

Among the many possible materials, ethylene vinyl acetate sheets (EVA, also known as *expanded rubber* or *foam rubber*) allow almost any kind of deformation, including flexural flow and flexural slip as well as tangential-longitudinal strain. It has an amorphous structure, its density can vary widely, from 50 to 200 kg/m^3, and it has very low water absorption (≈0.07%). On the other hand, its tensile strength ranges from 2 to 10 N/cm^2, while tear strength varies between 2 and 4 N/cm^2, and it can be elongated by as much as 500 %, although common values are around 200-300 %. Due to its versatility in industrial applications, it is commercially available in thicknesses covering three orders of magnitude (0.5 to 500 mm). The stacking of a given number of EVA sheets (stuck together or free to move) also allows the stratigraphic thickness of the model and the expected mechanism of deformation to be varied. Unlike other materials, EVA's radiological contrast is high enough, and its boundaries can be imaged with sufficient clarity to be accurately redrawn by the image processing software. Alternatively, ethylene propylene diene monomer rubber (EPDM [M-class] rubber) can also be used.

Alternation of different mechanical properties, thicknesses and cohesion between layers produces infinite possibilities and allows modeling any case under study. The thicknesses of the modeled stratigraphic pile and the wavelength of the folds have to be adapted to the limited size of the CT scanner (usually less than 60 cm in diameter) and the circular geometry of the CT sections has to be taken into account in the model design.

Figure 3.3: Modelization and scanner of several analogs.

In addition to the layer modeling, the reference system characterization is of crucial importance. This reference system is defined with two sets of orthogonal parallel grid lines. We tested many different kinds of materials to simulate the sets of lines: plastic and metallic meshes, strings and cords, and even cloth with linear relief. In most cases, however, there was insufficient radiological contrast, while in the case of metallic lines the absorption was so high that the radiological image was over-exposed. Moreover, the use of specific layers such as plastic meshes to simulate the set of grid lines has mechanical consequences: 1) it implies detachment from the underlying bed; 2) it does not allow the effect of deformation on the grid lines to be quantified; and 3) the change of the rheology has also consequences for the final geometry. Solid linear elements (cords, strings, wires, etc.) cannot effectively be stuck to an EVA sheet (different mechanical properties) and if they are free to move, they cannot be trusted by definition to provide an accurate reference system. Similarly, the use of cuts or marks in EVA sheets also affects the rheology.

Therefore, to define the reference system we decided to paint a set of parallel lines on the sheet using highly X-ray absorbing inks, liquids and paints. A wide variety of materials were tested for this purpose, all of them having high electrical conductivity (Fig. 3.4A), including graphite, gold and silver inks, aluminum paints, various types of glitter, etc. Of these, minium (red tetraoxide lead) paint was, by far, the most successful material. We found it gives a sharp radiological signal without serious streak artifacts in the CT image. Other potentially suitable materials such as graphite, gold, silver and aluminum had too little mass to absorb enough X-ray photons and hence were not detected in the signal or they were but only in a very faintly way. The minium was screen-printed onto the EVA sheets, which can be done with a good accuracy. Indeed, current screen printing technologies allow computer-aided design of the screen mesh (usually made of nylon and polyester) and mesh sizes up to 0.5 mm. Minium can be used in place of the usual screen printing inks without affecting the performance of the printing process.

The grid that constitutes the reference system (needed to monitor internal deformation in 3D) is made by two orthogonal sets of parallel lines. We explored screen printing the second set of parallel grid lines using a mixture with a different ratio of minium and turpentine or, alternatively, a different quantity of ink. The amount of ink can be varied by changing the line width and an advantage of this approach is that the minium/turpentine mixture for the main and secondary sets of parallel grid lines can be applied at the same time. We found that varying the line width between 0.5 and 2 mm in the screen worked well. These different amounts of minium produced sufficiently different intensities to allow identification of each set of lines in the CT images (Fig. 3.4B).

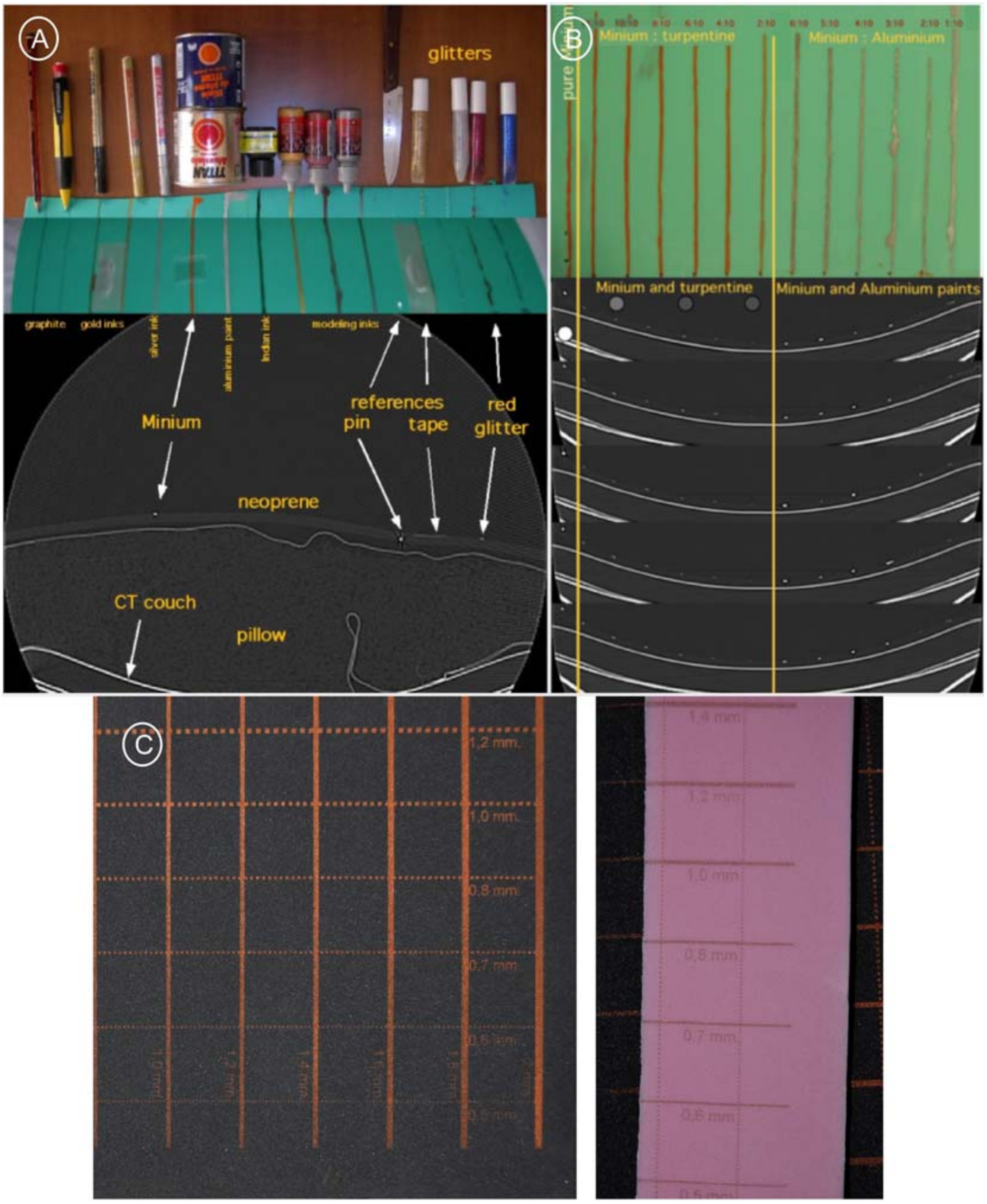

Figure 3.4: A) CT image of lines applied with the different conducting materials tested. B) CT image of lines containing different proportions of minium (left to right) to reproduce a secondary reference grid. Note that the signal from the minium mixture does not change from the top to the bottom section. C) Screen-painted EVA plates using dissolved minium. Different “ink” width (dash and continuous) trials to test the different radiological brightness.

The positioning of the model on the scanner table is also of crucial importance. To clearly identify a line in a CT image it should be perpendicular to the cross-section: the more oblique the greater the scatter; a line is indistinguishable when it is parallel to the section plane. The ideal orientation is with both sets of grid lines oblique to the cross sections. This is not always possible, however, especially for complex folds with considerable rotation and almost vertical or overturned limbs, a complexity that makes reconstruction more difficult. We can then make 2-3 serial sections, but the amount of work increases in the same proportion.

3.1.4 Processing of data: reconstruction

Digital Imaging and Communications in Medicine (DICOM, also known as the NEMA Standard PS3©) is the standard computer format for handling many different sources of medical images (among them CT). Together with a communication protocol, the file contains a header that provides information concerning the relative position of the different CT sections (location, orientation, spacing, etc.), and this enables us to geo-reference our model. A simple processing based on the data in the header fields (Image Position, Pixel Spacing, Rows and Columns) allows the images to be used like seismic sections in most 3D reconstruction software packages (i.e. gOcad).

Medical software (e.g., *Mimics*™[1]) allows processing and editing of 2D image data from CT (and other medical imaging techniques) and it is useful for 3D reconstruction of models. Unfortunately, it was not found to be very effective for the reconstruction of geological models due to the difficulty of accurately identifying important elements such as the different bedding surfaces or the grid lines (Fig. 3.5).

For this reason, we decided to use geological software and treat the CT images as geo-referenced cross-section images in gOcad (*Paradigm*) (Fig. 3.6). The versatile capabilities of gOcad have allowed us to accurately reconstruct the model surfaces and the grid lines paths over the surface as if the dataset were a series of seismic sections in SEGY format. Since with CT we can measure closely spaced slices, 3D reconstructions can be highly reliable, far above the average in the case of reconstructions based on field data.

[1] http://biomedical.materialise.com/mimics

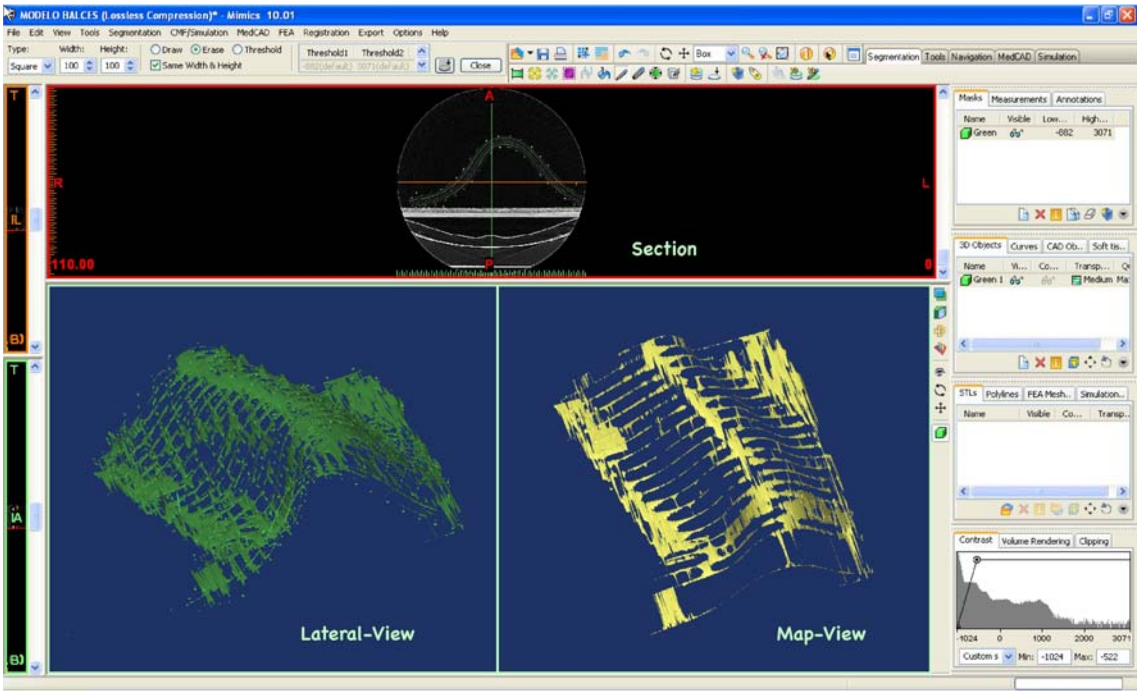

Figure 3.5: Atempt of reconstruction with the software Mimics.

This process can be quickly described but it is rather demanding. In each cross-section we draw the lines that define the surfaces and the points that define the lines. As we need the reference points of the grid, we need to reconstruct the lines and then mark the crossings between them. These points are the basis for the meshing. As it is a manual reconstruction it introduces precision errors difficult to quantify. Since this error is not systematic, it can be assumed to be self-balanced.

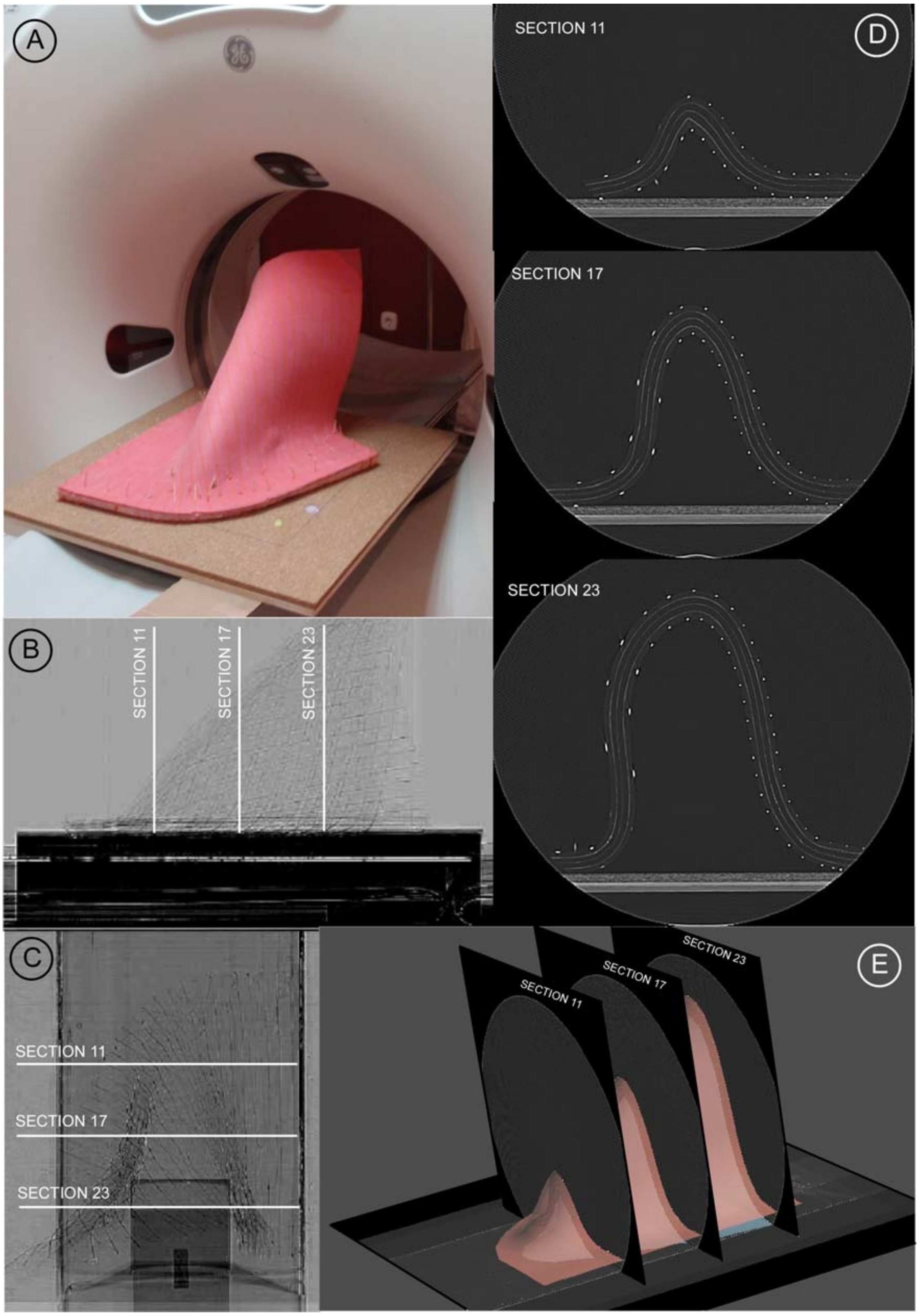

Figure 3.6: Analog model reconstruction with gOcad from the cross-section images obtained by CT: A) CT scanner set-up; B) Lateral view; C) Top view; D) Cross sections spaced 2 cm apart: 11, 17 & 23; and E) gOcad reconstruction of the upper and lower surfaces. San Marzal (first generation). Note the white points in the radiograms represent the "paleomagnetic vectors" (intersections of the reference grid).

The projection or *draping* of an orthophoto over the model surface can help further improve the reconstruction, providing in particular accurate data on the position of the lines. We took an orthophoto using a camera with a 300 mm zoom-lens mounted on a tripod. With the help of a laser level, the height of the center of the lens was matched to the center of the model, ensuring that the camera was perfectly perpendicular to the model at a distance of 16 m; this corresponded to an angle of less than 1° between the borders of the model (Fig. 3.7).

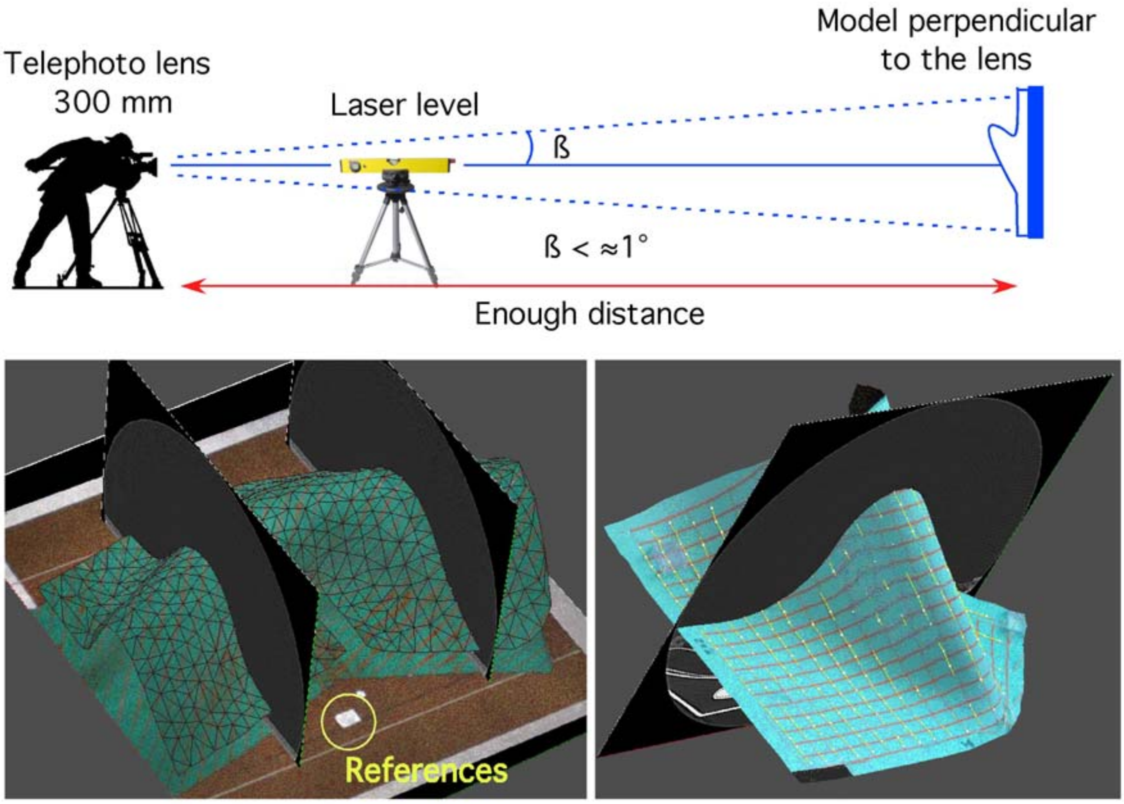

Figure 3.7: Orthophoto sketch and two analog models with the orthophoto drag on the digital reconstructed surfaces.

3.1.5 Post-processing: estimation of strain

A perfectly characterized reference system is key to understanding any folded lineation and to unravel deformation patterns (strain ellipses and ellipsoids) in 2D and 3D. To quantify the deformation, we need accurate measurements of the position of reference points of the structure in the undeformed and deformed states. The fact that this desirable information is unavailable in real cases is what makes analog models all the more important. We reconstruct the model with a tetrahedral mesh formed by the orthogonal set of lines. This reference system is the same in the original and folded states and consequently tracks the deformation. Therefore this allows us to predict the orientation of any passive lineation in the folded surface.

Thanks to the reference system, we are able to calculate the dilation and the strain ellipsoid for each individual tetrahedron (or triangle in surfaces). Obviously, the spacing of these tensors will be related to the density of our orthogonal reference system. The dilation parameter measures the change of volume (or area in surfaces), while the strain ellipsoid (or ellipse in 2D) measures the anisotropy of strain and the preferred orientation (stretching lineation). In order to assess the anisotropy of the ellipsoid, we also calculate the ratio between axes (*P'*) and the shape factor (*T*), this ranging between -1 (prolate) and 1 (oblate) and *T*=0 corresponding to pure triaxial ellipsoids. These parameters (Jelinek, 1981) are regularly used in magnetic fabric analysis and are similar to the axial ratios plotted on a Flinn (1962) diagram (L= max/int and F=int/min), although they are much more sensitive to small changes of the ellipsoid since they are based on a logarithmic scale.

The ellipsoid is calculated using the affine transformation matrix *M* that relates the points before and after deformation and characterizes the deformation. The matrix coefficients are determined using initial and final tetrahedron vertices. The application of this transformation to a sphere produces an ellipsoid and the eigenvalues and eigenvectors of the transformation matrix are the orientation and magnitude of the ellipsoid axes; the finite strain ellipsoid in terms of Ramsay (1967). We detail the mathematics right afterwards.

3.1.5.A Formulation

A tetrahedron is defined by its vertices v_i, $i \in \{0,1,2,3\}$. For the sake of simplicity, and without loss of generality, we take v_0 as the origin of the coordinate system (which is equivalent to substituting $v_i \rightarrow v_i - v_0$, $1 \leq i \leq 3$). Let V be the 3x3 matrix whose columns are the components of the column vectors v_i, $i \in \{1,2,3\}$. Any point on the volume of the tetrahedron x is given by $x = V \cdot \alpha$, where α is a column vector whose components indicate the position of x with respect to the vertices and satisfy $\alpha_i \geq 0, \sum_i \alpha_i \leq 1$. The volume of the tetrahedron can be expressed in terms of the determinant of V as $volume = 1/6 \cdot |\det(V)|$. As the three vectors are linearly independent, V is invertible.

If the tetrahedron undergoes a linear deformation, points are transformed so that their relative position with respect to the vertices remains the same: $x \rightarrow x' = V' \cdot \alpha$, where the columns of V' are the components of the transformed vertices v'_i, $i \in \{1,2,3\}$, with origin in v'_0. Thus

$$x' = V' \cdot \alpha = V' \cdot V^{-}1 \cdot V \cdot \alpha = M \cdot V \cdot \alpha = M \cdot x$$

with $M = V' \cdot V^{-1}$

In order to provide a quantitative measure of the deformation, we consider a sphere with radius 1 inscribed in the initial tetrahedron and study its transformation, it being distorted to an ellipsoid (Fig. 3.8).

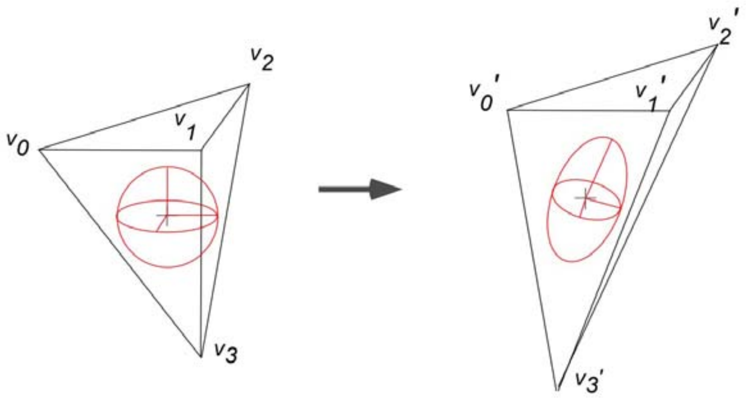

Figure 3.8: Deformation ellipsoid of a single deformed tetrahedron.

The ellipsoid is a quadric surface that satisfies the equation: $x^t \cdot A \cdot x = 1$, where A is a 3x3 symmetric real matrix, the sphere being a degenerate case. Specifically, for a sphere with radius equal to 1, A_{sphere} is the 3x3 identity matrix. Thus

$$1 = X^t \cdot A_{sphere} \cdot X = X^t \cdot X = \left(M^{-1} \cdot X'\right)^t \cdot \left(M^{-1} \cdot X'\right) = X''^t \cdot A_{ellipsoid} \cdot X'$$

where $A_{ellipsoid} = \left(M^{-1}\right)^t \cdot M^{-1}$

Let λ_1, λ_2, λ_3 be the eigenvalues of $A_{ellipsoid}$. The semi-axes of the resulting ellipsoid are $k_i = \lambda_i^{-1/2}$. In the following, we assume they are ordered so that $k_1 \geq k_2 \geq k_3$.

Finally, we reconstructed the model with a tetrahedral mesh formed by the orthogonal set of lines, where the intersections of lines are the nodes of the surface and the vertices of the tetrahedron. There are three tetrahedra for each triangular prism (Fig. 3.9) and we calculate its mean ellipsoid in order to have a mean value for the whole volume of this triangular prism.

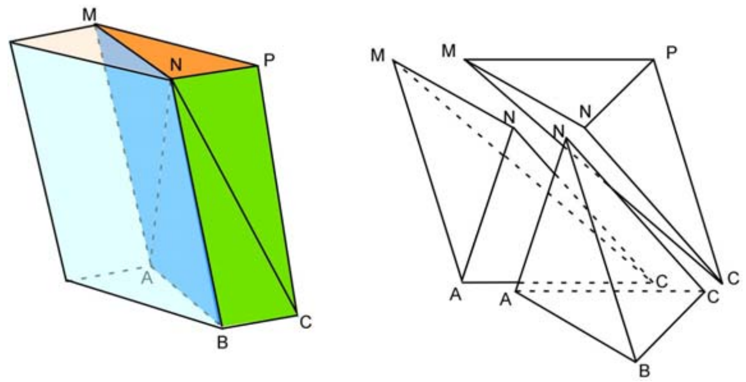

Figure 3.9: Volume tessellation

Dilation is the change of volume between initial and final tetrahedron:

$$dilation = \left(volume_{final} - volume_{initial}\right)/volume_{initial} = \left|\det(V')\right|/\det(V) - 1$$

Using basic properties of the determinant, it can easily be shown that

$\det(M) = \det(V')/\det(V)$. Moreover, $\det(A_{ellipsoid}) = \left(\det(M)\right)^{-2}$, and thus

$$dilation = \left|\det(M)\right| - 1 = \left(\det(A_{ellipsoid})\right)^{-1/2} = \frac{1}{\sqrt{\lambda_1 \cdot \lambda_2 \cdot \lambda_3}} - 1 = k_1 \cdot k_2 \cdot k_3 - 1$$

To describe the anisotropy of the ellipsoid, we calculate the *P'* and *T* parameters defined by Jelinek (1981). We are interested in the ratios of the semi-axes, rather than in their differences. As a measure of their scatter, we consider the normalized anisotropy: $P' = \exp\sqrt{2 \cdot \left[(\eta_1 - \overline{\eta})^2 + (\eta_2 - \overline{\eta})^2 + (\eta_3 - \overline{\eta})^2\right]}$ where η_i are the logarithms of the semi-axes $\eta_i = \ln(k_i)$, and $\overline{\eta}$ their mean value $\overline{\eta} = (\eta_1 + \eta_2 + \eta_3)/3$.

The shape factor, defined as $T = \dfrac{2\eta_2 - \eta_1 - \eta_3}{\eta_1 - \eta_3}$, characterizes the shape of the ellipsoid. An ellipsoid is said to be rotational prolate (prolate, neutral, oblate, rotational oblate) when $k_3 = k_2 \left(k_3 < k_2 < \tilde{k}, k_2 = \tilde{k}, \tilde{k} < k_2 < k_1, k_2 = k_1\right)$, and thus *T=-1(-1<T<0, T=0, 0<T<1, T=1).*

3.2 Analog models

With the analog models we do not pretend to accurately reproduce the structure of San Marzal and the Balzes Anticline, neither to do an exhaustive analysis about them. These structures are selected because of its complexity (a conical fold and an arched anticline with a related conical fold in its inner arch). Their geometry is a good case to test the capabilities of the restoration methods and the CT scanning.

In any case, and following the philosophy of analog modeling, our models assume an evaporitic core that has been modeled by air in the core of the anticline (a reasonable assumption considering the rheology). The cover rocks on top of the Middle Eocene platform (Boltaña Fm) has not been modeled, according to the deformation ages (syn-folding). The model was designed as a "static" reproduction of the evolution of the anticline (we apply the finite deformation at once, without considering the actual kinematic).

Several models have been developed based on this two complex structures (Marzal and Balzes) using different materials and scales (Fig. 3.10). It has been a laborious work in which we have learned the modelization and the reconstruction technique. At the end, we have selected two of the best reconstructed analogs to show the results of this technique and the restoration methods. We have reconstructed the San Marzal model using only photogrammetry and the Balzes Anticline with both techniques.

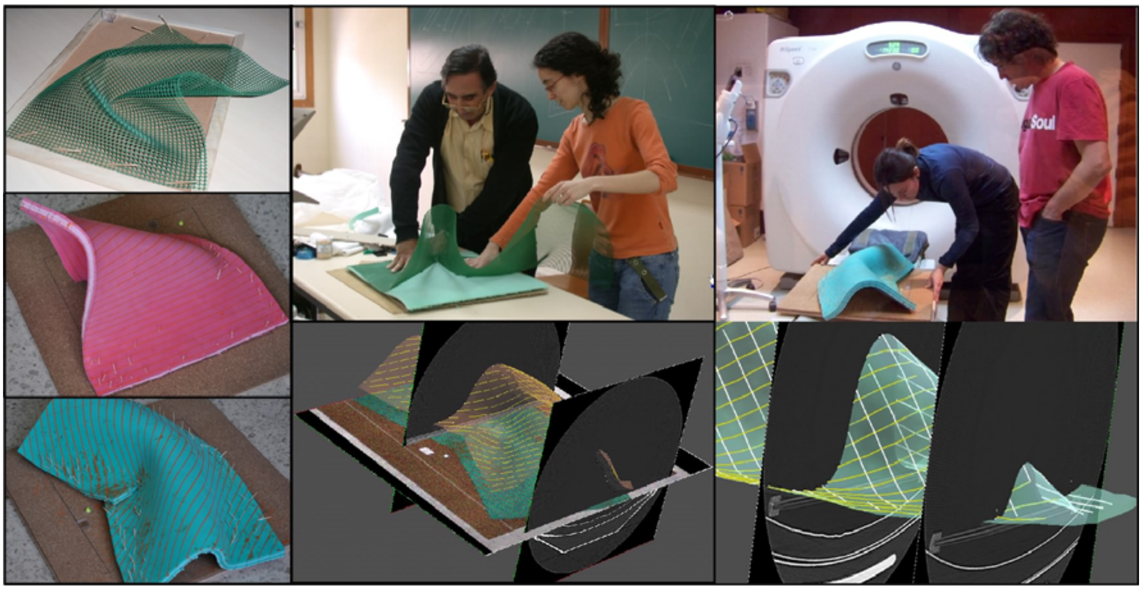

Figure 3.10: Analog modeling of several models of San Marzal and Balzes.

3.2.1 San Marzal Pericline

The San Marzal closure of the large-scale Sto. Domingo detachment anticline is modeled considering the pre-Campodarbe sequence, and particularly, the Guara Formation. The air within the anticline core represents the pre-Guara formations including the Triassic evaporites.

The analog reproduces five main structural features (Fig. 3.12): 1) approximately the San Marzal relation between the wavelength (≈ 8 km) and thickness of the modelled layer (≈ 180 m); 2) strong immersion of the fold axis; 3) pseudo-parallel flanks in the Sto. Domingo Anticline; 4) an approximately 45° clockwise rotation in the northern flank; 5) the southern flank is assumed to be in structural continuity with the Ebro foreland basin and it will be used as the pin-line.

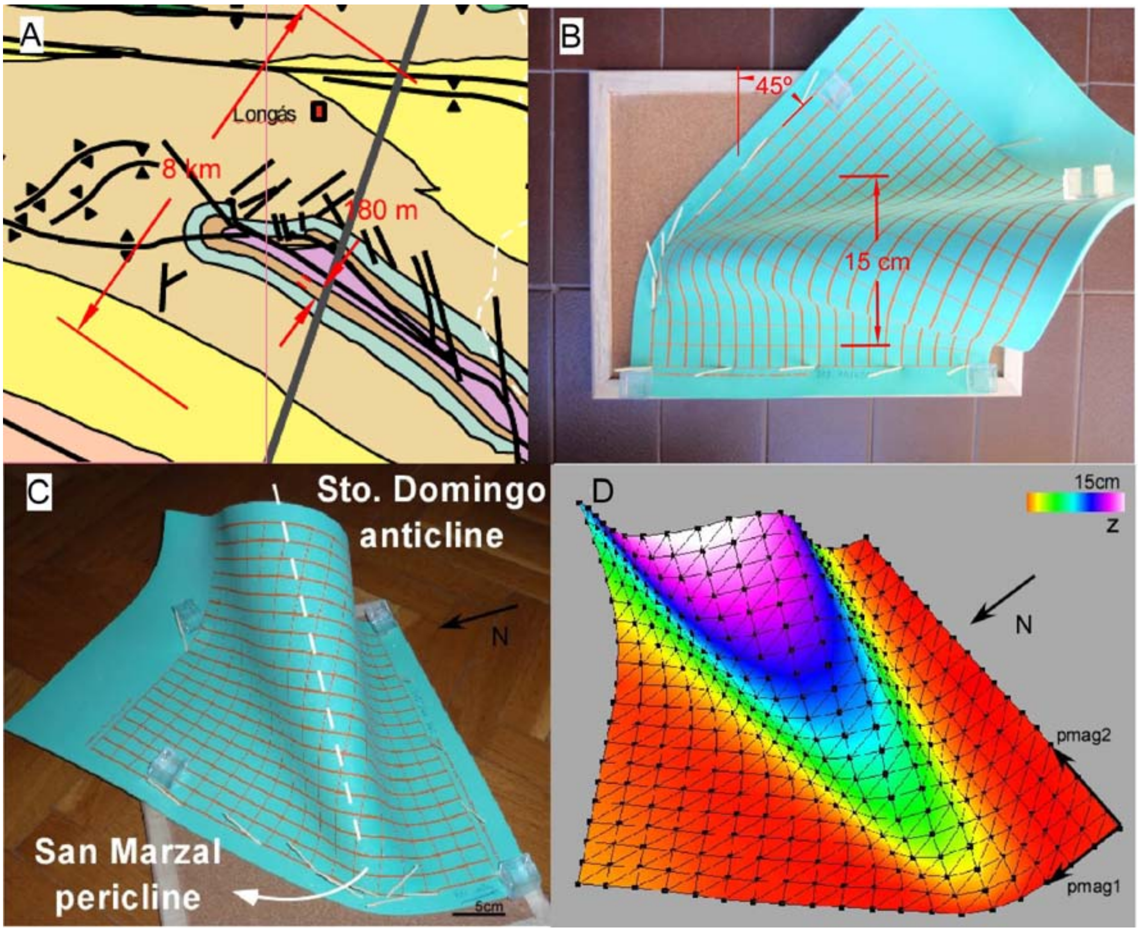

Figure 3.12: Analog model of the San Marzal Pericline. A) San Marzal cartography (from Fig. 2.13A). Approximate wavelength and thickness of the modelled layer displayed. B) *Orthophoto* of the analog model. Approximate wavelength and rotation of the northern flank displayed. C) EVA foam model on which lines parallel and perpendicular to the paleomagnetic reference vector have been screen-printed. D) Final 3D reconstruction of the model with the z coordinate displayed.

The model is built with an EVA plate of 0.3 cm thickness. Therefore, the relation between the wavelength and thickness is approximately 50 (15 cm / 0.3 cm) and is similar to one of the real structure ≈ 44 (8 km / 0.18 km). The paleomagnetic vectors (projection of the declination component) are featured as lines printed on the EVA surface. A rectangular grid screen-printed on the surface provides two possible references. The 20×20 grid is composed of rectangles of 1.5×2 cm (Fig. 3.12).

We have reconstructed the San Marzal model using only photogrammetry because after many attempts we have found the CT reconstruction impossible. For a plausible CT reconstruction, lineations must be as perpendicular as possible to the cross-sections. Because of the strong folding of the model (overturned limbs) and the strong differential rotation between the flanks we were unable to fulfill this premise.

3.2.2 Balzes Anticline

We model the upper and better exposed thrust sheet involved in the Boltaña Formation (unit 2 in Fig. 2.19). The evaporitic core is modeled by air and the syn-Guara Formation has not been modeled. Thus, the top surface of the model represents the base of the Guara Formation and the bottom surface the base of the Ypresian limestones.

The geometric scaling of the model obeys some key features: 1) the real variation in the fold axis trend (stereoplots in Fig. 2.18), 2) the relation between the wavelength of the anticline (≈ 6 km) and the thickness of the modeled stratigraphic pile (≈ 300 m), and 3) the differential vertical axis rotation between the northern and southern sectors (27°). Generating an oblique structure based on the Balzes Anticline, we see how a secondary fold is formed in the inner part, which could correspond to the Boltaña Anticline southern termination near Paules de Sarsa.

Using all this information the analog model is built with two EVA sheets of 58 x 38 x 0.5 cm glued together, giving a total thickness of 1 cm. In this case the relation between the wavelength and thickness is approximately 16 comparing with the approximately 20 of the real one. The EVA sheets are screen-printed with a squared grid of 1 x 1 cm and line widths of 1 and 1.5 mm. One sheet is screen-printed on only one side and the other on both sides, thus we model three surfaces that represent the base, the top and the middle (and neutral) surface of the stratigraphic pile under study.

First of all, we scan the EVA sheets in an undeformed state (horizontal) to set up the reference system. Subsequently, we deform the sheets following the Balzes kinematic model and scan it again (Fig. 3.13). We then reconstruct the model from the DICOM cross-sections in gOcad. We also check the reconstruction from CT images against the reconstruction of the upper surface obtained using photogrammetry.

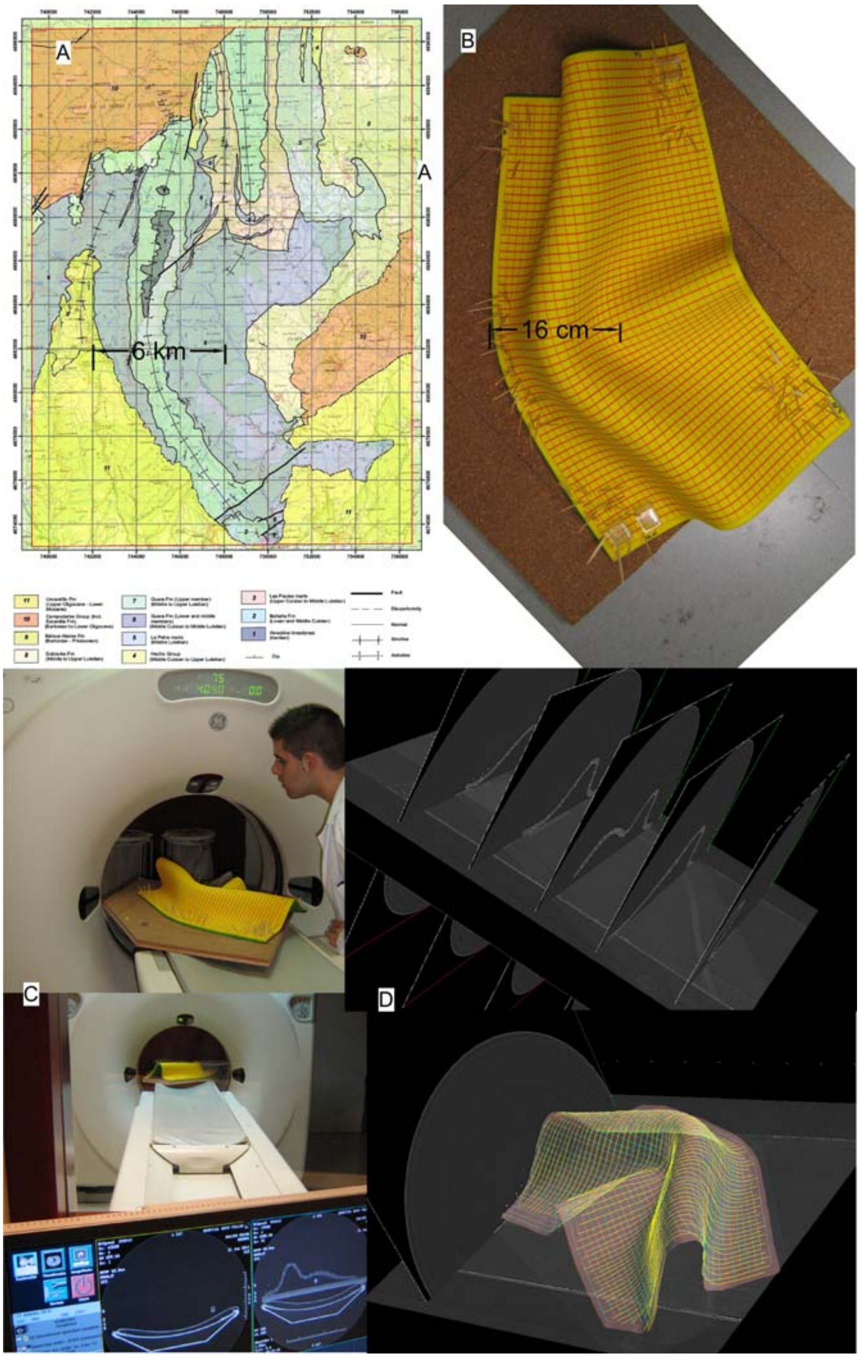

Figure 3.13: Analog model of the Balzes Anticline. A) Balzes Anticline cartography (Fig. 2.19). Approximate wavelength displayed. B) *Orthophoto* of the analog model. Approximate wavelength displayed. C) CT scanning of the analog model. D) Reconstruction with gOcad of the analog model from the CT images.

3.2.3 Analysis of Balzes Anticline CT model

With this example we want to show that these models can be very useful for understanding certain features related to complex settings: A) folded lineations, B) the 2D distribution of deformation ellipses on different surfaces within the model, and C) the 3D distribution of strain tensors in the folded volume.

3.2.3.A Lineation analysis

This technique is valid for studying any passive geological lineation. In this section, we compare the grid lines of the model with paleomagnetism, but we could study any other linear element (paleo-current, stress, etc.). Paleomagnetic vectors (their local projection on the model surface; that is to say, only the declination information) can be seen as a type of lineation (Sellés, 1988; Stewart, 1995; Pueyo et al., 2003) and are feasible structural markers that can be clearly established for both the pre-and post-deformation states. In this case, paleomagnetic data are assumed to be pre-folding. First, we need to rotate the entire model to converge to the real axes of the structure. As the reference set of lines in the model had no inclination, we need to apply a rigid-body rotation to our contrived paleomagnetic record (one of the sets of lines) to converge with the real dataset. Inclination has been modeled to fit the real data (≈40°) rather than the Eocene reference expected in the Pyrenees (53°).

Now, we consider lineation patterns separately in the northern and in the southern flank of the anticline. We select specific sites on the model simulating an outcrop on each side of the anticline. These data are approximately at the same structural location as the real dataset. We project paleomagnetic vectors before and after bedding correction (Fig. 3.14A). Paleomagnetic data before any correction are clustered into two groups corresponding to the western and eastern limbs of the anticline. As expected, data is grouped after the bedding correction (ABC), and the clustering is better than seen with the real noisy paleomagnetic data (Fig. 3.14B).

Given the secondary origin of the fold curvature (that we applied to the model), there is a 22° difference between the mean paleomagnetic direction in the northern and southern sectors. This difference is slightly smaller (4°) than detected in the real dataset. These small errors in the lineation, as well as those highlighted by the bedding poles, are not unreasonable. They are likely caused by the analog model, which does not perfectly reproduce the natural geometry. Once again, the fold axes of the sectors are similar but not exactly equal to those calculated for the real structure.

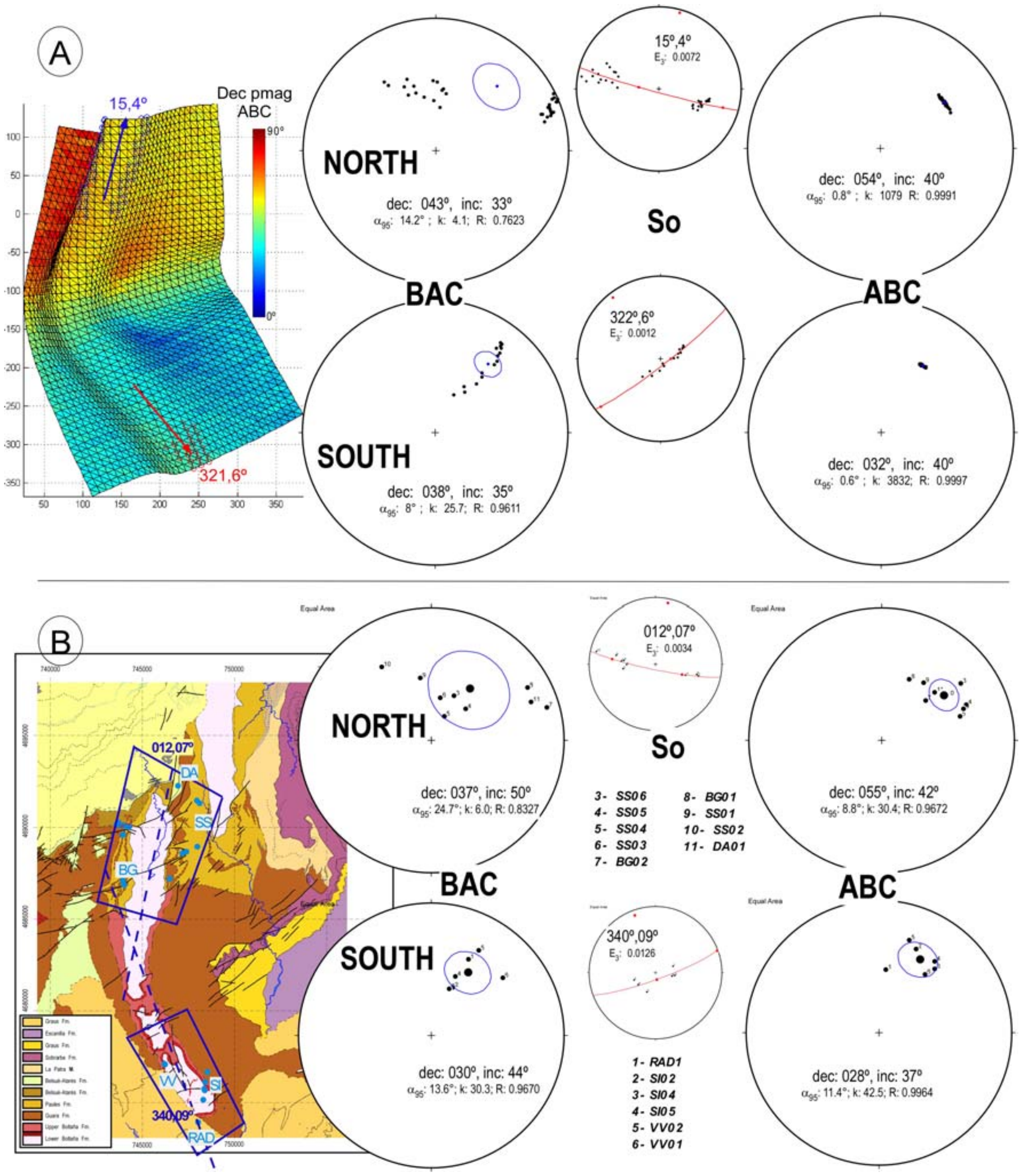

Figure 3.14: Paleomagnetic analysis of northern and southern flank. Stereographic projections of paleomagnetic data before and after bedding correction (BAC, ABC) as well as the bedding plane (S0) for each site with the calculation of the fold axis: A) Analog model; and B) Real data.

3.2.3.B Surface analysis

Before considering the internal deformation, we analyze the results of the uppermost surface, comparing the results obtained from the reconstruction of the CT images with those from photogrammetry, the complementary technique we use for surface reconstruction. Our aim with this was to validate the 3D reconstruction based on the CT images. First of all, we compare the distribution of dilation (=[$Area_{folded}$–$Area_{initial}$]/$Area_{initial}$) across the entire surface. The second technique is more accurate for the upper surface reconstruction and gives clearer results but they are equivalent in meaning (Fig. 3.15A). This is basically due to the greater accuracy of the photogrammetric method in reconstructing the exact location of the nodes (intersections between the two sets of lines).

If we now analyze all the three surfaces derived from the CT modeling (Fig. 3.15B), we observe tangential-longitudinal strain in line with Ramsay (1977) and Gairola (1978), extension in the anticlines outer hinges of the upper surface (positive dilation), conservation of area in the middle neutral surface and compression (negative dilation) of the inner hinges in the lower one. We observe consistent senses of dilation in the synclines: positive on the outer arc and negative on the inner one. It is worth noticing that the areas with clear dilation are significantly different at the two surfaces (upper and lower): in the lower surface the maximum dilation is concentrated in a much smaller area and is more intense than in the upper one. This observation fully agrees with the expected differences in arc lengths between outer and inner hinges.

The most deformed areas are precisely the ones of maximum mean curvature (mean between the two principal normal curvatures: $M=(k1+k2)/2$). Since we are unable to derive the anisotropy from the curvature, we plot the strain ellipses in terms of the ratio of the axes and the orientation of the main axis. In the CT model, the areas of higher anisotropy (ratio between major and minor axis) correspond with areas of compression: the syncline between Balzes and Boltaña anticline in the upper surface (synclastic synform according to Lisle and Toimil, 2007) and both anticlines in the lower surface (synclastic antiform). This observation agrees with the distribution of dilation across the upper and lower surfaces. As suggested above, this may be caused by the concentration of deformation in the inner-arc zones, which have to accommodate an equal amount of volume change in a smaller deformed volume. On the other hand and, as it would be expectable, the Gaussian curvature ($G=k1 \cdot k2$; Gauss, 1827) is concentrated in the area of superposed folding (Boltaña-Balzes) and there are no significant differences between the three surfaces.

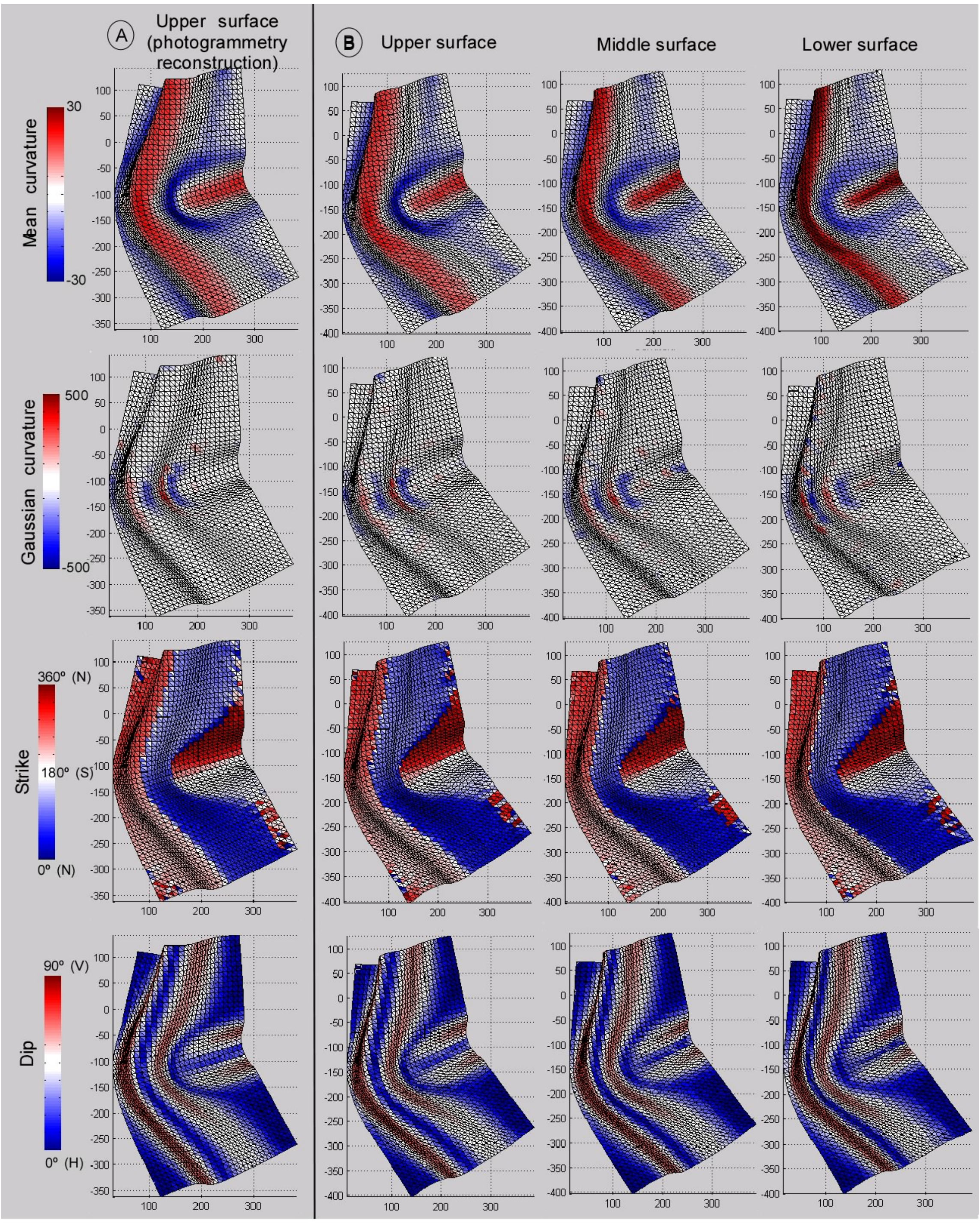

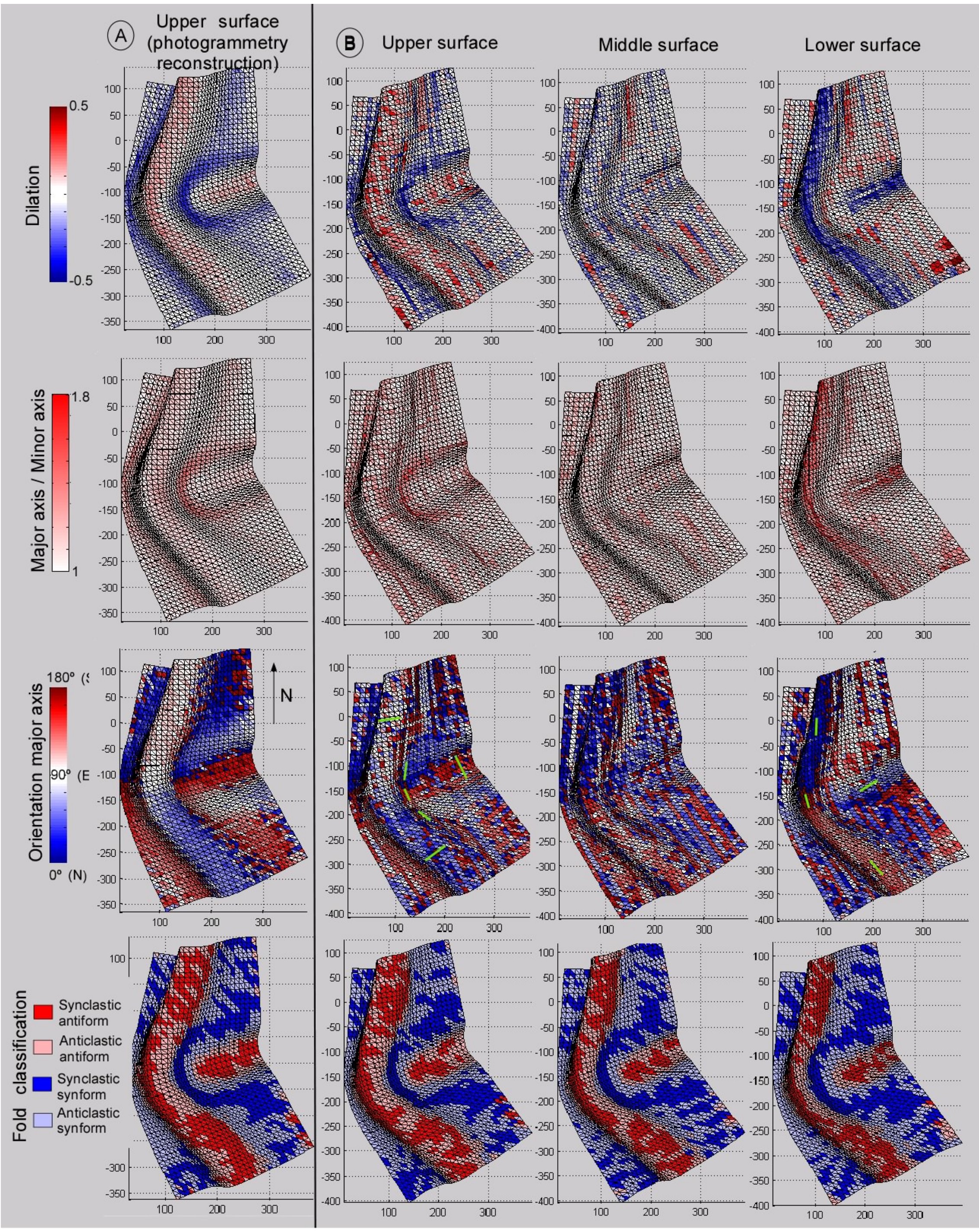

Figure 3.15 (continued): A) Dilation and strain ellipse (magnitude and orientation) of the upper surface digitalized with photogrammetry. Fold classification of Lisle & Toimil (2007): synclastic antiform (G>0, M>0), anticlastic antiform (G<0, M>0), synclastic synform (G>0, M<0) and anticlastic synform (G<0, M<0). Gaussian (G) and mean normal curvatures (M) are also displayed along with strike and dip maps; B) Dilation, strain ellipse and curvature patterns of the upper, middle and lower surfaces digitalized using cross section CT images.

The strain ellipse gives us extra information about anisotropy. As observed before, upper and lower surfaces display opposite results. The same applies for the orientation patterns. The directions of the major axis of the ellipse are perpendicular for upper and lower surfaces. In the middle (neutral) surface there is no clear preferential orientation of deformation (and, in any case, the magnitude is very small). Focusing on the upper surface, we observe that the main axis (elongation) orientation is perpendicular to the fold axis in both anticlines (Boltaña and Balzes) and parallel to the fold axis in the middle syncline. On the other hand, for the lower surface, the main axes of the ellipses follow the fold axis orientation, being located in the inner part of the anticline.

3.2.3.C Volume analysis

The volume analysis is carried out for the upper and lower volumes separately (Figs. 3.16 & 3.17). The main problem of the model is the low strain ratio (major axis/minor), caused by the small ratio between the modeled thickness and the fold wavelength.

The low anisotropy (mostly less than 2) is attested by the P' vs. T diagram (Jelinek, 1981). To explore the deformation, we decided to use these magnetic fabric parameters since they are more sensitive to variations in the tensor geometry than the simple axial ratio (i.e., Flinn diagram, 1962). Here, P' is proportional to the total eccentricity of the ellipsoid and T ranges between 1 (pure oblate) and -1 (pure prolate). In this graph (Fig. 3.16A), the points are widely scattered reflecting the low eccentricity of the ellipsoid. Similar evidence is obtained from the mean normal curvature vs. dilation diagram (Fig. 3.16A). Apart from the narrow ranges of variation (-0.03 to 0.03 and -0.6 to 0.6 respectively), most data fall close to the origin (non-deformation zone), although some data points on the upper surface with negative dilations spread towards negative curvatures (synclinal hinges), and some points on the lower surface with negative dilations tend to positive curvatures (anticlinal hinges).

Due to the considerable noise caused by the low anisotropy and the large number of tensors, we tried classifying the data according to some simple variables (Fig. 3.16B). First, curvature readily allows localization of the hinges, both anticlines (positive values) and synclines (negative ones). Second, the bedding dip constrains the boundary between flanks and hinges. Dips $< 30°$ can be unambiguously classified as fold hinges. Finally, small dips ($< 30°$) and low curvature values ($< |10|$) represent the flat and undeformed portions of the model. Therefore a clear distinction can be established between all these model zones.

The mean curvature allows a quick (and coarse) segregation of anticline and syncline hinges. The distribution of the shape of the ellipsoid (T) is very noisy (Fig. 3.16C) when we plot the data all together. If, however, we concentrate only on the hinges (flat and flanks zones not considered) some patterns can be seen: curvature varies over a narrower range (between 10 and 20) in the anticlines than in the synclines (between –10 to -30). This must be related to the relatively large non-coaxial deformation in the curved syncline (Fig. 3.16B), compared to the anticline. The volume tensors seem to be slightly more oblate, and this could be related to the tangential-longitudinal deformation in hinge zones.

Despite the generally low anisotropy, this parameter is related to map view location (Fig. 3.16D). Selecting the ellipsoids with P' > 1.5, we can see that they tend to be localized in specific zones, namely, the fold hinges. Consistent with the model design (the sheets were fixed), most deformation accommodated in the hinges and very little in the flanks. Additionally, there is more deformation in the northern sector (relatively closely spaced points with P' > 1.5) than the southern one (more scattered points). Finally, we plotted on the map the shape of the tensor (T) of the hinge zones alone (only those with significant anisotropies: P' > 1.3). Despite the remaining noise, oblate ellipsoids seem to be localized in the outer hinges (Balzes anticline and the curved syncline).

Interesting results to understand the distribution of deformation across the model can be also derived from exploring key variables in map view. This example in Figure 3.17 shows a general compression of the structure especially in the synclastic antiform of the inner arc (lower volume). The expected preservation of volume is not completely respected because there is no clear extension in the upper volume. This can be attributed, according to the surface analysis, to the values of compression in the lower surface being higher than those of extension in the upper surface. Moreover, deformation is concentrated in a smaller volume in the lower sheet than the upper one. As observed before, the normalized anisotropy (P' parameter ≈ major axis/minor) is higher in areas of compression where more deformation is concentrated in less space. This is consistent with the surface analysis: the anticline hinge anisotropy seems to be smaller and more diffuse in the upper volume than in the lower one.

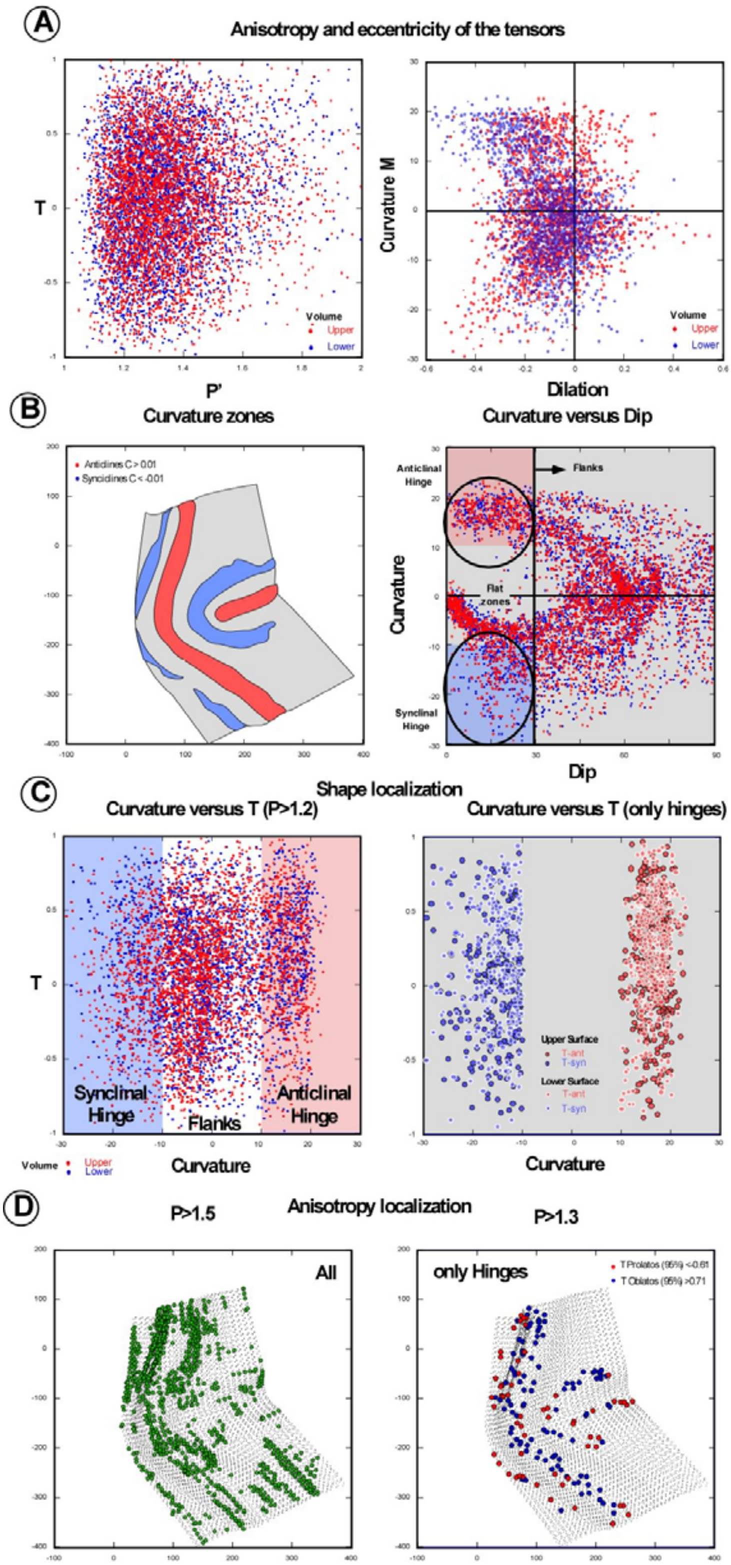

Figure 3.16: Tensor analysis: A) Anisotropy and eccentricity of the tensor; B) Classification of zones as a function of surface mean curvature and bedding dip; C) Shape localization: Anticlines and syncline curvatures versus the shape of the tensor (T); and D) Anisotropy localization in map-view: All tetrahedra (P' >1.5), and only hinges (P'> 1.3)

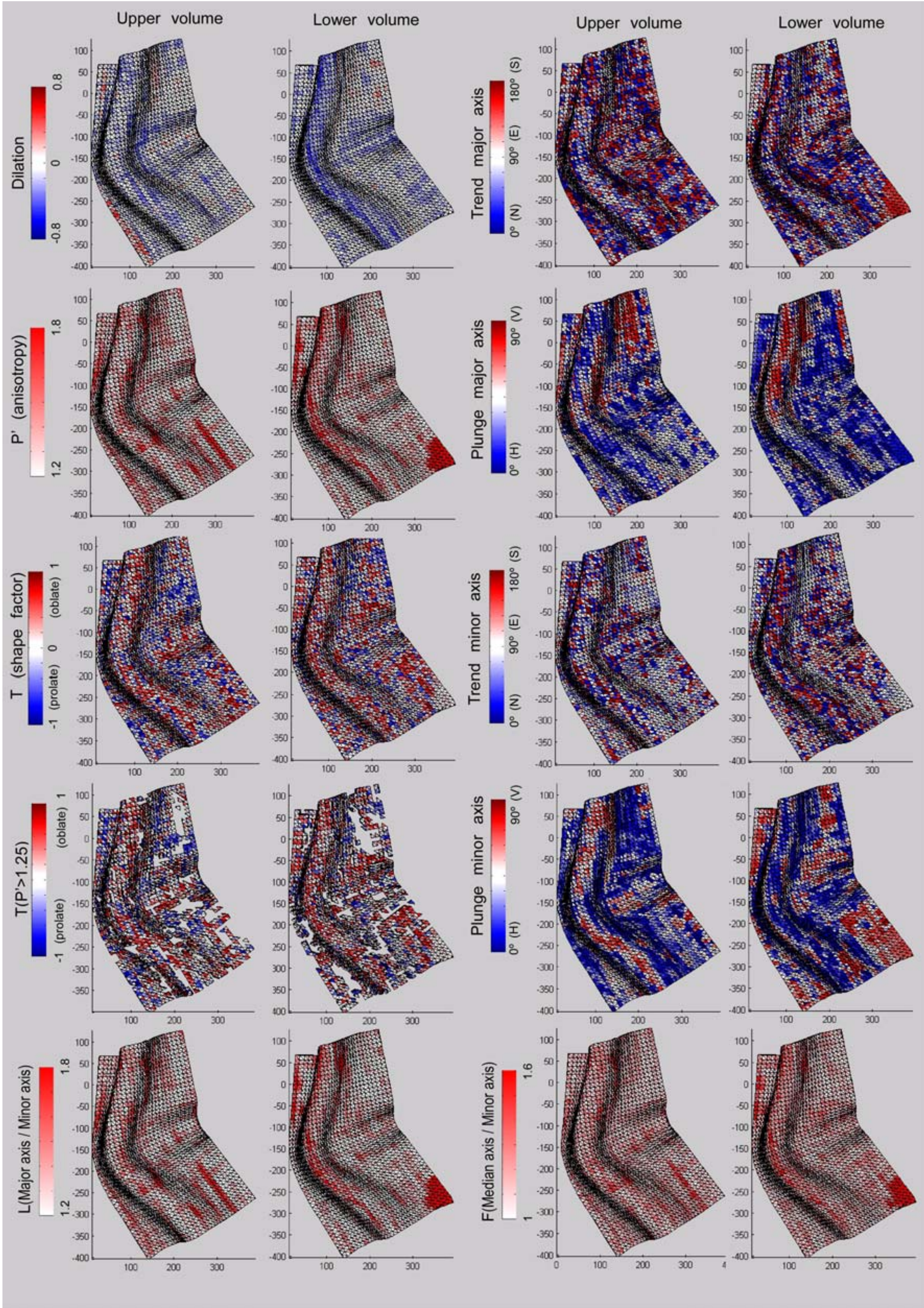

Figure 3.17: Volumetric analysis: upper and lower volumes of the structure. Dilation (volume change), anisotropy parameter (P'), shape factor (T), orientation (trend and plunge) of the major and minor axes of the deformation ellipsoid.

Since anisotropy is quite small (close to 1) there is no clear shape factor distribution. Nevertheless, oblate ellipsoids[1] tend to concentrate in the anticline. We could expect to find oblate ellipsoids in the upper volume and prolate ellipsoids in the lower volume but in this case layers are not thick enough for that pattern to be observed. The orientation of the minor axis is, however, coherent with the expected values: vertical in the upper volume and horizontal in the lower volume. The major axis is not that clear because it is very similar to the intermediate axis in oblate ellipsoids.

In future models, use of greater thicknesses (modeling more than one stratigraphic unit) will help to produce larger anisotropies in tangential-longitudinal strain folds for an equivalent wavelength. This can be expected to strengthen the results, confirming the usefulness of the models to predict any deformation pattern and to double-check restoration results.

[1] $T \approx 1$, major axis ≈ intermediate > minor

4 Surface restoration methods using paleomagnetism

In this chapter, we introduce the two surface restoration methods that leverage paleomagnetic vectors as a primary reference. They are valid for complexly folded structures. The first one is a simple geometric approach based on the piecewise restoration of a triangulated surface (Gratier et al., 1991 and Gratier and Gullier, 1993) into which paleomagnetic variables can be easily incorporated (Ramón et al., 2012). The surface is modeled by a mesh and the method starts from a pin-element. Triangles are laid flat and then fitted together to minimize distances between common vertices and paleomagnetic error. However, this first approach, as it will show later, is sensitive to the meshing and particularly to the pin-element. The second one is based on a parametric approach, whereby a curvilinear coordinate system is computed on the folded surface by numerical optimization. We use paleomagnetic data to define constraints for the computation of this frame, which significantly increases the robustness of the restoration method.

As in any restoration method, we need to establish some reasonable initial assumptions. We assume that:

1) Layers are horizontal in the undeformed surface; horizontality is the basic assumption in all restoration methods.

2) The folded surface is *developable*; it has been transformed by preserving angles, lengths and areas, so the Gaussian curvature is constant and zero. The method is also valid for *globally developable surfaces*, like those derived from rock volumes that have undergone flexural folding as described by Ramsay (1967), i.e., flexural flow on flanks or tangential longitudinal strain at hinges. In this case, total volume is assumed to be constant.

3) An even distribution of paleomagnetic vectors characterizes the folded surface. These vectors are primary (recorded at the time of deposition) and behave as passive markers during the deformation. In the analogs, these premises were clearly established, in the real databases, both the local and the paleomagnetic reference vectors have to be *reliable* in the sense used by Van der Voo (1990) and Pueyo (2010).

4.1 Piecewise approach

The starting point of this approach is the UNFOLD method developed by Gratier et al. (1991) and by Gratier and Guillier (1993), as it is a simple geometric approach into which paleomagnetic variables can be easily incorporated (Ramón et al., 2012). We also considered an alternative method (Williams et al., 1997) that minimized internal deformation instead of distances, preserving the triangle's area and allowing the modification of triangle's shape. But the more proper method to introduce the paleomagnetic constrain is the one defined by Gratier et al. (1991) because triangles rotate rigidly. The UNFOLD method, like most flexural restoration tools, requires the first two of the previous assumptions plus the paleomagnetic restrictions, which can be easily integrated. The horizon is defined as a mesh of triangular elements that are first laid flat, and then rearranged (translated and rotated) to minimize distances between neighbors. The main change on adding paleomagnetic data is that the rotation is not free when minimizing the distances, as it is constrained by the paleomagnetic reference vector (Fig. 4.1). The software (Pmag3Drest) has been developed using Matlab[1].

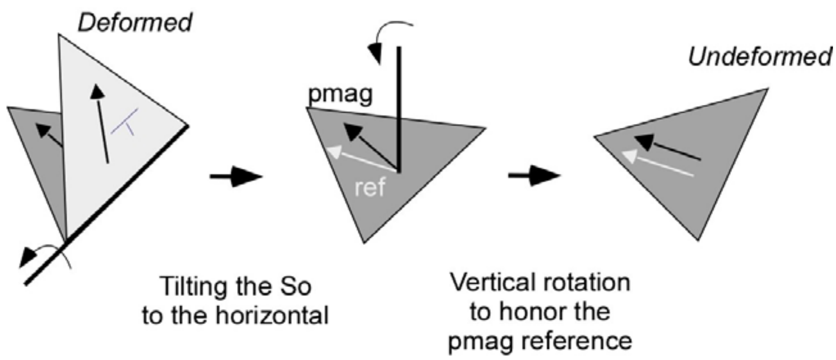

Figure 4.1: The concept: paleomagnetism as an additional tool in restoration methods. The surface is rotated to the horizontal with the bedding plane and then it is rotated around its vertical axis to fit with its paleomagnetic reference vector.

The method involves the following sequence of eight steps (Fig. 4.2):

1) <u>Surface definition</u>. A set of points with Cartesian coordinates describes the folded surface and determines the nodes of the rigid triangular elements of the mesh. To build the mesh, Delaunay (1934) or regular triangulation (Hjelle and Dæhlen, 2006) can be used. The most common triangulation is Delaunay's one which states that the

[1] www.mathworks.com

circumscribed circle of every triangle should not contain inside it any point of the mesh. It maximizes the minimum angle of all the angles of the triangles, which, as a practical result, avoids obtaining triangles with very small angles. However, in the analog models, we use the regular triangulation because it is much easier to obtain using commercial off-the-shelf wire meshes or by printing, in order to set the reference grid. In any case, we are going to evaluate the influence of the meshing type in the next chapter.

2) Incorporation of paleomagnetism. The method adds paleomagnetic vectors in triangular elements where paleomagnetic data is available, only considering the magnetic declination (the so-called *horizontal component*). The vector passes through the barycenter of the triangle (Fig. 4.3). The accuracy of the data, α_{95} (Fisher, 1953), can be related to the local paleomagnetic vector. In the case of sparse or poorly distributed vectors, it is possible to interpolate paleomagnetic data to all triangles of the surface using the algorithm described in Chapter 6.

3) Flattening. Each triangle is automatically laid flat to form a horizontal surface, by horizontal rotation about its strike axis. In the case of overturned beds, we treat the *stratigraphic polarity* as a vector in each element.

* Pin-element definition. Following 2D restoration techniques, the unfolding restoration tools select a pin-element (also called the seed in the parametric approach), which is used as a fixed reference position in a restored model. Two types of pin-elements can be defined for a surface: a *pin-point* is the first fixed triangle from where we start to unfold the surface, while the *pin-line* is the first row of triangles with fixed barycenters. The pin-element needs to be chosen with geological meaning because restoration is highly dependent on it, as it will be shown in next chapter. The pin is usually placed in the undeformed area of the surface which is considered not to have undergone deformation (i.e. the foreland).

4) Vertical-Axis Rotation. The paleomagnetic vector from the pin-element must converge with the paleomagnetic reference vector. Significant rotations are very unlikely since the pin-element should be chosen in the stable (undeformed) portion of the horizon. However, if there are substantial rotations, we apply an equal rigid-body rotation to the horizon at this stage.

5) Translation and rotation. Each triangle is translated and rotated in order to fit its neighbors using the method of least-squares. We minimize distances between shared vertices, bearing in mind the paleomagnetic reference. This step starts at the *pin-element*. If an element has paleomagnetic data, the related rotation is constrained by the paleomagnetic vector (Fig. 4.3), with a number of degrees of freedom that is determined by the α_{95} value. If the initial (undeformed) surface were completely developable (without any deformation), the restoration process would end at this step.

6) Iterating. The translation and rotation process is iterated a certain number of times, or for as long as the total distance error remains below a threshold, $e = \sum D / \sum M$. In this expression, *e* is the error, *D* the sum of distances between the vertices of each triangle and the triangular hole defined by its neighbors and *M* the sum of the medians of each triangle (Fig. 4.3). This step is especially important in the original UNFOLD method, where paleomagnetism is not considered (Gratier et. al., 1991) and rotation is free. When rotation is constrained this step is unnecessary.

7) Welding. After the iterative translation and rotation, the surface becomes discontinuous, with gaps and overlaps, assuming that the deformed surface that has been restored was not completely developable. In order to obtain a continuous surface, this step involves joining or *welding* the shared vertices of neighboring triangles through an average value, allowing internal deformation to take place.

8) Optimization process. This step is only performed when the restoration uses paleomagnetic data. At this point of the restoration process, the maximum paleomagnetic error (the difference between the local and the reference paleomagnetic vectors) is less than the α_{95} angle, and we may want to sacrifice accuracy in favor of area preservation. The vertices of the triangles are randomly modified to minimize a potential function (Eq. [1]), following the simulated annealing method (Kirkpatrick et al., 1983; Press et al., 1992). The potential function (*U*) includes the paleomagnetic error (1- cos[$ref\text{-}pmag_i$]) and the internal deformation (dilation in terms of area variation: [$area_0$-$area_i$]/$area_i$) with specific weights for each term (*A* and *B*).

$$U = A\sum_i \left[1 - \cos(ref - pmag_i)\right] + B\sum_i \left(\frac{area_{0i} - area_i}{area_i}\right) \quad [1]$$

This step was proposed for the restoration with paleomagnetism although practical experiments show that this step is avoidable because we lose primary information. The optimization algorithm tends to distribute the error across the entire surface. It is useful to obtain a smoother surface, when we are able to ensure there is no deformation. On the other hand, it is better to omit this last step when we are trying to identify a possible deformation, as it causes the model to lose information; the deformation always becomes weaker after the optimization (Fig. 4.4). Although the optimization process has been considered, we end the restoration at step 7 in the simulations shown later.

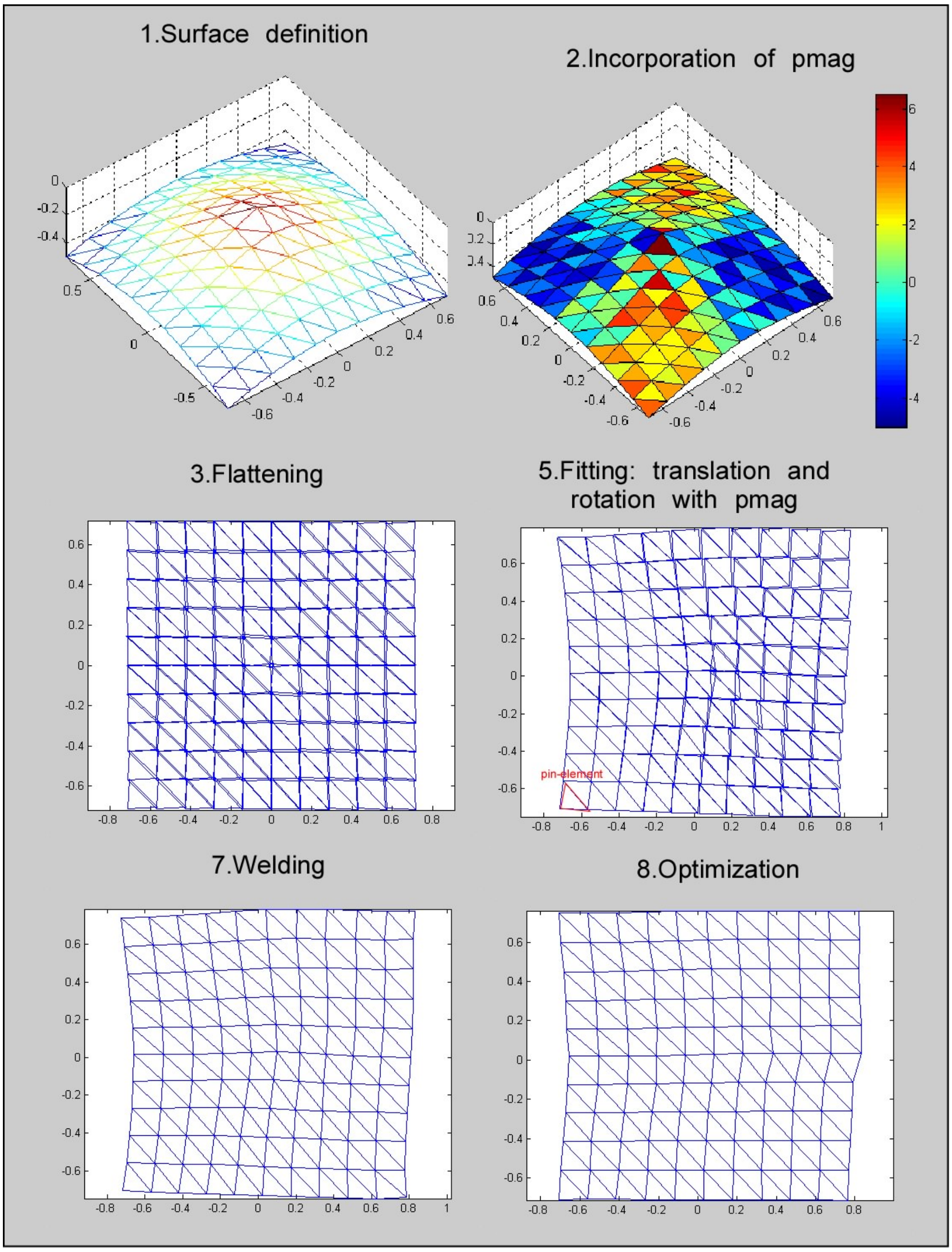

Figure 4.2: The method, step by step. 1) Surface definition. 2) Incorporation of paleomagnetic data. 3) Flattening. 4) Vertical axis rotation (unneeded in this example because paleomagnetic data of the pin-element fits with the reference). 5) Translation and rotation fitting. 6) Iterating process of step 5 with same results. 7) Welding of common vertices. 8) Optional optimization process.

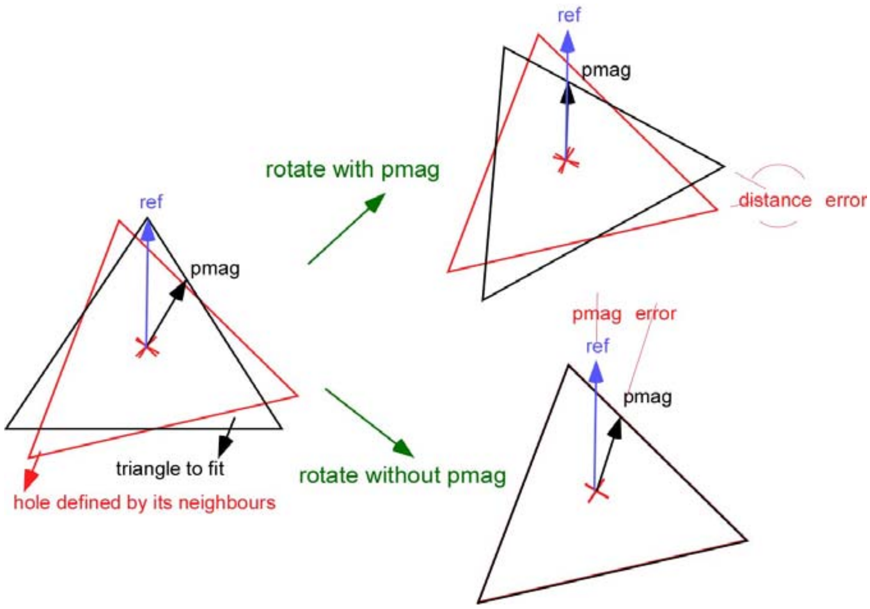

Figure 4.3: Rotation of an individual triangle with and without using the paleomagnetic vector. c_0 is the barycenter of the triangle. *pmag* is the paleomagnetic vector and *ref* its reference.

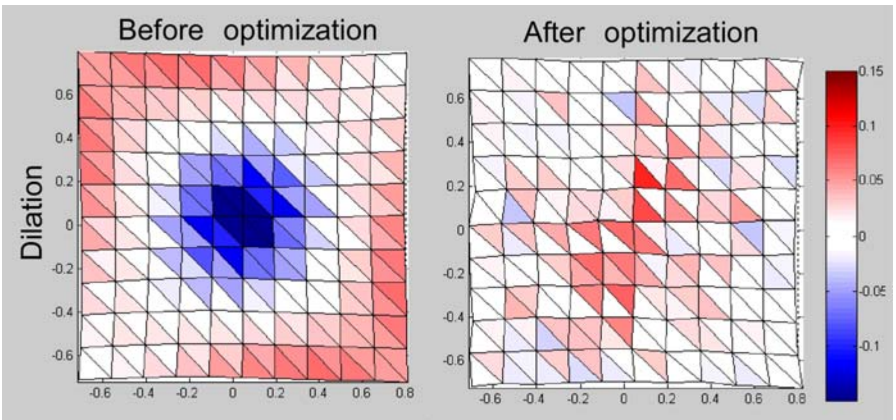

Figure 4.4: Dilation of the restored surface before and after the optimization step. Due to the optimization, the dilation decreases but the expected pattern disappears.

4.1.1 Formulation

We now detail the particular equations used in the code:

For a triangle defined by its vertices v_i, its barycenter is $c_0 = \frac{v_1 + v_2 + v_3}{3}$ and its normal vector is $N = v_1 c_0 \times v_2 c_0$.

The rotation matrix for the flattening step $v_i^{'} = R \cdot (v_i - c_0) + c_0$ is:

$$R = \begin{pmatrix} x^2 \cdot (1-\cos\psi) + \cos\psi & x \cdot y \cdot (1-\cos\psi) - z \cdot \sin\psi & x \cdot z \cdot (1-\cos\psi) + y \cdot \sin\psi \\ y \cdot x \cdot (1-\cos\psi) + z \cdot \sin\psi & y^2 \cdot (1-\cos\psi) + \cos\psi & y \cdot z \cdot (1-\cos\psi) - x \cdot \sin\psi \\ z \cdot x \cdot (1-\cos\psi) - y \cdot \sin\psi & z \cdot y \cdot (1-\cos\psi) + x \cdot \sin\psi & z^2 \cdot (1-\cos\psi) + \cos\psi \end{pmatrix}$$

where *xyz* is the rotation axis and ψ the magnitude. As the rotation axis is horizontal it is possible to write the rotation matrix as:

$$R = \begin{pmatrix} (\cos\phi)^2 \cdot (1-\cos\Psi) + \cos\Psi & \cos\phi \cdot sen\phi \cdot (1-\cos\Psi) & sen\phi \cdot sen\Psi \\ \cos\phi \cdot sen\phi \cdot (1-\cos\Psi) & (sen\phi)^2 \cdot (1-\cos\Psi) + \cos\Psi & -\cos\phi \cdot sen\Psi \\ -sen\phi \cdot sen\Psi & \cos\phi \cdot sen\Psi & \cos\Psi \end{pmatrix}$$

where $\begin{matrix} \phi = dec(N) - 90 \\ \psi = 90 - inc(N) \end{matrix}$ If the surface is inverted: $\psi_{inv} = 180 - \psi$

The fitting process of translation and rotation is an iterative process:

1) Fix *pin-element* triangles.
2) Seek for neighbourhoods.
3) If *pmag* is defined → Rotate to fit with its reference:

$$\alpha = ref - pmag \,,\; R = \begin{pmatrix} \cos\alpha & -\sin\alpha \\ \sin\alpha & \cos\alpha \end{pmatrix},\; v_i' = R \cdot (v_i - c_0) + c_0$$

4) Translation and rotation. Objective: minimize distance between vertices.

Distance: $d = \sum_{i=1}^{3} dist(v_{bi}, v_i) = \sum_{i=1}^{3} \sqrt{(x_{bi} - x_i)^2 + (y_{bi} - y_i)^2}$

Minimizing distance: $\frac{\partial d}{\partial x} = 0, \frac{\partial d}{\partial y} = 0, \frac{\partial d}{\partial \alpha} = 0$

New vertices: $v_i' = \begin{pmatrix} \cos\alpha & -\sin\alpha \\ \sin\alpha & \cos\alpha \end{pmatrix} \cdot (v_i - c_0) + translation + c_0$

- 2 vertices fixed

Translation when 2 vertices are fixed (rotation is determined by *pmag*):

$translation = (v_{b1} - v_{a1} + v_{b2} - v_{a2})/2$ where *a* is the initial triangle and *b* the fixed.

Translation and rotation with 2 vertices of the triangles fixed (only if pmag is not defined or if it has some error allowed; $\alpha_{95} > 0$):

$$\alpha = a\tan\left(\frac{-y_{a1}\cdot x_{b1}+x_{a1}\cdot y_{b2}-y_{a2}\cdot x_{b2}+x_{a2}\cdot y_{b2}+y_{a1}\cdot x_{b2}+y_{a2}\cdot x_{b1}-x_{a1}\cdot y_{b2}-x_{a2}\cdot y_{b1}}{x_{a1}\cdot x_{b1}+y_{a1}\cdot y_{b1}+x_{a2}\cdot x_{b2}+y_{a2}\cdot y_{b2}-x_{a1}\cdot x_{b2}-x_{a2}\cdot x_{b1}-y_{a1}\cdot y_{b2}-y_{a2}\cdot y_{b1}}\right)$$

If $\alpha > \alpha_{95} \rightarrow \alpha = \alpha_{95}$, $translation = \begin{bmatrix} 1/2\cdot(x_{b1}+x_{b2}-(x_{a1}+x_{a2})\cdot\cos\alpha+(y_{a1}+y_{a2})\cdot\sin\alpha) \\ 1/2\cdot(y_{b1}+y_{b2}-(x_{a1}+x_{a2})\cdot\sin\alpha-(y_{a1}+y_{a2})\cdot\cos\alpha) \end{bmatrix}$

- 3 vertices fixed

Translation with 3 vertices of the triangle fixed. The triangle must have the same centroid than the hole made by the mean vertices of its neighbours:

$translation = c_{b0} - c_{a0}$

Only rotation with 3 vertices of the triangles fixed:

$$\alpha = a\tan\left(\frac{y_{a1}\cdot x_{b1}-x_{a1}\cdot y_{b1}+y_{a2}\cdot x_{b2}-x_{a2}\cdot y_{b2}+y_{a3}\cdot x_{b3}-x_{a3}\cdot y_{b3}}{x_{a1}\cdot x_{b1}+y_{a1}\cdot y_{b1}+x_{a2}\cdot x_{b2}+y_{a2}\cdot y_{b2}+x_{a3}\cdot x_{b3}+y_{a3}\cdot y_{b3}}\right)$$

5) After fitting each triangle, come back to the point 2.

The optional optimization step is based on the Simulated Annealing method. Nodes are moved randomly to decrease a potential function U (Eq. [1]). The change is accepted if $U_1 < U_0$ and if $e^{-\frac{(U_1-U_0)}{k\cdot T}} > a$ (some local worsen is allowed in order to find the global minimum and not only a local one). The *temperature* (T) decreases with the number of iterations, at the end only changes that really decreases U are allowed $T = T_0\left(1-\frac{m}{M+1}\right)^{\alpha}$ where m is the actual iteration and M the total number of iterations.

By default: $a = 0.9, k = 0.02, T_0 = 1, \alpha = 1$

4.2 Parametric approach

This proposed alternative approach incorporates paleomagnetic information in an unfolding algorithm based on the parameterization of the surface, a method also valid for surfaces folded under flexural conditions (Ramón et al., in review). We have incorporated this constraint in the gOcad (by Paradigm[2]) code (Massot, 2002).

[2] http://www.pdgm.com

Any surface S ($\Re^3$) can be projected onto a map C ($\Re^2$) using a parametric representation (Fig. 4.4). This so-called surface parameterization problem has been extensively studied in the computer graphics community. We summarize the main ideas below and refer the reader to Botsch et al. (2010) and Floater and Hormann (2005) for further details and discussions, and Mallet (2002), Moretti et al. (2005) and Moretti (2008) for more details about the application of the free boundary parameterization to surface restoration. Each point in C defined by the coordinates **u**=*(u,v)* has a unique associated image in S **x**(**u**) with coordinates *(x,y,z)*:

$$\mathbf{u} = \begin{bmatrix} u \\ v \end{bmatrix} \in C \underset{\mathbf{u}(\mathbf{x})}{\overset{\mathbf{x}(\mathbf{u})}{\rightleftarrows}} \mathbf{x} = \begin{bmatrix} x \\ y \\ z \end{bmatrix} \in S \qquad [2]$$

For a single surface there are many possible parametric representations. However, for any parameterization it is possible to define the metric tensor *G(u,v)* which defines the intrinsic properties of the surface.

The main assumption of most restoration algorithms is the horizontality of the initial surface. Thus, the restoration problem is equivalent to look for a particular parameterization **u**(**x**). Moreover, we focus on surfaces folded under flexural conditions that lead to *globally developable* surfaces (Gaussian curvature equal to zero almost everywhere). This assumption implies the preservation of lengths and angles in the folded surface.

The paleo-geographic coordinate system *(u,v)* can be freely and arbitrarily chosen and because of simplicity it is assumed to be rectilinear and orthonormal. Because of the principle of minimum deformation, the metric tensor G associated with the local parameterization must be close to the unit tensor (Eq. [3]).

$$\varepsilon = 1/2 \cdot \left(G(u,v) - I\right) \cong 0 \rightarrow G(u,v) \cong I = \begin{bmatrix} 1 & 0 \\ 0 & 1 \end{bmatrix} \qquad [3]$$

From a given 3D surface, the restoration problem can be addressed by computing two coordinates (u,v) on the surface so that:

$$\begin{aligned} \nabla u \cdot \nabla v &= 0 \\ \|\nabla u\| = \|\nabla v\| &= 1 \end{aligned} \qquad [4]$$

The first constraint means that both gradients are orthogonal and the second that they have the same norm (Fig. 4.4). These two conformality constraints can be discretized on the surface in order to compute the parameterization, e.g. see Lévy and Mallet, (1999) or Levy et al. (2002). In this work, we started with a parameterization method developed by Massot (2002), which starts from a pin-element on the surface where two directions ∇u_0 and ∇v_0 are chosen so as to be mutually orthogonal and orthogonal to the local normal vector $\mathbf{n}_0$ (Fig. 4.4B). This method starts by propagating this local frame to all the nodes of the surface. For this, the frame is rotated along an axis l given by the cross product of the normal at the pin-point $\mathbf{n}_0$ and the normal at the current point $\mathbf{n}_1$. (Figs. 4.4B&C). Last, the u and v coordinates are integrated numerically from the pin-point coordinate using a least-squares method so as to honor the input gradients at all locations (Fig. 4.4D), see details in Massot, (2002) and Mallet (2002).

Although this method often provides good results in moderately deformed areas, it remains quite sensitive to the initial solution and fails for complexly folded structures. We improve this restoration approach by using paleomagnetic data. The idea is to use the paleomagnetic values defined in all points of the surface as the initial gradient values ∇u. The gradient is a vector contained in the surface, thus, the initial paleomagnetic vector is rotated to have null inclination and so to be embedded in the surface. Paleomagnetic data is known in specific sites and then interpolated to the entire surface as described in Chapter 6.

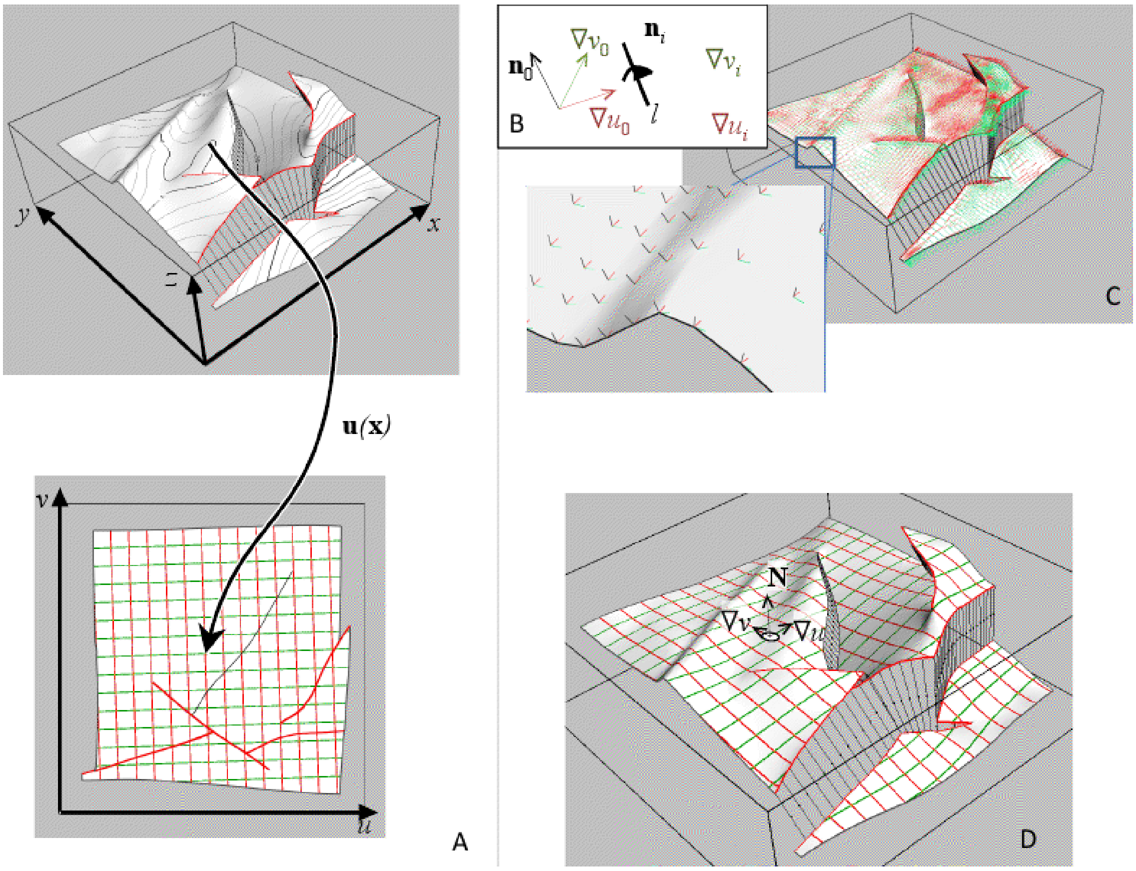

Figure 4.4: Parameterization of the surface. A) 3D surface can be mapped onto a 2D plane by computing a curvilinear coordinate system u(x,y,z) which is chosen to be rectilinear and orthonormal. B-C) Algorithm used to compute the initial parameterization. D) Parameterized surface.

4.3 Control parameters

The control parameters are basically the dilation and the strain ellipse described in the previous chapter (section 3.1.5) for the analysis of deformation of analog models. In our examples it is possible to calculate the real values of deformation because we know all points of the surface before and after deformation. However, in a real case, only estimated values can be obtained from the restored surface. If we compare the folded surface with the initial one we have the real values of deformation and if we compare the folded surface with the restored one we calculate the retro-deformation or the estimated values of deformation (Fig. 4.5).

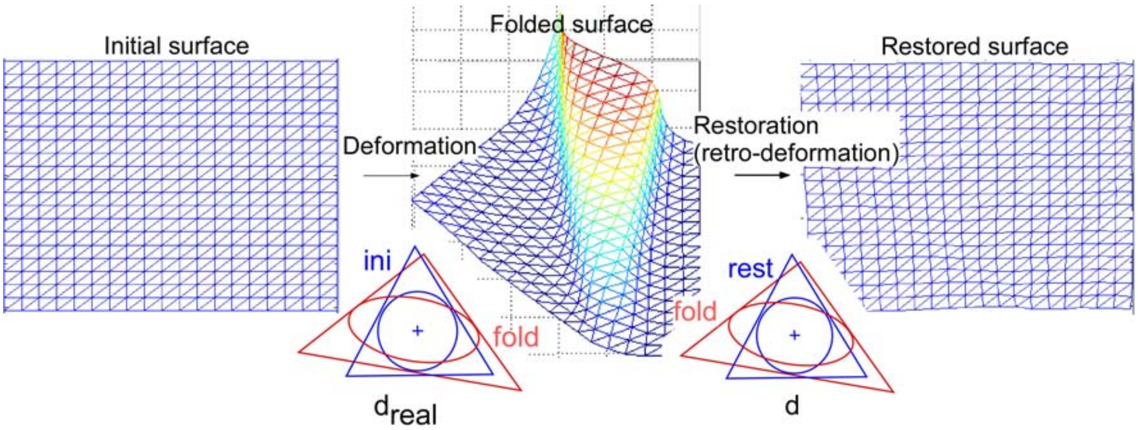

Figure 4.5: Deformation states (initial, folded and restored). Real deformation and dilation (d_{real}) compare folded and initial surfaces while retro-deformation (d) compares folded with restored surface.

Ideally, deformation and retro-deformation may coincide, but it strongly depends on the restoration process applied. Deformation of the restored surface (retro-deformation) may be used to validate the restoration process and provide an idea of the real deformation that has undergone the folded structure. However, deformation results of the restoration must be carefully evaluated, because they may be influenced by several causes:

1) Bad reconstruction of the folded surface. All geological information must be included and contrasted in the model. However, when little information is available, the reconstruction is based on assumptions and thus, the importance of a feedback between restoration and reconstruction. Curvature analysis may also help evaluate reconstruction problems (i.e. high values of Gaussian curvature show a non-developable area; Lisle, 1992).

2) Bad restoration of the surface. Any restoration algorithm is valid under certain assumptions that must be checked; structures folded under flexural or simple shear mechanisms must be restored with different algorithms. Moreover, algorithms produce particular artifacts that must be recognized (i.e. the pin-element dependency). Thus, the importance of checking the methods with well known analog models.

3) Real deformation. Although it is difficult that a restoration method perfectly reproduce the deformation process, it may provide an idea of the deformation that has suffered the structure during folding. Actually, this process helps in the decision-making and helps acquiring more data.

The parameter we have mostly used to evaluate the restoration and to compare results is the dilation calculated for each triangle. When we assume that restoration is correct a further analysis can be done calculating the strain ellipse to evaluate magnitude and orientation of deformation. Additioanlly, we can characterize the folded surface with a curvature analysis.

Dilation measures the area variation within the triangles. Negative or positive dilation respectively correspond to contraction or expansion of the folded surface, with respect to the restored (Eq. [5]) or initial surface (Eq. [7]). A completely developable surface folded under flexural conditions (isometric constraints) would have null dilation everywhere. The restoration methods developed here are valid for globally developable surfaces in which this condition is nearly fulfilled, thus, the mean dilation (Eq. [6]) must have low values. Moreover, the distribution of maximum dilation values in a good restoration process may correspond with those expected; in order to quantify the difference between the real and calculated dilation values we measure the mean error between them (Eq. [8]). Although the absolute mean values d_{mean} and e provide a numerical value, a qualitatively analysis is also necessary. On the other hand, we cannot forget that only d and d_{mean} can be computed in a real case whereas that d_{real} and e require the knowledge of the initial surface, unknown in nature.

Dilation of restored surface (retro-dilation): $d = \frac{Area_{folded} - Area_{restored}}{Area_{restored}}$ [5]

Mean dilation in absolute value: $d_{mean} = 1/N \sum |d|$ [6]

Real dilation: $d_{real} = \frac{Area_{folded} - Area_{initial}}{Area_{initial}}$ [7]

Mean error between real and retro-dilation in absolute value: $e = 1/N \sum |d_{real} - d|$ [8]

Strain ellipse is a measure of the anisotropy of the deformation. As described in section 3.1.5, we first compute the affine transformation matrix M that relates the points in the two states. The matrix coefficients are determined using the coordinates of the vertices of the folded and restored surfaces. Second, we consider a circle centered on the barycenter of each triangle in the restored state, and apply the transformation matrix M to the canonical matrix of the circle. The circles become deformation ellipses. The magnitude of the deformation is then calculated as the ratio between the major and minor axis of the deformation ellipse, while the orientation of the deformation is the is the trend of the major axis. We usually plot the strain ellipse in the restored state, but we always assume that the restored state is equivalent to the initial and therefore the undeformed.

Moreover, we can perform a curvature analysis of the surface (in terms of Lisle and Toimil, 2007). The mean normal curvature is the arithmetic average of the two principal curvatures ($M=(k1+k2)/2$) and expresses the general degree of convexity ($M > 0$) or concavity ($M < 0$) of the surface at that point. The Gaussian curvature is the product of the two principal curvatures ($G=k1*k2$) and is an indicator of the develoapility of the surface. Lisle and Toimil (2007) propose a clasification of folds that uses both curvatures: synclastic antiform ($M>0$, $G>0$), anticlastic antiform ($M>0$, $G<0$), synclastic synform ($M<0$, $G>0$) and anticlastic synform ($M<0$, $G<0$).

5 Checking the consistency of the restoration methods: surface sensitivity

In this chapter we analyze the consistency of the methods assuming that paleomagnetic variable is completely reliable and perfectly know in all points of the surface. In next chapter we deal with the effects of paleomagnetism resolution and confidence.

First tests to check the consistency of the methods were done with completely developable surfaces, like a cylinder, which were theoretically described (using Matlab). All restoration methods for this kind of surfaces, independently of the approach and the usage or not of paleomagnetism, lead to equivalent solutions. On the other hand, we usually find complex structures in geology that have undergone some deformation even though they had been folded under flexural conditions. These are the type of structures we have simulated with the analog models described in Chapter 3, which we will use now to test the proposed restoration methods: a conical fold based on the San Marzal Pericline (Fig. 5.1) and a curved fold based on the Balzes Anticline (Fig. 5.3).

We must remember that the goodness of analogs is that we can completely characterize the structure before and after deformation because we know the surfaces with their reference system in both the initial and folded states. Thus, before evaluating the results of restoration, we are going to calculate in the first section the real deformation suffered by the upper surface of the models.

5.1 Expected results

Ideally, the restored surface should correspond with the initial surface. Therefore, the expected results are those obtained by comparing the initial and the folded surface (Fig. 4.5). As detailed in section 4.3, we calculate the real dilation (change of area) and the strain ellipse for all triangles. Additionally, we perform the curvature analysis.

The first model we are going to analyze is the conical fold based on the San Marzal Pericline (Fig. 5.1) because it is less complicated and has a lower mesh density than the curved fold based on the Balzes Anticline (Fig. 5.3). Curvatures are calculated in the folded surface but we visualize their values in the initial undeformed surface in order to easily compare all properties (Fig. 5.2). Gaussian curvature is the property that allows us to assess if the surface is developable. It has low values almost everywhere except in the pericline closure, and therefore we can state that the surface is globally developable. Mean normal curvature is positive (red colors) in the anticline and negative (blue colors) in the synclines. The fold classification (Lisle and Toimil, 2007) clearly distinguishes between antiforms and synforms, although synclastic and anticlastic areas are more ambiguous.

Dilation is the main property used to measure deformation. The areas of maximum dilation values correspond with those of maximum normal curvature. Positive dilation values indicate expansion of the surface (tangential-longitudinal strain) and are located in the anticline hinge (synclastic and anticlastic antiform), while negative values mean compression and are located in the synclines (inner hinges). The strain ellipse offers extra information about the anisotropy of the deformation. The areas with higher values of strain ratio are compression areas, arguably because deformation concentrates in less space (inner hinges). Moreover, there is an orientation trend in these areas that corresponds with the fold axis.

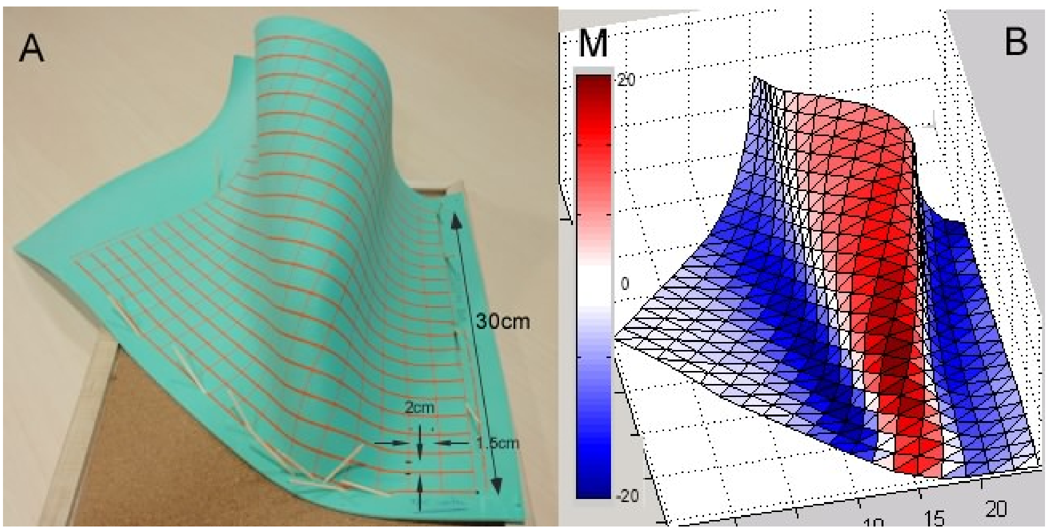

Figure 5.1: Conical fold. A) Analog model based on the San Marzal pericline. B) Digitalized model with values of normal curvature (M) displayed.

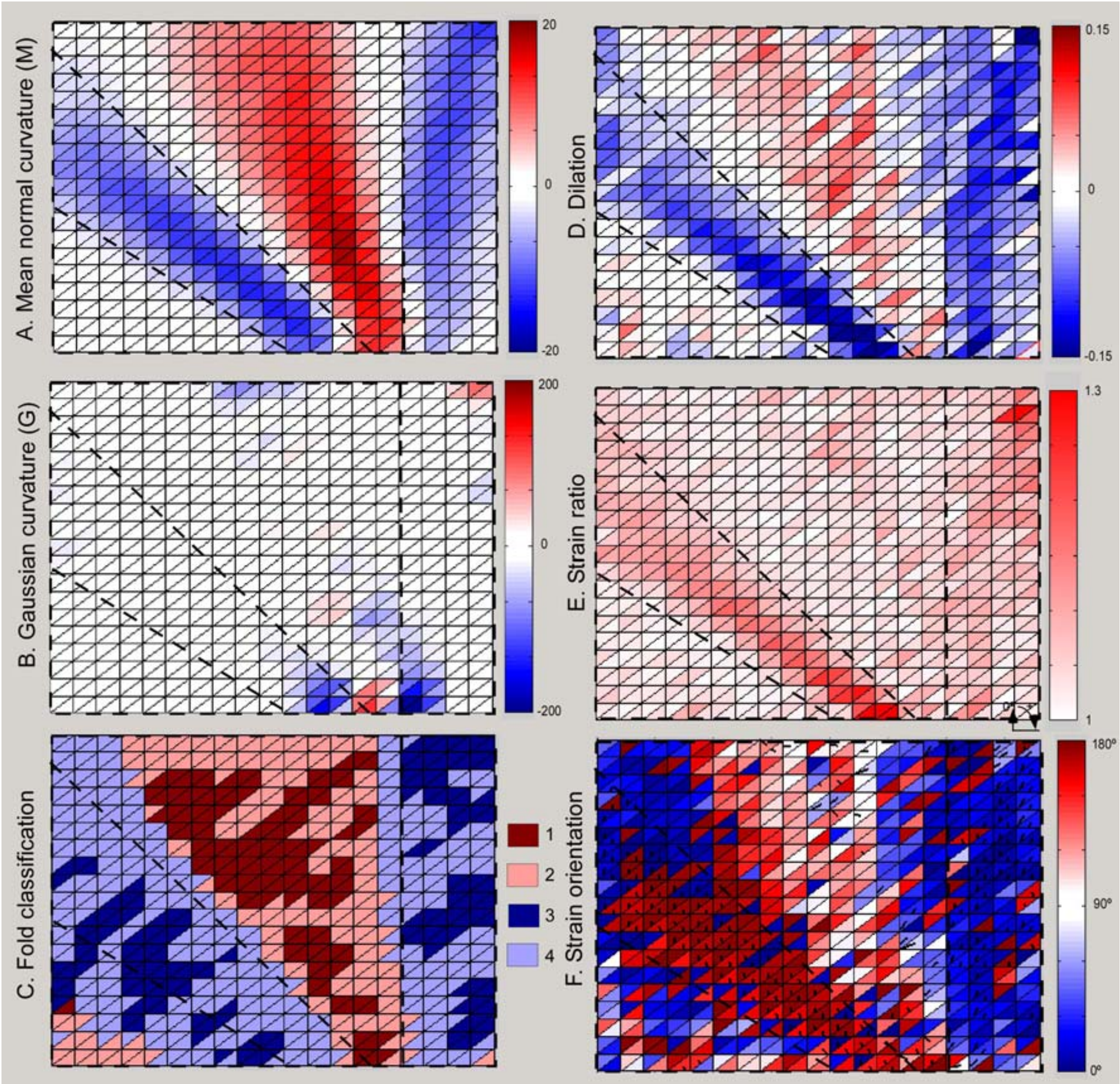

Figure 5.2: Curvature analysis and real deformation of the San Marzal model. Properties are displayed in the initial horizontal surface. Dashed black lines divide the maximum dilation areas. A) Mean normal curvature (*M=(k1+k2)/2*). B) Gaussian curvature (*G=k1*k2*). C) Fold classification described by Lisle and Toimil (2007): 1.synclastic antiform (*M>0, G>0*), 2.anticlastic antiform (*M>0, G<0*), 3.synclastic synform (*M<0, G>0*), 4.anticlastic synform (*M<0, G<0*). D) Real dilation ($d_{real}=(A_{folded}-A_{initial})/A_{initial}$). E) Anisotropy of the strain ellipse; strain ratio: major axis / minor axis. F) Strain orientation. Major axis orientation. Axis displayed in those triangles with meaningful strain ratio (>1.07).

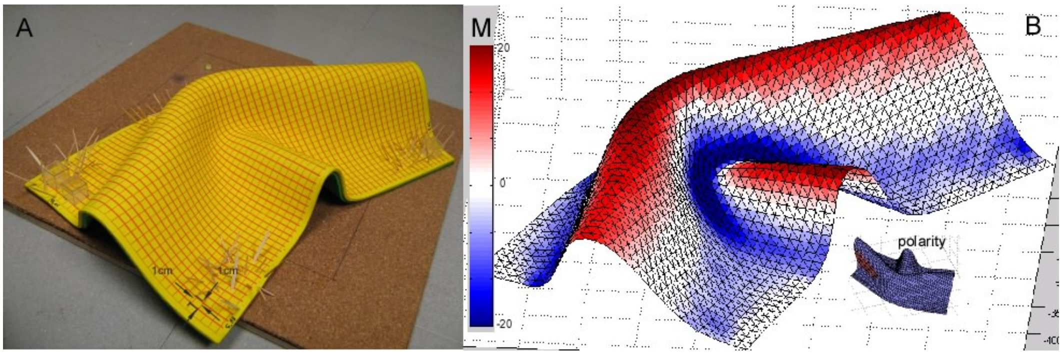

Figure 5.3: Curved fold. A) Analog model based on the Balzes Anticline. B) Digitalized model with values of normal curvature (M) displayed. The small picture shows the inverted area.

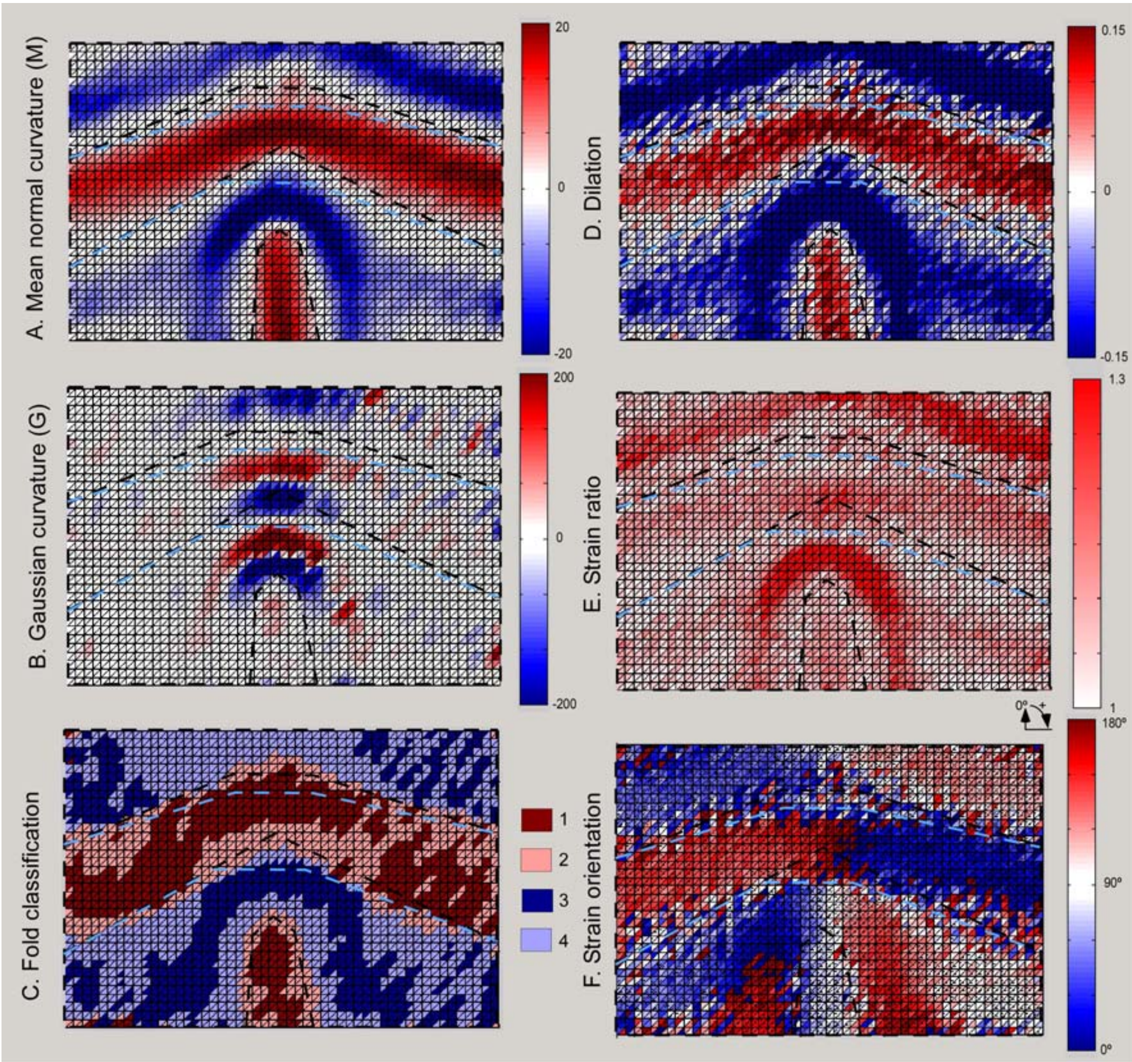

Figure 5.4: Curvature analysis and real deformation of the Balzes model. Dashed black lines divide the maximum dilation areas and dashed blue lines the maximum strain ratio areas. A) Mean normal curvature. B) Gaussian curvature. C) Fold classification: 1.synclastic antiform, 2.anticlastic antiform, 3.synclastic synform, 4.anticlastic synform. D) Real dilation. E) Strain ration. F) Strain orientation. Major axis orientation. Axis displayed in those triangles with meaningful strain ratio (>1.07).

A similar analysis is done for the second analog model; the Balzes Anticline (Fig. 5.4). Again, maximum dilation areas correspond with those of maximum curvature, all located at the hinges of the folds where tangential-longitudinal strain has taken place. However, in this case, the maximum strain ratio has a bit different pattern and it is possible to associate it with the Gaussian curvature. The most deformed areas are those with maximum Gaussian curvature (no matter the sign). The orientation of the major axis of the strain ellipse seems to be perpendicular to the fold axis orientation in the outer hinges (as expectable from the Gairola's [1967] models) where there is dilation and parallel to the fold axis in the inner hinges where there is contraction.

5.2 Restoration with and without paleomagnetism

After this round through the real deformation parameters we are going to test the incorporation of the paleomagnetic constraint into the restoration methods. We are going to unfold the surfaces with the piecewise approach using and not using paleomagnetism (Pmag3DRest and UNFOLD methods respectively) as well as with the parametric approach (gOcad method with and without the paleomagnetic constraint).

The piecewise restoration is quite sensitive to the pin-element selection, as we will see in Section 5.4, but for our current purpose we stick to the traditional approach ofplacing a pin-element in the undeformed area, although not in the border. The orientation of the paleomagnetic vector also has some influence in the results; for this example we try to select one oblique to the main structures that better registers the deformation, but of course this depends on the real geology setting in natural cases. Eventually, in these simulations we consider paleomagnetism defined in all triangles.

We first analyze the piecewise restoration of the San Marzal model using and not using paleomagnetism (Fig. 5.5, Table 5.1). Restoration without paleomagnetism seems to be pretty good in terms of mean dilation (d_{mean} without pmag < d_{mean} with pmag) but restoration with paleomagnetism better locates real deformation (*e* with pmag < *e* without pmag). The restoration without paleomagnetism achieves the restored surface with minimum deformation because triangles are free to find the best fitting. However, the paleomagnetic constraint yields a restored surface more similar to the initial one. Dilation values of the restored surface with paleomagnetism are mostly coherent with the real dilation in the expected areas: expansion in the anticline and compression in the synclines. On the other hand, absolute values are always smaller than those expected ($d_{mean} < d_{real\_mean}$, $e >> 0$) because of the restoration method itself which try to minimize deformation.

Additionally, the anisotropy of deformation (strain ellipse) is coherent for the restoration with paleomagnetism and has less meaning for the restoration without paleomagnetism. The compression area with maximum strain ratio coincides with the real one and shares the same orientation. Moreover, the shape of the surface restored with paleomagnetism is closer to the expected rectangle.

This is a good example where piecewise restoration works well and paleomagnetism provides additional information about the real deformation of the surface. Let us compare now this results with the second method based on the parameterization.

The parametric approach without the incorporation of paleomagnetism is unable to reach a proper restoration of the surface (Fig. 5.6B) and mean dilation values are to high ($d_{mean} \approx 10\%$ [Table 5.1]). We can say that this restoration method is only valid for smoothly folded structures and not for complex folds such as this example. This method is too dependant on the initial solution and for this reason the usage of paleomagnetism is crucial to define it (particularly in non-cylindrical and non-coaxial structures).

The shape of the restored surface with paleomagnetism almost perfectly matches the expected one and orthogonality is preserved in the restored state. The distribution of maximum dilation values roughly corresponds with those expected, although the signs do not match in this case (restored surface does not show the contraction area). On the other hand, maximum strain orientation approximately coincides with the expected one.

The restoration method assumes isometric parameterization based on developable surfaces folded under flexural conditions but we have used it to restore globally developable surfaces with small deformation in complex folded areas. Therefore, the unfolding algorithm minimizes the deformation showing dilation patterns similar to those real, but it could never predict the real deformation. Because of that, we recommend the usage of several restoration methods in order to compare results. In this case for example, the strain orientation of the compression area with a maximum strain ratio is trustable because almost coincides with both techniques.

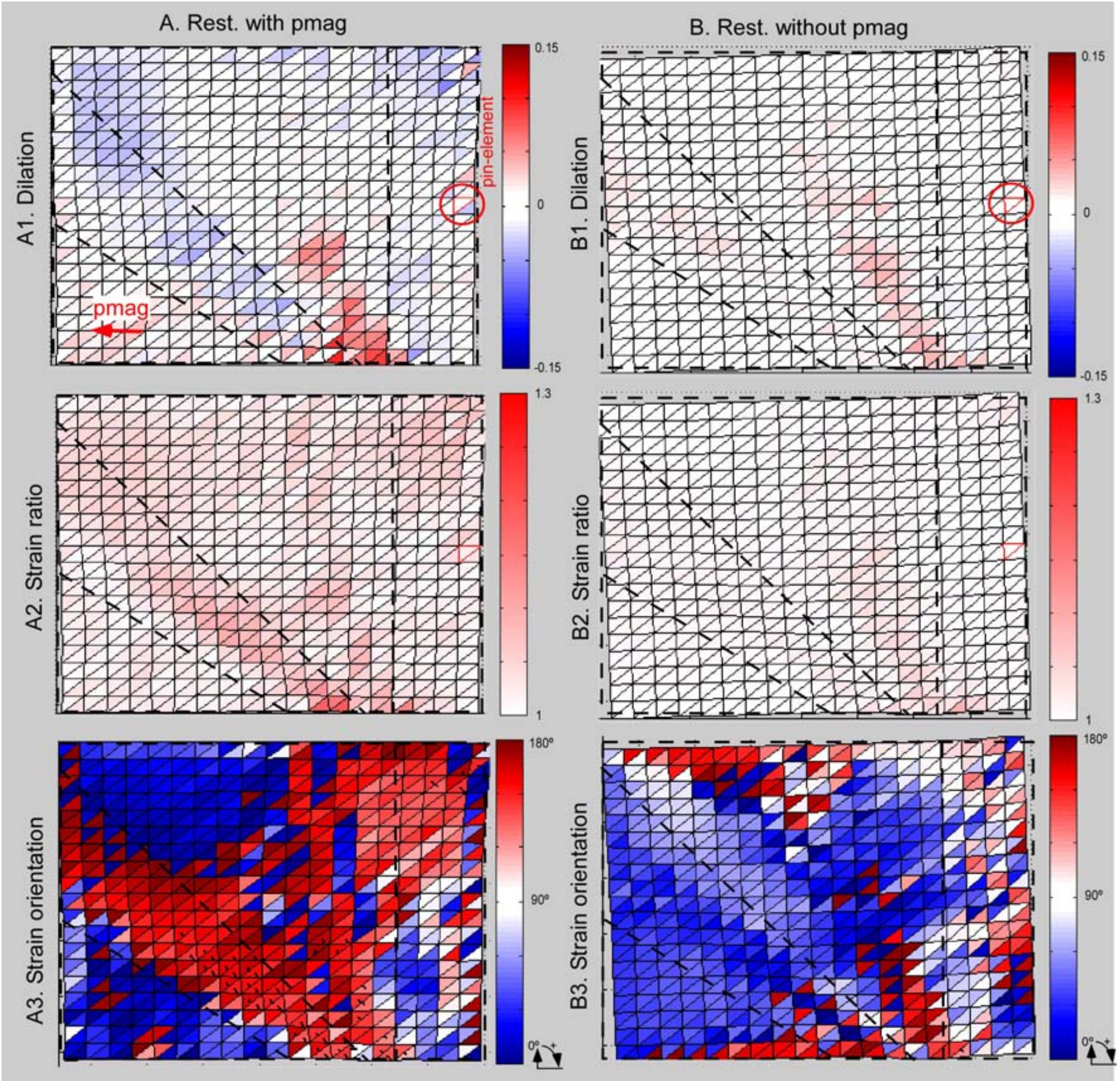

Figure 5.5: Piecewise restoration of the San Marzal model (regular triangulation, original mesh density). Dashed black lines are useful to compare the restored surface with the initial one and real values of deformation (Fig. 5.2). The pin-element is highlighted with a red circle. A) Restoration using paleomagnetism (Pmag3DRest method). The red arrow is the paleomagnetic orientation. B) Restoration without paleomagnetism (UNFOLD method [Gratier et al., 1991]). 1) Dilation ($d=(A_{folded}-A_{restored})/A_{restored}$). 2) Strain ratio: major axis / minor axis. 3) Strain orientation: major axis displayed in those triangles with meaningful strain ratio (>1.07).

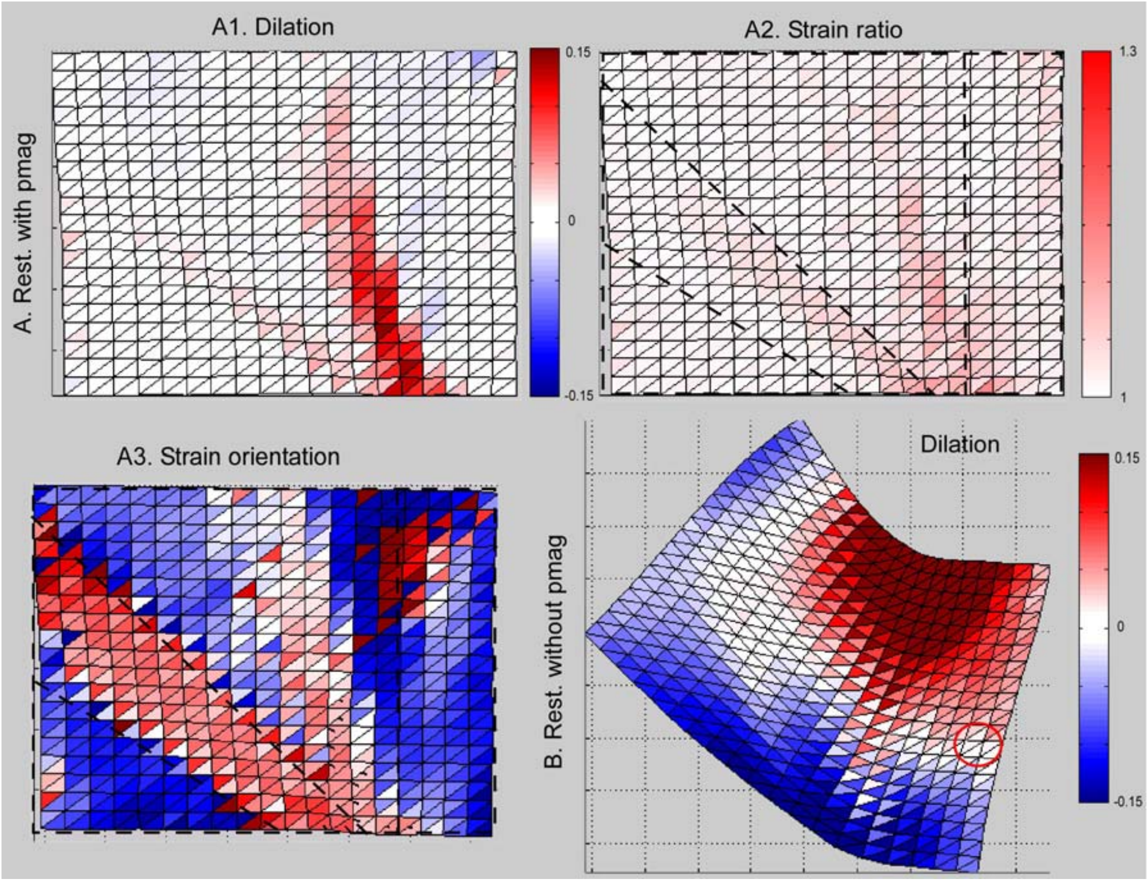

Figure 5.6: Parametric restoration of the San Marzal model. Dashed black lines are useful to compare the restored surface with the initial one and real values of deformation (Fig. 5.2). A) Restoration using paleomagnetism: 1) dilation, 2) strain ratio, 3) strain orientation. B) Restoration without paleomagnetism with dilation values.

SAN MARZAL (d_{real_mean}=0.0433)				
	Piecewise restoration		Parametric restoration	
	with pmag	without	with pmag	without
e	0.0392	0.0442	0.0459	0.0964
d_{mean}	0.0174	0.0086	0.0164	0.0925

Table 5.1: Mean dilation values for the restoration of San Marzal. Mean error between real and retro-dilation in absolute value: $e = 1/N \sum |d_{real} - d|$ (Eq. [8]) Mean dilation in absolute value: $d_{mean} = 1/N \sum |d|$ (Eq. [6]). Mean real dilation in absolute value: d_{real_mean}.

The next example (curved fold based on the Balzes Anticline) is more complicated than the previous because it has more deformation (higher d_{real_mean}) and the surface is less developable (higher Gaussian curvature). Moreover, the meshing is denser, hampering the piecewise restoration.

Piecewise restoration (Fig. 5.7, Table 5.2) is not as accurate for this example and the benefits of paleomagnetism are not as clear (e & d_{mean} without pmag < e & d_{mean} with pmag). Dilation increases towards the opposite part of the pin-element due to the propagation of errors. Moreover, the dilation values seem to be more related to the areas of higher Gaussian curvature than with the real dilation, particularly in the interference syncline between both anticlines.

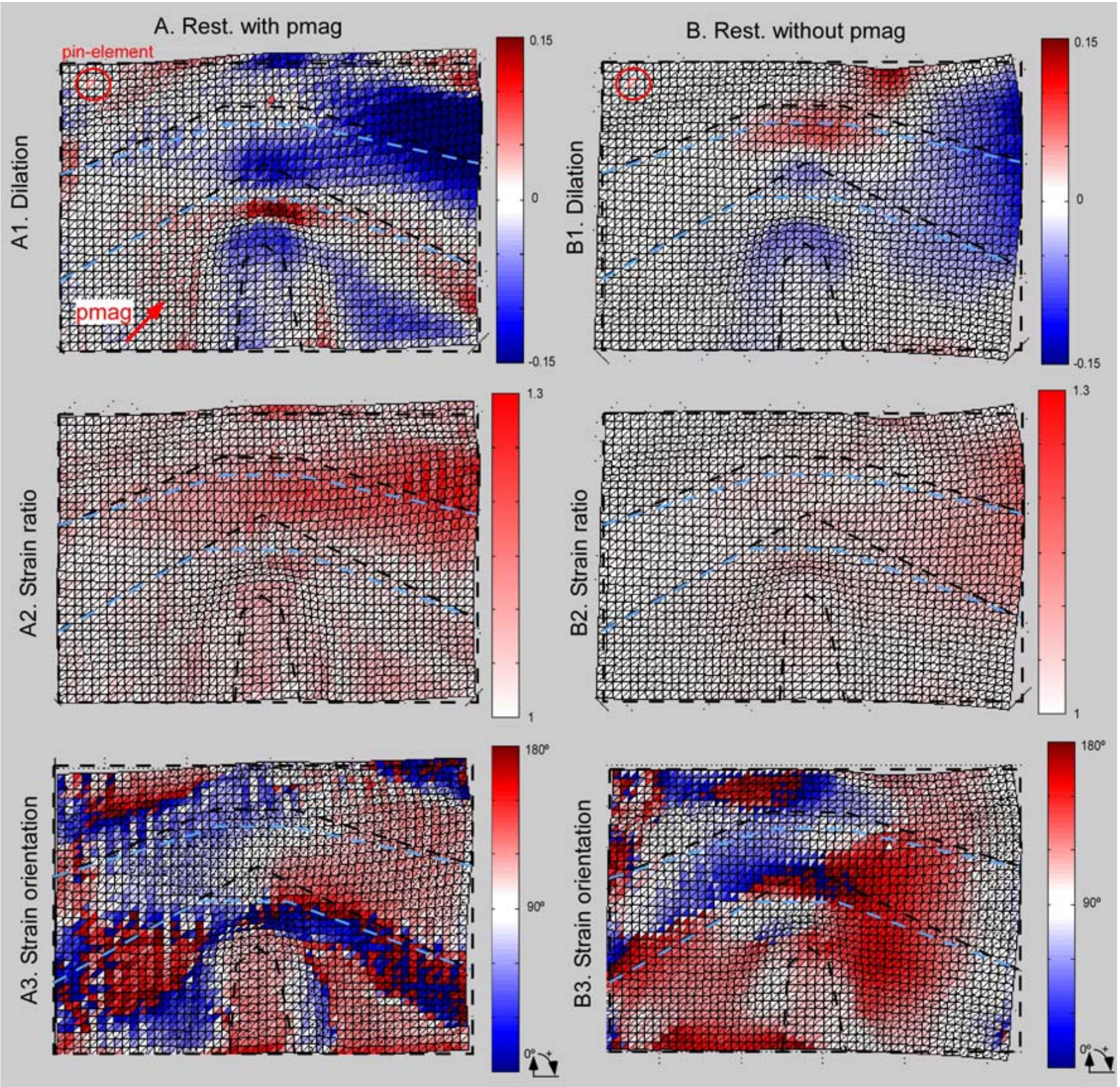

Figure 5.7: Piecewise restoration of the Balzes model. Dashed lines are useful to compare the restored surface with the initial one and real values of deformation (Fig. 5.4). The pin-element is highlighted with a red circle. A) Restoration using paleomagnetism (Pmag3DRest). The red arrow is the paleomagnetic orientation. B) Restoration without paleomagnetism (UNFOLD). 1) Dilation. 2) Strain ratio. 3) Strain orientation.

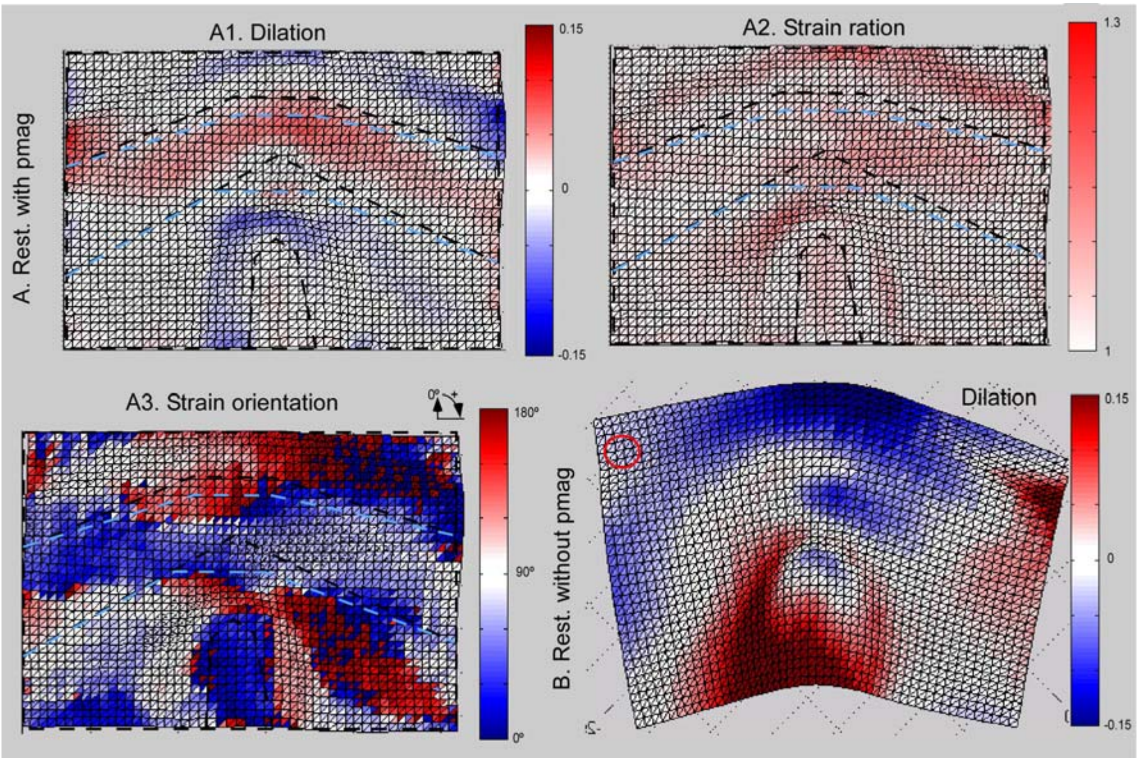

Figure 5.8: Parametric restoration of the Balzes model. Dashed lines are useful to compare the restored surface with the initial one and real values of deformation (Fig. 5.4). A) Restoration using paleomagnetism: 1) dilation, 2) strain ratio, 3) strain orientation. B) Restoration without paleomagnetism with dilation values.

In this situation, it seems more convenient to unfold the surface with the second restoration method, the parametric approach, because the results are really encouraging (Fig. 5.8). As in the example of San Marzal, the method does not work well without the paleomagnetic constraint. Thus, we focus on the restoration with paleomagnetism. Dilation and strain ratio patterns are fairly similar to those expected. Strain orientation is more confuse this time.

BALZES (d_{real_mean}=0.0989)				
	Piecewise restoration		Parametric restoration	
	with pmag	without	with pmag	without
e	0.1087	0.0988	0.0856	0.1166
d_{mean}	0.0415	0.0240	0.0228	0.0572

Table 5.2: Mean dilation values for the restoration of Balzes.

5.3 Mesh sensitivity

In discrete computer-based models some algorithms may lead to artifacts when surface sampling changes. Therefore, we check the robustness of the method towards variations in density and structure of the mesh (Ramón et al., in review).

5.3.1 Mesh density sensitivity

The impact of mesh density is evaluated by decimating the initial point set defined by the nodes of the reference grid and preserving the meshing method and boundary of the surface. We decimate the initial nodes by a factor of two for rows and columns. The San Marzal model initially has 722 triangles and 400 nodes and after decimation: 200 triangles and 121 nodes. The Balzes model has 3570 triangles and 1872 nodes and after decimation: 936 triangles and 513 nodes.

The impact of mesh density for the simple geometry model (San Marzal) is only evident when analyzing the values of dilation for the restored surface because it has a proper rectangular shape (Fig. 5.9). With a higher mesh density, dilation in the restored surface is more localized along the hinges of the fold, whereas the lower mesh density model has a greater dispersion of dilation, partly due to the difference in triangle size (Fig. 5.9 vs. Fig. 5.5 & Fig. 5.6). However, differences in mean dilation between low and high density models are not great (Table 5.3 vs. Table 5.1), indicating that mesh density has a limited impact on restoration results.

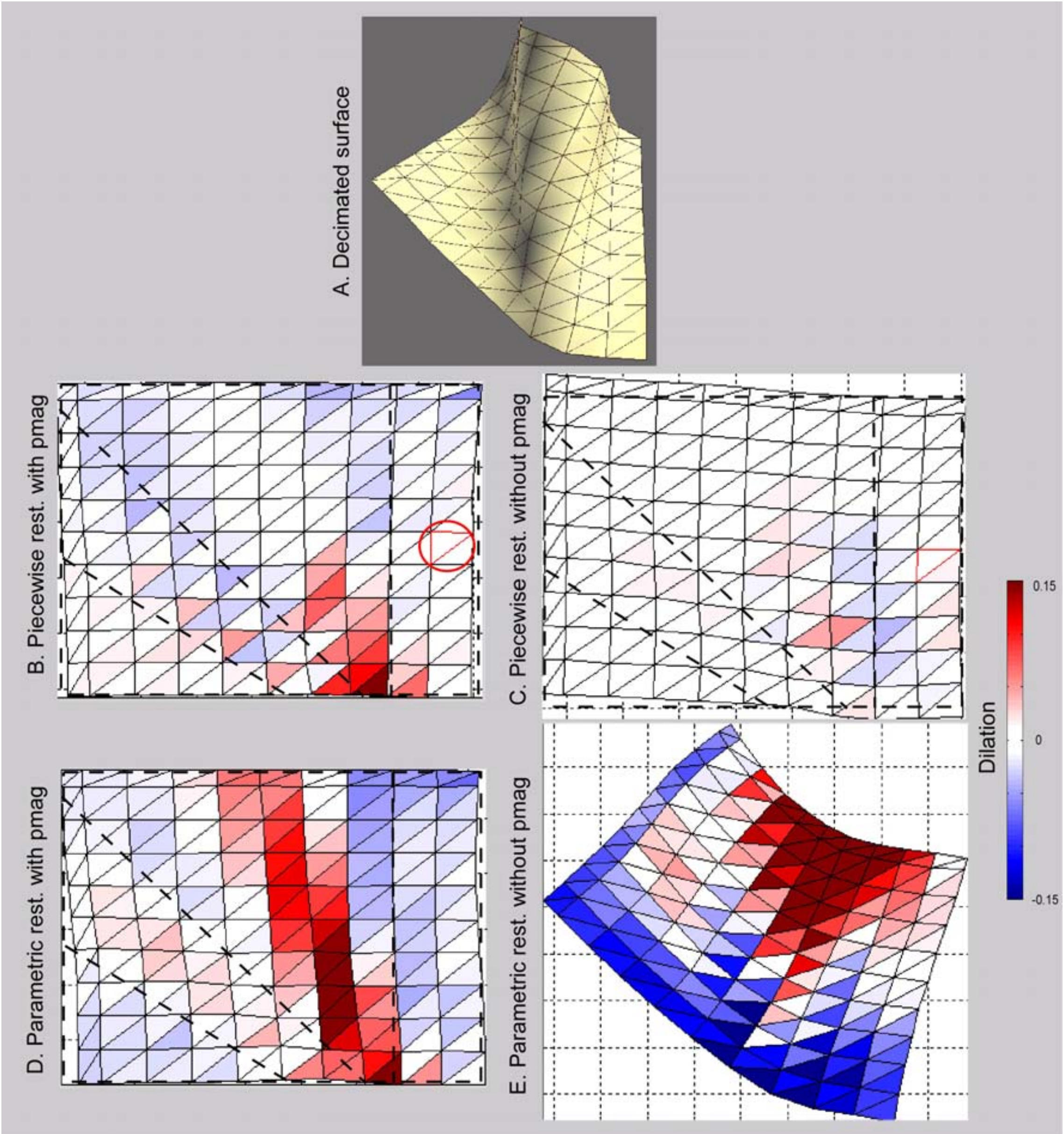

Figure 5.9: Mesh density analysis of San Marzal (regular triangulation). A) Decimated initial surface (with boundary preservation). B) Restored surface using the piecewise approach with paleomagnetism. Dilation values displayed. C) Piecewise restoration without paleomagnetism. D) Parametric restoration with paleomagnetism. E) Parametric restoration without paleomagnetism.

Similar considerations can be done for the second model of a curved fold (Balzes) (Fig. 5.10). Areas of maximum and minimum dilation obtained with both restoration methods are equivalent for the surfaces with more and less mesh density (Fig. 5.10 vs. Fig. 5.7 & Fig. 5.8). However, in this case there is an additional error produced by the influence of the border, particularly in the neighborhood of the pin-element where the size of triangles is smaller in order to preserve the boundary of the initial surface. This error causes an increase on the mean dilation value (Table 5.3 vs. Table 5.2).

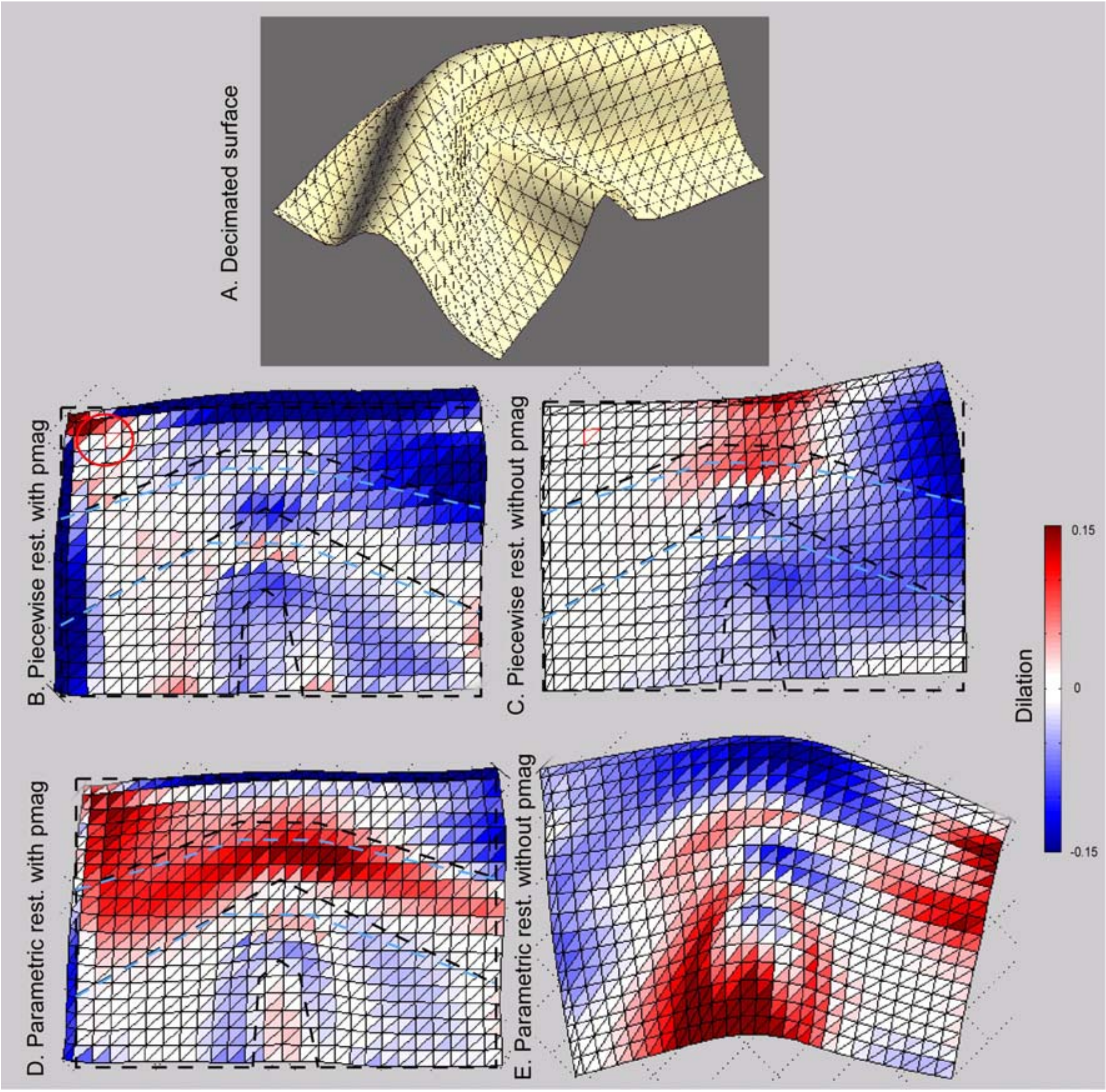

Figure 5.10: Mesh density analysis of Balzes. A) Decimated initial surface (with boundary preservation). B) Restored surface using the piecewise approach with paleomagnetism. Dilation values displayed. C) Piecewise restoration without paleomagnetism. D) Parametric restoration with paleomagnetism. E) Parametric restoration without paleomagnetism.

d_{mean}	Piecewise restoration		Parametric restoration	
	with pmag	without	with pmag	without
San Marzal Decimated	0.0197	0.0084	0.0362	0.0879
Balzes Decimated	0.0707	0.0381	0.0500	0.0550

Table 5.3: Mean dilation values (d_{mean}) for decimated and re-meshed restored surfaces.

5.3.2 Mesh-type sensitivity

The initial mesh of the surface is a regular triangulation formed with right-angled triangles defined by joining neighboring nodes of the reference mesh. We try a second triangulation method: an equilateral grid obtained by adaptive Delaunay's sampling. The equilaterality of triangles is maximized, but the nodes of the triangulated surface do not coincide with those of the actual reference mesh. This triangulation method is performed in gOcad™ using the "beautify for equilaterality" command (Mallet, 2002). Paleomagnetism is interpolated into the new mesh. This may introduce some noise that does not influence significantly the final restoration result.

Both triangulations (regular and equilateral) lead to equivalent dilation patterns of the restored surfaces of the San Marzal model (Fig. 5.11 vs. Fig. 5.5 & Fig. 5.6) and almost equivalent for the Balzes model (Fig. 5.12 vs. Fig. 5.7 & Fig. 5.8). Yet, for the piecewise approach, the restored surface with the regular mesh matches the expected undeformed state with less scattering. This can be particularly observed in the Balzes model where d_{mean} increases (Table 5.4 vs. Table 5.2) and dilation pattern is blurred. Piecewise restoration without paleomagnetism is unable to reach a good solution in this case. Therefore, we can say that for a dense initial mesh, the meshing type may influence the restoration for the piecewise approach, especially, when paleomagnetism is not considered. On the other hand, piecewise restoration of the Balzes model was uncertain also with the regular mesh.

Summarizing, the restored surfaces and the dilation patterns are equivalent for both the regular and the equilateral grid. The decimated regular mesh leads to an equivalent result although with smoother definition of the dilation pattern. Apart from this consideration, paleomagnetism still guarantees the reliability of the result and the difference with the restoration results when the paleomagnetic vectors are not considered is notable.

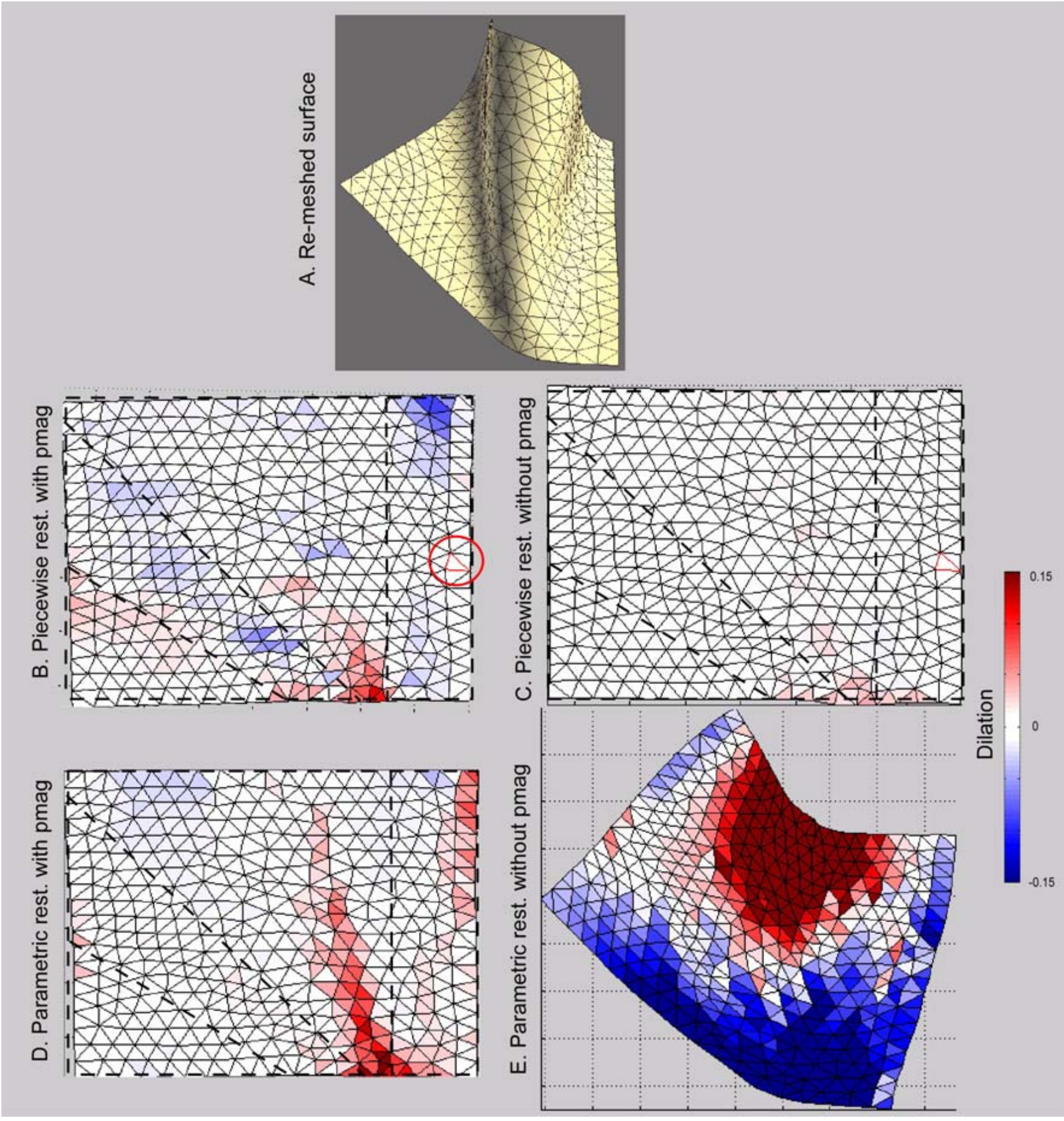

Figure 5.11: Mesh-type analysis of San Marzal. A) Initial surface triangulated with an equilateral mesh (initial nodes of the reference mesh are not maintained, but density is mantained). B) Restored surface using the piecewise approach with paleomagnetism. Dilation values displayed. C) Piecewise restoration without paleomagnetism. D) Parametric restoration with paleomagnetism. E) Parametric restoration without paleomagnetism.

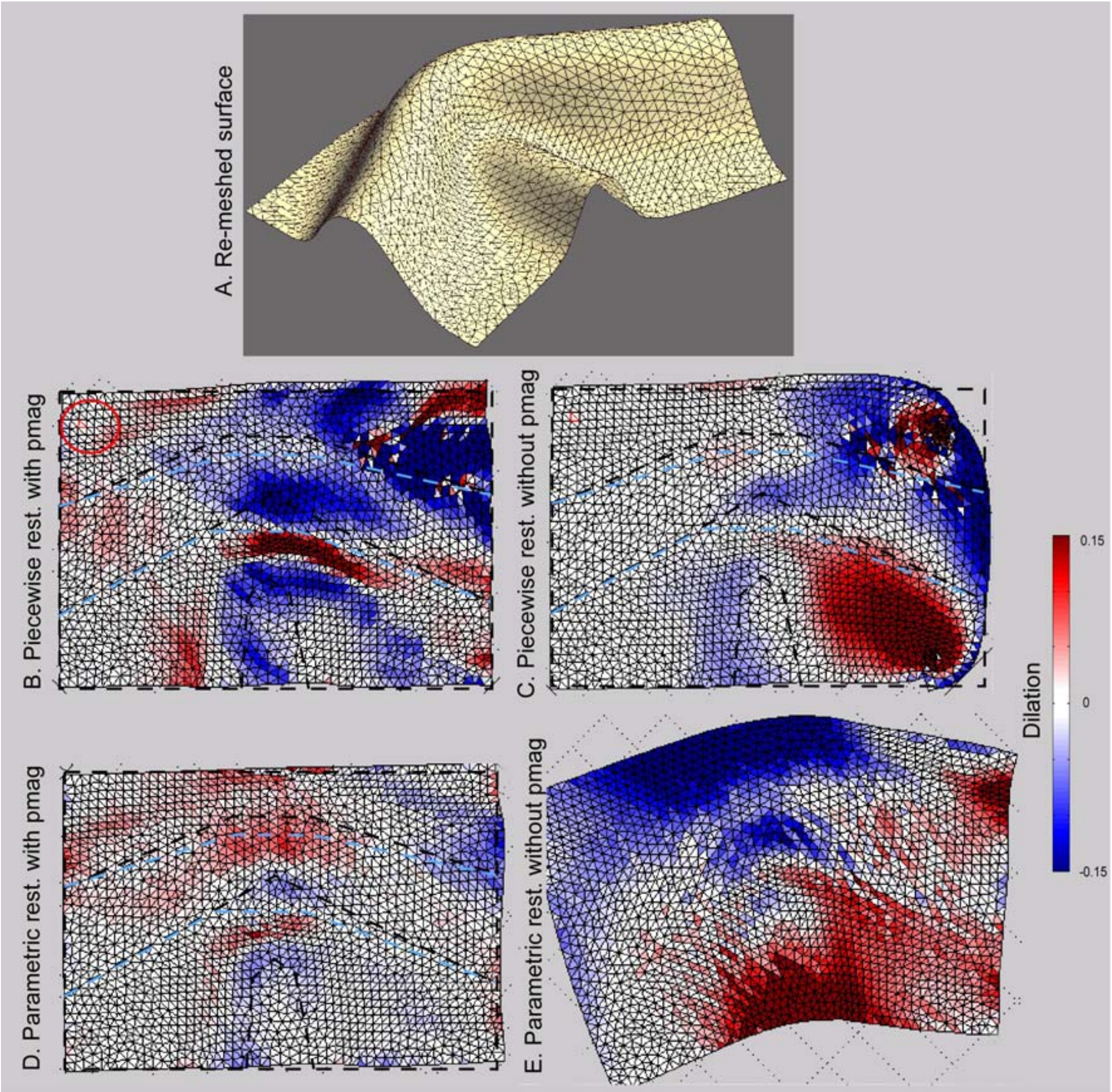

Figure 5.12: Mesh-type analysis of Balzes. A) Initial surface triangulated with an equilateral mesh (initial nodes of the reference mesh are not maintained). B) Restored surface using the piecewise approach with paleomagnetism. Dilation values displayed. C) Piecewise restoration without paleomagnetism. D) Parametric restoration with paleomagnetism. E) Parametric restoration without paleomagnetism.

d_{mean}	Piecewise restoration		Parametric restoration	
	with pmag	without	with pmag	without
San Marzal Re-meshed	0.0151	0.0053	0.0171	0.1165
Balzes Re-meshed	0.0660	0.1805	0.0220	0.0653

Table 5.4: Mean dilation values (d_{mean}) for decimated and re-meshed restored surfaces.

5.4 Pin-element sensitivity

The pin-element or seed is the starting point to unfold the surface. In the piecewise restoration, the pin-element is the first triangle laid flat with fixed barycenter, while in the parametric restoration, the pin-element is the node from which starts the propagation of the initial solution. Piecewise restoration and calculus of the initial solution in the parametric restoration are both iterative processes and thus, too dependent on the starting point (the pin-element). Moreover, parametric restoration is largely conditioned for the initial solution. Fortunately, in the parametric restoration with paleomagnetism, the latter determines the initial solution and then, it is independent on the pin-element. Therefore, we are going to analyze the effect of the pin-element on the piecewise restoration and on the parametric restoration without paleomagnetism (Ramón et al., in review).

As a general idea, the pin-element should be chosen with geological meaning; it is normally placed in the undeformed area of the surface as the foreland. However, any pin-element can be chosen to run the unfolding algorithm. The only requirement to have a final restored surface with geological meaning is to translate and rotate it (rigid block movement) to fit the known fixed reference. Thus, we are going to locate the pin-element in deformed and undeformed, anchored and free areas in order to evaluate its effect.

In general terms, we can say that the piecewise restoration works fairly well for the simpler model (San Marzal) while it presents some problems for the more complicated one (Balzes), particularly when paleomagnetism is not considered (Fig. 5.13).

We can see from the San Marzal model that the worse solution is to locate the pin-element in a corner of the surface. It is a fixed and undeformed area with geological meaning, but the proximity of the border introduce mathematical effects that we should avoid. Therefore it seems advisable to choose the pin-element inside the surface or at least not in the corner.

On the other hand, we have also restored the surface using a pin-line instead a pin-point, because as a matter of fact, a complete side of the model is fixed. Restoration with paleomagnetism is coherent with expected results, while restoration without this constraint is unable to reach a proper solution, displaying high dilation values caused by a propagation error.

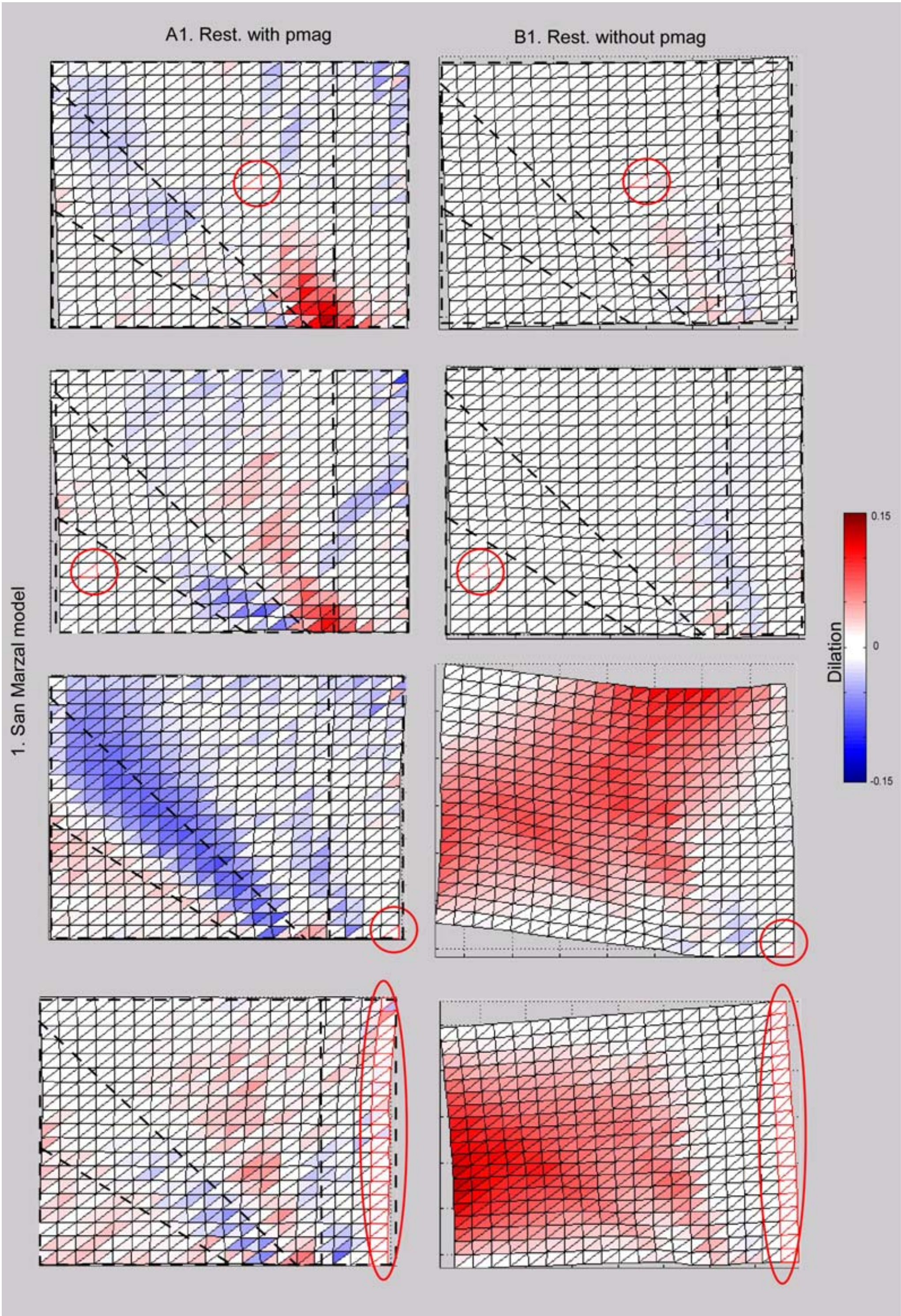

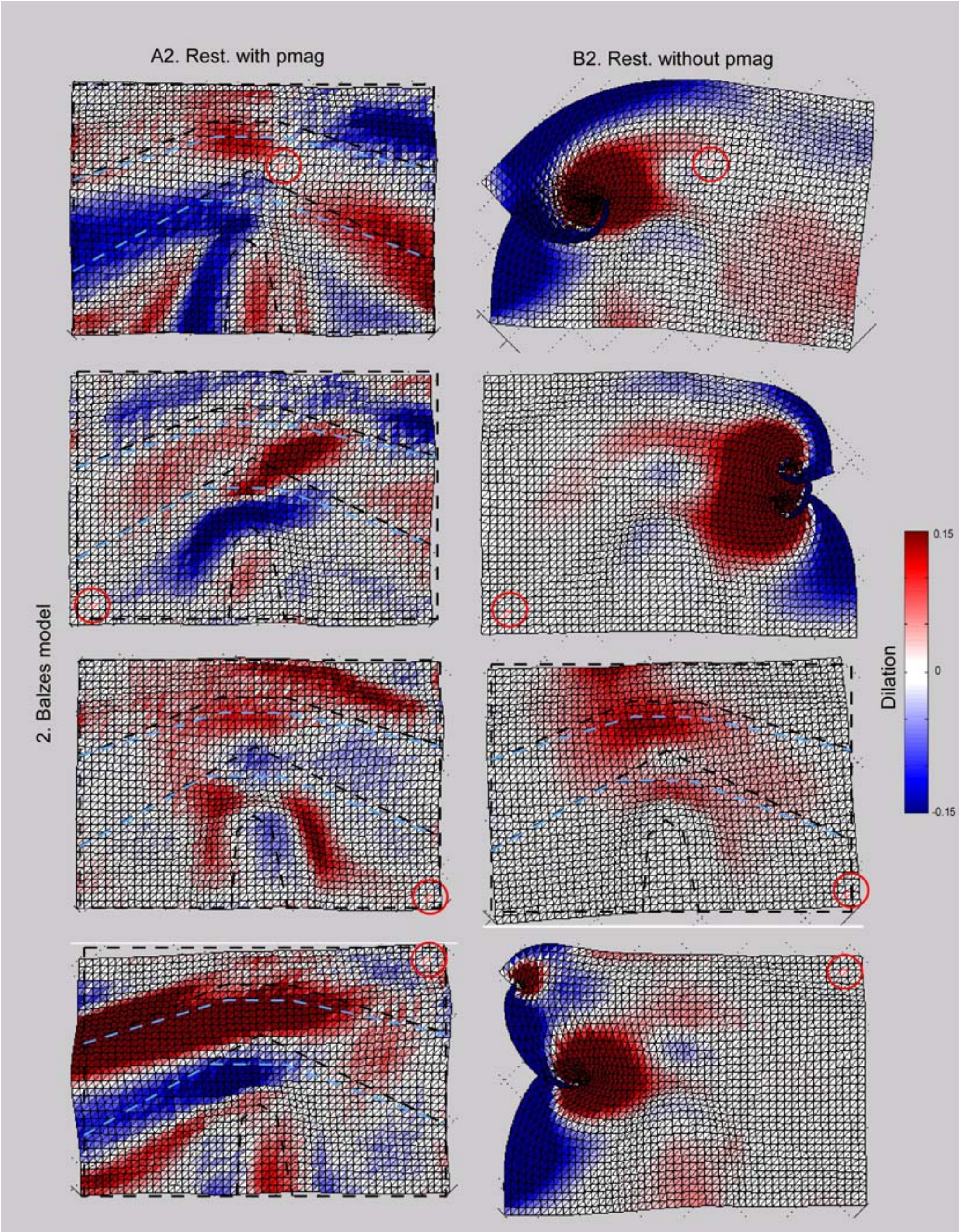

Figure 5.13 (continued): Pin-element analysis, piecewise restoration starting from different points. 1) San Marzal model. 2) Balzes model. A) Restoration with paleomagnetism. B) Restoration without paleomagnetism. Dilation values displayed.

The restoration of the Balzes model is more uncertain in any case. Dilation patterns of restored surfaces highly vary as the pin-element placement changes. This difference among solutions raises the question of whether the deformation obtained with the restoration represents the real one or not. In any case, the restoration with paleomagnetism clearly improves the solution yielding the proper rectangular shape of the initial surface.

Another consideration we can make by observing the results (particularly from the Balzes model) is that generally, the deformation concentrates far from the pin-element. Therefore, if we want to use the restoration to predict real deformation, we should avoid placing the pin-element in a deformed area (as in the first simulation of Fig. 5.13).

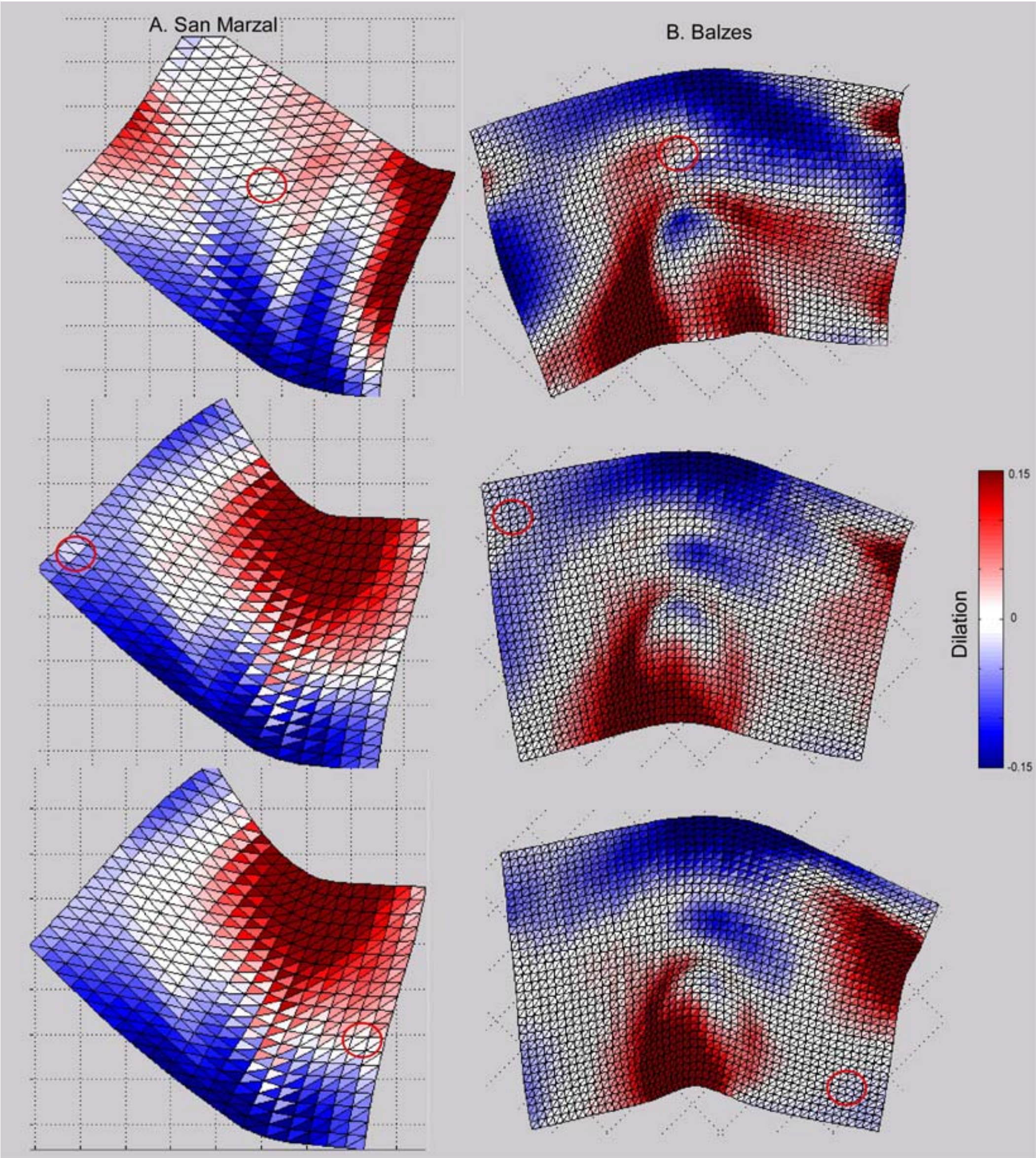

Figure 5.14: Pin-element analysis for the parametric restoration without paleomagnetism. 1) San Marzal model. 2) Balzes model. Dilation values displayed.

The parametric restoration is sensitive to this variable only when restoring without paleomagnetism, on the other hand, only useful to restore simpler structures. The main difference is the selection of the pin-element inside or outside the main structure (Fig.

5.14): a pin-element located inside the main structure where deformation has taken place seems to be a better choice in order to get a restored surface more similar to the initial one.

5.5 Multi-surface restoration

The restoration methods developed in this work unfolds single surfaces and do not consider volumes. However, multi-surface restoration is the first step for a multi-map volume restoration and it may be a good approximation to the real 3D problem.

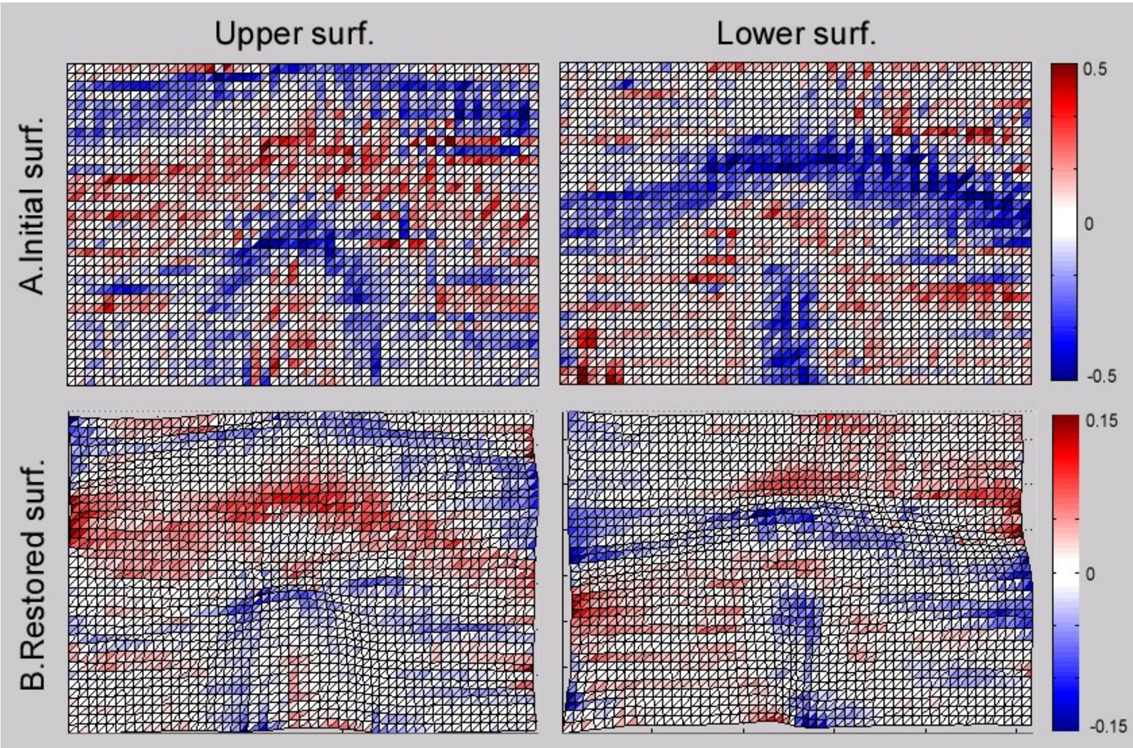

Figure 5.15: Multi-surface restoration of the Balzes model. A) Initial surfaces (upper and lower) with real dilation values. B) Restored surfaces with retro-dilation values. Note: the range of dilation is not the same for initial and restored surfaces, being higher for the first.

Thanks to the CT scanner we are able to reconstruct internal surfaces of the models and we can characterize completely the Balzes, although the resolution is worse than in the case of photogrammetric reconstruction. The restoration method we are going to apply to the model obtained with the CT scanner is the parametric approach with orientation of paleomagnetic data of *pmag3* because it is the one that has shown better results. We restore separately the upper and lower surfaces of the model (just the most representatives) and compare them with the expected results. Real dilation values (already analyzed in Section 3.2.3 Fig.3.17) show extension in the outer parts of the anticline and compression in the inner parts, in accordance with the tangential-longitudinal deformation described by Ramsay (1977).

Restored surfaces (Fig. 5.15) display opposite signs of dilation which suggest the real behavior of the volume: extension in the outer parts of the anticline and compression in the inner parts. Dilation is higher in the real case than in the restoration, but the consistency in the difference between both surfaces (opposite dilation signs) is quite encouraging.

5.5.1 Comparison with a 3D restoration method

We may think that multi-surface restoration is far from recent real 3D restoration methods based on geomechanical approaches. However, for highly folded surfaces as those of our examples, these methods assume elasticity of materials and present several limitations we analyze in this Section

We used Dynel3D (IGEOSS[1]; Maerten & Maerten, 2006) to restore the Balzes model. The stratigraphic units in Dynel3D are discretized with tetrahedral elements that are assigned elastic properties. The tetrahedral elements deform elastically in response to constraints such as applied and/or internal forces, displacements and interface contacts. Dynel3D uses an iterative, explicit solver that preserves mass and allows forces to be transmitted from node to node through the entire system until equilibrium is reached.

One of the characteristics of the finite element methods (FEM) as this one, it is that requires strong boundary conditions, treating the geological body as a separate individual system delimited by a volume within which the calculations take place. A closed boundary or bounding box must be defined prior to the volume generation (Fig. 5.16A). On the other hand, the physical-based restoration algorithm run in Dynel3D needs several rock mechanical properties to be set up. As these mechanical properties vary with lithology, we set the typology of a sandstone (Young's modulus: 2.2E10Pa, Poisson's ratio: 0.24, density: 2480kg/m^3). The method also permits to model the

[1] http://www.igeoss.com

behavior of the contact between units. Since the two layers of the model represent the same stratigraphic unit, we have blocked them in Dynel3D.

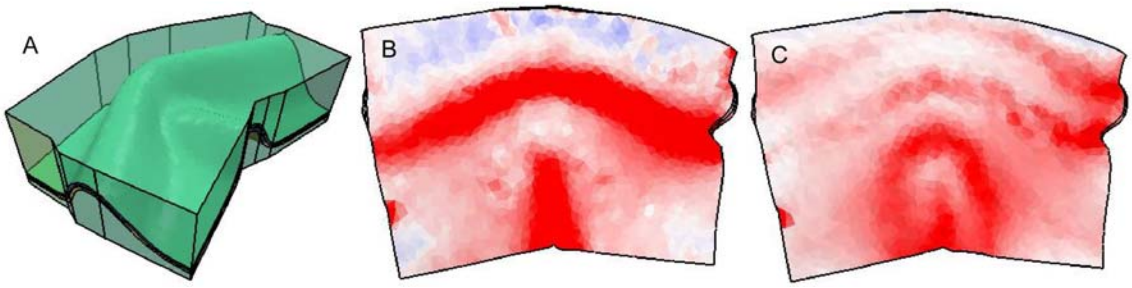

Figure 5.16: Volumetric restoration of the Balzes model with Dynel3D. A) Initial model with its boundary box. B) Restored upper layer. C) Restored lower layer. Volumetric strain displayed: E1+E2+E3.

With these initial settings, we unfold the layers assuming horizontality of initial state. The properties calculated are different than the used in our methods, but we can qualitatively compare results. We display the volumetric strain which is the sum of all main strains.

The restoration method is unable to undo the deformation process because it can reach the initial rectangular shape of the surface (Figs. 5.16B&C). Strain consistently accumulates in the hinge anticlines of the upper layer and hinge synclines of the lower layer. However this strain is always positive, indicating than the volume needs to expand to reach the folded surface, and therefore, an unreal change of volume has occurred.

5.6 Conclusions

In this chapter, we have evaluated the goodness of the piecewise and parametric restoration methods using paleomagnetism, which is defined in all points of the surface. The paleomagnetic constraint improves the resultant surface in most cases achieving in general more similar deformation patterns to those expected. Particularly, we can highlight the importance of paleomagnetism when the methods present higher limitations: 1) the strong sensitivity to the pin-element of the piecewise restoration; and even more important, 2) the impossibility of the parametric restoration to achieve the expected solution for strongly folded surfaces (Table 5.5).

Additionally, we recommend the multi-surface restoration as previous step to real 3D restoration. If horizons are correctly modeled and the surface restoration method applied works properly for one surface; the multi-surface restoration is able to indicate differences between surfaces offering volumetric information. We also emphasize the importance of CT analogs to test 3D restoration methods.

	Piecewise rest.	Parametric rest.
Restoration	Rest. with pmag better locates deformation patterns	Rest. w/o pmag is invalid for complex structures
Sensitivity to meshing	Dilation patterns are equivalent	Dilation patterns are equivalent
Sensitivity to pin-element	Too sensitive (although pmag improves the results)	Insensitive with pmag
Multi-surface restoration		Good 3D approximation

Table 5.5: Summarizing table.

6 Checking the consistency of the restoration methods: paleomagnetic sensitivity

In this chapter we analyze the influence of the initial paleomagnetic dataset on the results of the restoration methods. Specifically we analyze:

- The influence of the initial orientation of paleomagnetic vectors.

- The sensitivity to the error degree inherent to the definition of paleomagnetism for a given site.

- The sensitivity to data availability and distribution, since in a real scenario paleomagnetic data is not defined in all points of the surface, being only available in scattered sites. Additionally, we propose an interpolation algorithm to extend sparse data to the whole surface. Then, we analyze the usage of scattered and interpolated data.

6.1 Sensitivity to the initial paleomagnetic orientation

In this section we analyze the effect on the orientation of the paleomagnetic vectors. In a real case we can not modify this parameter but we need to know if the orientation of initial paleomagnetic data conditions the result. Paleomagnetism in the analog models is defined by the sides of the triangles, and therefore we have three possible initial datasets. We restore the two analog models with the two restoration methods using the three paleomagnetic datasets (Fig. 6.1).

The San Marzal model presents two preferred orientations with lower mean dilation and error values (Table 6.1) and better location of maximum dilation areas: *pmag1* (dataset used in previous examples) and *pmag3* although the observed dilation is always smaller than the expected one. These orientations are oblique to the main structure, while *pmag2* is rather parallel to the fold axis. Although with this single observation is not feasible to generalize the result.

The restoration of the Balzes model with the piecewise approach is more uncertain than the restoration with the parametric approach and, accordingly, we especially focus on the second method. The three restored surfaces present positive dilation in the main anticline and negative dilation in the main syncline between both folds. Main differences appear in areas of maximum Gaussian curvature and at the boundary. Between the three simulations, the one restored with *pmag3* has the minimum mean dilation error (*e*, Table 6.1) and presents the dilation pattern closest to the expected. This is the dataset used in previous examples, and again, is the most oblique to both folds.

These results show that the methods examined are quite robust to the paleomagnetic data orientation. Although there are some variations in the dilation patterns, they are much less significant than the ones we observed for other factors, like for example the pin-element variation. That is quite reassuring, because, as mentioned before, in a real case we can not vary the paleomagnetic data.

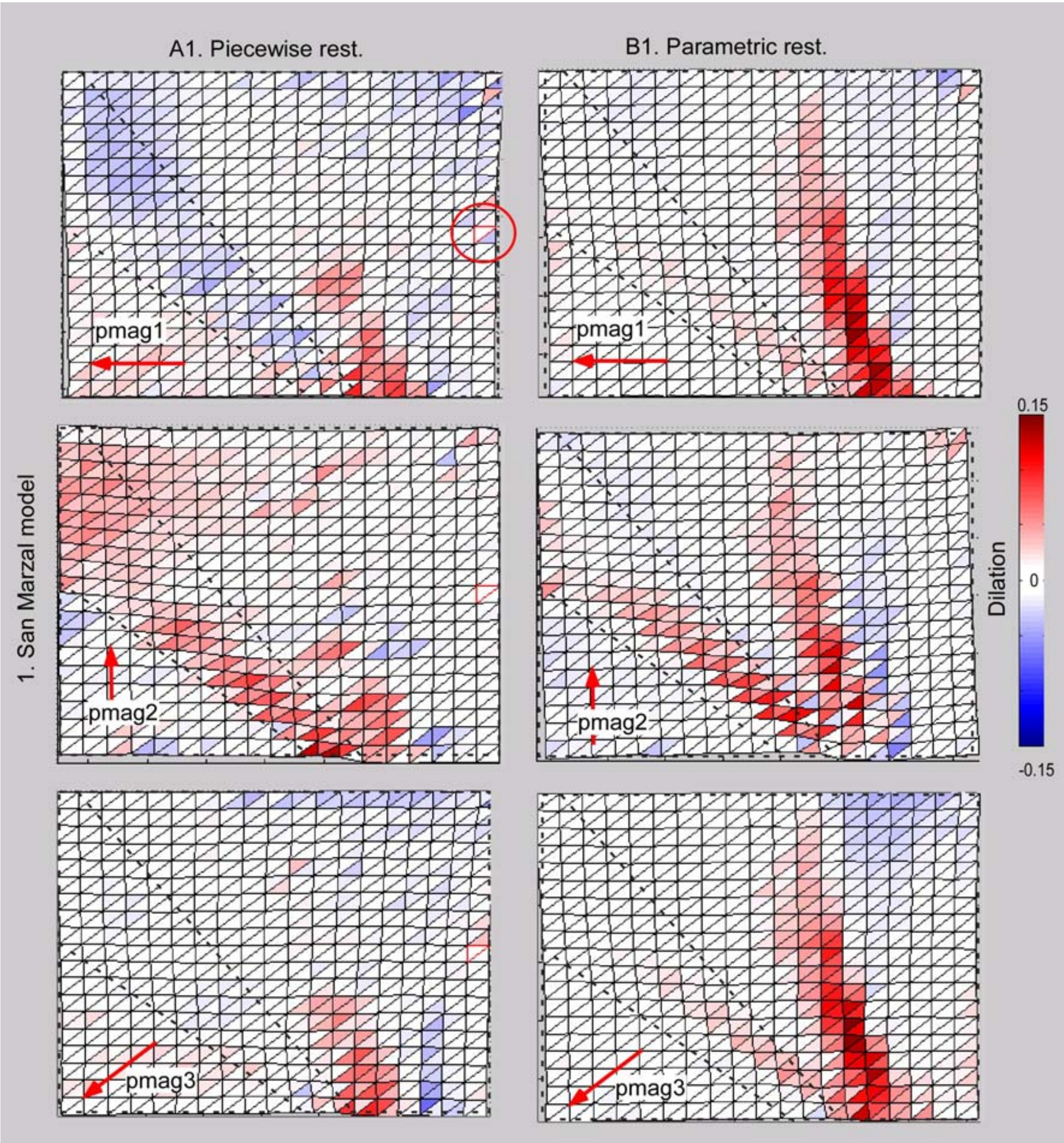

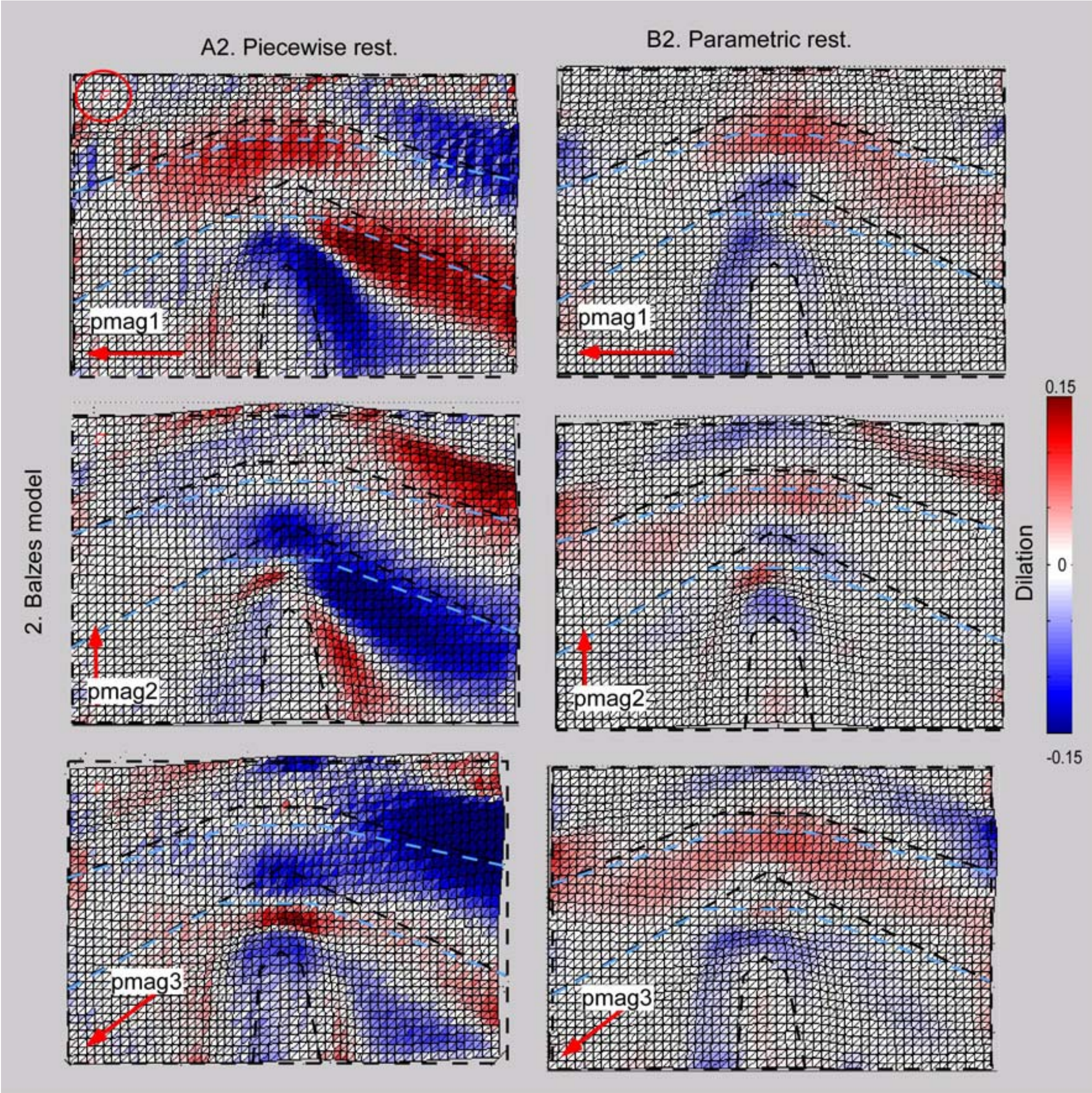

Figure 6.1 (continued): Paleomagnetic orientation analysis. Paleomagnetism is defined with the different sides of the triangles: *pmag1*, *pmag2*, *pmag3*. 1) San Marzal model. Previous examples used *pmag1*. 2) Balzes model. Previous examples used *pmag3*. A) Piecewise restoration with paleomagnetism. B) Parametric restoration with paleomagnetism. Dilation values displayed.

			pmag1	*pmag2*	*pmag3*
San Marzal model	Piecewise rest.	e	0.0392	0.0519	0.0391
		d_{mean}	0.0174	0.0191	0.0123
	Parametric rest.	e	0.0459	0.0473	0.0451
		d_{mean}	0.0164	0.0186	0.0169
Balzes model	Piecewise rest.	e	0.0993	0.1051	0.1087
		d_{mean}	0.0460	0.0415	0.0415
	Parametric rest.	e	0.0924	0.0952	0.0856
		d_{mean}	0.0198	0.0177	0.0228

Table 6.1: Mean error and dilation values for restored surfaces using different initial datasets.

6.2 Sensitivity to the paleomagnetic accuracy

Paleomagnetic data must be a reliable record of the magnetic field at the time of rock formation (Van der Voo, 1990; Pueyo, 2010) and it is always defined with a given accuracy (α_{95}). In this section we analyze the effects of the paleomagnetic error degree. We define two initial datasets: 1) with a random error ≤5º with a confidence level of 0.95 (α_{95}=15º) and 2) with a random error ≤15º with a confidence level of 0.95 (α_{95}=15º). We restore the two analog models with the two restoration methods using both paleomagnetic datasets (Fig. 6.2). For the piecewise restoration there are two options: 1) use the paleomagnetic data as hard data although it is not completely accurate (Fig. 6.2B) and 2) use it with its angular variation (α_{95}) allowing a free rotation of triangles according to that (Fig. 6.2C). This second option needs the iterative step used in the restoration without paleomagnetism (step 6 described in Section 4.1).

In order to quantify the difference between the restored surface using and not using accurate data, we measure the mean error dilation between the surface restored from accurate paleomagnetic data and the surface restored (with the same method) from inaccurate paleomagnetic data ($e_{rest}=mean(|d_{rest0}-d_{restAlfa95}|$, Table 6.2). In this case we do not compare the real dilation with the restored one (e) as we did in previous cases, but the dilation of the restored surface using ideal and real initial datasets (e_{rest}).

For the initial dataset defined with an error minor than 5º and for both models, the piecewise restoration that uses initial data as hard data, without allowing free rotation of triangles, (option 1) produces lower mean error dilation (e_{rest}) than the piecewise restoration that allows free rotation (option 2). This agrees with dilation patterns. It can be observed that the first option leads to similar restored surface patterns than those obtained with the piecewise restoration using paleomagnetic data (Fig. 6.2A vs. Figs. 5.5A & 5.7A) while the second option is similar to the restoration without paleomagnetism (Fig. 6.2B vs. Figs. 5.5B & 5.7B).

In the same way, for the initial dataset with α_{95}=15º, the dilation patterns of piecewise restored surface without free rotation (option 1 vs. option 2) are similar to the dilation patterns of the restoration with paleomagnetism and α_{95}=0º, although the former have much more deformation. Because of that, the mean error dilation increases this time. Due to this deterioration of the results, we encourage to do an effort to achieve a reliable paleomagnetic dataset. We particularly propose in the appendices two ways to improve the accuracy of paleomagnetic data: 1) we develop a program to help obtaining a better characteristic remanent component (Appendix 1) and 2) we model the effect of several structural sources of errors to help its identification (Appendix 2).

Parametric restoration significantly improves results. The initial dataset with α_{95}=5º yields result almost equal to those using the accurate dataset with α_{95}=0º (e_{rest}=0.0055 and 0.0035 in San Marzal and Balzes respectively). An initial dataset with α_{95}=15º adds some undesirable deformation but still match pretty well. Again, parametric restoration shows lower sensitivity to the paleomagnetic uncertainties than piecewise restoration.

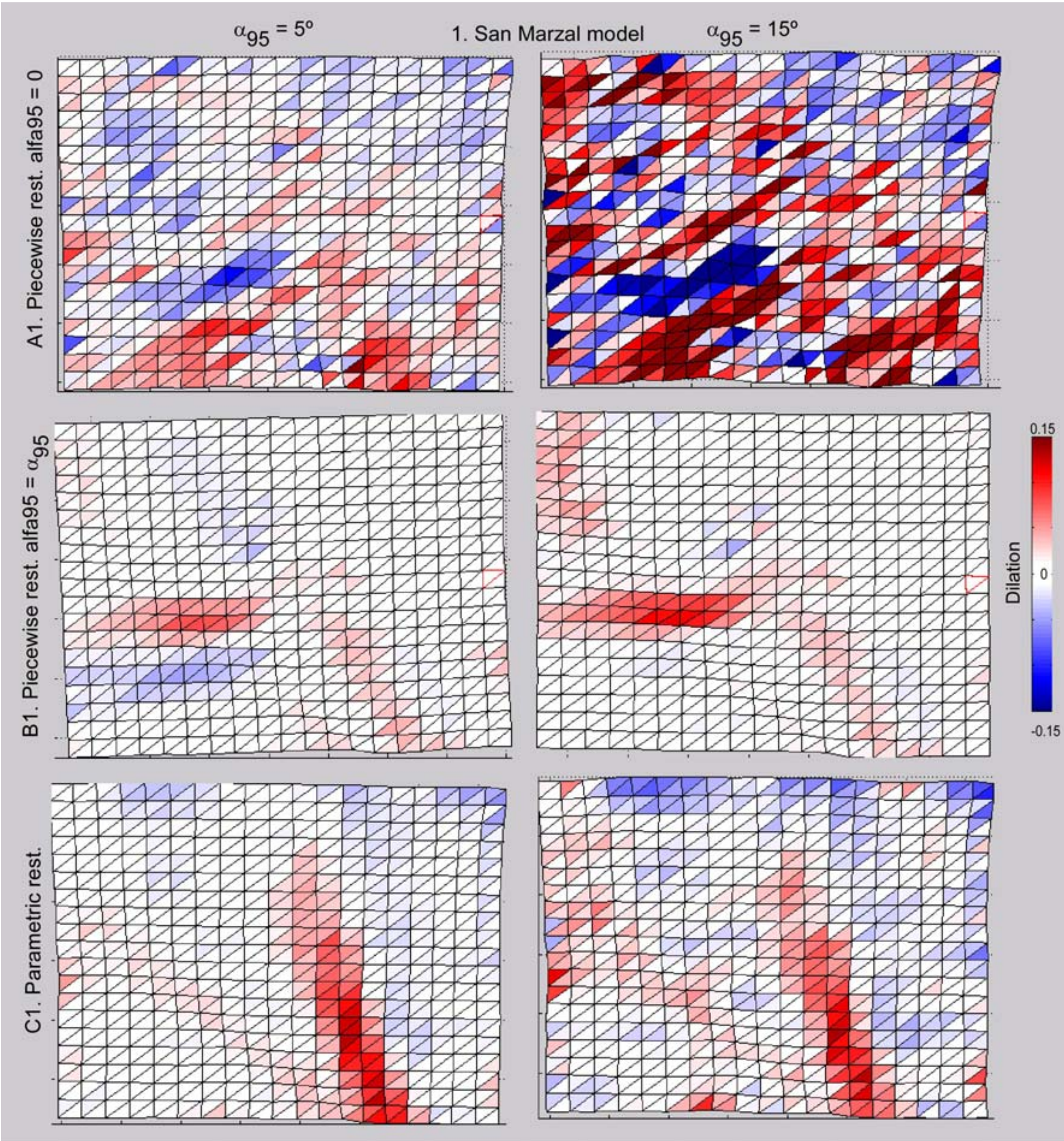

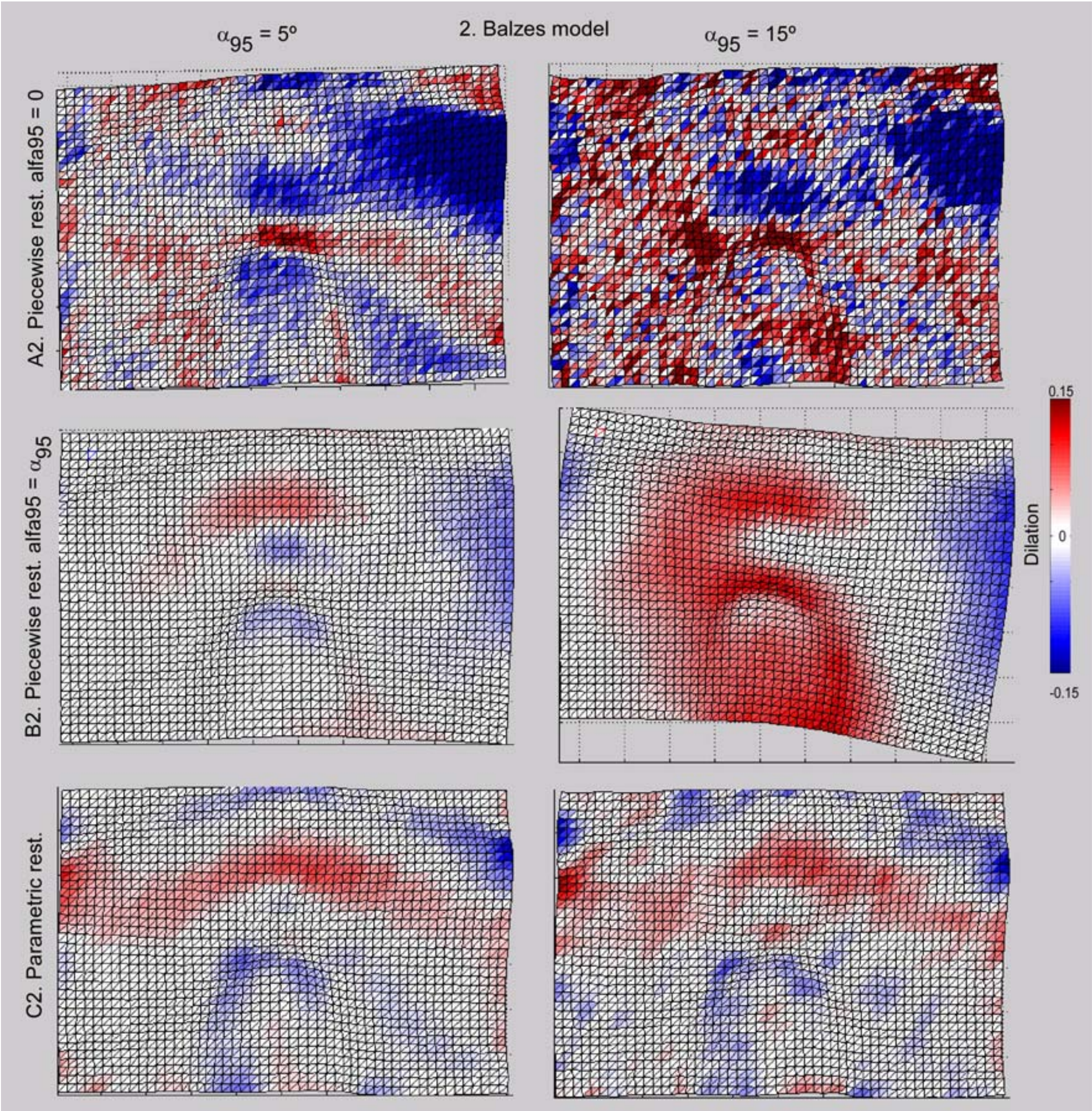

Figure 6.2 (continued): Paleomagnetic accuracy analysis using two initial datasets defined with an error minor than 5º and 15º respectively. 1) San Marzal model. 2) Balzes model. A) Piecewise restoration without free angular variation. B) Piecewise restoration with free angular variation corresponding with the paleomagnetic accuracy (α_{95}). C) Parametric restoration.

		$e_{restAlfa95}$; α_{95}=5º	$e_{restAlfa95}$; α_{95}=15º
San Marzal model	Piecewise rest. alfa95=0	0.0181	0.0431
	Piecewise rest. alfa95=α_{95}	0.0241	0.0241
	Parametric rest.	0.0055	0.0163
Balzes model	Piecewise rest. alfa95=0	0.0161	0.0624
	Piecewise rest. alfa95=α_{95}	0.0412	0.0609
	Parametric rest.	0.0035	0.0125

Table 6.2: Mean error dilation between restored surface with paleomagnetism defined accurately and restored surface with an inaccuracy minor than α_{95} ($e_{restAlfa95}=mean(|d_{rest0}-d_{restAlfa95}|)$).

6.3 Sensitivity to paleomagnetic spatial resolution

The most important factor in methods involving paleomagnetism is the resolution of the initial paleomagnetic dataset because in natural cases paleomagnetic vectors are only known in scattered sites. For the piecewise approach, paleomagnetism can be considered just where it is defined with no compulsory extrapolation, but for the parametric approach it must be defined everywhere, as it is used as the initial *u* gradient. This is the reason why we propose an interpolation algorithm, described in the next section. Before going into that, we analyze here the importance of having a dense initial dataset available for piecewise restoration without interpolation.

We define two initial datasets (Fig. 6.3): decimated sites by a factor of four, and scattered sites defined only in a simulated outcrop (sites cutting the topographic surface) plus the foreland (corresponding with the pin-element). The second dataset would mimic a more realistic scenario. The foreland data could be derived from a borehole or reasonably assumed, like for example in the San Marzal model where the southern limb is in continuity with the undeformed Miocene rocks of the Ebro Basin. Equivalently to the previous section, we define the mean error dilation between the restored surface using paleomagnetism defined in all points and the restored surface using scattered data: $e_{rest}=mean(|d_{rest0}-d_{restScatt}|)$. Mean error increases as the density of initial datasets decreases (Table 6.3). With the scarcity of data, the restoration worsens because the deformation increases not in the expected areas.

		$e_{restScatt}$ decimated sites	$e_{restScatt}$ scattered sites
San Marzal model	Piecewise rest.	0.0141	0.0264
Balzes model	Piecewise rest.	0.0397	0.0704

Table 6.3: Mean error dilation between restored surface with paleomagnetism defined in all points and scattered data ($e_{restScattp}=mean(|d_{rest0}-d_{restScatt}|)$). Decimated sites are the initial dataset divided by four and scattered sites are 14 and 16 for San Marzal and Balzes respectively located in contrived outcrops and also in the foreland.

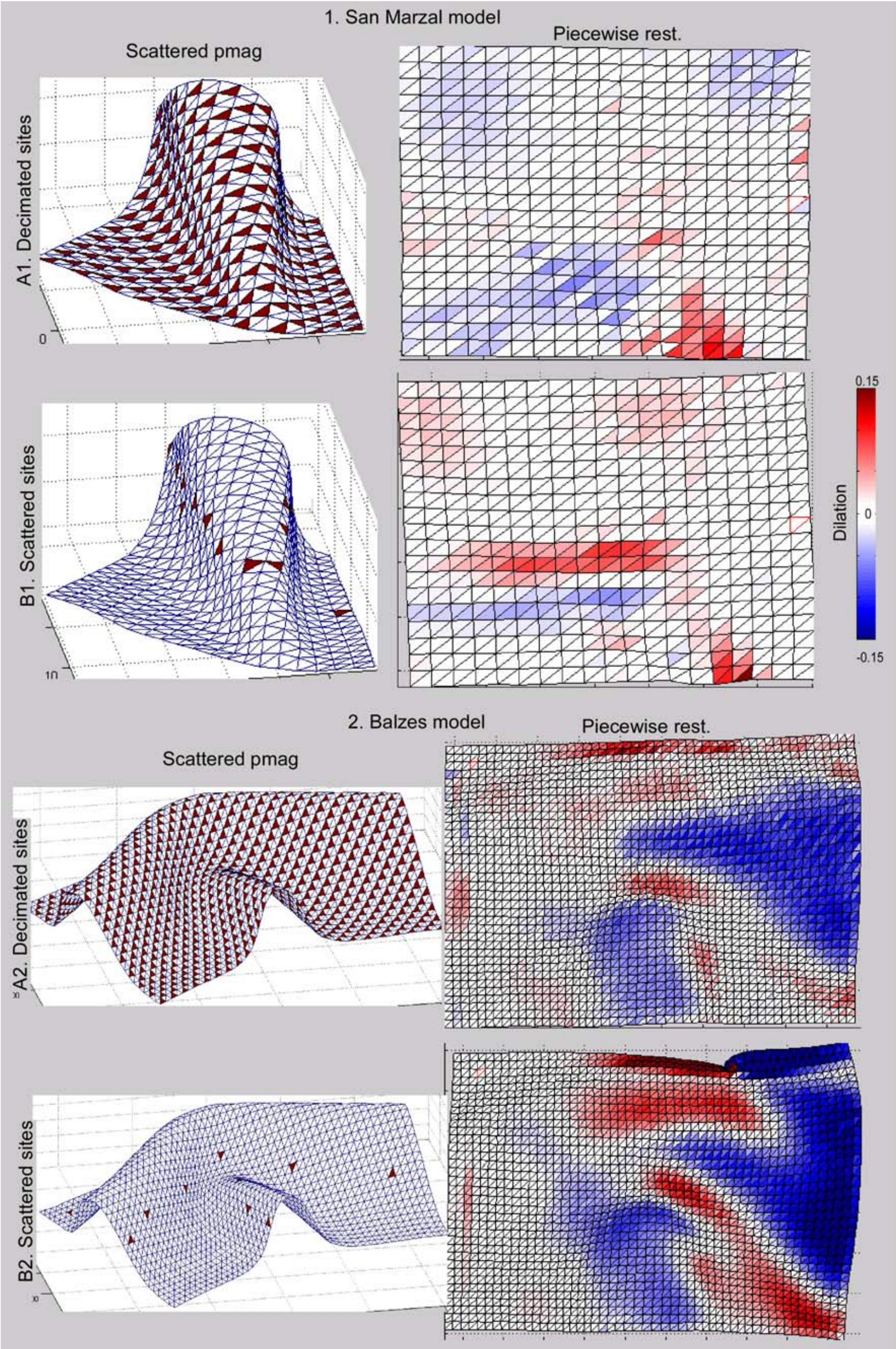

Figure 6.3: Paleomagnetic accuracy analysis using two initial datasets: A) decimated sites by a factor of four and B) scattered sites located in contrived outcrops and in the foreland. Piecewise restoration of San Marzal and Balzes model.

6.4 Interpolation of paleomagnetic data

Interpolation algorithms are mandatory in the case of parametric restoration. In addition to that, the results of the previous section show that interpolation is convenient in piecewise restoration.

We initially proposed an extrapolation technique based on the *dip-azimuth domains,* similar to the *dip-domain* concept of Suppe (1985) and Fernández et al. (2003). Neighbor triangles with similar orientation (i.e., those in the same bedding plane) will have the same paleomagnetic vector. However, this technique is not valid to extrapolate data to the whole surface strongly folded. Therefore, a second technique was developed. The core idea of this new interpolation algorithm is the propagation of the initial paleomagnetic data to all points, assuming the surface is completely developable.

The paleomagnetic vector of a specific triangle is propagated to its neighbor by rotating the vector with the same global rotation that was applied to the triangle. The axis of rotation is the common side between both triangles and the angle of rotation is the angle between the normal vectors (Fig. 6.4A). The propagation of paleomagnetic vectors is an iterative process. Firstly, the initial paleomagnetic vector of one triangle is propagated to all its neighbors. Secondly, all neighbors with new data are used for the next iterations, propagating the paleomagnetic vector to all its neighbors and so forth (Fig. 6.4B). We propagate the paleomagnetic data to the entire surface for all single paleomagnetic sites. After that process each triangle has as many paleomagnetic values as initial sites. The final value is the mean of all of them. If the initial paleomagnetic sites have different precision (given by the confidence angle α_{95}) it can be used to weight the mean. We have also tested other criteria like inverse distance to weigh the mean, but we obtained no clear improvements in the outcome. It is worth noticing that this method can be only applied in continuous surfaces.

In order to evaluate the soundness of this interpolation algorithm, we firstly apply it to the San Marzal model with primary paleomagnetic data defined everywhere in the surface (in all its points). The interpolated paleomagnetism is the mean of all initially propagated vectors. The error between interpolated and real paleomagnetic data depends directly on the developability of the initial surface; this error is not very high in this case (Fig. 6.4C). In any case, the difference between measured and interpolated data is 1.2º on average and is always < 6º, which is acceptable with regard to the typical deviation error of α_{95} = 10º in most paleomagnetic sites (not far from the real resolution of the technique, Bazhenov, 1988).

Secondly, we simulate the more realistic case advanced in the previous section with primary paleomagnetic vectors defined in only a few discrete sites of the fold and also in the foreland, taken as the reference (Fig. 6.4D). The interpolation of the paleomagnetic dataset is similar to the one with the paleomagnetism defined in the entire surface (Fig. 6.4E); the mean error between real and interpolated data is 1.3º in this case. These results encourage using this method in real cases (continuous surfaces) with sparse paleomagnetic data.

Although this algorithm is feasible for the restoration methods used here, further improvements may be done in this area. Moreover, we also encourage the development of restoration methods that only consider scattered data in order to avoid any possible influence of interpolation. As we already mentioned, the algorithm explained here is only valid for continuous folds. Therefore, further efforts should be done to deal with discontinuities of the models (thrust planes and faults).

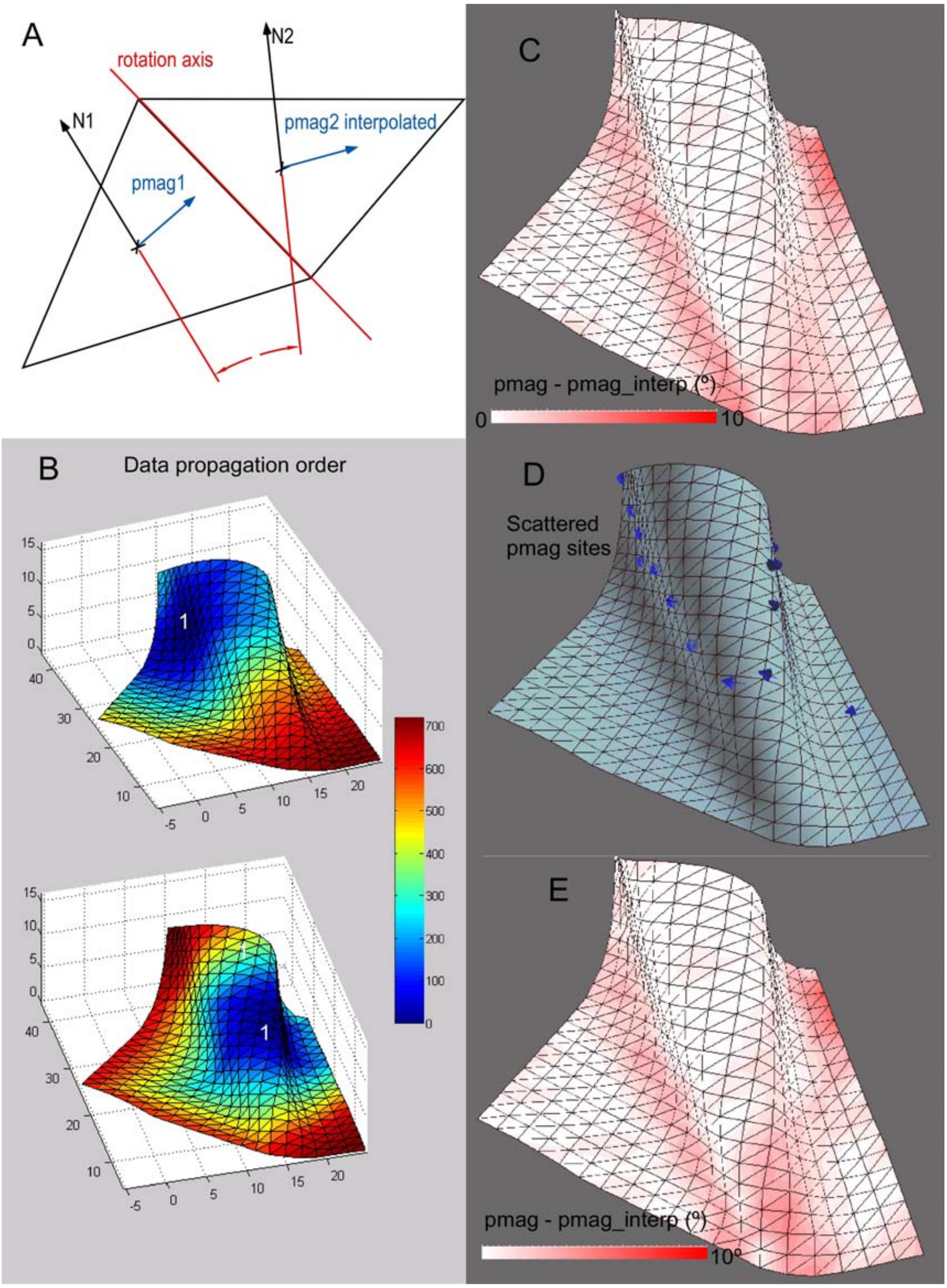

Figure 6.4: Paleomagnetism interpolation. A) Rotation of the paleomagnetic vector to propagate it from triangle to triangle. B) Propagation order starting from two different initial sites. The next step computes the average of both paleomagnetic propagated datasets. C) The interpolated paleomagnetism is calculated using all points of the surface as initial data. We plot the difference in degrees between real and interpolated paleomagnetic data. D) Initial paleomagnetic sites location simulating a real case with sparse data. E) Difference between real and interpolated paleomagnetic data from the initial sites plotted in figure D.

6.5 Real-world case: sensitivity to accuracy and resolution

Finally, we simulate a real scenario with inaccurate and scattered initial data that are interpolated. We reproduce the scattered datasets described in Section 6.3; 14 sites for the San Marzal model and 15 sites for the Balzes model (Fig. 6.3B). For these sites, we define two different initial paleomagnetic datasets, one with total accuracy (α_{95}=0º) and the other with a random error ≤15º with a confidence level of 0.95 (α_{95}=15º). These datasets are interpolated with the algorithm described in previous section.

First of all, we need to find the error introduced by the interpolation algorithm. To do so, we calculate the difference between the real dataset with paleomagnetism defined in all points and the interpolated datasets from the scattered sites (both defined with and without total accuracy) (Fig. 6.5A). The simpler model has mean errors of 1.47º and 2.69º for the interpolated datasets of α_{95}=0º and α_{95}=15º respectively, while the more complicated model has mean errors of 2.92º and 3.54º. Again, error is never too big in comparison with the usual paleomagnetism resolution ($\alpha_{95} \approx$ 10º).

Secondly, we restore the surfaces using the interpolated datasets and compare the results with those obtained with paleomagnetism defined in all points (Figs. 5.5A, 5.6A, 5.7A and 5.8A). For the piecewise restoration we must clarify the following issue; in the translation and rotation step, we do not allow a free angular variation related to the α_{95} value, but use paleomagnetism as hard data. We do it this way because if we set a free variation of 15º (as α_{95}) the restored surface is equivalent to the one restored without paleomagnetism as observed in Section 6.2.

Observing the restoration of the San Marzal model we can say that the restoration method based on the parameterization of the surface becomes more robust. Results define with more accuracy the main deformation area in the anticline hinge (maximum dilation). Even more important is that dilation patterns are similar in all three situations. This observation is stronger in the Balzes model; although dilation patterns become diffuse and are closer to a Gaussian curvature than to the real dilation, they are more coherent for the parametric restoration than for the piecewise restoration.

In order to quantify the difference between the restored surface using interpolated dataset and the initial one, we measure the mean error dilation between the surface restored with paleomagnetism defined in all points and the surface restored with interpolated data ($e_{Rest}=mean(|d_{rest0}-d_{restInterp}|)$). The method based on the parameterization has lower values (Table 6.4) in both examples. That means, in general terms, that parametric restoration is more stable than piecewise restoration.

On the other hand, restored surfaces of the Balzes model are almost independent on the initial paleomagnetic dataset (α_{95}=0º or α_{95}=15º). The reason is that the paleomagnetism is averaged with the interpolated algorithm, and the interpolation of paleomagnetic values with more or less accuracy leads to similar results. This makes the method appropriate to be used in real cases.

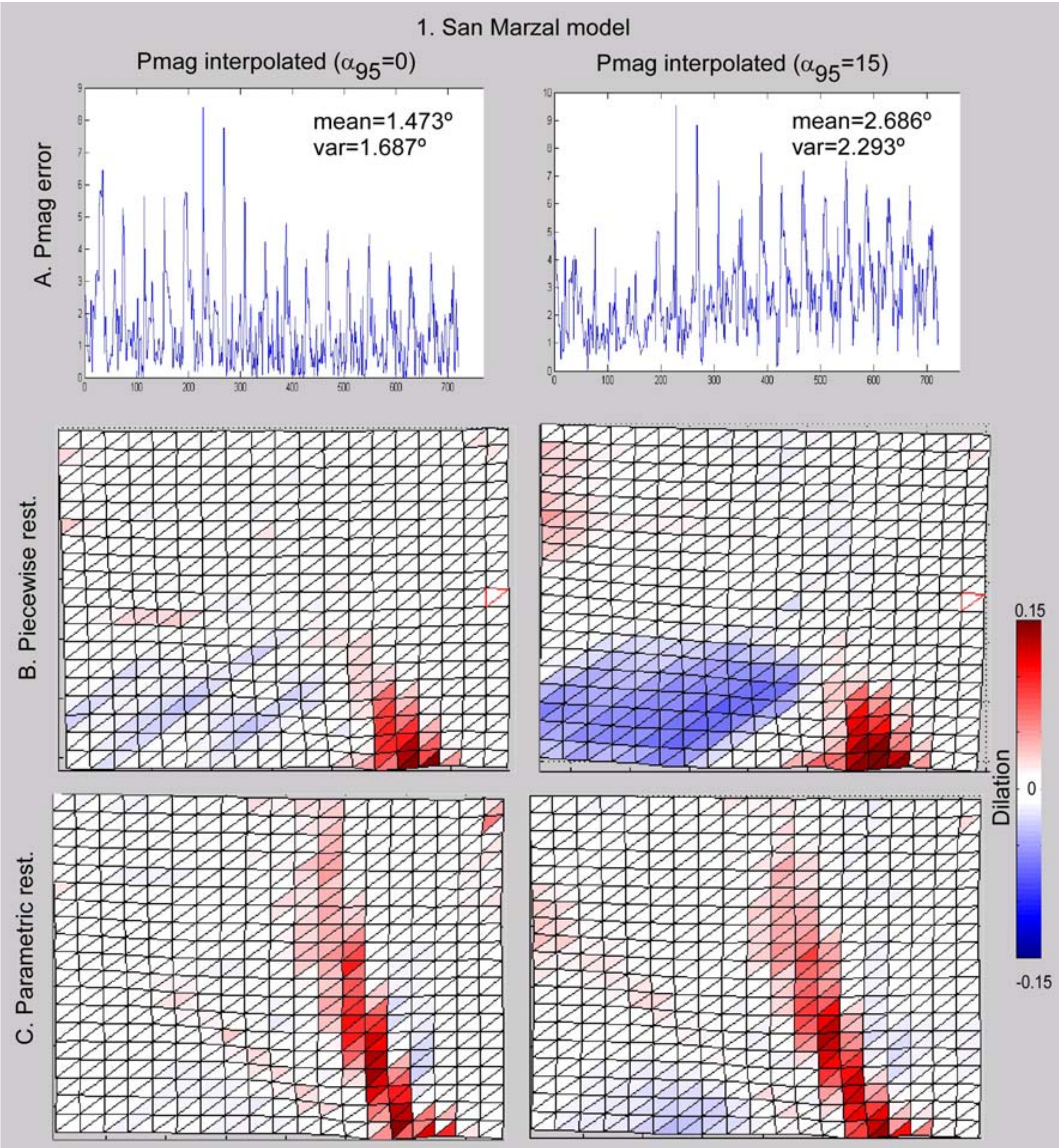

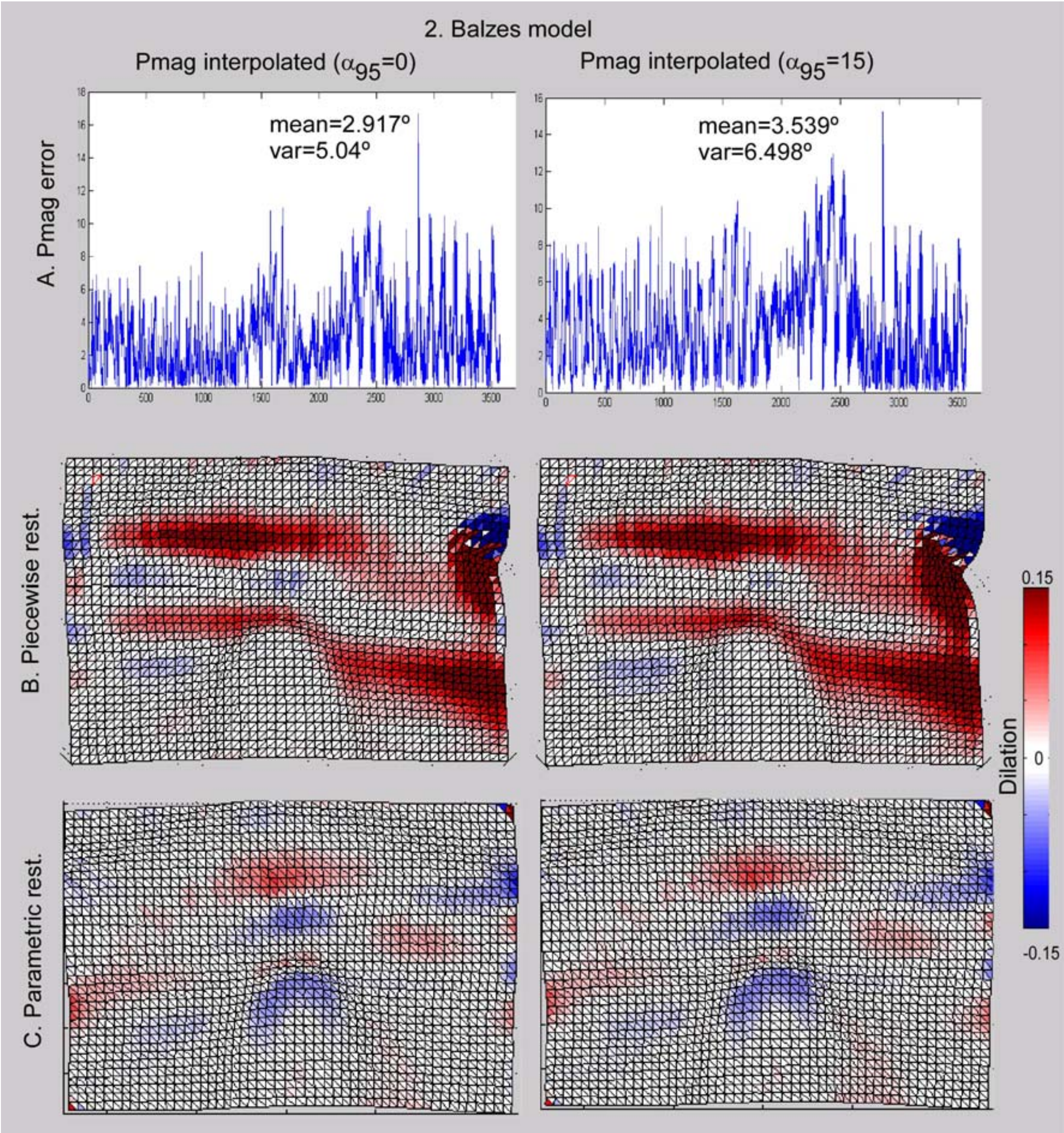

Figure 6.5 (continued): Paleomagnetic accuracy and resolution analysis. Initial scattered paleomagnetic datasets already defined in Figure 6.3B with total accuracy (α_{95}=0º) and with random error minor than 15º (α_{95}=15º). 1) San Marzal model. 2) Balzes model. A) Paleomagnetic error (in degrees) between the real dataset with paleomagnetism defined in all points and the interpolated dataset from the scattered sites. B) Piecewise and C) parametric restoration.

		eRest Interp. α_{95}=0º	*eRest* Interp. α_{95}=15º
San Marzal model	Piecewise rest.	0.0191	0.0272
	Parametric rest.	0.0079	0.0113
Balzes model	Piecewise rest.	0.0681	0.0825
	Parametric rest.	0.0203	0.0208

Table 6.4: Mean error dilation between restored surface with paleomagnetism defined in all points and restored surface with interpolated data ($e_{restInterp}=mean(|d_{rest0}-d_{restInterp}|)$).

6.6 Conclusions

Summarizing, the proposed restoration methods remain valid for a real case with scattered paleomagnetic sites, thanks to the interpolation algorithm. However, the parametric approach is more robust than the piecewise approach. On the other hand, we should not forget that the dilation patterns obtained with the restoration are just an aid to determine the real dilation, but they never provide the real dilation because they are conditioned for the restoration procedure.

7 Map-view restoration

In this chapter we explore the usage of paleomagnetism in map-view restoration techniques. Map-view restorations based on balanced cross-sections, also known as palinspastic restorations, have been long used to understand 3D patterns in fold and thrust belts (Kay, 1945 and 1954). Together with structural, isolith and isopach maps, they are very useful in underground oil and gas exploration. Palinspastic maps display folded or faulted strata restored to their paleogeographical location before deformation took place (folding or faulting). Classic (see for example Dalhstrom, 1969), or even recent approaches (Price and Sears, 2000), are based on balanced cross sections (2D). To ensure the map-view reconstruction effectively considers the entire volume of the materials represented and, therefore, respects the lengths of lines and the thicknesses of individual layers. The term *palinspastic* is derived from the Greek *palin* meaning *again*, and *spastikos* meaning *pulling* (Allaby and Allaby, 1999). We could consider this approach as an early 3D restoration technique. The map-view restoration approach proposed in this chapter does not concern surface restoration of individual structures; here we propose a cartographic map view restoration applicable at local and regional scales. The main goal of this map-view restoration method is to unravel the vertical axis rotations.

We first need to establish some assumptions (and derived limitations) as well as the aims and scope of the method:

1) Vertical Axis Rotations (VARs) may produce severe *room problems* in fold and thrust belts. Therefore, the removal of VARs at the regional scale is equivalent to the removal of the lateral gradient of shortening (in the sense used by Pueyo et al., 2004 and Sussman et al., 2012). This means that only parallel and constant translation will remain in the thrust front after the restoration of the map before the rotational period. The restored map will not represent a real image. Additional work should be done in the future to implement the combined restoration of VARs and translations due to cylindrical folding and thrusting.

2) The second assumption deals with the rotational time. Several evidences from the Pyrenees point to a narrow rotational window during the Eocene-Oligocene: Lutetian-Priabonian in the Southwestern (Pueyo, 2000; Pueyo et al., 2002; Mochales et al., 2012;

Rodríguez et al., 2013c; Muñoz et al., 2013) and in the Southeastern Pyrenees (Sussman et al., 2004), and similar ages both in the Northwestern (Mouleon basin) and in the Northeastern (Corbiers) (see works by Oliva et al. (2010) and Rouvier et al. (2012) respectively). Therefore, the map-view restoration will offer an imprecise snapshot of that moment, just before the out-of-plane movements began.

3) We also assume the geological map as a flat and horizontal surface. The final goal is to observe the structural trends before the rotational period.

Within these three assumptions, our cartographic restoration technique aims to localize the expected gaps and overlaps between in relation to their cartographic location, and does not pretend to be a trustworthy reconstruction of the past. An additional advantage of our map-view reconstruction is its ability to identify the anisotropy related to the gaps and overlaps.

Extension of surface restoration (2.5D) techniques by Audibert (1991) and by Rouby et al. (1993) using paleomagnetic vectors were developed by Arriagada et al., (2008) and applied to map-view (2D) in the Bolivian orocline. This technique, based on the least-square minimization of fault-boundaries blocks, assumes that the initial surface (geologic map) can be entirely divided by discontinuities in a set of discrete domains (heave maps). Although some interesting results can be derived from this technique, the problem is that many heave faults lack for geological expression or meaning, or at least they are scale-dependent in the sense used by Rouby et al., 2000, and this adds uncertainty to the restoration results.

Our idea is somehow similar to the one developed by Arriagada et al. (2008), but in our approach, we divide the map in random triangles and not in blocks bounded by faults and heaves. In other words, we keep the continuity of the map. As we said, the map-view restoration only considers the coordinates *xy*, and structures are roughly assumed flat.

We present two techniques based on the piecewise and parametric approaches. The first technique is equivalent to the fitting step of the piecewise restoration detailed in Section 4.1, which comes after the flattening step. Gaps and overlaps of the restored map (before the welding step) indicate areas were maximum deformation has taken place. After welding we can visualize the cartographic image in the restored map to approximate the initial location of the structures. This restoration technique is essentially based on the rotation determined by paleomagnetic data: triangles with known data rotate according to this constraint, while the others fit minimizing distances between vertices. The second technique is the parametric restoration described in Section 4.2 in which the rotation data determines the gradient of one of the parameters. Whereas the drawback in the first technique is the pin-element location, the drawback in the second technique is that rotation data needs to be established everywhere.

Again, paleomagnetism is the key-stone that allows quantifying vertical-axis-rotations (VARs). However, VAR magnitudes can be now derived not only from primary vectors (like in the surface restoration) but also from secondary components (synfolding or postfolding) since they are still valid to quantify and date VARs (see Pyrenan examples in Oliva and Pueyo, 2007b). On the other hand, VARs are known in specific sites while the structural trend (or strike direction) can be easily determined in more points using geologic maps or field data. The proposed idea is to find some law to relate these two variables in order to have a large rotation dataset relevant for the restoration. To cope with this aim, we develop two distinct procedures: firstly, the use of specific vectors as the initial dataset (raw data), and secondly, leveraging strike vs. rotation relations, interpolated following the strike-VAR law.

We apply this palinspastic restoration method at two different scales in two case studies, the Balzes Anticline (regional scale) and the South Central Pyrenees (tectonic scale). A vast paleomagnetic dataset is available in both cases (Rodríguez-Pintó et al., 2013c and López et al., 2008 respectively)

7.1 The method

This palinspastic or map view restoration method starts from the cartographic map of the area of interest and the georeferenced rotation dataset, obtained from punctual paleomagnetic data [Section 7.1.1] or from paleomagnetic and structural data [Section 7.1.2].

The procedure is based on the piecewise approach as stated above, and therefore it involves a sequence of five steps:

1) Map triangulation. As in similar methods, the first step consists in the discretization of the area we want to restore. The cartographic map is meshed with a

Delaunay triangulation, targeting the homogeneity of the triangles. As discussed in the previous chapter (Section 5.3) the type of mesh hardly conditions the result, and therefore other approaches like regular triangulation can be employed. However, mesh density must be carefully chosen. It must be dense enough to represent all the structures and rotation data, and wide enough to minimize propagation errors.

2) Incorporation of rotation data and pin-element. The rotation vectors are added in the barycenter of triangles wherever they are known. Rotation data can be obtained from individual VARs, as detailed later, or be inferred from strike data. Moreover, it is really important to add null values in the foreland where we know structures are unrotated. Regarding the pin-element, we must select it with care and geological sense because the restoration process depends heavily on it. We should preferably select the foreland as pin-area.

3) Translation and rotation. This step is equivalent to the piecewise surface restoration method and we use the same code. Triangles are rigidly translated and rotated to minimize distances between common vertices and to fulfill the rotation constraints. An angle of free rotation is allowed, subject to the precision of data (α_{95}), but it is better to use the rotation data as rough data.

4) Welding. After the fitting process, triangles are welded in order to have a continuous map. This step adds measurable deformation.

5) Calculus of deformation and visualization of results. We display the dilation (change in area) because it has proven to be the most representative control parameter. The anisotropy of the strain ellipse can be easily calculated from the restoration procedure. We can also display the displacement vector map, which provides relevant information as well. Moreover, we visualize the cartographic map in the restored state to facilitate the evaluation of results. This requires deforming the raster image as the restored mesh. With this purpose we have developed a C program based on openGL[1], available in the companion CD with Supplementary Material. We treat the cartographic map as a texture. We triangulate this texture and then apply the proper deformation to the triangles, according to the restoration.

The procedure based on the parametric approach has the same initial and final steps that the piecewise approach:

[1] www.opengl.org

1) Map triangulation.

2) Incorporation of rotation data. Rotation data determines the gradient of one of the parameters of the coordinate system (∇u). In this case, we need to interpolate the initial dataset into all points of the meshed map.

3) Restoration procedure. This step is equivalent to the parametric surface restoration method and therefore we employ the same gOcad plugging. Note that the main idea is that the coordinate system is assumed to be rectilinear and orthonormal.

4) Calculus of deformation and visualization of results.

7.1.1 Rotation data using Vertical Axis Rotations (VARs)

The initial rotation dataset is defined by VARs wherever they are determined by paleomagnetism. Each data value is specified with its confidence angle (α_{95}). The first option, only valid for the piecewise approach, is to use isolated paleomagnetic data where triangles without rotation information can rotate freely. For each triangle we assign the closest rotation data to the barycenter within a maximum distance. The second option is to interpolate the initial dataset into the whole map, which we do by using the discrete smooth interpolator (DSI) implemented in *gOcad*™ (Mallet, 1992).

7.1.2 Rotation data using the strike vs. VAR relationship

Paleomagnetic data is more difficult and time-consuming to acquire than the structural position of a site. Strike values can be derived from the cartographic traces directly drawn on a map, and numerous data can be easily acquired in a field campaign. For this reason, we want to determine a *strike vs. rotation* law to infer rotation data from strike information. As a matter of fact, this is an old and well-founded idea used to unravel the primary or secondary origin of curved orogenic belts. Oroclinal diagrams (Elredge et al., 1985) clearly establish that strike-VAR relationships are fairly constant at the orogenic scale (see compilations by Weil and Sussman, 2004; Yonkee and Weil, 2010 and the recent review of the Cantabrian mountains by Weil et al., 2013). Although this is an approximation, it can help to clear up the spatial resolution problem in some areas. We need two initial datasets to establish the law and run the method. On the one hand, the points in which strike and VAR information are known (available in or drawn from paleomagnetic works). On the other hand, the strikes measured from the cartographic traces. To establish a proper strike vs. rotation law, we need filtering the initial data (dataset 1) and keep only reliable data from which to obtain a mean by sectors (see more details later). The strike map (dataset 2) is defined in three steps: vectoring structural trends, removing topographic effects (V-rule) and smoothing remaining trends. Additionally, as in the previous case, we can use the resulting rotation data in specific triangles or interpolated to the whole map using DSI.

7.2 Case studies

We apply this method as a first attempt to two case studies: 1) the Balzes Anticline at regional scale and 2) South Central Pyrenees at tectonic scale.

7.2.1 Balzes Anticline

Rodríguez-Pintó et al. (2013c) have fully studied the Balzes Anticline calculating 75 paleomagnetic vectors and their derived VARs. More than 30° of clockwise (CW) rotation characterizes the Balzes Anticline on average, although this value change in individual sites from negligible magnitudes up to more than 80° of CW VAR. This variability is related to the fold curvature (Fig. 7.1). It is possible to reprocess the paleomagnetic vectors considering their structural location, the relative location respect to the fold curvature.

After filtering low-quality and unreliable data and grouping sites in structural sectors (sharing a common strike) (Table 7.1), Rodríguez-Pintó et al. (2013c) have built a strike vs. VAR diagram (Fig. 7.2). This plot is the equivalent, at fold scale, of the *oroclinal diagram* by Elredge et al. (1982). Fold axes vary from 195° in the northern part (N-NNE to S-SSW) to 142° in the southern one (NW-SE), giving more than 50° of observed bending. The curvature displayed by the Balzes anticline in map-view is a combination between a primary curvature (related to the thrust geometry before any VAR) and a secondary one related to the thrust rotational activity; 25° of VAR are related to 50° of fold axis bending. This relation follows a well defined regression;

VAR= - 46° + 0.511 * strike (R = 0.9724), that could be used to infer the expected VAR in other positions. Finally, the rotational activity of the Balzes Anticline took place during the deposit of the Lutetian to Bartonian rocks, synchronous to the folding and thrusting period (Rodríguez-Pintó et al., 2013a), which fulfils the second assumption of the method (see more details in section 2.4.4).

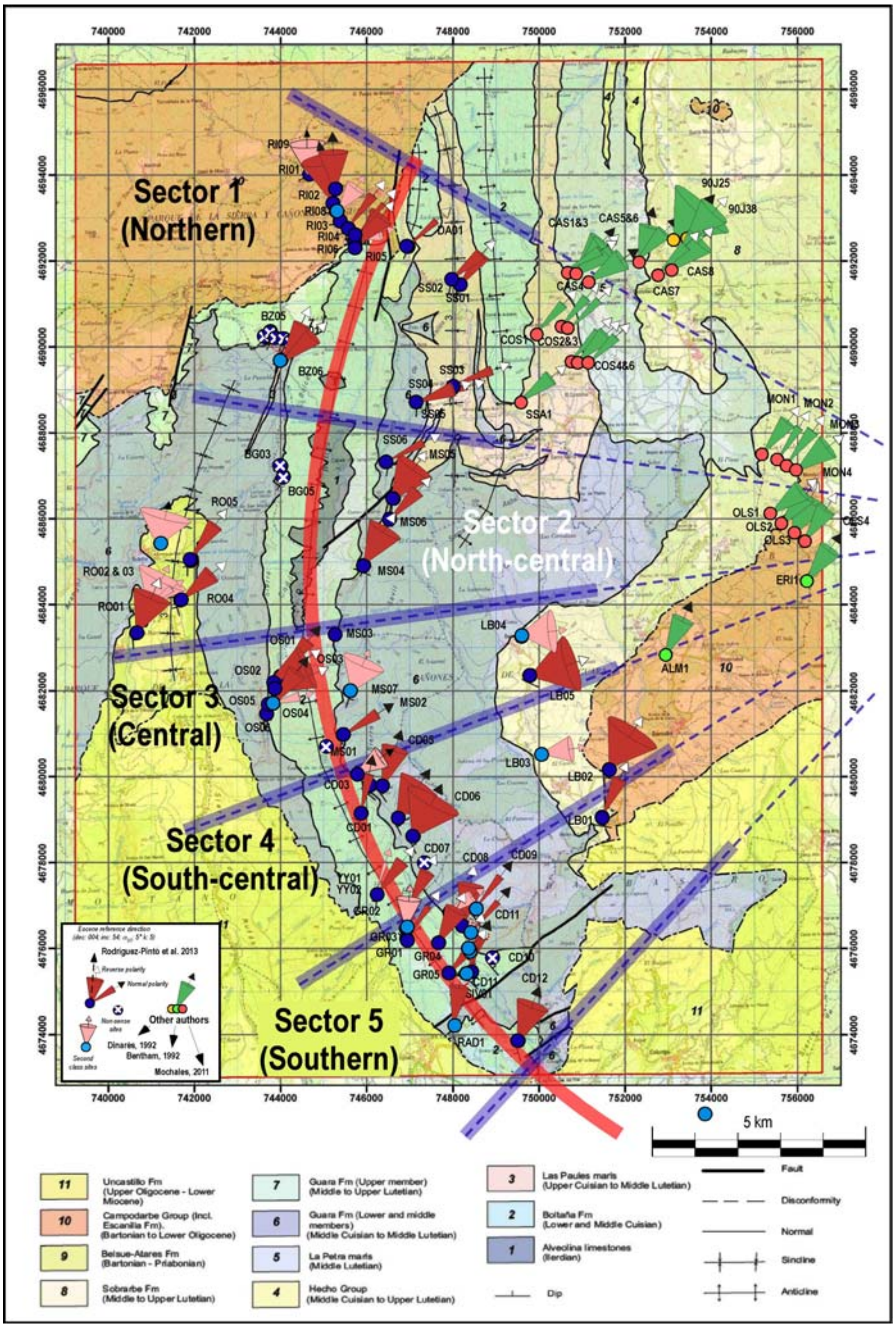

Figure 7.1: Vertical axis rotation deduced in the Balzes anticline (Rodríguez-Pintó et al., 2013c). The axis of each cone represents the VAR and its semi-apical angle is the confidence cone (α_{95}). A portion of arc (red line) has been fitted to the fold axis. Several radii of this arc, all of them converging in the same point) help to split the data in different pseudo-homogeneous sectors (between 12 and 17° of semi-arc).

Sector	Site	X (30T)	Y (30T)	n	N	DEC bac	INC bac	alfa	K	Strike (RHR)	dip	DD	DEC abc	INC abc	alfa	K	VAR
1	BG01	743958	4689597	14	16	241	-18	15	6	194	54	W	208	-48	15	7	24
1	BG02	743932	4689577	16	17	254	-10	11	13	195	57	W	228	-53	11	12	44
2	BG03	743949	4687096	8	8	112	-17	25	7	190	43	W	113	25	24	7	109
2	BG04	743938	4687094	6	12	192	-46	21	14	190	43	W	157	-33	21	14	-27
2	BG05	744011	4686846	11	18	184	-59	4	142	208	38	W	152	-33	4	146	-32
1	BZ01	744295	4690040	9	13	207	-44	19	8	207	50	W	174	-24	19	8	-10
1	BZ02	744167	4690032	18	50	201	-46	16	6	200	56	W	160	-25	14	7	-24
1	BZ03	744023	4690090	35	53	204	-51	7	14	197	46	W	155	-40	6	20	-29
1	BZ04	743781	4690118	34	44	130	-39	17	3	209	47	W	123	-12	17	3	-61
1	BZ05	743581	4690132	14	17	210	-59	15	9	226	25	W	178	-44	15	9	-6
1	BZ06	743705	4690262	16	17	199	-48	21	4	205	35	W	170	-35	21	4	-14
4	CD01	745834	4678936	9	9	3	54	7	55	302	22	N	12	34	7	55	8
4	CD03	746039	4679593	3	10	61	46	21	52	310	24	N	56	24	21	52	52
4	CD04	746704	4678825	4	11	40	31	28	15	152	18	S	34	48	28	15	30
4	CD05	746334	4679584	6	10	34	41	19	15	146	23	S	20	61	19	15	16
4	CD06	747057	4678398	5	11	35	17	34	8	155	23	S	29	36	34	8	25
4	CD07	747316	4677772	3	11	94	39	38	17	175	34	W	108	72	38	17	104
5	CD08	747911	4676602	10	12	246	0	13	16	248	25	N	236	-29	13	16	52
5	CD09	748207	4676291	9	10	188	-33	18	11	90	16	S	190	-49	18	11	6
5	CD10	748915	4675543	7	10	141	-16	16	18	320	31	N	149	-14	16	18	-35
5	CD11	748424	4675207	11	11	179	-56	5	110	315	12	N	189	-47	5	110	5
5	CD12	749516	4673585	10	11	28	15	22	24	164	23	S	21	30	22	24	17
1	DA01	746930	4692255	63	63	249	-20	5	15	200	40	W	228	-45	5	15	44
5	GR01	746897	4675985	7	11	199	-46	5	154	15	16	S	215	-43	5	154	31
5	GR02	746938	4676716	3	9	172	-37	11	187	208	38	S	208	-50	11	187	24
5	GR03	746893	4676221	6	9	186	16	22	13	130	40	S	186	-18	22	13	2
5	GR04	747650	4675890	11	13	182	-47	16	10	20	23	S	208	-49	16	10	24
5	GR05	747892	4675180	8	12	200	-29	9	45	49	30	S	220	-39	9	45	36
4	LB01	751480	4678843	9	10	208	-59	10	31	280	8	N	205	-51	10	31	21
4	LB02	751649	4679964	6	10	215	-40	34	6	280	8	N	213	-32	34	6	29
4	LB03	750065	4680317	6	10	263	5	23	11	200	26	N	261	-18	23	11	77
3	LB04	749592	4683091	5	10	273	-27	32	9	265	17	N	264	-28	32	9	80
3	LB05	749794	4682177	4	10	274	-51	34	11	296	16	N	253	-50	34	11	69
4	MS01	745016	4680503	8	10	322	10	24	7	147	8	S	321	10	24	7	-35
3	MS02	745407	4680779	9	9	50	45	8	44	18	11	S	58	38	8	44	54
3	MS03	745221	4683134	9	10	112	14	29	5	350	28	N	112	-10	29	5	108
2	MS04	745892	4684760	4	10	210	-40	24	21	112	11	S	211	-51	24	21	27
2	MS05	746589	4686334	5	6	187	-52	27	11	3	27	S	216	-44	27	11	32
2	MS06	746497	4685849	8	9	208	-51	10	38	17	15	S	224	-46	10	38	40
3	MS07	745583	4681816	4	11	198	-24	37	10	18	11	S	203	-24	37	10	19
3	OS01	743945	4682154	8	9	54	-21	10	40	174	83	W	39	49	10	40	35
3	OS02	743783	4682010	5	12	234	44	20	20	357	95	E	238	-42	20	20	54
3	OS03	743824	4681863	6	10	237	57	19	16	170	95	E	246	-35	19	16	62
3	OS04	743764	4681519	8	10	61	-18	14	20	174	89	W	36	60	14	20	32
3	OS05	743656	4681497	7	9	247	54	9	53	180	82	W	255	-25	9	53	71
3	OS06	743619	4681274	8	10	352	52	13	21	173	84	S	301	4	13	21	-55
5	RAD1	748026	4673943	19	19	26	36	12	8	160	23	W	9	50	13	7	5
1	RI01	745235	4693615	13	15	4	55	18	6	259	23	N	359	32	18	7	1
1	RI02	745171	4693278	10	15	31	75	15	12	256	24	N	4	54	15	12	-8
1	RI03	745343	4692858	3	16	36	46	13	133	265	38	N	23	14	13	133	
1	RI04	745532	4692683	11	11	243	-50	7	44	247	24	N	218	-43	7	44	34
1	RI05	745692	4692230	10	15	264	-54	14	15	258	32	N	225	-46	14	15	36
1	RI06	745678	4692385	11	11	274	-27	15	12	264	34	N	256	-27	15	12	72
1	RI07	745694	4692534	11	11	256	-54	4	128	259	32	N	221	-42	4	128	37
1	RI08	745248	4693096	8	11	242	-48	17	13	275	46	N	221	-15	17	13	33
1	RI09	744623	4693959	7	11	9	67	29	6	247	25	N	354	44	29	6	2
2	RO01	740566	4683174	6	12	207	-44	26	9	175	5	W	203	-46	26	9	19
2	RO02	740987	4683818	10	10	236	-12	7	49	175	14	S	234	-25	7	49	50
2	RO03	740951	4683821	5	10	30	19	41	6	175	8	W	28	23	41	6	24
2	RO04	741597	4683942	8	9	236	-46	13	22	165	12	W	230	-57	13	22	46
2	RO05	741839	4684872	10	10	228	-27	11	21	180	22	W	216	-42	11	21	32
2	RO06	741129	4685279	4	10	16	50	38	9	120	5	W	15	55	38	9	11
5	SI01	748304	4675166	14	35	7	52	7	27	287	28	E	10	25	6	44	6
5	SI02	748385	4675683	14	27	24	57	8	29	294	26	E	24	31	6	47	20
5	SI03	748349	4675760	15	40	8	38	5	19	303	25	E	13	15	3	138	9
5	SI04	748406	4676131	6	36	21	59	10	25	341	28	E	41	36	5	223	37
5	SI05	748529	4676683	18	29	22	50	8	35	325	26	E	38	32	6	32	34
1	SS01	748105	4691307	7	10	170	-50	12	33	7	40	E	216	-45	11	33	32
1	SS02	747957	4691454	5	11	146	-33	8	104	12	81	E	229	-41	9	86	45
1	SS03	747978	4688942	11	12	192	-63	6	58	13	51	E	249	-34	7	54	65
1	SS04	747387	4688669	11	11	208	-73	5	114	5	43	E	253	-38	5	97	69
1	SS05	747160	4688582	7	21	227	-61	10	14	5	36	E	250	-31	10	14	66
2	SS06	746484	4687200	17	17	207	-59	6	35	8	41	E	243	-33	6	35	59
4	VV01	746198	4677120	18	19	231	-31	10	12	192	21	W	218	-43	10	12	34
4	VV02	746228	4677095	12	12	209	-27	4	49	188	24	W	198	-27	4	49	14

Table 7.1. Paleomagnetic vectors in the Balzes anticline (Rodríguez-Pintó et al. (2013c). Raw data before any reliability filtering.

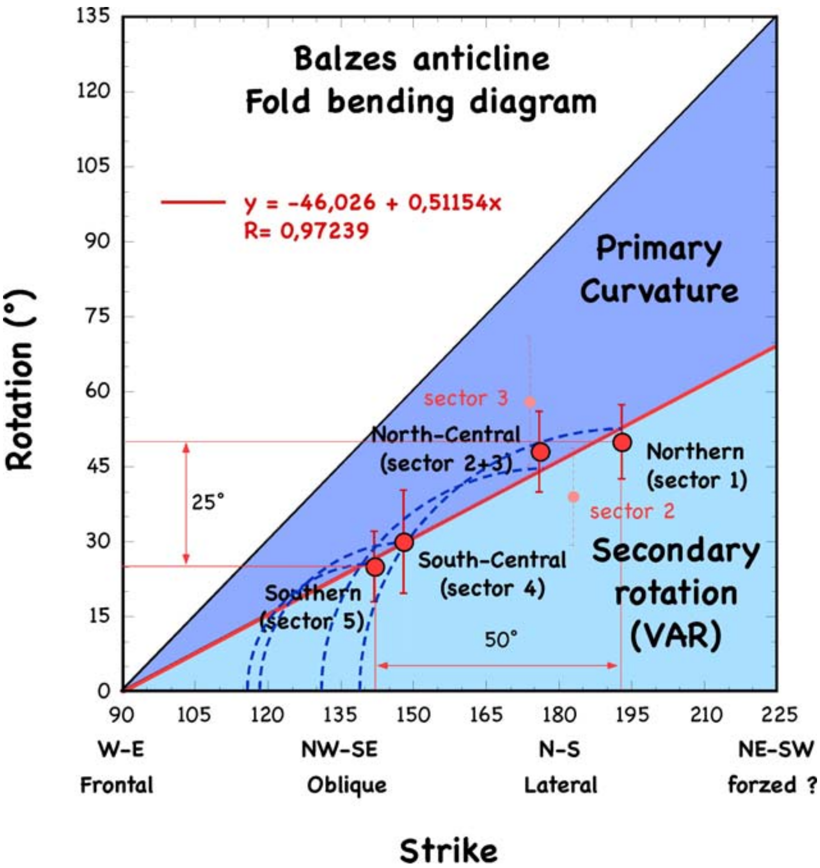

Figure 7.2: Strike vs. VAR diagram in Balzes Anticline (Rodríguez-Pintó et al., 2013c).

The geologic map from the Balzes anticline comes from the MAGNA program (Barnolas et al. in press) but additional improvements have been done considering recent advances in the stratigraphy of the region (Barnolas and Gil, 2001) as well as the GEODE program (Robador et al., 2011) with the help of Antonio Barnolas and Javier Ramajo (Fig. 7.1).

Therefore, we draw on this map the cartographic traces and use them to assign rotation values using the aforementioned law (Fig. 7.3A). To mesh the initial map we have used a Delaunay triangulation with a mean length of triangle sides around 100 m. Initial scattered rotation data is assigned to the nearest triangles within a maximum distance corresponding to this mean length triangle side (Fig. 7.3B). Individual data is interpolated to the whole map using gOcad (Fig. 7.3C).

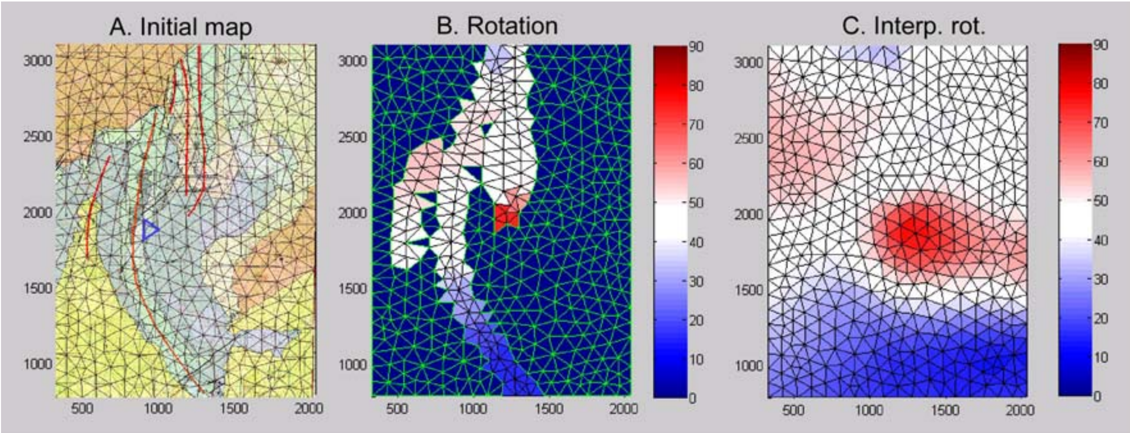

Figure 7.3: A) Meshed initial cartographic map with cartographic traces. The red triangle is the pin-element selected for the piecewise restoration. B) Scattered rotation dataset derived from the strike vs. rotation law (VAR= - 46° + 0.511 * strike). Green contour triangles are no data value. C) Interpolated rotation dataset.

A relevant point to consider in the piecewise restoration is the selection of the pin-element, because it severely conditions the result. The logic selection should be the unrotated area of the foreland. However, the area selected for this example is too small and has suffered rotations everywhere. Thus, we could select the pin-element where rotation is known and preferably in the main trace (Balzes Anticline) and also in the middle of the structure so that the propagation error is as small as possible. Nevertheless, the result will be rather uncertain because this selection is arbitrary. Hence, the usage of two different restoration techniques helps to check the results.

We restore the cartographic map with the two techniques described before and using the scattered and interpolated rotation dataset derived from the structural trends (Fig. 7.4). Before completely trust the results we should answer two questions: 1) is the initial rotation dataset representative enough? and 2) is the pin-element well selected?

If the initial rotation dataset is representative enough, the piecewise restoration using the scattered and interpolated dataset should be equivalent in meaning. Definitely, the restoration with the scattered data would have less deformation because many triangles lack of rotation data and can freely move to fit with their neighbors, but there should not be much difference. In this example (Figs. 7.4 A&B) we appreciate dilation patterns similarly distributed but unlikely equal. Moreover, the shape of the restored map is also different. Therefore, we can not ensure that interpolated data match the real scenary neither the initial rotation data have enough relevance to determine the proper restored map. On the other hand we can certainly observe the deformation trend: to undo the curved fold it is necessary to expand the inner part (blue dilation color in the eastern area) and to contract the outer part (red dilation color in the western area).

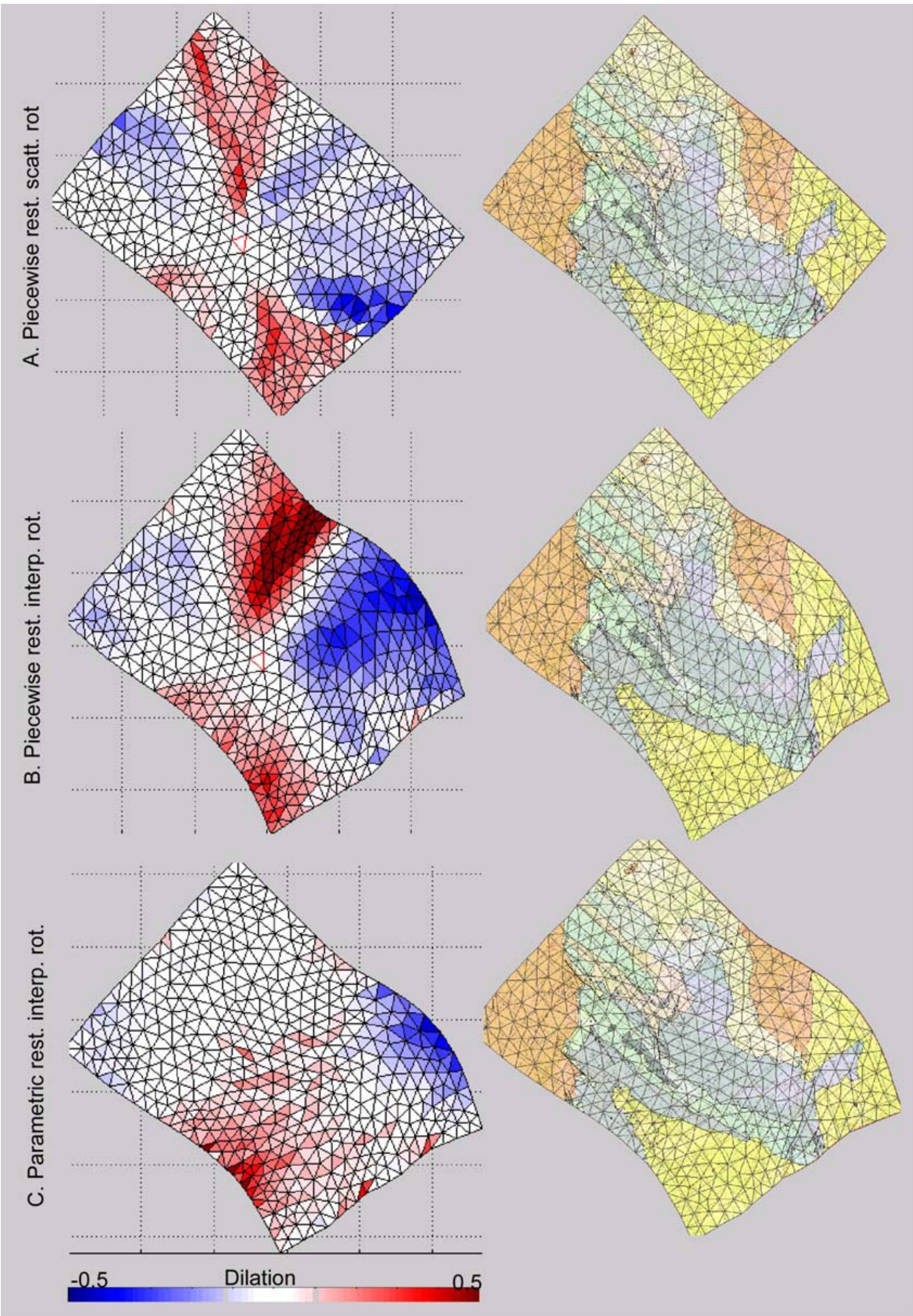

Figure 7.4: Map-view restoration of Balzes Anticline using the structural trends to infer the rotation data. A) Piecewise restoration using the initial scattered rotation dataset. B) Piecewise restoration using interpolated data. C) Parametric restoration using interpolated data.

Despite the plausible lack of accuracy, this result has a clear geological meaning. Negative dilation areas are located in the inner part of the Balzes curvature (southeastern sector of the map). This means this region will be affected by additional compression during the bending of the anticline (rotational period), and corresponds to the area where several diapiric bodies are concentrated (Naval, La Puebla de Castro, Estadilla, etc… Martínez-Peña, 1991; Salvany and Bastida, 2004; Muñoz et al., 2013). The restricted size of the map impedes to see this feature with more accuracy and highlights the importance of the selection of the initial map and the problems on the border. Unfortunately, the expected extension in the outer arc of the fold (south western region), where positive dilation is located, is fossilized by the Tertiary deposits of the Ebro Basin (Sariñena Formation).

Concerning the pin-element location, we evaluate its consistency comparing the piecewise restoration using the interpolated dataset (Figs. 7.4A&B) with the parametric restoration (Fig. 7.4C) in which the pin has no influence at all. The shape and dilation pattern of the restored maps are similar apart from an important area in the north-east. That suggests that parametric restoration is more certain but also that pin-element location was not a bad choice. On the other hand, it is possible to observe that dilation increases in areas distant from the pin-element, reminding us its influence.

It is important to underline the influence of the selected area in the restoration results. In this example all the structures are rotated and we do not have a fixed foreland as the boundary condition. Therefore, the rotation accommodates from the starting point to the borders. Borders are always the most uncertain area for a restoration method.

7.2.2 South Central Pyrenees

To solve part of the border and size effects, the map-view restoration method has been applied at tectonic scale to the South Central Pyrenees. This region comprises high quality databases and the constraints needed for our restoration method: Orogen-scale geologic and structural maps (Choukroune and Seguret, 1973; Barnolas et al., 2008), and a vast paleomagnetic dataset (López et al., 2008; San Miguel et al., 2010) with an exceptional control of the rotational period recorded in syntectonic materials (Pueyo et al., 2002; Sussman et al., 2004; Mochales et al., 2012a, Muñoz et al., 2013).

7.2.2A Geologic map

The base-geologic map was recently published by the BRGM & IGME (Barnolas et al., 2008). Despite the apparent large scale (1:400.000) this map displays plenty of structural features (fold axes, thrust traces, etc) and has the additional advantage of being georeferenced in modern GIS platforms (Fig. 7.5A). Besides, we were granted access to the map in fully digital format. However, this map has many more cartographic details than needed for our purposes. Therefore, we have cloned the style of the classic Choukroune and Seguret's structural map (1973) of the Pyrenees (Fig. 7.5B). This implies a drastic simplification of lithologies and represented ages but it still holds plenty of structural details (Fig. 7.5C). Javier Ramajo helped us in the GIS during this process.

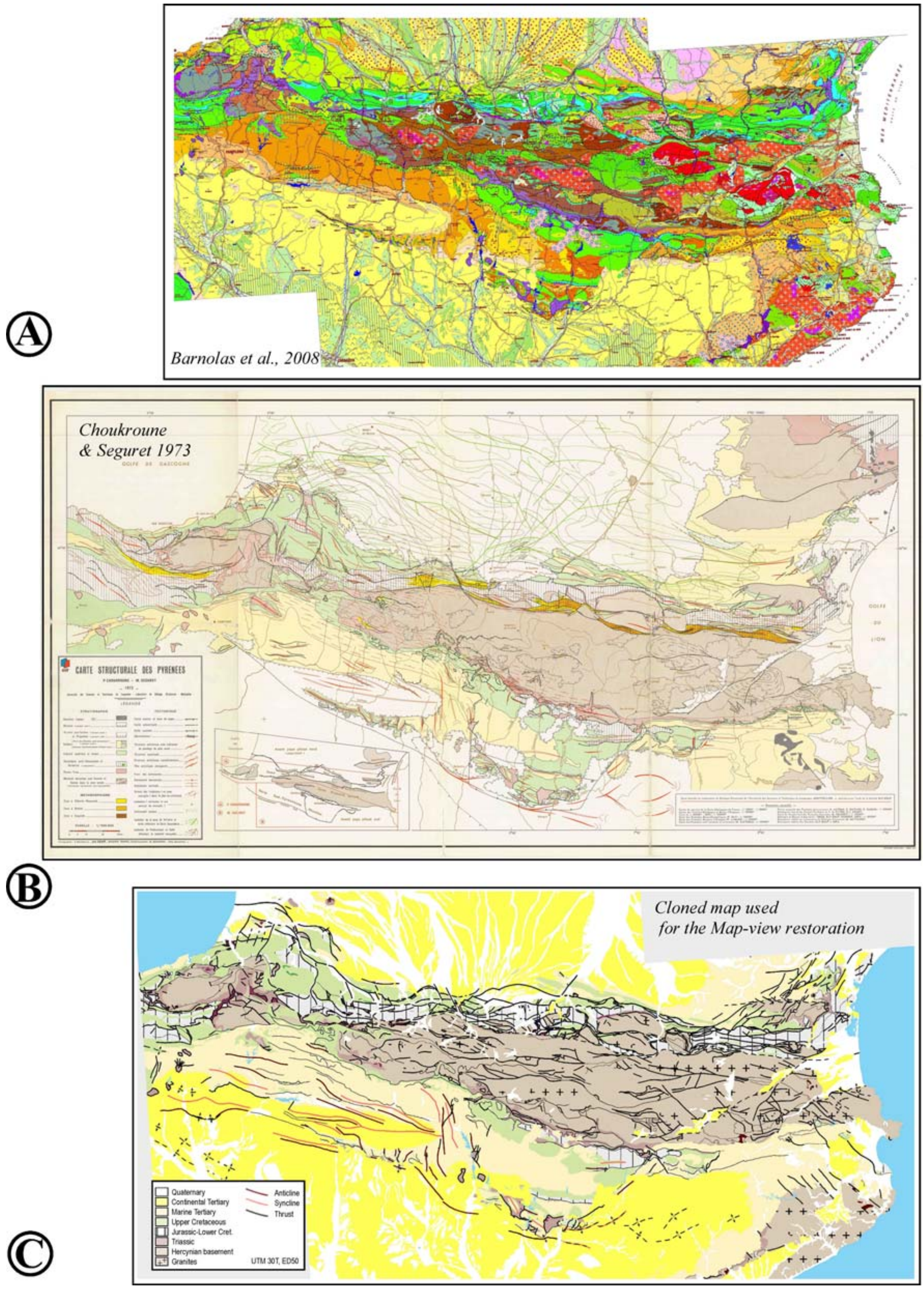

Figure 7.5. Geologic maps used for the map-view restoration of the Southern Pyreenes.

7.2.2B Paleomagnetic data

Paleomagnetic studies have been conducted in the Pyrenees (and their foreland basins; Aquitaine and Ebro) since this technique appeared (Van der Lingen, 1960 and Schwarz, 1962) and have continued during the next five decades. At the moment research interest is still growing as regards of the increasing number of ongoing projects and PhDs and the subsequent publication of many peer-reviewed papers (more than 200). This high amount of information is due to several reasons including the availability of synorogenic materials (allowing an accurate dating of deformation), the excellent outcrop conditions (including stratigraphic sequences with global interest), the existence of well-exposed zones of lateral transference of deformation etc. This enviable frame has produced one of the densest and most homogeneous nets of paleomagnetic sites when comparing with any other orogenic area. Besides, the compilation work carried out by the Geokin3DPyr group during the last years (Pueyo et al., 2005, 2006; Lopez et al., 2008; San Miguel, 2010) under the financial support of the Pyrenean Network (European INTERREG program) has allowed completing data collection and homogenization. Additional work has been done in the frame of this PhD to implement new data from 2010 to 2013 in the database.

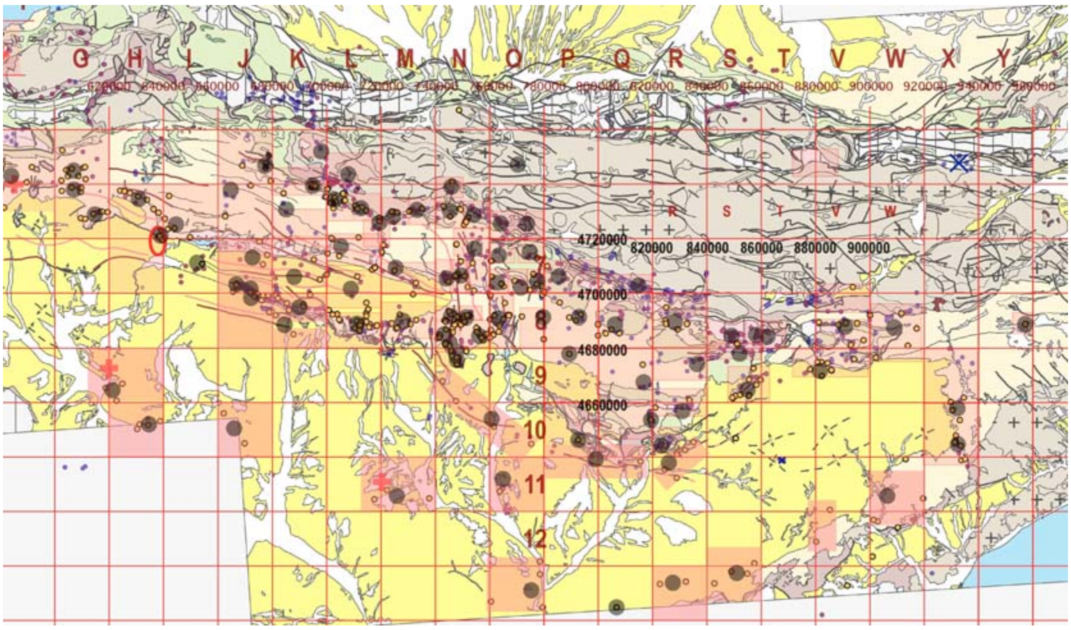

Figure 7.6: Paleomagnetic sites and magnetostratigraphic profiles in the Pyrenees and Ebro Basin. Initial (raw) data: blue points; data comprising both strike and VAR information: red points; filtered data following quality and reliability criteria: yellow points; averaged data by sectors (grouping means): black spots. The orthogonal net in the map has been used to group the data, although the structural trend (similar strike) was the mean criteria for the grouping.

Overall, more than 30.000 demagnetizations coming from more than 1.800 sampling points, ≈150 of them magnestostratigraphic profiles (>85 kilometers of sections), were synthesized. Within this large dataset, the northern Pyrenees are very densely sampled in the Corbieres sector, Eastern corner (Rouvier et al., 2001, 2012; Henry et al., 2006) and in the Mouleon basin, the westernmost one (Oliva et al., 2010) but there are very few data in the largest central portion, for that reason it has been not considered. We have focused our restoration on the Southern Pyrenees where ≈85% of the data is located. The Pamplona Fault constitutes the western boundary, and the Western Cadi Range the easternmost one. The Ebro Basin attached to this large portion of the mountains was also taken into account (Fig. 7.6). Several structural domains can be identified and display abundant paleomagnetic references (in brackets).

- Pamplona Basin (Larrasoaña, 2000; Larrasoaña et al., 2003).

- Internal Sierras (Oliva, 2004; Oliva and Pueyo, 2007a&b; Oliva et al., 2008; Oliva et al., 2012a).

- Turbiditic basin (Pueyo, 2000; Oms et al., 2003; Oliva and Pueyo, 2007; Pueyo et al., in prep).

- External Sierras (Hogan, 1993; Hogan and Burbank,1996; Pueyo, 2000, Pueyo et al., 1997; 2002, 2003a&b, 2004; Kodama et al., 2010; Oliva et al., 2012a and 2012b; Rodríguez-Pintó et al., 2012a&b, 2013a&b).

- Jaca Basin (Hogan, 1993; Hogan and Burbank, 1996; Pueyo, 2000; Pueyo-Anchuela et al., 2012).

- Ainsa Oblique zone (Dinarès-Turell, 1992; Bentham 1992; Holl and Anastasio, 1993; Parés and Dinarés, 1993; Bentham and Burbank, 1992; 1996; Fernández, 2003; Oms et al., 2006; Mochales, 2011; Mochales et al., 2012a&b; Muñoz et al., 2013).

- South Pyrenean Central Unit (Bentham 1992; Dinarès-Turell, 1992; Pascual, 1992; Pascual et al., 1990, 1991, 1992a&b; Meigs, 1995 and 1998; Meigs et al., 1996, 1997; Beamud et al., 2003, 2004; 2011; Galbrun et al., 1992; Dinarès-Turell, and García-Senz, 2000; Gong, 2008; Gong et al., 2008a&b, 2009).

- Eastern portion of the South Pyrenean Central Unit (SPCU)- Oliana sector (Dinarès-Turell, 1992; Burbank et al., 1992a&b; Keller 1992; Keller et al., 1992, 1994, 1996; Sussman et al., 2004).

- Pedraforca and Cadi Easternmost units (Dinarés, 1992; Keller, 1992).

- Ebro Foreland Basin (Barberá, 1999; Barberá et al., 1994; 2001; Gomis, 1997; Gomis et al., 1997; Taberner et al., 1999; Perez-Rivarés et al., 2002, 2004; Larrasoaña et al., 2006; Cascella and Dinarès-Turell, 2009; Costa et al., 2010, 2011, 2013; Gómez-Paccard et al., 2012).

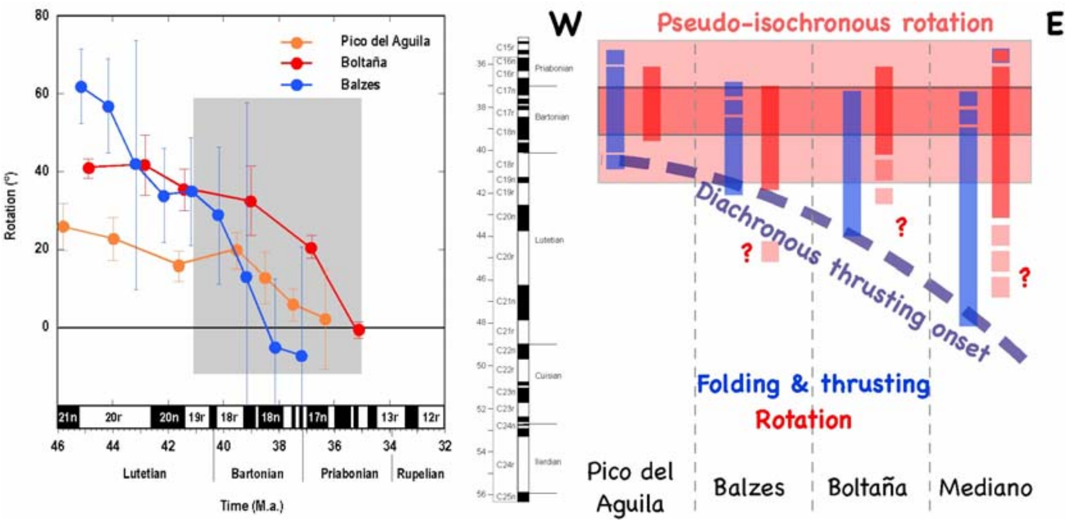

Figure 7.7: Rotational and thrusting dating of oblique structures in the Southwestern Pyrenees (Pueyo et al., 2013). Mediano data by Muñoz, et al. (2013), Boltaña by Mochales et al. (2012b), Balzes by Rodríguez-Pintó et al., (2013c) and Pico del Aguila by Pueyo et al. (2002)

Besides, and due to, the syntectonic record, the first rotation velocities of individual thrusts and fold-related thrusts have been defined in the Southern Pyrenees (Pueyo et al., 2002; Mochales et al., 2012a, Rodríguez-Pintó et al., 2013c; Muñoz et al., 2013). These data are derived from dense sampling along well-dated magnetostratigraphic profiles and allow constraining the main rotational activity of the External Sierras and Ainsa oblique zone during Upper Lutetian-Bartonian-Priabonian times (Fig. 7.7). This period is coincident with other important rotation ages in other locations of the Pyrenees; Oliana anticline (Sussman et al., 2004), Cerveres (Rovier et al., 2012); Mauleon (Oliva et al., 2010).

Despite the large paleomagnetic dataset, only part of it honors standard and objective quality criteria and therefore it has been filtered with the following criteria:

-Data with $\alpha_{95} > 25°$ or without α95 were deleted (1110 data remain from the initial 1227).

-Sites with little number of samples were removed; $n < 5$ or without this information (179 + 7; remain 924).

-Data with more than 100Ma (229); this criteria filters pre-Pyrenean vectors (Paleozoic, Triassic to Lower Cretaceous), which in turn may be also affected by the rotational kinematics of Iberia. Most remaining data are Cenozoic (695 mean vectors).

- Remaining North-Central Pyrenean data (5) are removed too.

-Extreme and anomalous declinations (normally related to secondary remagnetizations) VAR < -90° (11 sites mainly from Cotiella) and VAR > 90° (9).

-Anomalous inclination < |30°| (66) and > |70°| (8). Likely linked to internal deformation, inclination shallowing etc). Therefore, we have adopted a conservative approach to avoid the noise caused by these sources of error.

-Sites with $15° > \alpha_{95} < 25°$, are treated with caution in grouping stage. 511 mean vectors survived the filtering routine.

The resultant database that we consider as the initial passes a second filter. This filter consists on grouping VAR data by structures and sectors (Table 7.2 and Fig. 7.8). We calculate the mean VAR, with its α_{95} and k values, the mean position and the mean structural trend. This last one includes the Bingham's (1964) matrix as well as its Woodcock's (1977) parameters. This treatment aims to quantify the quality of both datasets (VARs and structural trends) and to establish objective criteria to removed unreliable data.

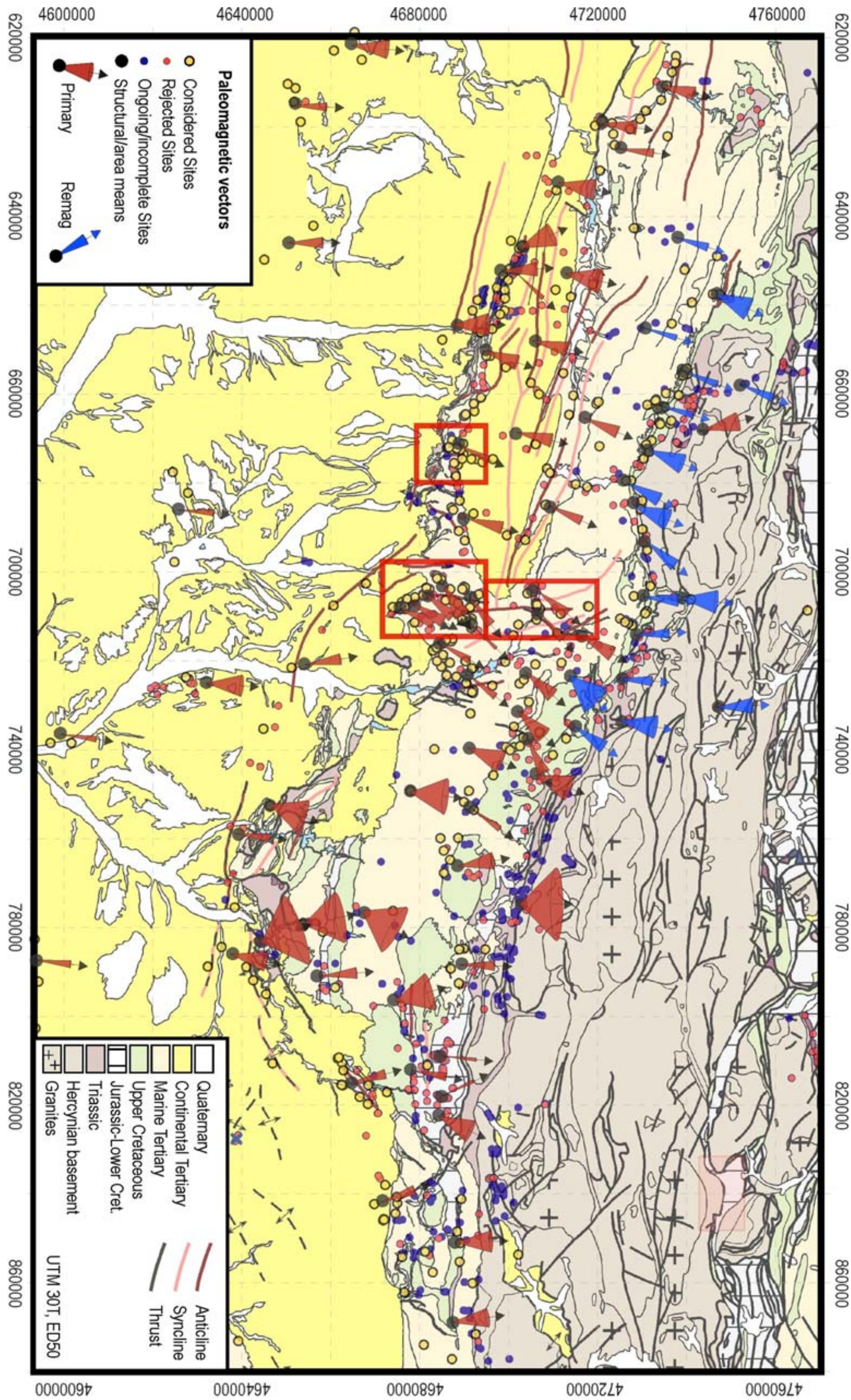

Figure 7.8: Mean rotational magnitudes in several structural sectors the Southwestern Pyrenees and in the Ebro Basin (Pueyo et al., 2013). Red triangles indicate the structures where rotation velocities are well constraint.

	Sector	Name	s	S	X	Y	Struct. Trend			Bingham				Woodcock										
							Trend	Plunge	Δ	|E1|	|E2|	|E3|	∑|Ei|	Cw	Gw	Kw	Aw	∑n	Pol	Rot	Inc	α95	k	R
1	F5-F6	Diapiros Navarros	6	6	584000	4743111	**104**	3	40	0,6102	0,3779	0,0119	1,0000	0,48	3,46	0,14	3,9372	57	N+R	**9,8**	43,8	6,7	84,9	0,9918
2	G5	Pamplona N	9	9	606959	4744981	**108**	1	30	0,7766	0,1831	0,0403	1,0000	1,44	1,51	0,76	2,9586	92	N+R	**8,3**	50,9	8,8	31,5	0,9749
3	G6-s	Pamplona S	4	4	607059	4738041	**109**	1	40	0,8268	0,1426	0,0306	1,0000	1,76	1,54	0,85	3,2966	33	N+R	**8,4**	59,1	11,1	51,9	0,9892
4	G6	Alaiz	6	6	614824	4728909	**96**	1	25	0,9428	0,0523	0,0049	1,0000	2,89	2,37	0,88	5,2596	50	N	**9,1**	48	6,6	87,8	0,9921
5	H7+H6-s	Lumbier	4	4	638958	4721135	**95**	3	25	0,7674	0,2301	0,0025	1,0000	1,20	4,52	0,26	5,7267	35	N	**8,5**	51,5	10,9	54	0,9896
6	H6	Izaga	7	7	630956	4734566	**116**	-9	60	0,7183	0,2346	0,0472	1,0001	1,12	1,60	0,61	2,7225	61	N	**13,2**	55	11,2	25,7	0,9715
7	H9+G9	Tudela-NW	4	4	621270	4664616	**90**	Ref										161	N+R	**10,3**	45,5	14,7	29,9	0,9812
8	H10	Tudela-SE	6	6	634692	4652052	**90**	Ref										151	N+R	**6,2**	44,5	7,1	75,3	0,9908
9	I6	Leyre	6	6	644666	4725241	**104**	0		0,8373	0,1234	0,0392	0,9999	1,91	1,15	1,03	3,0615	56	N	**6,1**	50,5	7,6	65,6	0,9894
10	I7	Onsella	8	8	652380	4711144	**107**	6	26	0,6806	0,3054	0,0141	1,0001	0,80	3,08	0,25	3,8768	75	N+R	**10,5**	34,3	16,7	13,6	0,9267
11	J5	Anso	9	9	677483	4746867	**109**	-4	50	0,6525	0,3413	0,0062	1,0000	0,65	4,01	0,16	4,6563	131	N+R	**24,3**	44,2	17,8	13,4	0,9438
12	J6	Esca	16	16	664831	4738013	**105**	8	60	0,5534	0,4031	0,0435	1,0000	0,32	2,23	0,14	2,5433	178	R	**16,5**	53,2	3,5	15,1	0,9345
13	J7-N	Artieda	6	6	672798	4713099	**121.4**	18.3	44	0,7770	0,2062	0,0167	0,9999	1,33	2,51	0,49	3,8400	70	N+R	**11,6**	40,6	20,3	14,2	0,9297
14	J7-C	Sto. Domingo-N	15	15	672082	4701719	**126**	-50	70	0,8704	0,0971	0,0325	1,0000	2,19	1,09	1,11	3,2877	165	N+R	**44**	36	3,5	9,6	0,863
15	J7-S	San Marzal	3	3	666874	4703229	**138**	-60	40	0,8902	0,1097	0,0001	1,0000	2,09	7,00	0,29	9,0940	44	N+R	**-22,8**	43,6	19,7	32	0,9834
16	J7-8-Ebro	Luesia	8	8	672273	4698229	**117**	7	20	0,9728	0,0198	0,0074	1,0000	3,89	0,98	1,32	4,8787	327	N+R	**-3,1**	42,5	11,3	14,9	0,965
17	J10	Castejon	4	4	666051	4650571	**90**	Ref										152	N+R	**0,8**	49,1	9	79,3	0,9929
18	K5-S	Bisaurin-Aspe	10	10	695052	4739466	**104**	-7	70	0,8653	0,1159	0,0188	1,0000	2,01	1,82	0,84	3,8292	77	R	**21,3**	45,6	5,6	67,6	0,988
19	K5-N	Gave d'Azpe	10	10	698109	4752040	**105**	16	70	0,7080	0,2418	0,0502	1,0000	1,07	1,57	0,60	2,6464	57	R	**22**	41	7	8,7	0,758
20	K6-S	Subordán	11	11	685246	4730740	**122**	0	90	0,6751	0,2948	0,0301	1,0000	0,83	2,28	0,35	3,1103	148	R	**17,3**	55,9	2,6	20,2	0,9508
21	K7	San Juan de la Peña	21	21	688160	4706034	**98**	-2	40	0,5578	0,4012	0,0411	1,0001	0,33	2,28	0,14	2,6080	380	N+R	**13,3**	36,9	11,1	9,2	0,896
22	K8-N	Riglos-Loarre	14	14	690137	4694860	**132**	-33	80	0,7716	0,2057	0,0227	1,0000	1,32	2,20	0,54	3,5261	178	N+R	**18,6**	35,3	12	12,9	0,9222
23	K8-S	Ayerbe-Agüero	4	4	684602	4688487	**111**	2	70	0,6143	0,3855	0,0002	1,0000	0,47	7,56	0,06	8,0299	113	N+R	**-0,4**	30	18,4	34,5	0,971
24	L5	Anayet-Somport	23	23	708039	4743671	**104**	-7	80	0,6497	0,2815	0,0688	1,0000	0,84	1,41	0,54	2,2453	211	N+R	**-13,5**	36	15,4	6	0,8422
25	L6-W	Collarada	19	19	703218	4734319	**113**	-4	70	0,8598	0,1075	0,0327	1,0000	2,08	1,19	1,05	3,2693	161	R	**16,3**	41,2	5,6	36,6	0,9741
26	L6-E	Partacua	7	9	712759	4731196	**97**	5	80	0,7840	0,1647	0,0512	0,9999	1,56	1,17	0,93	2,7287	74	R	**22,1**	53,9	15,9	17,8	0,9439
27	LM-6-7	Sta. Elena	6	6	719479	4725815	**103**	14	75	0,6222	0,2518	0,1260	1,0000	0,90	0,69	0,92	1,5970	41	R	**28,3**	33,6	10,7	48,2	0,9792
28	L7	Sabiñánigo	8	9	705359	4717169	**104**	10	50	0,7710	0,1978	0,0312	1,0000	1,36	1,85	0,63	3,2073	90	N+R	**22,9**	46	9,6	39	0,9744
29	L7-8	Monrepós	13	13	709008	4701607	**13**	-5	40	0,7669	0,2233	0,0098	1,0000	1,23	3,13	0,38	4,3600	193	N+R	**12,7**	40	11,3	15,8	0,9365
30	L8	Bentué-Aguila	35	35	711216	4688797	**174**	-29	40	0,8829	0,1140	0,0032	1,0001	2,05	3,57	0,52	5,6201	571	N+R	**24,8**	44,3	6,6	14,3	0,932
31	M6-W	Tendenera	7	7	724533	4728071	**53**	-32	50	0,8215	0,1711	0,0074	1,0000	1,57	3,14	0,46	4,7097	52	R	**22,5**	40,3	16,5	16,8	0,9404
32	M6-E	Otal	7	7	733330	4730564	**98**	5	40	0,7409	0,2079	0,0512	1,0000	1,27	1,40	0,74	2,6721	85	R	**40**	49	9,5	3,7	0,614
33	M7	Basa	13	14	725531	4709321	**114**	13	30	0,5625	0,4131	0,0244	1,0000	0,31	2,83	0,11	3,1378	338	N+R	**23,4**	41	7,6	33,4	0,97
34	M8	Guara	12	13	728190	4689853	**81**	-1	35	0,9244	0,0652	0,0104	1,0000	2,65	1,84	0,97	4,4873	113	N+R	**15,1**	37,7	9,2	23,2	0,9569
35	M11	Monegros	6	6	725961	4625746	**90**	Ref										414	N+R	**5,2**	44	5,2	199	0,995
36	N6-N	Gavarnie	2	2	745966	4739080	**107**	21	0	0,9382	0,0618	0,0001	1,0001	2,72	6,43	0,40	9,1465	15	R	**6**	60	18,3	9,3	0,806
37	N6-E	Pineta	15	15	754164	4728693	**131**	7	90	0,6942	0,2750	0,0308	1,0000	0,93	2,19	0,40	3,1152	113	R	**-3,1**	39,5	8,3	24	0,9584
38	N6-W	Perdido	10	10	745456	4730263	**83**	4	60	0,5319	0,4361	0,0320	1,0000	0,20	2,61	0,08	2,8107	65	R	**5**	39,7	10,4	25,2	0,9602
39	N6-7	Añisclo-N	9	9	754542	4716411	**171**	2	70	0,9230	0,0621	0,0149	1,0000	2,70	1,43	1,08	4,1263	58	N+R	**28,8**	30	11,7	22,7	0,956
40	N7-SE	Boltaña-NW	17	17	744271	4705366	**249**	75	80	0,7758	0,1811	0,0431	1,0000	1,45	1,44	0,79	2,8904	154	N+R	**37,8**	42,4	8,6	18	0,9478
41	N7-S	Boltaña-N	22	23	749505	4706499	**188**	7	55	0,6733	0,3133	0,0134	1,0000	0,77	3,15	0,24	3,9169	196	N+R	**49,3**	43,1	6,5	23,7	0,9598
42	N8-NE	Boltaña-S	16	16	751438	4691171	**170**	2	20	0,9760	0,0229	0,0011	1,0000	3,75	3,04	0,89	6,7882	148	N+R	**44,3**	49,6	3,4	117	0,992
43	N8-N	Balzes-N	13	18	745845	4691509	**195**	-13	15	0,6202	0,3687	0,0111	1,0000	0,52	3,50	0,15	4,0231	232	N+R	**51,8**	40,1	8,3	28,2	0,9646
44	N8-C	Balzes-CN	10	11	743316	4685104	**187**	3	20	0,8694	0,1276	0,0030	1,0000	1,92	3,75	0,47	5,6692	77	N+R	**38,8**	43,1	9,7	28,7	0,9652
45	N8-CS	Balzes-C	9	9	745483	4681878	**175**	-6	25	0,5574	0,4279	0,0148	1,0001	0,26	3,36	0,08	3,6287	56	N+R	**58,1**	40,7	13,1	18,4	0,9455
46	N8-S	Balzes-CS	9	10	747759	4678868	**148**	-9	70	0,9073	0,0807	0,0120	1,0000	2,42	1,91	0,90	4,3256	78	N+R	**30**	40,2	10,3	29	0,9656

							Struct. Trend			Bingham				Woodcock										
	Sector	Name	s	S	X	Y	Trend	Plunge	Δ	|E1|	|E2|	|E3|	∑|Ei|	Cw	Gw	Kw	Aw	∑n	Pol	Rot	Inc	α95	k	R
47	N9-N	Balzes-S	19	19	748078	4675662	135	4	75	0,8246	0,1067	0,0687	1,0000	2,04	0,44	1,36	2,4851	168	N+R	20,7	36,6	9,9	15	0,9373
48	N9-S	Barbastro-W	7	7	760839	4654043	126	4	60	0,6872	0,2741	0,0386	0,9999	0,92	1,96	0,44	2,8794	58	N+R	351	57	9,1	2,2	0,559
49	N8-SE	Buil	22	22	756213	4684468	197	6	80	0,9492	0,0351	0,0157	1,0000	3,30	0,80	1,33	4,1020	252	N+R	28,8	42,3	5,6	31,5	0,9697
50	R10-11	Barbastro-E	5	5	826010	4637961	86	-5	45	0,6459	0,3331	0,0210	1,0000	0,66	2,76	0,24	3,4261	51	R	12,3	39,6	16,3	28,7	0,9651
51	PQ10-11	Barbastro-C	6	7	799140	4639269	102	-9	70	0,6604	0,2864	0,0533	1,0001	0,84	1,68	0,46	2,5169	58	N+R	7	50	7	3,5	0,702
52	O13	Fraga	10	10	775406	4591060	90	Ref										557	N+R	7,8	51	5,1	101	0,9901
53	O11	Albalate	12	12	764988	4631987	90	Ref										51	N+R	4,4	56,5	17,1	8,1	0,876
54	O8-W	Mediano	27	27	763276	4690733	180	1	45	0,8775	0,0936	0,0289	1,0000	2,24	1,18	1,09	3,4132	603	N+R	37,5	47,9	6	24,1	0,9601
55	O8-E	La Fueva	4	4	779764	4691172	122	3	25	0,5540	0,4433	0,0027	1,0000	0,22	5,10	0,04	5,3239	150	N+R	23,3	40,2	18,3	35	0,9714
56	O7SW	Peña Montañesa	6	6	762867	4703821	137	5	40	0,9032	0,0932	0,0036	1,0000	2,27	3,25	0,61	5,5250	41	N+R	39,5	45,3	11,7	40,5	0,9753
57	O7SC	Sª Ferrera	7	7	771540	4701999	143	-2	75	0,6878	0,2844	0,0278	1,0000	0,88	2,33	0,36	3,2085	38	N+R	43,8	52,6	14,5	21,4	0,9532
58	O7SE	Campo	15	15	777599	4704339	152	35	80	0,6113	0,3118	0,0768	0,9999	0,67	1,40	0,45	2,0744	167	N+R	64,6	61,5	10,3	22,6	0,9557
59	O7-NW	Cotiella-W	4	4	763512	4713887	121	2	45	0,7991	0,1969	0,0040	1,0000	1,40	3,90	0,35	5,2972	30	N+R	43,1	32,1	25,3	18,8	0,9469
60	O7-NE	Cotiella-E	4	4	774843	4715040	130	0	15	0,9230	0,0764	0,0006	1,0000	2,49	4,85	0,47	7,3385	37	R	35,9	42	10,7	99,8	0,99
61	O6-W	Bielsa	11	11	764118	4725569	121	4	35	0,6800	0,3102	0,0097	0,9999	0,78	3,47	0,22	4,2500	77	R	4,6	40,6	8,2	35,2	0,9716
62	O6-E	Gistain	4	4	773794	4725480	118	5	80	0,6784	0,2520	0,0696	1,0000	0,99	1,29	0,66	2,2770	36	R	9,5	35	18,4	34,7	0,9711
63	06-NE	Neste D'Aure	5	5	770441	4747195	113	9	20	0,9087	0,0874	0,0039	1,0000	2,34	3,11	0,65	5,4510	101	N+R	-3,1	10,8	11,8	53,6	0,9813
64	P7-S	Lierp-Bonansa	11	11	785508	4706127	120	8	90	0,7206	0,1918	0,0876	1,0000	1,32	0,78	1,04	2,1073	66	N+R	20,9	43,1	20,3	6,6	0,8495
65	P8	Isábena	8	8	793010	4691255	127	8	45	0,7650	0,2183	0,0167	1,0000	1,25	2,57	0,45	3,8245	114	N+R	36,3	50,9	5,1	136	0,9927
66	P9	Benabarre	2	2	789399	4677936	110	Ref										50	N+R	5,7	46	26,8	177	0,9944
67	P10	Baldellou	2	2	792693	4646350	90	Ref										90	N+R	19,1	41,1	26,1	187	0,9946
68	P15	Gandesa	2	2	789099	4550613	90	Ref										124	N+R	2	44,5	21,9	265	0,9962
69	Q7-S	Gervas-Pubill	3	5	814829	4702844	99	-17	75	0,7888	0,1377	0,0735	1,0001	1,75	0,63	1,23	2,3732	20	N+R	25,4	32,8	70,3	6,2	0,8397
70	Q8	Gurp	9	11	806213	4688493	98	2	55	0,7517	0,2295	0,0188	1,0001	1,19	2,50	0,44	3,6885	93	N+R	-9,2	53,9	12,8	19,3	0,9483
71	Q9	Tremp	4	4	816744	4667533	147	-14	0	0,6221	0,3778	0,0001	1,0001	0,50	8,24	0,06	8,7357	38	N+R	30	47,3	38	9,1	0,8898
72	Q10	Ager	2	2	819476	4653720	75	Ref										67	N+R	-10,7	57,2	35,3	105	0,9904
73	Q13	Serral Aubagues	2	2	806789	4584835	90	Ref										54	N+R	6,6	39	19,5	333	0,997
74	R8	Pobla de Segur	10	10	828283	4689460	117	-4	50	0,8145	0,1813	0,0042	1,0001	1,50	3,77	0,38	5,2675	282	N+R	1,8	45	8,2	40,1	0,975
75	R9-C	Isona	4	4	836394	4674149	60	4	20	0,6539	0,3423	0,0038	1,0001	0,65	4,50	0,14	5,1480	22	N+R	-15,2	53,6	28,4	15,3	0,9346
76	R9-10	Monsec-Rubies	12	12	831024	4656881	70	7	55	0,8367	0,1492	0,0141	1,0001	1,72	2,36	0,63	4,0833	337	N+R	-5,4	35	8,7	28	0,9643
77	R10-SW	Sant Mamet	4	4	823303	4644271	51	21	70	0,7940	0,1629	0,0431	1,0001	1,58	1,33	0,87	2,9136	10	N	-19,9	46,9	53,7	5,2	0,8078
78	R13	Cervia	4	4	827529	4593835	90	Ref										190	N+R	7,4	43,6	6,3	282	0,9964
79	S8-W	Prada-Ares	41	41	858118	4684933	108	3	30	0,6629	0,3103	0,0268	1,0001	0,76	2,45	0,30	3,2082	532	N	-25,1	57,4	2,9	59,4	0,9836
80	S8-E	Figols-E100	37	37	849107	4684583	102	3	40	0,9260	0,0651	0,0089	1,0001	2,65	1,99	0,93	4,6448	281	N	5,5	57,4	3	61,8	0,9843
81	S8-9	Organya	8	8	852084	4677952	81	8	70	0,5448	0,3852	0,0700	1,0001	0,35	1,71	0,20	2,0519	49	N	11,3	52	7,1	71,5	0,986
82	S9-T9	Oliana	30	30	855035	4664723	49	0	80	0,8029	0,1415	0,0556	1,0001	1,74	0,93	1,08	2,6700	520	N+R	-14,5	42,2	8	11,7	0,9172
83	S12-13	Tarrès	8	8	851054	4597450	90	Ref										122	N+R	0,9	43,7	5,8	106	0,9906
84	T8	Organya-E	4	4	862347	4684281	136	8	50	0,6568	0,2984	0,0448	1,0001	0,79	1,90	0,39	2,6852	26	N	24,8	43,7	18,2	35,3	0,9716
85	TV8	Busa (Pedraforca-S)	16	16	881587	4671663	99	-5	60	0,6413	0,3327	0,0261	1,0001	0,66	2,55	0,25	3,2016	139	N+R	-19,5	52	7,9	28,3	0,9647
86	V8	Figols (Pedraforca-N)	15	15	890967	4687859	87	7	60	0,7955	0,1954	0,0090	1,0001	1,40	3,08	0,43	4,4817	344	N+R	-2,3	34,1	16,7	7,7	0,8703
87	W11-12	Monserrat	5	5	906390	4625741	90	Ref										427	N+R	5,4	45,4	13,9	39,3	0,9746
88	W8	Ripoll	10	10	908980	4687487	84	-7	80	0,6758	0,2502	0,0741	1,0001	0,99	1,22	0,68	2,2105	404	N+R	-7,7	43,7	14,7	13,1	0,9236
89	X9	Manlleu	11	11	932399	4644711	90	Ref										117	N+R	2,3	47,6	4,6	110	0,9909
90	X10	Vic	7	7	932280	4657921	90	Ref										309	N+R	2,8	46,7	4,5	212	0,9953
91	Y8	Olot	7	7	957198	4688676	90	Ref										50	N	-3,7	53,3	10,1	42,8	0,9767

Table 7.2: Mean Vertical Axis Rotations (filtered raw data) deduced from paleomagnetic data in the Southern Pyrenees. s/S: considered/available sites. X,Y: UTM coordinates (ED50 30T zone). Structural trend referred to 0-180° scale (exceeded in exceptional cases). Bingham's (1964) distribution. Eigenvalues of the orientation matrix (bedding planes). Woodcock's (1977) parameters to constrain the shape and strength of the trend distribution. Sn: total number of demagnetized samples. Rotation vector (final orientation with geological meaning to quantify the VAR).

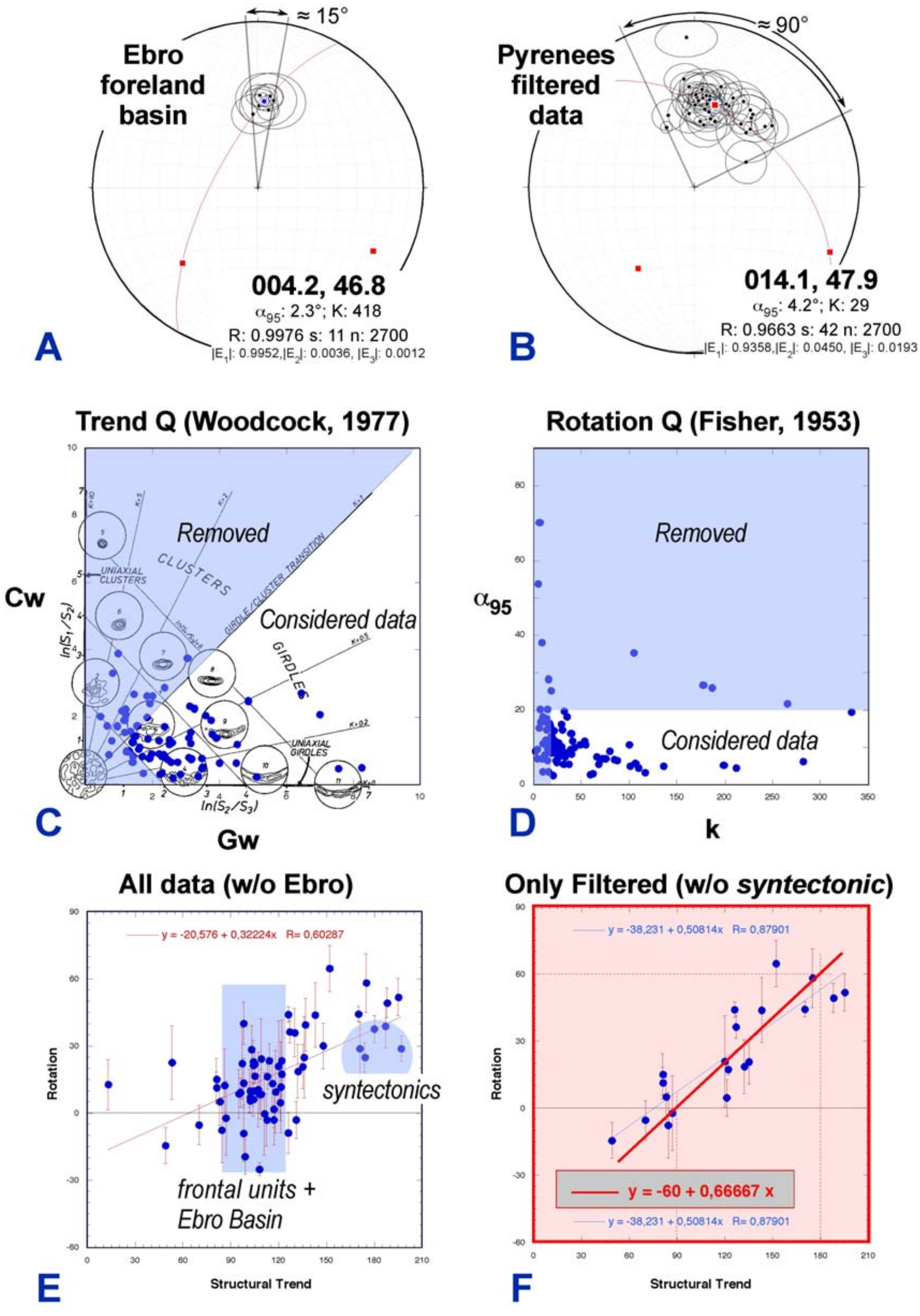

Figure 7.9: A) Stereographic projection of unrotated data from the Ebro foreland basin (only filtered sectors). B) Paleomagnetic robust rotations (only filtered sectors). C) Woodcock diagram (1977) of mean strike values calculated by sector. Only girdled distributions have been used in the following steps. D) Rotation Q diagram (Fisher, 1953) of mean VAR values calculated by sector. E) Strike vs. rotation diagram with not well grouped data deleted. F) Strike vs. rotation diagram with all filtered data except the foreland.

Filtered data averaged by sectors is not equally representative; thus, we delete not well-grouped data. Sector VAR's are only considered with α_{95}<15°, k> 20 and R>0.9500 (Fig. 7.9D). Structural trends are only considered if they are based in well-defined girdle distributions of bedding poles (Fig. 7.9C); Woodcock's K<1 and total eccentricity (E1/E3) > 2). Moreover, unrotated data from the Ebro foreland basin (Fig. 7.9A) are only considered for the definition of the pin area. Strike vs. rotation diagram is plotted in order to establish the law to infer rotation data from structural trends (Figs. 7.9E&F). We calculate the theoretical regression line but we prefer to adjust it manually because far data is still biased by syntectonic records (Fig. 7.9F). The resultant equation is VAR = -60 + 0.67 * strike, which is not far from the obtained in the Balzes Anticline (VAR= - 46° + 0.511 * strike).

A surprising result from the VAR vs. trend diagrams is the definition of frontal unrotated structures. In both cases, Balzes and Southern Pyrenees, this orientation seems to be N090E in contrast with the so-called mean Pyrenean direction, which is assumed to be N100E-N120E and often assumed to be perpendicular to tectonic shortening.

Another observation is the *banana-like* scattering of the Pyrenean data (≈90° scattering in declination) if compared with the pronounced clustering of the Ebro Basin data (14°). This is what we expected, since the Ebro Basin is supposed to be undeformed in contrast with the Pyrenean rotated structures. In this sense, the small difference between both means (10°) has to be evaluated within this frame. Finally, the consistent (almost) unrotated data from the Ebro Basin has been a key fact for the definition of the pin-area in the piecewise restoration and thus, we have selected the entire portion of the Basin included in the target map. The geological meaning is quite obvious; this large pin-area can be considered the absolute footwall of the Pyrenean basal thrust (autochthonous).

7.2.2C Restoration settings

We use several initial rotation datasets: all VARs, filtered VARs (sector means), and rotation inferred from the structural trends using both laws. Strikes at the map-scale are obtained from the cartographic traces vectorized directly from the map (Fig. 7.10).

Initial traces are filtered removing topographic effects (V-rule) and smoothing remaining trends.

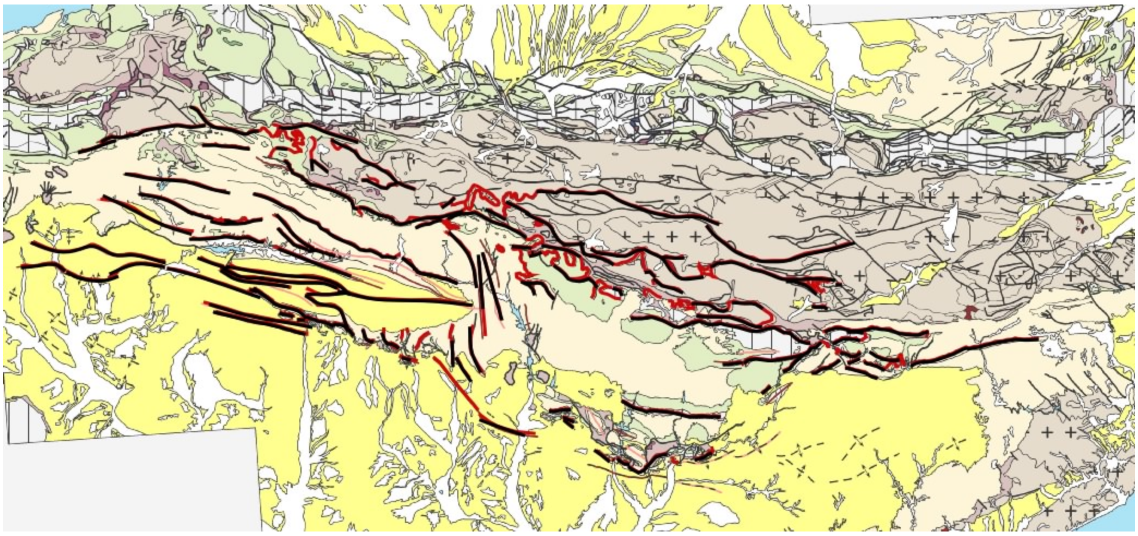

Figure 7.10: Structural trends: initial (red lines) and filtered (black lines).

Once the rotation data has been defined, we need to establish the meshing of the map. In order to be coherent with the rotation data density, the mean side of mesh triangles is around 5 km. Following the conclusions from previous sections (where we advise about the influence of the area selected, particularly at the borders) we chose two initial meshes to restore in order to compare the results (Fig. 7.11). Anyway, first we analyze the influence of the initial rotation dataset using the mesh of smaller area.

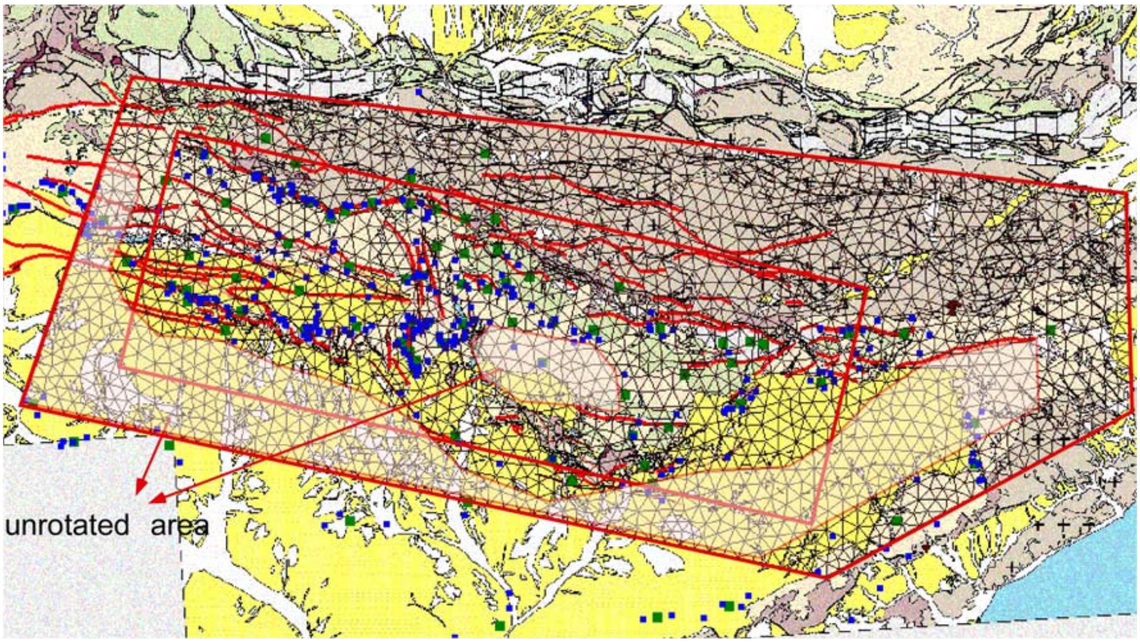

Figure 7.11: Initial map with two different meshes. Blue points: all VARs; green points: filtered VARs (sector means); red lines: structural trends.

We restore the map with the piecewise approach using scattered and interpolated rotation data, and with the parametric approach using only interpolated data. However, in order to focus on the initial rotation dataset used for the restoration, we do not discuss neither the restoration method nor the pin-element for the moment. We use several rotation datasets (Figs. 7.12 & 7.13): 1) scattered and interpolated from individual VARs (yellow points of Fig. 7.8), 2) scattered and interpolated filtered VARs, sector means (black points of Fig. 7.8 or Table 7.2), 3) scattered and interpolated rotation derived from strike vs. VAR laws (black lines of Fig. 7.10) following the equation determined only for the Balzes Anticline area (VAR= - 46° + 0.511 * strike) and 4) scattered and interpolated rotation derived from strikes (black lines of Fig. 7.10) following the equation manually determined for the entire South-Central Pyrenees (VAR = -60 + 0.67 * strike).

The first observation we can make, regarding the consistency of the method, is that results derived from scattered and interpolated data (piecewise restoration) are similar for all the initial rotation datasets. Therefore, the initial density of data is enough and the discrete smooth interpolation of gOcad is accurate.

Similarly, initial and filtered VARs (also scattered as interpolated) are equivalent datasets because they lead to comparable restoration maps (Figs. 7.12 A&B vs. C&D). Filtered VARs are smoother data that produce less extreme dilation patterns in the restored state.

Regarding the rotation datasets derived from the strike vs. VAR law, we may say that the precision of the strike vs. rotation law is not that determinant. The restored map using the equation calculated at regional scale (Balzes Anticline) extrapolated to the whole area does not differ much from the restoration using the properly calculated equation at tectonic scale (Figs. 7.13 A&B vs. C&D).

We have to answer now the most important question: are the rotation datasets derived from strikes equivalent to VARs? Before answering this question we need to know which restored map we have to pay attention to, because, in true and total fact, the piecewise restoration produces an important propagation error conditioned by the pin-line (although we have tried to select a significant portion of unrotated area).

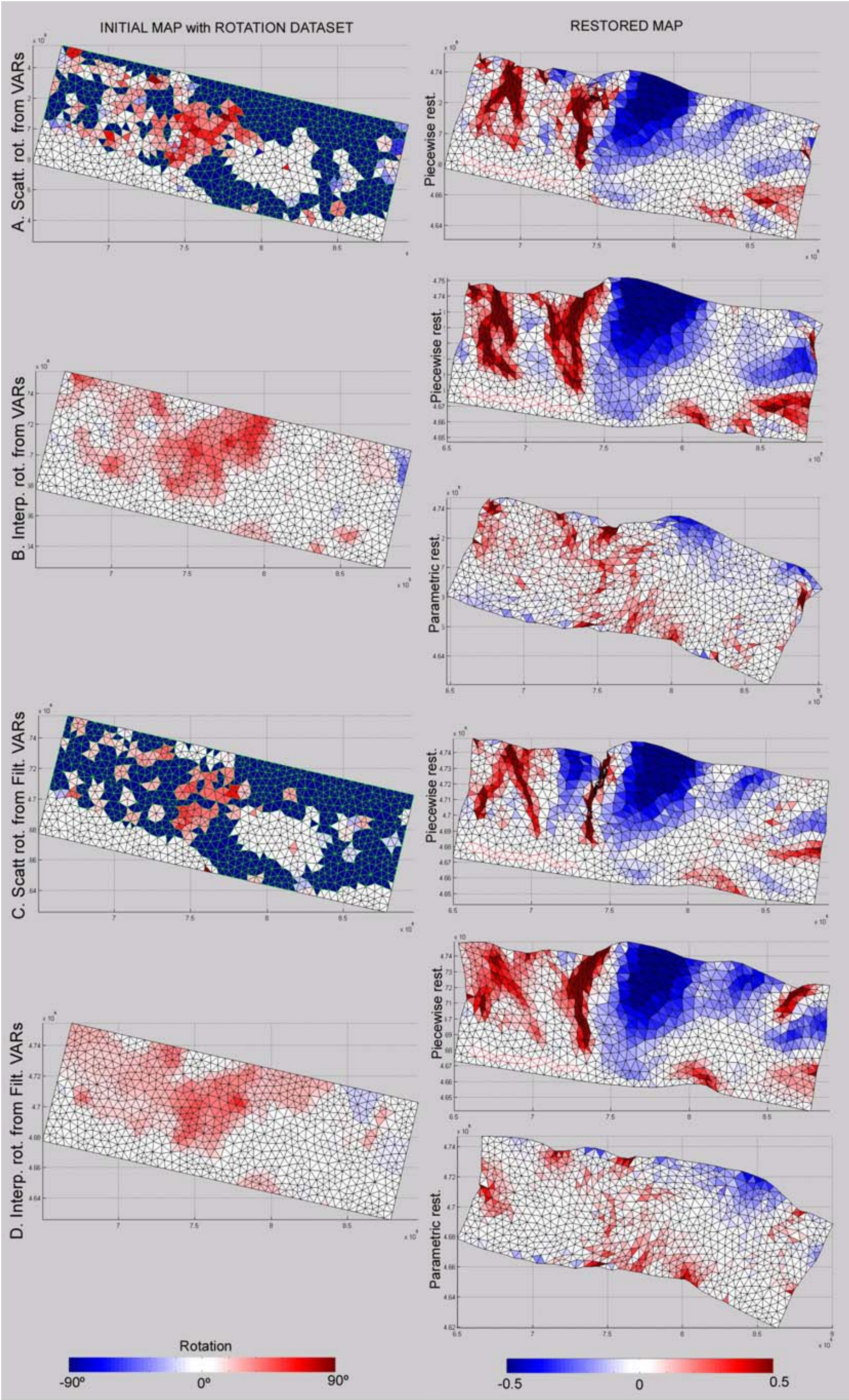

Figure 7.12: First column) Rotation datasets from VARs: A) scattered VARs, B) interpolated VARs, C) scattered filtered VARs and D) interpolated filtered VARs. Second column) Restored map with dilation.

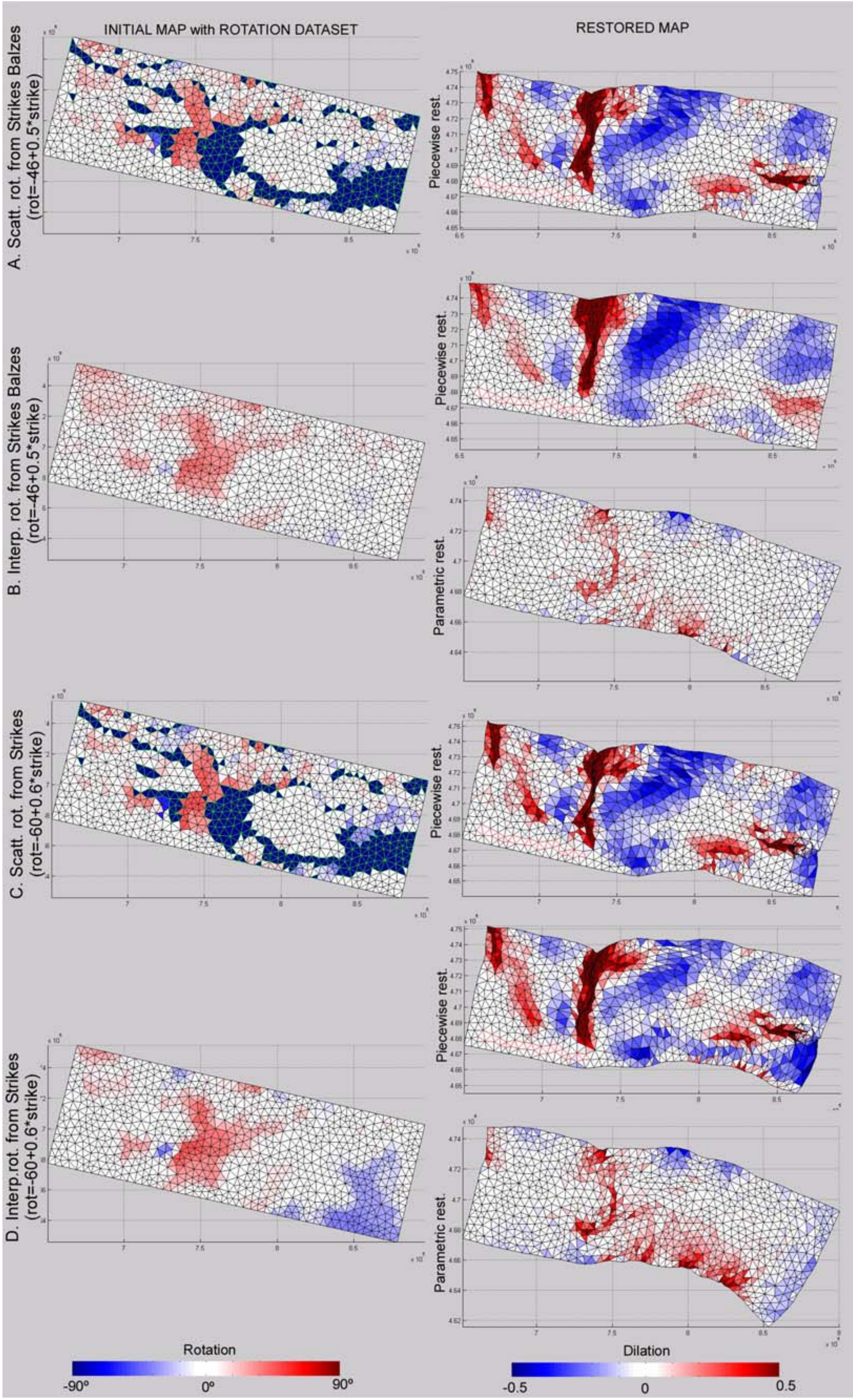

Figure 7.13: First column) Rotation datasets from the strike vs VAR law A&B) following the equation determined for the Balzes Anticline and C&D) following the equation determined for the South Central Pyrenees. Second column) Restored map with dilation.

Thus, parametric restoration seems more reliable. Hopefully, we observe how restored maps using VARs are similar to those using strikes (Fig. 7.12 vs. 7.13). Therefore, we have reached a positive answer to the initial question. Considering the two restoration techniques separately, we have obtained very similar results independently of the initial rotation database. This is very important, because a solid strike vs. VAR law can be very useful in cases with less abundant data.

Hereafter, and considering the previous evidences, we only use the interpolated rotation dataset derived from strikes using the law calculated at tectonic scale. We want to check the influence on the limits of the selected area to restore in the boundary effects. To do so, we use considered an extended mesh in addition to the one used before, both of them displayed in Figure 7.11. Interpolated rotation datasets are slightly different but may not have significant effects (Fig. 7.14).

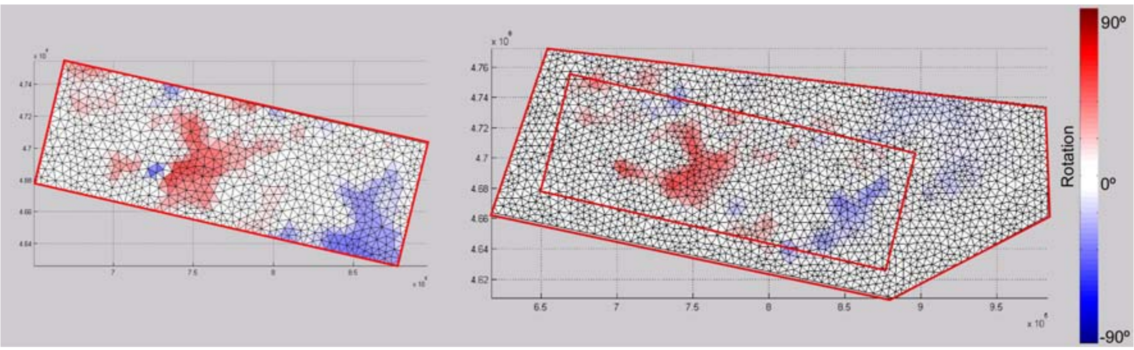

Figure 7.14: Parametric restoration; two initial meshes with the rotation dataset derived from strikes.

Now we want to establish the differences between both restoration techniques. Piecewise restoration (Fig. 7.15A) is extremely conditioned by the pin-area in both meshes. That is particularly observable in the vector displacement map where longer vectors are in the opposite side to the pin. On the other side, both meshes share a main positive dilation area (red line on the figure). However, the mesh with higher area displays a well-defined positive dilation area at the eastern edge of the SPCU and this is not present in the other mesh. On the contrary, parametric restoration (Fig. 7.15B) gives relatively similar results for both meshes. On one side, the dilation close to the borders could be questionable. On the other side, both restored maps share two main positive dilation areas (red lines on the figure) and now there are not significant differences between them.

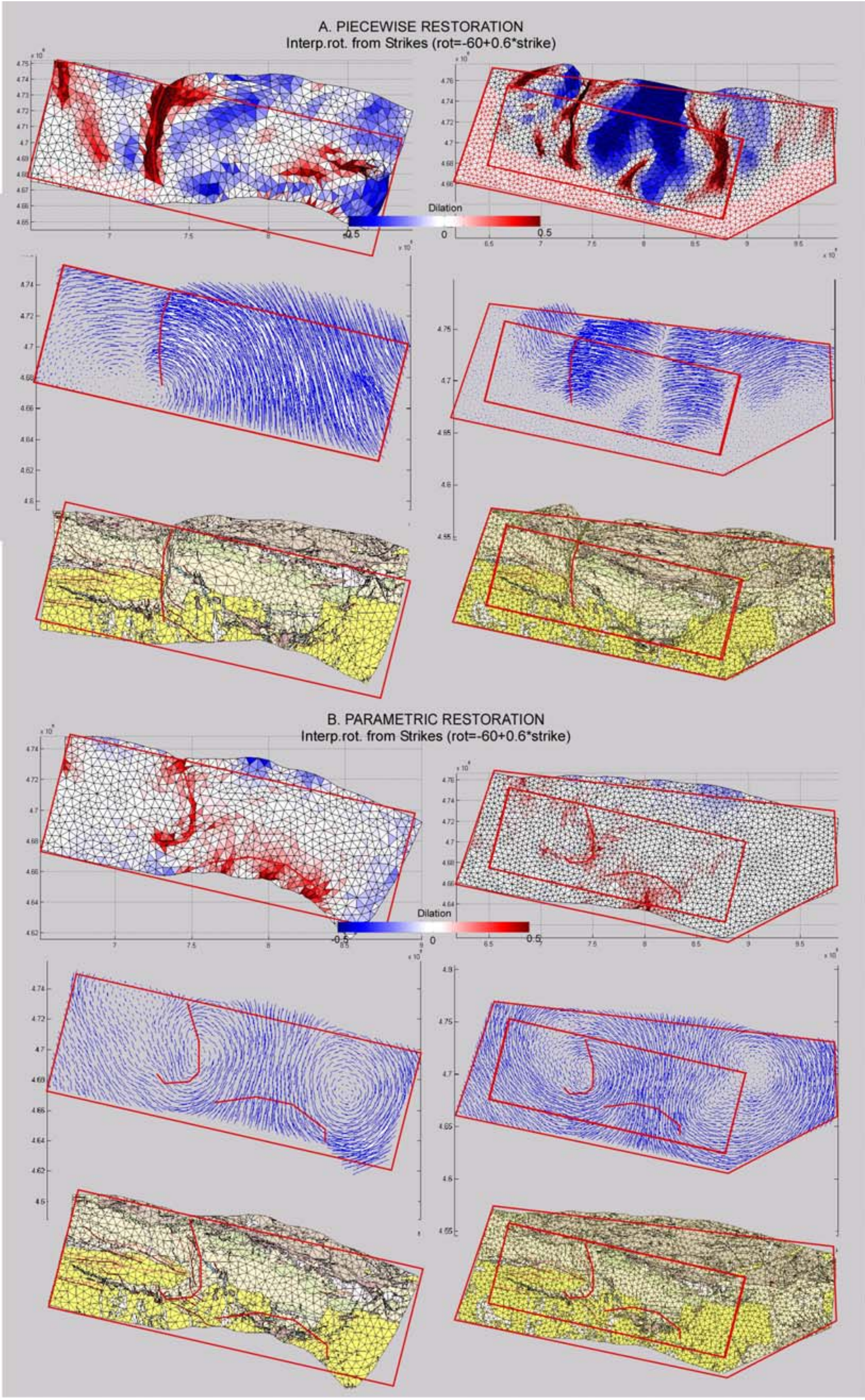

Figure 7.15: Restoration using the rotation dataset from strikes for two initial meshes: dilation pattern, displacement vector and cartographic map in restored state. A) Piecewise restoration. B) Parametric restoration.

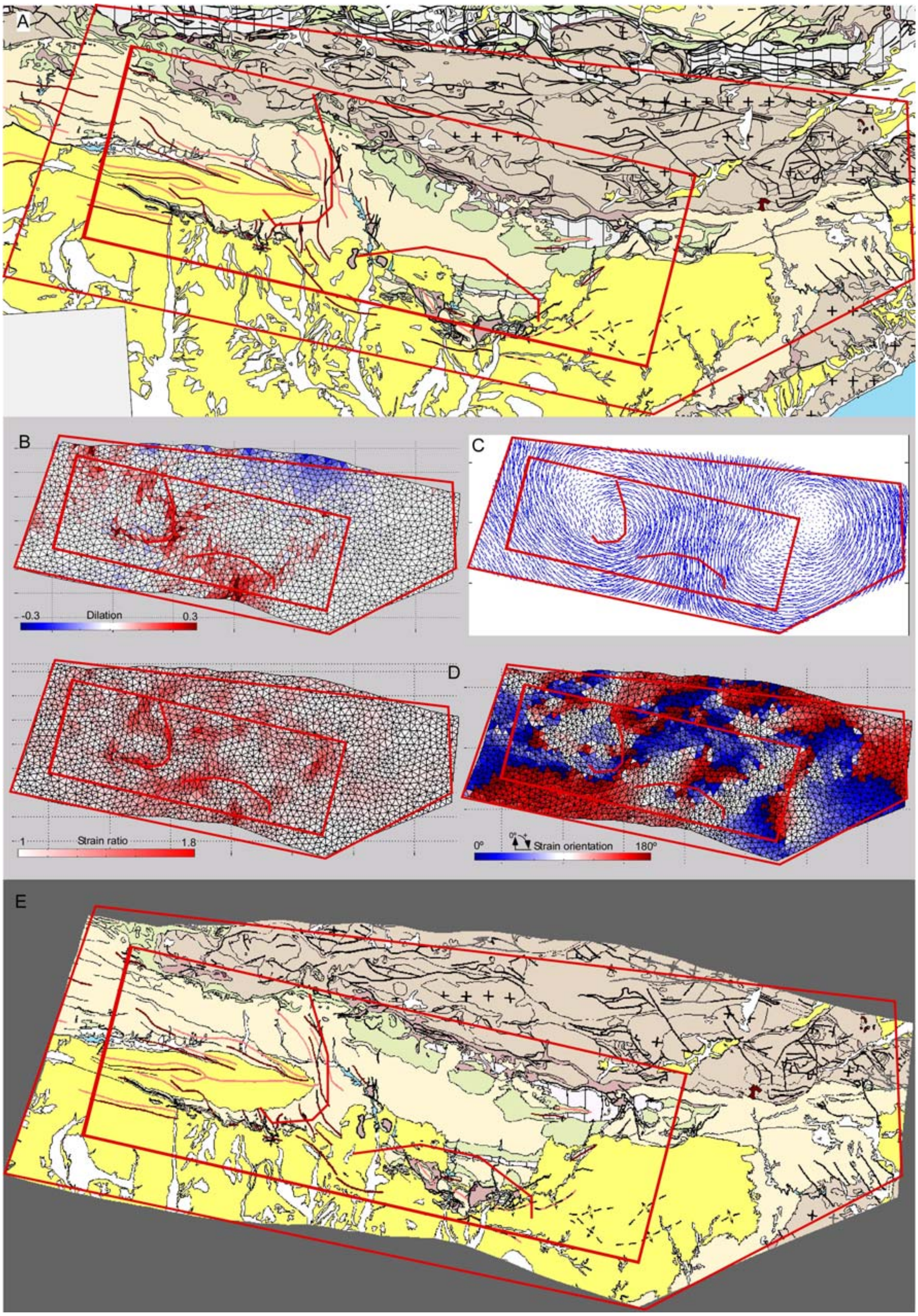

Figure 7.16: Parametric restoration using the rotation dataset from strike vs. VAR law and the densest mesh: A) initial map, B) dilation pattern, C) displacement vector, D) strain ellipse (ration between major and minor axis and orientation of major axis) and E) cartographic map in restored state.

7.2.2D Geological meaning of the restoration

In order to evaluate the geological meaning of the map-view restoration we consider all the aforementioned conclusions: 1) Parametric instead of piecewise restoration. 2) VARs derived from the strike law interpolated with the DSI of gOcad, which yields an evenly distributed dataset. 3) An extended mesh on the initial map to minimize border effects.

Positive dilations (Fig. 7.16B) are mostly located in the Western Pyrenees. The most significant dilation overlaps the External Sierras and the Ainsa oblique zone, although the Internal Sierras can also be delineated with this pattern. Besides, this highest dilation zone is located in the inner arc of the oblique structures, where maximum lateral shortening had to take place. This is what we should expect, although dilation has a sign opposite to the expected (extension instead of compression during the deformation process). We must take into account that the restoration method does not retro-deform the frontal displacement. The most strongly rotated structures have no space to be accommodated during the restoration because the foreland is undeformed. Therefore, this dilation patterns simply locate the main areas of out-of-plane motions. Additionally, there is another positive dilation area related to the Marginal Ranges frontal units, but this is likely related to the absence of real frontal structures in this domain (several diapirs, Estopiñan oblique syncline etc). However, this area as well as the central northern sector (blue area) could be affected by border effects. The eastern SPCU edge seems to be much less important than the equivalent western border; this is somehow reasonable since rotations are much more moderate in that sector.

Displacement vector field (Fig. 7.16C). Perfectly delineates the center of the SPCU, where very small VARs have taken place. This field displays a main N010E displacement direction, which is comparable with the expected one in frontal structures (N000E). The two symmetric vortexes locate the main Pyrenean oblique zones at both edges of the SPCU. The western one is much more pronounced than the eastern one

It is worth noticing that the real displacement field would be the result of the addition of the frontal displacement (not restored by our method) to our restoration result, which in fact would present a more clear N-S pattern. Figure 7.16C only displays the displacement field related to the lateral gradient of shortening.

Anisotropy of deformation (Fig. 7.16D) presents limited geological meaning since translations are not considered in the restoration process and dilation patterns display opposite signs.

Despite this map does not represent the complete retro-deformation (just the VAR removal) some important paleo-geographical consequences are derived:

1) The apparent E-W transition between platform and talus facies found in the present coordinate system in the Ainsa oblique zone seems to display a more logic NNW-SSE orientation in our restored map.

2) An apparent continuity or, better saying, alignment is observed when comparing the restored front location of the External and Marginal Sierras.

3) Our map, gives an idea of the initial oblique geometry of the thrust front before any rotation took place. This structural trend is consistent with the expected shortening direction at that time.

7.3 Conclusions

This new map-view approach aims to unravel the vertical axis rotations (VARs) occurred during a "narrow" window of time. Of course, it is an inaccurate restoration because only VARs, and not displacement fields and anisotropies, are considered. On the other hand, this restoration leads to an approximate pre-rotational map in which we can appreciate the problems of space.

The application to the two case studies allows us to state some practical conclusions about the method:

- The selection of an appropriate and well delimited area is important to avoid undesirable errors on the borders. Ideally, the map should be surrounded by an unrotated area. And this is likely and important drawback of the restoration of the Southern Pyrenees that we have performed.

- The mesh density must be related to the initial rotation data density.

- The discrete smooth interpolator of gOcad is a proper tool to extend the scarce rotation data to the whole map.

- A solid strike vs. VAR law allows the usage of structural trends to determine the rotation data. This is very useful in cases with fewer paleomagnetic data.

- The parametric restoration is more consistent than the piecewise restoration, particularly because it is independent from the pin-element.

Future work must be done to obtain a correct restored map. The implementation of translations in the method is essential. This implies tackling the problem of discontinuous deformation, thrusting and major faults.

8 Conclusions

This thesis proposes paleomagnetism as a primary source of information in restoration methods. The usage of paleomagnetism is particularly relevant for complex geometries found in fold and thrust belts like non-cylindrical, non-coaxial or areas undergoing vertical axis rotations. We have opened up this avenue showing promising results in two surface restoration methods valid for globally developable surfaces (flexural unfolding). Moreover, we introduce a first approach of a new map-view restoration algorithm to unravel the vertical axis rotations at regional and tectonic scale.

8.1 Analog models

Analog models are a very useful tool in many ways. In this thesis we use geometric static simulations to test restoration methods, and we show their capabilities to analyze deformation patterns. A reference system drawn in the models allows us to compare the geometry before and after the deformation process. We can observe the real deformation calculating the dilation (change of volume or area in surfaces) and the strain ellipsoid in all grid cells. We show these models are useful to calculate the expected orientation of any linear element, particularly for understanding paleomagnetic vectors, to determine deformation patterns of surfaces and to obtain the distribution of the strain tensors in 3D.

The digitalization of analog models is not an obvious task. We leveraged two techniques: photogrammetry, more precise for surface reconstruction, and CT scanning for structures in 3D, where models are built up from a series of CT slices treated as seismic sections using geological software. Deformation mechanisms can be reproduced depending on the scaling and the rheology of the materials employed in the model. The model resolution can be tuned as required by changing the density of an orthogonal reference system and the density of CT slices. Sheets of EVA (ethylene vinyl acetate) were selected to build the analog models because this material provides enough radiological contrast and presents an appropriate and diverse rheology to simulate active folds. The screen-printing of lines with different thicknesses of minium paint allows a suitable orthogonal reference system to be set up.

We have produced two idealistic simple models inspired in complex geometries from External Sierras (Pyrenees). The San Marzal Pericline is the western termination of a conical fold (the Sto. Domingo Anticline). The Balzes Anticline is a curved fold. Both examples are used to test the restoration methods, but additionally, the Balzes model is used to show the capabilities of the modelization technique. We successfully compare one of the grid lines of the model with real paleomagnetic data in the northern and southern sides of the anticline. The deformation analysis identifies dilation of opposite senses in upper and lower surfaces, with higher magnitudes in areas of compression. Surface anisotropy reflects a perpendicular orientation of the main axis with respect to the fold axis in the anticlines. Volume anisotropy is smaller, although it is possible to distinguish horizontal ellipsoids in the upper volume and vertical ellipsoids in the lower one.

CT scan models have additional applications. They can be used to check the reliability of automatic reconstruction methods because they can be designed to achieve a high level of accuracy (e.g. by closely spacing the radiological slices). They can also be used to leverage partial or biased information, but in this case the geometrical and geomechanical properties must be properly scaled to identify the materials, model stratigraphic volumes and to reproduce the mechanical properties of rocks. Likewise, CT scan models allow validating 3D restoration methods and the reliability of other software because the geometry and kinematics of the model are perfectly known, and the geometry of the undeformed state is also fixed. Finally, the proposed technique could also be applied to sandbox or centrifuge analog models to monitor the strain pattern over time (4D).

8.2 Surface restoration methods

The main part of this thesis is the modification of two unfolding algorithms to include the paleomagnetic constraint with the purpose of reducing the uncertainty of geological reconstruction. The first method is based on a piecewise approach (Gratier et al., 1991 and Gratier and Guillier, 1993) in which paleomagnetism determines the rotation (code developed in Matlab). The second one is based on a parametric approach (Massot, 2002) and paleomagnetism determines the initial solution (code modified in gOcad).

We must remember three initial assumptions before any valuation of the restoration methods developed: firstly, the horizontality of the initial surface, secondly, the developability of the folded surface (Gaussian curvature equal to zero everywhere), and finally, a sufficient set of primary and passive paleomagnetic vectors. The first assumption is forced by most restoration methods; we transform the 3D coordinates into 2D by flattening the triangles in the first restoration method, and by parameterization in the second. The third assumption is an initial condition: if paleomagnetism is not reliable data results become uncertain. We should use only certain initial data.

The second assumption (developability of folded surface) is more delicate because we only fulfil it partially. For non-complex developable surfaces no method present difficulties; if there is no deformation during the folding process, the unfolding is performed successfully. However, we suggest the usage of these methods to restore globally developable surfaces in which specific deformation has taken place in some areas (global conservation concept). The restoration process treats the surface as if it were developable because it tends to minimize the deformation everywhere (minimizing distances between common vertices in the piecewise approach and seeking an orthonormal parameterization in the second approach). Therefore, the resultant deformation parameters from restoration would never match exactly the real ones, although in a good restored surface they may indicate real deformation areas in those parts where the restoration process presents more problems.

In order to evaluate the methods, we have performed several simulations with the two analog models developed: the conical structure (San Marzal) and the curved fold structure (Balzes). In the case of the parametric approach it is clearly observable in both examples that the restoration with paleomagnetism considerably improves results, and that otherwise the restoration is unable to reach the initial rectangular shape of the surface. At first glance, the usage of paleomagnetism is not that determinant for the piecewise approach, particularly for the complex example of Balzes for which this restoration technique presents some limitations.

Overall tough, restoration with paleomagnetism better locates the deformation areas. Moreover, it is less sensitive to the pin-element location (starting point of the restoration), which really conditions the result in the piecewise restoration without paleomagnetism. A good location of the pin-element may be an undeformed area (but not the border) in order to do not mask deformation but avoid propagation errors. On the other hand, the parametric approach is not conditioned by this variable, which is a strong point. Additionally, we performed mesh-sensitivity tests, but density and mesh type do not condition the results as much as the pin-element. In any case, the usage of paleomagnetism always improves the results.

We also introduce the multi-surface restoration as a first approach to real 3D restoration. For the best restoration of the Balzes model (parametric approach with paleomagnetism oblique to the main structures) we appreciate differences between the upper and lower surfaces according to the real outer hinge dilation and inner hinge contraction of the structure. This is a good starting point, especially if we compare the results with a real volumetric restoration. We have restored the structure with a geomechanical tool (Dynel3D) being unable to reach the expected rectangular shape of the initial surface.

In a real scenario, paleomagnetism is defined with a certain degree of error and in scattered sites of the outcrop, (not in all points of the surface). This uncertainty reduces the precision of the proposed restoration methods. Therefore, in addition to improve the quality of the initial paleomagnetic data (see Section 7.4), we propose the interpolation of data. We define an interpolation algorithm based on the developability of the surface to propagate paleomagnetic data to the entire surface. The rationale behind is that restoration with interpolated data is common or mandatory in methods like the parametric approach, and therefore it can work in the case of exploiting paleomagnetic data in real-world cases. We also consider paleomagnetic data defined with an angle of error (α_{95}). Thanks to the interpolation algorithm, this error hardly affects the results. A drawback is that the initial orientation of paleomagnetism slightly conditions the deformation patterns obtained with restoration. Hence, restoration results must be always carefully evaluated.

Summarizing, we encourage the usage of reliable paleomagnetic data in restoration methods, particularly for complex structures that underwent non-cylindrical or non-coaxial VARs. We propose the parametric restoration for surfaces folded under flexural conditions. The piecewise approach is more sensitive to certain input parameters but greatly improves when using paleomagnetic data. However, we must keep in mind that the deformation patterns of restoration are just indicative and do not show the real deformation, because they depend on the initial assumptions of the simplified restoration method which is applied.

8.3 Map-view restoration

In addition to surface restoration we propose the usage of paleomagnetism in map-view restoration techniques. Particularly, we extend the usage of the previous methods with this purpose. This is a first approach in which we apply the piecewise and parametric approach in map-view (2D) with only one single constraint, the rotation data. This initial dataset can be interpolated from scattered vertical axial rotations (VARs) or derived from structural trends with a rotation law. The best approach to run this restoration is the parametric method using the interpolated dataset derived from strikes.

We apply this technique in two case studies: the Balzes Anticline at regional scale and the South Central Pyrenees at tectonic scale. The geological meaning of the restoration is limited because lateral translations are not considered. However, we can get an idea of the pre-rotational moment showing the areas that have undergone the maximum deformation.

8.4 Paleomagnetism

As we have already mentioned, we must make sure that the paleomagnetic data we want to introduce in the restoration methods are reliable. In this way, we have followed two work lines (described in the appendices): achieving the optimal information from paleomagnetic analysis, and characterizing structural paleomagnetic errors. In the first line, we have developed the program VPD and proved it is a useful tool to obtain a global view of the paleomagnetic behavior of a site. It is particularly useful when dealing with homogeneous and large data sets because it allows a rapid estimation of the characteristic remanent component. Moreover, an automatic calculus of the demagnetization interval is proposed. Besides the "virtual directions" approach, the program implements the classical method of principal component analysis and others more automatic: the stacking routine and the linear spectrum analysis, which is very useful to compare results.

On the other hand, paleomagnetic vectors are biased by numerous sources of scattering but we mathematically describe here three particular cases with structural control: overlapping of vectors, internal deformation (shear) and errors restoring superposed folds. Overlapping of vectors produces declination and inclination errors controlled by the secondary vector and the magnitude of overlapping, as well as the structural position. Simple shear affects paleomagnetic vectors at the flanks of the folds producing declination and inclination errors controlled by the shear as well as the structural position. The geometry of a superposed fold is equivalent to a tilting fold, but standard restoration of paleomagnetic vectors (simple bedding correction) is different and not considering it causes declination errors controlled by the tilting of the two steps of foliation. Error characterization is of great help for the identification of the sources of error and later correction.

8.5 Further developments

The usage of sparse paleomagnetic data in restoration methods is conditioned by the interpolation of this data. Therefore, we need to pay attention to the interpolation algorithm trying to improve it. Moreover, the parametric approach can be improved by adding the possibility to run it with scarce initial data.

In this work we have only considered surface restoration methods and not real 3D. Next step should be including in the restoration fault discontinuities and not only isolated surfaces, without losing sight of 3D restorations. Besides, we have only considered static restorations because paleomagnetism is known in the initial and final state, and a next step here should be to consider the time variable.

In any way, it seems important to evaluate and numerically quantify the differences between the different restoration methods available.

Concerning the analog models, we already suggested that they can be used to test any restoration and reconstruction algorithm and software. In this thesis, they have been the key-stones to validate our methods. On the other hand, we can not forget that restoration methods are designed for geological reconstructions of the subsurface, thus, we should test them with real examples and not only with models. Therefore, next step will be to perform the restoration at the Balzes Anticline structure where a dense set of paleomagnetism is available (Rodriguez-Pintó et al., 2012) as well as the reconstruction of some starting horizons (Calvin et al., in preparation).

Following the goodness of analogs, we think about building a catalog of complex geometries based on CT simulations. Moreover, we do not forget the aforementioned possibility of adding the time variable and build dynamic models (4D).

In the line of the map-view restoration proposed, it is important to remind the need of the implementation of translations in the method considering thrusts and major faults.

Conclusiones

Con esta tesis pretendemos abrir una nueva puerta a los modelos de restitución existentes: proponemos la incorporación del paleomagnetismo como variable de entrada para reducir así el número de incertidumbres. En concreto, en este trabajo hemos incorporado el paleomagnetismo a dos métodos de restitución de superficie válidos para desplegar superficies globalmente desarrollables. El uso del paleomagnetismo es especialmente relevante en la restitución de estructuras de geometrías complejas (no cilíndricas, no coaxiales o afectadas por gradientes laterales de acortamiento) donde los métodos existentes suelen presentar serias limitaciones. Adicionalmente, proponemos un método de restitución cartográfica con el objetivo de deshacer las rotaciones de eje vertical a escala tanto regional como tectónica.

1 Modelos análogos

Para poder evaluar los resultados de los métodos de restitución se han desarrollo modelos análogos. Estos modelos son una herramienta muy útil en muchos aspectos y nos pueden servir para analizar cualquier patrón de deformación. Para ello se dibuja un cuadrícula en cada capa del modelo a modo de sistema de referencia; ésta nos permite caracterizar el modelo de forma completa antes y después de la deformación. Para cuantificar la deformación se calcula para cada celda la dilatación (cambio de volumen o área en superficie) y el elipsoide de deformación. De esta manera, los modelos son de gran utilidad para determinar tanto la orientación de cualquier elemento lineal como puede ser el paleomagnetismo, como los patrones de deformación en superficie y volumen.

Una vez construidos los modelos, la digitalización de los mismos no es una tarea sencilla. En este trabajo proponemos dos técnicas: la fotogrametría para la reconstrucción de superficies y el escáner de rayos X para la reconstrucción de volúmenes a partir de secciones. La primera es más precisa pero únicamente nos permite reconstruir la superficie superior del modelo. Los modelos análogos son válidos para reproducir cualquier tipo de mecanismo de deformación modificando la reología y escalado de los materiales utilizados. Para el desarrollo de pliegues flexurales hemos utilizado planchas de goma EVA. El sistema de referencia se ha serigrafiado en las distintas planchas con pintura de minio puesto que presenta un buen contraste radiológico.

Mediante esta técnica se desarrollan dos modelos sencillos inspirados en estructuras complejas que encontramos en los Pirineos: un pliegue cónico basado en el cierre periclinal de San Marzal y un pliegue curvo basado en el anticlinal del Balzes. Ambos ejemplos los utilizamos para evaluar los métodos de restitución, pero además hacemos una descripción completa del modelo del Balzes para mostrar las posibilidades que pueden ofrecer estos modelos. Se compara coherentemente una de las lineaciones del sistema de referencia con el paleomagnetismo real al norte y sur del anticlinal. Mediante el análisis de deformación en superficie se observa dilatación en la parte exterior del anticlinal y compresión en la interior siendo ésta de mayores magnitudes y se observa como la orientación de la deformación es perpendicular al eje de pliegue. La anisotropía volumétrica, en este caso, es menor debido probablemente al escaso espesor modelizado, sin embargo se pueden observar elipsoides horizontales en el volumen superior y verticales en el inferior.

Estos modelos tienen además aplicaciones adicionales. Son una herramienta muy útil para evaluar los métodos y programas de reconstrucción geológica puesto que son modelos en los que disponemos de tanta precisión como deseemos (disminuyendo el espaciado del sistema de referencia y de las secciones escaneadas). Además, la técnica del escaneado podría ser aplicada a modelos dinámicos de arena para ver la evolución en el tiempo y monitorizar la deformación en 4D.

2 Métodos de restitución de superficie

La parte principal de la tesis es la modificación de dos algoritmos de restitución de superficie para que incluyan la restricción del paleomagnetismo. El primer método está basado en la triangulación de la superficie y el paleomagnetismo determina la rotación de los triángulos (código desarrollado en Matlab). El segundo es una aproximación paramétrica en la que la solución inicial viene determinada por el paleomagnetismo (código modificado en gOcad).

Antes de pasar a evaluar los resultados debemos recordar los supuestos de partida en los que se basa el método: en primer lugar el estado inicial de la superficie se considera horizontal, en segundo lugar suponemos que las capas plegadas son desarrollables y por último asumimos que contamos con un conjunto suficiente de datos paleomagnéticos primarios que se comportan como vectores pasivos. La primera suposición de partida viene forzada por ambos métodos ya que se convierten las coordenadas 3D en coordenadas 2D; en el primer caso abatiendo los triángulos a la horizontal y en el segundo mediante la parametrización. La tercera suposición es una condición inicial, si los datos paleomagnéticos no son fiables se introduce error en el resultado de la restitución; sólo se deberían utilizar en el método aquellos datos que se sabe que son certeros.

En cuanto al segundo supuesto de que las superficies a desplegar son desarrollables vemos que es un poco más delicado porque es una condición que sólo se cumple de forma parcial; ya que hemos dicho que el método sirve para desplegar superficies globalmente desarrollables. Ninguno de los métodos presenta problemas a la hora de desplegar superficies sencillas completamente desarrollables; las dificultades aparecen cuando la superficie ha sufrido algún tipo de deformación normalmente en las zonas de mayor curvatura. Los métodos de restitución suponen superficies desarrollables y buscan minimizar la deformación (minimizando la distancia entre los vértices comunes en el primer método y con una parametrización ortonormal en el segundo). Por ello, la deformación resultante de la restitución no va a ser nunca la restitución real; sin embargo, en una buena restitución sí que va a ser un indicador de cuáles son las áreas que han sufrido una mayor deformación, ya que son las zonas que presentan mayor dificultad para ser desplegadas.

Para poder evaluar los métodos de restitución se han hecho una serie de simulaciones con los dos modelos análogos desarrollados: el pliegue cónico (San Marzal) y el pliegue curvo (Balzes). En la restitución paramétrica se observa claramente como los resultados mejoran al utilizar los datos paleomagnéticos; en caso contrario, el método no es capaz de alcanzar la superficie rectangular inicial. Los resultados no son tan evidentes para el otro método de restitución basado en la triangulación, especialmente para el modelo más complejo, el del Balzes, para el que aparecen ciertas limitaciones del método, tanto con, como sin paleomagnetismo. Sin embargo, vemos como para el modelo de San Marzal, la restitución con paleomagnetismo es capaz de localizar las zonas de deformación mientras que éstas quedan diluidas en la restitución sin paleomagnetismo.

Más importante es que el método con paleomagnetismo es mucho más estable a las distintas localizaciones del punto de inicio por el que se empieza a desplegar la superficie (pin-element). De todas formas, es bueno elegir este punto de inicio en una zona no deformada de la superficie pero que no esté muy cercana al borde; esto es para que no se enmascare la posible deformación real de la superficie y para evitar errores de propagación. Por otro lado, una ventaja importante del segundo método de restitución con paleomagnetismo, aproximación paramétrica, es que no es sensible a este punto de inicio. Se han hecho también pruebas con diferentes densidades de malla y tipos de mallado pero vemos que no condicionan tanto el resultado como puede hacerlo el punto de inicio.

Hasta ahora se ha considerado el paleomagnetismo definido en todos los puntos de la superficie, sin embargo, en un caso real, los datos paleomagnéticos provienen de estaciones aisladas de afloramientos puntuales. Es por ello que se desarrolla un algoritmo de interpolación para propagar el paleomagnetismo a toda la superficie y que pueda ser utilizado con relevancia en los métodos de restitución. Es alentador que los resultados utilizando los datos interpolados no difieren mucho de los obtenidos con el paleomagnetismo definido en todos los puntos, especialmente en el caso de restitución paramétrica. Además se ha definido un conjunto de datos iniciales definidos con cierto grado de error (α_{95}) para simular un escenario real. Gracias al algoritmo de interpolación (que en cierta manera promedia los datos) los resultados son bastante similares a los obtenidos con el paleomagnetismo definido de forma precisa. De cualquier modo, es importante asegurar un cierto grado de precisión en los datos de entrada (trabajo desarrollado en los apéndices que comentamos en la sección de paleomagnetismo). Un inconveniente es que la orientación inicial de los vectores paleomagnéticos afecta en cierta manera al resultado, variando ligeramente los patrones de deformación de la superficie restituida. Por lo tanto, es necesario siempre evaluar de forma crítica el resultado obtenido.

Finalizamos el estudio haciendo una restitución multi-superficie para compararla con una restitución 3D real. Restituimos la superficie inferior y superior del modelo del Balzes con el método de restitución paramétrica y utilizando los datos paleomagnéticos definidos de forma oblicua a las estructuras principales. Se pueden apreciar diferencias en los patrones de deformación de las superficies restituidas en concordancia con lo esperado; se observa dilatación en la parte exterior del anticlinal y contracción en la parte interna. Creemos que éste es un buen punto de partida previo a la restitución 3D y vemos de su necesidad al comprobar las limitaciones de los métodos de restitución volumétricos. Tratamos de restituir la estructura utilizando un programa de aproximación geomecánica (Dynel3D) sin lograr alcanzar la forma rectangular inicial de las capas.

Por todo ello, animamos a incluir datos paleomagnéticos certeros en los métodos de restitución, de forma especial para restituir estructuras complejas que hayan sufrido rotaciones. De forma concreta, proponemos el método de restitución paramétrica para desplegar superficies plegadas bajo condiciones flexurales. Vemos que el método basado en la triangulación es un poco más variable a ciertos parámetros de entrada, pero que también presenta mejoras al incorporar los datos paleomagnéticos. Sin embargo, no debemos olvidar en ningún caso que la deformación obtenida con la restitución es orientativa y no debe tomarse al pie de la letra ya que depende mucho del método de restitución utilizado.

3 Restitución cartográfica

De forma adicional a los métodos de restitución de superficie se recomienda el uso del paleomagnetismo en los métodos de restitución cartográfica. En concreto, lo que hemos hecho en este trabajo, ha sido extender el uso de los métodos desarrollados para superficie y aplicarlos en restitución cartográfica (2D). Se ha utilizado el método de restitución basado en la triangulación de la superficie y el basado en la parametrización para restituir un mapa con el único criterio de deshacer las rotaciones de eje vertical (sin tener en cuenta pliegues, cabalgamientos o fallas). Los datos de rotación se pueden obtener directamente de variaciones de eje vertical (VARs) o inferidos a partir de trazas estructurales por medio de una ley que relacione la dirección de la traza con el VAR. Los datos iniciales son interpolados para que tengan una mayor influencia en la restitución y puedan ser aplicados en ambos métodos. De nuevo, el método que mejor funciona, es el basado es la aproximación paramétrica.

Esta técnica es una primera aproximación que hemos aplicado en dos casos reales a diferentes escalas: el anticlinal del Balzes y el sistema surpirenaico central. La restitución no va a ser en ningún caso el estado inicial de la estructura puesto que solo estamos teniendo en cuenta las rotaciones y no los desplazamientos ni las deformaciones. Sin embargo, esta restitución es útil para ofrecer una idea de cómo estaba la cartografía antes de la rotación (generalmente localizada en un corto espacio de tiempo) y ver así las zonas de máxima deformación..

4 Paleomagnetismo

Como hemos mencionado con anterioridad, es necesario matizar que para poder utilizar los datos paleomagneticos en los métodos de restitución con cierta credibilidad, es imprescindible que se asegure en primer lugar su fiabilidad. En esta línea hemos trabajado en dos direcciones (apéndices): 1) obtener la información óptima a partir de un análisis paleomagnético y 2) caracterizar un conjunto de posibles errores estructurales. En cuanto al primer punto, se desarrolla el programa VPD para tratar de sacar la mayor y mejor información de las rutinas de desmagnetización. En primer lugar nos permite ver y evaluar una estación de forma rápida, pero lo más importante es el uso que se le puede dar para determinar las componentes naturales (NRM) de estaciones homogéneas y con numerosas muestras. El programa calcula todas las direcciones virtuales (VD) de cada estación, así como los métodos tradicionales de análisis de componentes principales (PCA) y otros más automáticos como el promediado (SR) o el análisis espectral de linearidad (LSA); permitiendo así comparar resultados.

En cuanto a la caracterización de posibles fuentes de error que desvían el dato paleomagnético nos centramos en tres, todas ellas con control estructural: 1) solapaminto, 2) cizalla de flanco y 3) dos etapas de plegamiento. El solapamiento de un vector secundario produce errores de declinación e inclinación controlados por el grado de solapamiento y la posición estructural (eje del pliegue y magnitud de la rotación). La cizalla de flanco produce también errores de declinación e inclinación controlados por el grado de cizalla y la posición estructural. Dos etapas de plegamiento son equivalentes a un pliegue inclinado pero la restitución del vector paleomagnético a la horizontal no es equivalente en ambos casos produciendo errores de declinación al restituir el primer caso como el segundo. La descripción matemática de estos errores, aún cuando los dos últimos son únicamente modelos preliminares, es de gran ayuda para simular cualquier situación y ayudar a identificar las causas de error para su posterior corrección.

5 Futuras líneas de investigación

Para poder usar cualquier método de restitución que incluya paleomagnetismo en casos reales es importante tener en cuenta que contamos únicamente con datos aislados. Por ello es importante seguir trabajando en métodos para interpolar estos datos de entrada, así como mejorar los métodos de restitución para que sean más eficaces en estas circunstancias.

En este trabajo nos hemos centrado en métodos de restitución de superficie. El siguiente paso sería incluir discontinuidades de falla para un posterior salto a reconstrucciones volumétricas. Del mismo modo nos hemos centrado únicamente en restituciones estáticas considerando el estado inicial y final (ya que es donde se conoce el valor del dato paleomagnético), el salto en este aspecto sería considerar el tiempo (restituciones dinámicas).

Si nos fijamos en el método de restitución cartográfica propuesto, el siguiente paso está claro, es necesario incorporar tanto desplazamientos causados por plegamientos y fallas como posibles deformaciones.

En cuanto a los modelos análogos ya apuntábamos que pueden ser de gran utilidad a la hora de evaluar técnicas y programas tanto de reconstrucción como de restitución. Del mismo modo, es posible utilizar estos modelos para crear un catálogo de estructuras complejas. Por otro lado, no cabe duda de que los métodos deben funcionar en casos reales, para reconstrucciones geológicas del subsuelo y no únicamente para modelos, por tanto, sería interesante testarlos en un caso real. Se cuenta con mucha información relativa al anticlinal del Balzes por lo que apunta a ser una buena estructura modelo.

References

Adam, J., Schreurs, G., Klinkmüller, M., Wieneke, 2008. 2D/3D Strain localization and fault simulation in analogue experiments: insights from X-ray computed tomography and tomographic image correlation. Boll. di Geofisica, 49, 21-22.

Allaby, A. and Allaby, M., 1999. A dictionary of earth sciences. Oxford University Press, 619 pp. ISBN 0192800795, 9780192800794.

Allerton, S., 1994. Vertical axis rotations associated with folding and thrusting: an example from the eastern Subbetic, southern Spain. Geology, 22 (11), 1039–1042.

Allmendinger, R.W., Cardozo, N., Fisher, D.M., 2012. Structural Geology Algo- rithms: Vectors and Tensors. Cambridge University Press.

Almela, A. and Ríos, J.M., 1951. Mapa Geol. de España 1:50.000, serie antigua, hoja nº 248 (Apiés). I.G.M.E. Ed., Madrid: 94 pp., 1 mapa.

Anastasio, D. J., 1992. Structural evolution of the External Sierra, Southern Pyrenees, Spain. In: Structural Geology of Fold and Thrust Belts (Ed. S. Mitra & G.W. Fisher) Johns Hopkins Univ. Press, 239-251.

Anastasio, D.J. and Holl, J.E., 2001. Transverse fold evolution in the External Sierra, southern Pyrenees, Spain. Journal of Structural Geology, 23, 379-392.

Arenas, C., 1993. Sedimentología y paleogeografía del Terciario del margen pirenaico y sector central de la Cuenca del Ebro (zona aragonesa occidental). Tesis Doctoral, Universidad de Zaragoza, 858 pp.

Arenas, C., Millán, H., Pardo, G., Pocoví, A., 2001. Ebro Basin continental sedimentation associated with late compresional pyrenean tectonics (NE Iberia): controls on margin fans and alluvial systems. Basin Research, 13, 65-89.

Arriagada, C., 2004. Rotations tectoniques et déformation de l'avant arc des Andes centrales au cours du Cénozoïque. Mémoires de Géosciences-Rennes, 107, 1-308.

Arriagada, C., Roperch, P., Mpodozis, C., Cobbold, P., 2008. Paleogene building of the Bolivian Orocline: Tectonic restoration of the central Andes in 2-D map view. Tectonics, 27, TC6014; 14 p. doi: 10.1029/2008TC002269.

Audiber, M., 1991. Déformation Discontinue et Rotations de Blocs, Méthodes Numériques de Restauration, Mém. Doc. Cent. Armoricain Etud. Struc. Socles, 40, 239 pp., Géosci, Rennes, France.

Bailey, R.C. and Halls, H.C., 1984. Estimate of confidence in paleomagnetic directions derived from mixed remagnetization circle and direct observatio-nal data. Journal of Geophysics, 54, 174-182.

Barberá, X., 1999. Magnetoestratigrafia de líOligocé del sector sud-oriental de la conca de líEbre: implicacions magnetocronolÚgiques i seq¸encials. Tesis doctoral, Univ. de Barcelona, 247 p.

Barberá, X., Parés, J. M., Cabrera, L., Anadón, P., 1994. High resolution magnetic stratigraphy across the Oligocene-Miocene boundary in an alluvial-lacustrine succession (Ebro Basin, NE Spain), Phys. Earth Planet. Inter., 85, 181-193.

Barberá, X., Cabrera, L., Marzo, M., Parés, J. M., Agustí, J., 2001. A complete terrestrial Oligocene magnetobiostratigraphy from the Ebro basin, Spain. Earth Planet. Sci. Letters, 187, 1-16.

Barnolas, A. and Teixell, A., 1994. Platform sedimentation and collapse in a carbonate-dominated margin of a foreland basin (Jaca basin, Eocene, southern Pyrenees). Geology (ISSN: 0091-7613), 22, 1107-1110.

Barnolas, A. and Gil.Peña, I., 2001. Estructura secuencial del relleno sedimentario de la Cuenca de antepaís surpirenaica y su relación con la evolución del orógeno. Geotemas, 2, 37-41.

Barnolas, A., Gil-Peña, I., Alfageme, S., Ternet, Y., Baudin, T., Laumonier, B., 2008. Mapa geológico de los Pirineos a escala 1:400 000. IGME/BRGM ISBN: 978-2-7159-2168-9.

Barnolas, A., Samsó J.Mª., Malagón, J., Gil-Peña, I., Montes, M., Rico, M., (in press).- Mapa geológico y memoria de la Hoja nº 249, Alquezar, del Mapa Geológico de España a escala 1:50.000 (MAGNA). Instituto Geológico y Minero de España, Madrid.

Bazhenov, M.L., 1988. Analysis of the resolution of the paleomagnetic method in solving Tectonic Problems. Geotectonics, 22 (3), 204-212.

Beamud, B., Garcés, M., Cabrera, L., Muñoz, J.A., Almar, Y., 2003. A new middle to late Eocene continental chronostratigraphy from NE Spain. Earth and Planetary Science Letters, 216, 501-514.

Beamud, E., Garcés, M., Muñoz, J.A., Cabrera, L., Almar, Y., 2004. Distribución de las rotaciones paleomagnéticas en la cuenca de Graus-Tremp durante el Terciario. Geotemas, 6 (4), 283-286.

Beamud, E., Muñoz, J.A., Fitzgerald, P.G., Baldwin, S.L., Garcés, M., Cabrera, L., Metcalf, J.R., 2011. Magnetostratigraphy and detrital apatite fission track thermochronology in syntectonic conglomerates: constraints on the exhumation of the South-Central Pyrenees. Basin Research, 23 (3), 309-331.

Bentham, P.A., 1992. The tectono-stratigraphic development of the western oblique ramp of the south-central Pyrenean thrust system, Northern Spain. Ph.D. University of Southern California, 253pp.

Bentham, P., Burbank, D.W., Puigdefábregas, C., 1992. Temporal and spatial controls on the alluvial architecture of an axial drainage system: Late Eocene Escanilla Formation, southern Pyrenean foreland basin, Spain. Basin Research, 4, 335-352.

Bentham, P and Burbank, D.W., 1996. Chronology of Eocene foreland basin evolution along the western oblique margin of the South-Central Pyrenees. In: Tertiary basin of Spain. Edit: Friend, P.F., Dabrio, C.J. Cambridge Univ. Press, pp. 144-152.

Bingham C., 1974. An antipodally symmetric distribution on the sphere. Ann. Statist., 2, 1201-1225.

Bonhommet N., Cobbold P.R., Perroud H., Richardson A., 1981. Paleomagnetism and cross-folding in a key area of the Asturian Arc (Spain). Journal of Geophysical Research, 86, 1873-1887.

Borradaile, G. J., 1997. Deformation and Paleomagnetism. Surveys in Geophysics **18:** 405–435, 1997.

Borradaile, G., and Mothersill, J., 1989. Tectonic strain and paleomagnetism: experimental investigation, Physics of the Earth and Planetary Interiors, 56, 254-265.

Bourgeois, O., Cobbold, P.R., Rouby, D., Thomas, J.C., Shein, V., 1997. Least squares restoration of Tertiary thrust sheets in map view, Tajik Depression, Central Asia. Journal of Geophysical Research, B, Solid Earth and Planets, 102 (12), 27553-27573.

Buddin, T.S., Kane, S.J., Williams, G.D., Egan, S.S., 1997. A sensitivity analysis of 3-dimensional restoration techniques using vertical and inclined shear constructions. Tectonophysics, 269 (1-2), 33-50.

Burbank, K.D.W., Hogan, P., King, M., Jolley, Z. J., 1987. Preliminary results of magnetostrati-graphic studies in the South Pyrenean foreland basin. Workshop of paleomagnetism in the Iberian Peninsula. Servei Geològic de Catalunya. Abstracts, 1-2

Burbank, D.W., Puigdefabregas, C., Munoz, J.A., 1992a. The chronology of the Eocene tectonic and stratigraphic development of the eastern Pyrenean foreland basin, Northeast Spain. Geological Society of America Bulletin, 104 (9), 1101-1120.

Burbank, D.W., Vergés, J., Muñoz, J.A., Bentham, P., 1992b. Coeval hindward- and forward- imbricating thrusting in the South-Central Pyrenees, Spain: Timing and rates of shortening and deposition. Geological Society of America Bulletin, 104, 3-17.

Butler, R.F., 1992. Paleomagnetism, Magnetic Domains to Geologic Terranes, Boston, Blackwell, 319 p.

Calvin, P., Casas, A.M., Rodríguez-Pintó, A., Pueyo, E.L., (2013 in prep). Kinematic implications of the geometry of the basal ramp in oblique zones; a case study in the Eastern External Sierras (Southern Pyrenees).

Cámara, P., Klimowitz, J., 1985, Interpretación geodinámica de la vertiente centro-occidental surpirenaica (Cuencas de Jaca-Tremp). Estudios geológicos, 41, 391–404.

Cardozo, N.; Allmendinger, R.W., 2013. Spherical projections with OSXStereonet. Computers & Geosciences 51, 193–205

Carlson, W.D., 2006. Three-dimensional imaging of earth and planetary materials. Earth and Planetary Science Letters, 249, 133–147.

Casas, A.M., Pardo, G., 2004. Estructura pirenaica y evolución de las cuencas sedimentarias en la transversal Huesca-Oloron. In: Itinerarios geológicos por Aragón (Edited by Colombo, F., Liesa, C.L., Meléndez, G., Pocovi, A., Sancho, C., Soria A.R.), Geo Guías (Sociedad Geológica de España), 1, 63-96 (ISBN: 84-930160-2-0).

Cascella, A., Dinarès-Turell, J., 2009. Integrated calcareous nannofossil biostratigraphy and magnetostratigraphy from the uppermost marine Eocene deposits of the southeastern Pyrenean foreland basin: evidences for marine Priabonian deposition. Geologica Acta, 7,

Caumon, G., Collon-Drouaillet, P., Le Carlier De Veslud, C., Viseur, S., Sausse, J., 2009. Surface-based 3D modeling of geological structures. Mathematical Geosciences, 41 (8), 927–945.

Chamberlin, R.T., 1910. The Appalachian folds of central Pennsylvania. Journal of Geology 18, 228–251.

Chan, L.S., 1988. Apparent tectonic rotations, declination anomaly equations and declination anomaly charts. Jour. Geophys. Res., 93, B10, 12151-12158.

Choukroune P. and Séguret, M. 1973. Carte structurale des Pyrénées, 1/500.000, Université de Montpellier -ELF Aquitaine

Choukroune, P. and ECORS team, 1989. The ECORS Pyrenean deep seismic profile reflection data and the overall structure of an orogenic belt. Tectonics, 8 (1), 23-39.

Cioppa, M.T. and K.P. Kodama, Evaulation of paleomagnetic and finite strain relationships due to the Alleghanian Orogeny in the Mississippian Mauch Chunk Formation, Pennsylvania, J. Geophys. Res., 108, B2, EPM8, 1-16, 2003.

Cobbold P.R. and Percevault M.N., 1983. Spatial integration of strains using finite elements. Journal of Structural Geology, 5, 299-305.

Cogné, J.P. and Perround, H., 1985. Strain removal applied to paleomagnetic directions in an orogenic belt: the Permian red slates of the Alpes Maritimes, France. Earth Planet. Sci. Lett., 72, 125-140.

Colletta, B., Letouzey, J., Pinedo, R., Ballard, J.F., Balé, P., 1991. Computerized X-ray tomography analysis of sandbox models: Examples of thin-skinned thrust systems. Geology, 19 (11), 1063-1067.

Cooper, M.A., 1983. The calculation of bulk strain in oblique and inclined balanced sections. Journal of Structural Geology, 5 (2), 161-165.

Costa, E., Garcés, M., López-Blanco, M., Serra-Kiel, J., Bernaola, G., Cabrera, L., Beamud, E., 2013. The Bartonian-Priabonian marine record of the eastern South Pyrenean Foreland Basin (NE Spain): A new calibration of the larger foraminifers and calcareous nannofossil biozonation. Geologica Acta. 01/2013; in press.

Costa, E., Garcés, M., Sáez, A., Cabrera, L., 2011. The age of the “Grande Coupure” mammal turnover: New constraints from the Eocene–Oligocene record of the Eastern Ebro Basin (NE Spain). Palaeogeography Palaeoclimatology Palaeoecology 01/2011; 301:97-107.

Costa, E., Garcés, M., Miguel López-Blanco, M., Beamud, E.; Gómez-Paccard, M., Larrasoaña, J.C., 2010. Closing and continentalization of the South Pyrenean foreland basin (NE Spain): magnetochronological constraints. Basin Research 12/2010; 22(6):904 - 917. ·

Dahlstrom, C.D., 1969. Balanced cross sections. Canadian Journal Earth Sciences, 6, 743-757.

De Federico, A., 1981. La sedimentación de talud en el sector occidental de la cuenca paleógena de Aínsa. Publ. de Geología, University of Barcelona, 12, 271 pp.

Delaunay B., 1934. Sur la sphère vide. Bulletin of the Academy of Sciences of the U.S.S.R., Classe des Sciences Mathématiques et Naturelle 7 (6), 793-800.

Dinarès-Turell, J. and McClelland, E., 1991. A cautionary tale for palaeomagnetists; a spurious apparent single component remanence due to overlap of blocking-temperature spectra of two components. Geophysical Research Letters, 18 (7), 1297-1300.

Dinarès, J., McClelland, E., Santanach, P., 1992. Contrasting rotations within thrust sheets and kinematics of thrust tectonics as derived from palaeomagnetic data: an example from the Southern Pyrenees. In: K.R. McClay (ed.), Thrust tectonics , pp. 265-276, Chapman & Hall Eds., London, 447 pp.

Dinarès, J., 1992, Paleomagnetisme a les Unitats Sudpirinenques Superiors. Implicacions estructurals. Tesis Doctoral. Universidad de Barcelona. 462 pp.

Dinarès, J. and Garcia-Senz, J., 2000. Remagnetization of Lower Cretaceous limestones from the southern Pyrenees and relation to the Iberian Plate geodynamic evolution. Journal of Geophysical Research, B, Solid Earth and Planets, 105, 8, 19405-19418.

Dunbar, J.A. and Cook, R.W., 2003. Palinspastic reconstruction of structure maps: an automated finite element approach with heterogeneous strain. Journal of Structural Geology, 26, 1021–1036

Durand-Riard, P., Caumon, G., Muron, P., 2010. Balanced restoration of geological volumes with relaxed meshing constraints. Computers & Geosciences, 36 (4) 441-452.

ECORS Pyrenees Team, 1988. The ECORS deep reflexion seismic survey across the Pyrenees. Nature, 331: 508-511.

Elliott, D., 1983. The construction of balanced cross-sections. Journal of Structural Geology, 5(2), 101-101.

Elredge, S., Bachtadse, V., Van der Voo, R., 1985. Paleomagnetism and the orocline hypothesis. Tectonphysics, 119, 153-179.

Facer, R.A.: 1983. Folding, strain, and Graham’s fold test in paleomagnetic investigations. Geophys.J. Roy. Astron. Soc. 72, 165–171.

Fernández O., Muñoz J.A., Arbués P., 2003. Quantifying and correcting errors derived from apparent dip in the construction of dip-domain cross-sections. Journal of Structural Geology, 25, 35–42.

Fischer, M.P. and Keating, D.P., 2005. Photogrammetric techniques for analyzing displacement, strain, and structural geometry in physical models: Application to the growth of monoclinal basement uplifts. Geological Society of America Bulletin, 117 (3-4), 369-382.

Fisher, R.A., 1953. Dispersion on a sphere, Proc. R. Soc. London, Ser. A, 217, 295 – 305.

Flinn, D. 1962. On folding during three-dimensional progressive deformation. Geol. Soc. London Quaterly Journal, 118, 385-433.

Floater, M.S., and Hormann, K., 2005, Surface Parameterization: a Tutorial and Survey, in Dodgson, N.A., Floater, M.S., and Sabin, M.A. eds., Advances in Multiresolution for Geometric Modelling, Mathematics and Visualization, Springer Berlin Heidelberg, p. 157–186.

Gairola, V.K., 1978. Strain distribution across an experimental single-layer fold. Tectonophysics, 44, 27-40.

Galbrun, B., Feist, M., Colombo, F., Rocchia, R., Tamabareau, Y., 1993. Magnetostratigraphy and biostratigraphy of Cretaceous-Tertiary continental deposits, Ager Basin, Province of Lerida, Spain. Paleogeography, Paleoclimatology, Paleoecology, 102, 41-52.

Gauss, K.F., 1827. Disquisitiones circa generales superficies curvas. First published in Commentationes societatis regiae scientiarum Gottingensis recentionres, VI, 1828.

Gibbs, A.D., 1983. Balanced cross-section construction from seismic sections in areas of extensional tectonics. Journal of Structural Geology, 5, 153–160.

Gil, J.A. and Jurado, M.J., 1998. Geological interpretation and numerical modelling of salt movement in the Barbastro–Balaguer anticline, southern Pyrenees. Tectonophysics, 293 (3-4), 141-155.

Goguel, J., 1952. Traité de tectonique. Comptes Rendus Critiques. Paris, Masson, in-8°, 383 p. (translated in 1962 as Tectonics [San Francisco, Freeman, 384p]. by H.E. Thalman).

Gómez-Paccard, M., López-Blanco, M., Costa, E., Garcés, M., Beamud, E., Larrasoaña, J.C., 2012. Tectonic and climatic controls on the sequential arrangement of an alluvial fan/fan-delta complex (Montserrat, Eocene, Ebro Basin, NE Spain). Basin Research 01/2012, 24:437-455.

Gomis, E, 1997. Precisión sobre la magnetoestratigrafía de las sucesiones del Oligoceno Superior-Mioceno Inferior en los valles del Cinca, Segre y Ebro (sector SE de la Cuenca del Ebro, provincias de Zaragoza, Lerida y Huesca). Tesis de licenciatura Universidad de Barcelona, 104 pp.

Gomis, E., Parés, J.M., Cabrera, L., 1997 Nuevos datos magnetostratigráficos del tránsito Oligoceno-Mioceno en el sector SE de la Cuenca del Ebro (provincias de Lleida, Zaragoza y Huesca, NE de España), Acta Geol. Hisp., 32, 185-199.

Gong, Z., 2008. The rotation of Iberia during the Aptian and consequences for pervasive Cretaceous remagnetization. PhD Universiteit Utrecht. Geologica Ultraiectina, 292, 103pp

Gong, Z., Dekkers, M.J., Dinarès-Turell, J., Mullender, T.A.T., 2008a. Remagnetization mechanism of Lower Cretaceous rocks from the Organyà Basin (Pyrenees, Spain). Stud. Geophys. Geod., 52, 187–210.

Gong, Z., Langereis, C.G., Mullender, T.A.T., 2008b. The rotation of Iberia during the Aptian and the opening of the Bay of Biscay. Earth and Planetary Science Letters 273, 80–93.

Gong, Z., van Hinsbergen, D.J.J., Dekkers, M.J., 2009. Diachronous pervasive remagnetization in northern Iberian basins during Cretaceous rotation and extensión. Earth and Planetary Science Letters, 284, 292–301.

Gratier J.P. and Guiller B., 1993. Compatibility constraints on folded and faulted strata and calculation of total displacement using computational restoration (UNFOLD program). Journal of Structural Geology, 15, 391–402.

Gratier, J.P., Guillier, B., Delorme, A., Odonne, F., 1991. Restoration and balance of a folded and faulted surface by best-fitting of finite elements; principle and applications. Journal of Structural Geology, 13 (1), 111-115.

Griffiths, P. and Maerten, L., 2007. Workflows for geomechanical restoration and forward modelling in fold and thrust belts; comparison with geometric methodologies, applications and limitations. Abstracts: Annual Meeting - American Association of Petroleum Geologists, 2007, 56-56.

Griffiths, P., Jones, S., Salter, N., Schaefer, F., Osfield, R., Reiser R., 2002. A new technique for 3D-flexural-slip restoration. Jouranl of Structurar Geology, 24, 733-782.

Groshong, R., 2006. 3-D Structural Geology. Second ed. Springer, Heidelberg.

Groshong R., Bond C., Gibbs A., Ratliff R., Wiltschko D., 2012. Preface: Structural balancing at the start of the 21st century: 100 years since Chamberlin. Journal of Structural Geology, 41, 1-5.

Grujic, D., Walter, T.R., Gärtne, H., 2002. Shape and structure of .analogue models of) refolded layers Journal of Structural Geology, 24, 1313-1326

Guzofski, C.A., Mueller, J.P., Shaw, J.H., Muron, P., Medwedeff,D.A., Bilotti, F., Rivero, C., 2009. Insights into the mechanisms of fault-related folding provided by volumetric structural restorations using spatially varying mechanical constraints. AAPG Bull., 93(4), 479–502.

Halls, H.C., 1976. A least-squares method to find a remanence direction from converging remagnetization circles. Geophys. J.R. Astron. Sot., 45, 297-304.

Hindle, D., Burkhard, M., 1999. Strain, displacement and rotation associated with the formation of curvature in fold belts; an example from the Jura arc. J. Struct. Geol. 21, 1089-1101.

Hjelle Ø. and Dæhlen M., 2006. Triangulations and applications,” in Mathematics and Visualization, G. Farin, H. C. Hege, D. Hoffman, C. R. Johnson, K. Polthier, and M. Rumpf, eds. Springer, Berlin. 234 pp

Hoffman, K.A. and Day R., 1978. Separation of multi-component NRM: A general method. Earth and Planetary Sciences Letter, 40, 433-438.

Hogan, P.J. 1993. Geocrohonologic, tectonic and stratigraphic evolution of the Southwest Pyrenean foreland basin, Northern Spain. Unpublised PhD thesis, University of Southern California. 219 pp.

Hogan, P.J. and Burbank D.W., 1996. Evolution of the Jaca piggyback basin and emergence of the External Sierra, southern Pyrenees. In: Tertiary basins of Spain. Edit: Friend, P.F., Dabrio, C.J. Cambridge Univ. Press.

Holl, J.E. and Anastasio, D.J., 1993. Paleomagnetically derived folding rates, southern Pyrenees, Spain. Geology (Boulder), 21 (3), 271-274.

Hossack, J.R., 1979. The use of balanced cross-sections in the calculation of orogenic contraction: a review. Jour. Geol. Soc. London, 136, 705-711.

Hubbert, M.K., 1937. Theory of scale models as applied to the study of geologic structures. Geol. Soc. Amer. Bull., 48, 1459-1520.

Huyghe, D.; Mouthereau, F.; Castelltort, S.; Filleaudeau, P. Y.; Emmanuel, L., 2009. Paleogene propagation of the southern Pyrenean thrust wedge revealed by finite strain analysis in frontal thrust sheets: Implication for mountain building. Earth and Planetary Science Interiors 288, Issues 3 & 4; 421-433. doi: 10.1016/j.epsl.2009.10.002.

Jelinek, V., 1981. Characterization of the magnetic fabric of rocks. Tectonophysics, 79, 63–67.

Jones, D.L., Robertson, I.D.M., McFadden, P.L., 1975. A palaeomagnetic study of the Precambrian dyke swarms associated with the Great Dyke of Rhodesia. Trans. Geological Society of South Africa, 78, 57-65.

Kay, G.M, 1945. Paleogeographic and Palinspastic Maps. AAPG Bulletin, 29, 426-450

Kay, G.M, 1954. Isolith, isopach, and palinspastic maps. AAPG Bulletin, 38, 916-917

Keller, P., 1992. Palaeomagnetische und strukturgeologische Untersuchungen als Beitrag zur Tektogenese der SE-Pyrenaen. Ph Thesis ETH-Z¸rich 122 pp.

Keller, P. and Gehring, A. U., 1992. Different weathering stages indicated by the magnetization of limestones; an example from the Southeast Pyrenees, Spain. Earth and Planetary Science Letters, 111 (1), 49-57.

Keller, P., Lowrie,W., Gehring, A. U., 1994. Palaeomagnetic evidence for post-thrusting tectonic rotation in the Southeast Pyrenees, Spain. Tectonophysics, 239 (1-4), 29-42.

Keller, P. and Gehring, A. U., 1996. Consequences of post-collisional deformation on the reconstruction of the East Pyrenees. In: Palaeomagnetism and Tectonics of the Mediterranean Region (Eds: Morris, A. & Tarling, D. H.). Geological Society Special Publication, 105, 101-109.

Kent, J.T., Briden, J.C., Mardia, K.V., 1983. Linear and planar structure in ordered multivariate data as applied to progresive demagnetization of paleomagnetic remanence. Geophysical Journal of the Royal Astronimal Society, 62, 699-718.

Kerr H.G., White N., Brun J.P., 1993. An automatic method for determining three-dimensional normal fault geometries. Journal Geophysical Research, 98, 17837–17857.

Kirkpatrick, S., Gelatt, C.D., Vecchi M.P., 1983. Optimization by Simulated Annealing. Science. New Series, 220 (4598), 671-680.

Kirschvink, J.L., 1980. The least-squares line and plane and the analysis of the paleomagnetic data. Geophysical Journal of the Royal Astronimal Society, 62, 699-718.

Kligfield, R., Geiser, P., Geiser, J., 1986. Construction of geological cross-section using micro-computer systems. Geobyte Spring, 60–67.

Kodama, K.P. 1988. Remanence rotation due to rock strain during folding and the stepwise application of the fold test. Journal of Geophysical Research, B, Solid Earth and Planets, 93 (4), 3357-3371.

Kodama, K.P., Anastasio, D.J., Newton, M.L., Pares, J.M., Hinnov, L.A., 2010. High resolution rock magnetic cyclostratigraphy in an Eocene flysch, Spanish Pyrenees. Geochemistry, Geophysics, Geosystems, 11, 22 pp.

Kodama, K.P., 2012. Paleomagnetism of Sedimentary Rocks: Process and Interpretation. Wiley, 164 pp. ISBN: 978-1-4443-3502-6

Kodama, K.P. and A.G. Goldstein, 1991. Experimental simple shear deformation of magnetic remanence, Earth and Planet. Sci. Letters, 104, 80-88.

Labaume, P., Séguret, M., Seyve, C., 1985. Evolution of a turbiditic foreland basin and analogy with an accretionary prism: Example of the Eocene South-Pyrenean basin. Tectonics, 4 (7), 661-685.

Lanaja, J.M., 1987. Contribución de la exploración petrolífera al conocimiento de la Geología de España. (Inst.Geol.Mine.España Ed.). 465 pp., 17 mapas.

Larrasoaña, J.C., 2000. Estudio magnetotectónico de la zona de transición entre el Pirieno central y occidental; implicaciones estruucturales y geodinámicas. Tesis doctoral Universidad de Zaragoza, 287 pp.

Larrasoaña, J.C, Parés, J.C., del Valle, J., Millán, H., 2003a. Triassic paleomagnetism from the Western Pyrenees revisited: implications for the IberianñEurasian Mesozoic plate boundary. In: Paleomagnetism applied to tectonics; a tribute to Rob Van der Voo. Edited by: Mac Niocaill, C.; Torsvick, T. H.; van der Pluijm, B. A. Tectonophyisics, 362 (1-4), 161-182. doi: 10.1016/S0040-1951(02)00636-4.

Larrasoaña, J.C., Parés, J.M., Millán, H., del Valle, J., Pueyo, E.L., 2003b. Paleomagnetic, structural, and stratigraphic constraints on transverse fault kinematics during basin inversion: the Pamplona fault (Pyrenees, north Spain). Tectonics, 22 (6) 1071. doi: 10.1029/2002TC001446.

Larrasoaña, J.C, Parés, J.C., Pueyo, E.L., 2003c. Stable Eocene magnetization carried by magnetite and magnetic iron sulphides in marine marls (Pamplona-Arguis Formation, southern Pyrenees, N Spain). Studia Geophysica Geodetica, 47, 237-254. doi:10.1023/A:1023770106613.

Larrasoaña, J.C., Murelaga, X., Garcés, M., 2006. Magnetobiochronology of Lower Miocene (Ramblian) continental sediments from the Tudela Formation (western Ebro basin, Spain). Earth and Planetary Science Letters, 243, 409-423.

Leger M., Thibaut M., Gratier J.P., Morvan J.M., 1997. A least-squares method for multisurface unfolding. Journal of Structural Geology, 19 (5), 735-743.

Lévy, B. and Mallet, J.L., 1998, Non-distorted texture mapping for sheared triangulated meshes, in Proceedings of the 25th annual conference on Computer graphics and interactive techniques, ACM, 343–352.

Lisle, R., 1992. Constant bed-length folding: three-dimensional geometrical implications. Journal of Structural Geology, 14 (2), 245-252.

Lisle, R.J. and Toimil, N., 2007. Defining folds on three-dimensional surfaces. Geology 35 (6), 519-522.

López, M.A., Oliván, C., Oliva-Urcia, B., Pueyo, E.L., 2008. Pyrenean Paleomagnetic databases. Geotemas, 10, 1219-1222.

Lovely, P., Flodin, E., Guzofski, C., Maerten, F., Pollard, D.D., 2012. Pitfalls among the promises of mechanics-based restoration; addressing implications of unphysical boundary conditions. Journal of Structural Geology, 41, 47-63. doi:http://dx.doi.org/10.1016/j.jsg.2012.02.020

Lowrie, W., Hirt, A.M., Kligfield, R., 1986. Effects of tectonic deformation on the remanent magnetization of rocks. Tectonics, 5 (5), 713-722.

MacDonald, W.D., 1980. Net tectonic rotation, apparent tectonic rotation and the structural tilt correction in paleomagnetism studies. J. Geophys. Res., 85, 3659-3669.

Maerten L. and Maerten F., 2006. Chronologic modelling of faulted and fractured reservoirs using geomechanically based restoration: Technique and industry applications. AAPG Bulletin, 90 (8), 1201–1226.

Mallada, L., 1881. Descripción física y geológica de la provincia de Huesca. Mem. Com. Mapa Geol. de España, Madrid. 439 pp.

Mallet, J.L., 2002. Geomodeling. Applied Geostatistics. Oxford University Press.

Martínez-Peña, M.B., 1991. La estructura del límite occidental de la unidad surpirenaica central. Unpublished PhD Thesis. Universidad de Zaragoza. 380 pp.

Martínez-Peña, M.B. and Casas-Sainz A.M., 2003. Cretaceous-Tertiary tectonic inversion of the Cotiella Basin (Southern Pyrenees, Spain). International Journal of Earth Sciences (Geol. Rundsch.), 92, 99-113.

Marshak, S., M.S. Wilkerson, and A.T. Hsui, 1992. Generation of curved fold-thrust belts: Insight from simple physical and analytical models, in Thrust Tectonics, edited by K.R. McClay, pp. 83-93, Chapman & Hall, London.

Massot, J., 2002. Implémentation de méthodes de restauration équilibrée 3D. PhD thesis, Institut National Polytechnique de Lorraine, 157 pp.

McCaig A.M. and McClelland E., 1992. Palaeomagnetic techniques applied to thrust belts. In: Thrust Tectonics, (Ed. by K.R. McClay), pp. 209-216, Chapman y Hall Eds., London. 447 pp.

McClay, K. R. 1990. Extensional fault systems in sedimentary basins: a review of analogue model studies. Mar. Petrol. Geol. 7, 206-233.

McElroy, R., 1990. Thrust kinematics and syntectonic sedimentation: the Pyrenean frontal ramp, Huesca, Spain. Unpublished PhD thesis, University of Cambridge, 175 pp.

McFadden, P.L. and Lowes, F J., 1981. The discrimination of mean directions drawn from Fisher distributions. Geophysical Journal of the Royal Astronomical Society, 67 (1), 19–33.

McFadden, P.L. and McElhinny, M.W., 1988. The combined analysis of remagnetization circles and direct observations in paleomagnetism. Earth and Planetary Sciences Letter, 87, 161-342.

Meert, J.G., 2009. In GAD we trust. Nature Geoscience, 2 (10), 673-674.

Meigs, A.J., 1995. Thrust faults, thrust sheets, and thrust-belts; new insights from the Spanish Pyrenees. PhD Thesis University of Southern California. Los Angeles, CA, United States, 275pp.

Meigs, A.J., 1997. Sequential development of selected Pyrenean thrust faults. Journal of Structural Geology, 19 (3-4), 481-502.

Meigs, A.J., Vergés, J., Burbank, D.W., 1996. Ten-million-year history of a thrust sheet. Geol. Soc. Ame. Bull., 108 (12), 1608-1625 pp.

Meigs, A.J. and Burbank, D.W., 1997. Growth of the South Pyrenean orogenic wedge. Tectonics, 16, 239-258.

Millán, H., 1996. Estructura y cinemática del frente de cabalgamiento surpirenaico en las Sierras Exteriores Aragonesas. Tesis Doctoral Universidad de Zaragoza. 330 pp. Millán Garrido, H., 2006. Estructura y cinemática del frente de cabalgamiento surpirenaico en las Sierras Exteriores aragonesas. Colección de Estudios Altoaragoneses, 53. Instituto de Estudios Altoaragoneses ISBN 84-8127-165-9. Huesca, 398 pp.

Millán, H., Parés J.M., Pocoví A., 1992. Modelización sencilla de la estructura del sector occidental de las sierras marginales aragonesas (Prepirineo, provincias de Huesca y Zaragoza). III Congreso Geol. España. Simposios, 2, 140-149.

Millán, H., Aurell, M., Meléndez, A., 1994. Synchronous detachment folds and coeval sedimen-tation in the Prepyrenean External Sierras (Spain). A case study for a tectonic origin of sequences and system tracts. Sedimentology, 41, 1001-1024.

Millán H., Pocoví A., Casas A., 1995. El frente de cabalgamiento surpirenaico en el extremo occidental de las Sierras Exteriores: sistemas imbricados y pliegues de despegue. Revista de la Sociedad Geológica de España, 8 (1-2), 73-90.

Millán, H. , Pueyo Morer, E.L. y Pocoví, A., 1996. Estimación del acortamiento en áreas afectadas por rotaciones y su contrastación con datos paleomagnéticos. Geogaceta , 20(4), 755 - 758

Millán, H., Pueyo, E.L., Aurell, M., Luzón, A., Oliva, B., Martínez-Peña, M.B., Pocoví, A., 2000. Actividad tectónica registrada en los depósitos terciarios del frente meridional del Pirineo central. Rev. Soc. Geol. España, 13 (2), 279-300.

Mochales, T., 2011. Chronostratigraphy, vertical-axis rotations and AMS of the Boltaña anticline (Southern Pyrenees); kinematic implications. PhD University of Zaragoza, 222 pp.

Mochales, T., Casas, A.M., Pueyo, E.L., Barnolas, A., 2012. Rotational velocity for oblique structures (Boltaña anticline, southern Pyrenees). Journal of Structural Geology, 35, 2-16. doi:10.1016/j.jsg.2011.11.009

Mochales, T., Barnolas, A., Pueyo, E.L., Casas, A.M., Serra-Kiel, J., Samsó, J.M., J. Ramajo., 2012. Chronostratigraphy of the Boltaña anticline and the Ainsa Basin (Southern Pyrenees). Geological Society of American Bulletin, 124 (7-8), 1229-1250. doi:10.1130/B30418.1

Moretti, I,. 2008. Working in complex areas: New restoration workflow based on quality control, 2D and 3D restorations. Marine and Petroleum Geology, 25, 205-218.

Moretti, I. and Larrère, M., 1989. Locace: computer-aided construction of balanced geological cross-section. Geobyte 4, 1–24.

Moretti, I., Lepage, F., Guiton, M., 2006. 3D restoration: geometry and geomechanics. Oil and Gas Technology, 61 (2), 277–289.

Moretti, I., Lepage, F., Guiton, M., 2005. KINE3D: A new 3D restoration method based on a mixed approach linking geometry and geomechanics. Oils & Gas Science and Technology (Rev IFP), 60, 1-12.

Muñoz, J.A., 1992. Evolution of a Continental Collision Belt: ECORS-Pyrenees Crustal Balanced Cross-section. Thrust Tectonic, Ed. by K.R. McClay, 235-246.

Muron, 2005. Méthodes numériques 3-D de restauration des structures géologiques faillées. PhD École Nationale Supérieure de Géologie, Institut National Polytechnique de Lorraine.

Nilforoushan, F., Koyi, H., Swantesson, J.O.H., Talbot, C.J., 2008. Effect of basal friction on surface and volumetric strain in models of convergent settings measured by a laser scanner. Journal of Structural Geology, 30, 366–379.

Norris, D.K. and Black, R.F., 1961. Application of palaeomagnetism to thrust mechanics. Nature (London). 192; 4806, Pages 933-935.

Oliva-Urcia, B., 2000. Estructura y cinemática del frente surpirenaico en el sector central de la cuenca de Jaca-Pamplona. MSc thesis. Universidad de Zaragoza, 100 pp.

Oliva-Urcia, B. and Pueyo E.L., 2007a. Gradient of shortening and vertical-axis rotations in the Southern Pyrenees (Spain), insights from a synthesis of paleomagnetic data. Revista de la Sociedad Geológica de España, 20 (1-2), 105-118.

Oliva-Urcia, B. and Pueyo, E.L., 2007b. Rotational basament kinematics deduced from remagnetized cover rocks (Internal Sierras, southwestern Pyrenees). Tectonics, 26, TC4014, doi:10.1029/2006TC001955.

Oliva-Urcia, B., Pueyo, E.L.; Larrasoaña, J.C., 2008. Magnetic re-organization induced by pressure-solution; a potential mechanism for orogenic-scale remagnetizations. Earth and Planetary Sciences Letters , 265, 525-534. doi: 10.1016/j.epsl.2007.10.032.

Oliva-Urcia, B., Casas, A.M., Pueyo, E.L., Román-Berdiel, T., Geissman, J.W., 2010. Paleomagnetic evidence for dextral strike-slip motion in the Pyrenees during the Alpine convergence (Mauléon basin, France). Tectonophysics, 494, 165-179. doi:10.1016/j.tecto.2010.09.018.

Oliva-Urcia, B., Casas, A.M., Pueyo, E.L., Pocoví, A., 2012a. Structural and paleomagnetic evidence for non-rotational kinematics in the western termination of the External Sierras (southwestern central Pyrenees). Geologica Acta, 10 (1), 1-22.

Oliva-Urcia, B., Pueyo, E.L., Larrasoaña, J.C., Casas, A.M., Román, M.T., 2012b. Paleomagnetic data from Permo-Triassic red beds inthe West-Central Pyrenees: kinematic constraints of the Iberian-Europe plate bundary and the extension of Tertiary remagnetization. Tectonophysics, 522-532, 158-175. doi:10.1016/j.tecto.2011.11.023.

Oliva-Urcia, B., Beamud, B., Garcés, M., Soto, R., Pueyo, E.L., 2012c. Magnetoestratigrafía del relleno continental de la Cuenca del Ebro en su margen Norte (Fm. Campodarbe, Sierra de Santo Domingo, Pirineo). Geotemas, 13, 1212-125**.**

Oms, O., Dinarès-Turel, J., Remacha, E., 2003. Magnetic stratigraphy from deep clastic turbidites: an example from the Eocene Hecho group (southern Pyrenees). Studia Geophysica Geodetica, 47, 275-288.

Oms, O., Babault, J., Dinarès-Turell, J., Rouby, D., Remacha, E, Eichenseer, H., Urreiztieta, M., Nalpas, T., 2006. Validación de modelos geológicos y magnetotectónica. Ejemplo en la Cuenca Surpirenaica Central, MAGIBER I: Paleomagnetismo en la Península Ibérica. Editores: M. Calvo, M. Garcés, C. Gomes, J.C. Larrasoaña, E. Pueyo y J.J. Villalaín. Edit. Universidad de Burgos, 41-44.

Ori, G.G. and Friend, P.F., 1984. Sedimentary basins formed and carried piggyback on active thrust sheets. Geology 12, 475-478.

Parés, J.M. and Dinarés-Turell, J., 1993.Magnetic fabric in two sedimentary rock types from the Southern Pyrenees. Journal of Geomagnetism and Geoelectricity, 45, 193-205.

Park, 1.K., 1983. Paleomagnetism for Geologists. Geosciencie Canada, 10(4), 180-188.

Pascual, O., 1992. Magnetoestratigrafía del estratotipo y paraestratotipo del Ilerdiense, seciones de Tremp y Campo (Cuenca de Tremp-Graus). Tesis doctoral Universitat Autónoma de Barcelona.

Pascual, O., Parés, J.M., 1990. Estudio preliminar de los materiales comprendidos en el tránsito Eoceno-Oligoceno en el borde SE de la cuenca del Ebro., Rev. Soc. Geol. España, 3 (3-4), 323-333.

Pascual, J.O., Samsó, J.M., Tosquella, J., Pares, J.M.; Serra-Kiel, J., 1991. Magnetoestratigrafia y bioestratigrafia del estratotipo del Ilerdiense (Tremp, Lleida). In: I congreso del Grupo Espanol del Terciario. Colombo, F.; Ramos-Guerrero, E.; Riera, S. (Eds). I Congreso del Grupo Espanol del Terciario (Vic). pp 244-247.

Pascual, O., Parés, J.M., Langereis, C.G.; Zijderveld, J.D.A., 1992. Magnetoestratigraphy and rock magnetism of the Ilerdian stratotype at Tremp, Spain. Phys. Earth Plan. Int., 74, 139-157.

Pascual, J.O., Pares, J.M., Garcés, M., 1992. Magnetoestratigrafia y bioestratigrafia del Eoceno inferior; seccion de Campo (provincia de Huesca). In: Actas del Congreso Latinoamericano de Geologia. 8, 164-169.

Pavon-Carrasco, F J., Osete, M.L., Torta, J.M., Gaya-Pique, L.R., 2009. A regional archeomagnetic model for Europe for the last 3000 years, SCHA.DIF.3K; Applications to archeomagnetic dating. Geochemistry Geophysics and Geosystistics,10, Q03013, doi:10.1029/2008GC002244.

Pérez-Rivarés, F.J., Garcés, M., Arenas, C., Pardo, G., 2002. Magnetocronología de la sucesión miocena de la Sierra de Alcubierre (sector central de la Cuenca del Ebro). Revista de la Sociedad Geológica de España, 15, 210-225.

Pérez-Rivarés, F.J., Garcés, M., Arenas, C., Pardo, G., 2004. Magnetostratigraphy of the Miocene continental deposits of the Montes de Castejón (central Ebro basin, Spain): geochronological and paleoenvironmental implications. Geologica Acta, 2(3), 221-234.

Poblet, J & Lisle, R., 2011. Kinematic evolution and structural styles of fold-and-thrust belts. In: Poblet, J. and Lisle, R. (eds.): Kinematic evolution and structural styles of fold-and-thrust belts. Geological Society Special Publication, 349: 1-24. ISBN: 978-1-86239-320-2

Poblet, J.; Muñoz, J. A.; Travé, A.; Serra-Kiel, J., 1998. Quantifying the kinematics of detachment folds using three-dimensional geometry; application to the Mediano Anticline (Pyrenees, Spain). Geological Society of America Bulletin. 110; 1, Pages 111-125.

Press, W., Flannery B., Teukolsky S., Vetterling W., 1992. Numerical Recipes in C: The Art of Scientific Computing. Chapter 10.9 Simulated Annealing pp. 450-455.

Price, R.A. and Sears, J.W., 2000. A preliminary palinspastic map of the Mesoproteroiz Belt-Purcell Supergroup, Canada and USA: Implications for the tectonic setting and structural evolution of the Purcell anticlinorium and the Sullivan deposit; Chapter 5 in The Geological Environment of the Sullivan Deposit, British Columbia, (ed.) J.W. Lydon, T. Höy, J.F. Slack, and M.E. Knapp; Geological Association of Canada, Mineral Deposits Division, Special Publication No. 1, p.61-81.

Pueyo-Anchuela, O., Pueyo, E.L., Pocoví, A., Gil-Imaz, A., 2012. Vertical axis rotations in thrust and folds belts: calibration of AMS and paleomagnetic data in the Western External Sierras (Southern Pyrenees). Tectonophysics, doi:10.1016/j.tecto.2012.01.023.

Pueyo, E.L., 2000. Rotaciones paleomagnéticas en sistemas de pliegues y cabalgamientos. Tipos, causas, significado y aplicaciones (ejemplos del Pirineo Aragonés). Ph.D Thesis. Universidad de Zaragoza. 296 pp.

Pueyo, E.L., 2010. Evaluating the paleomagnetic reliability in fold and thrust belt studies. Trabajos de Geología, 30 (1), 145-154.

Pueyo, E.L., Millán, H., Pocoví, A., Parés, J.M., 1996. Correcciones geométricas en magnetotectónica: Filtrado de rotaciones aparentes debidas a pliegues. Geogaceta , 20(4), 1054-1057.

Pueyo, E.L., Millán, H., Pocoví, A., Parés, J.M., 1999. Cinemática rotacional del cabalgamiento basal surpirenaico en las Sierras Exteriores Aragonesas: Datos magnetotectónicos. Acta Geológica Hispánica, 32 (3-4), 119-138.

Pueyo, E.L., Millán, H., Pocoví, A., 2002a. Rotation velocity of a thrust: a paleomagnetic study in the External Sierras (Southern Pyrenees). Sedimentary Geology, 146, 191-208.

Pueyo, E.L., Pocoví, A, Parés, J.M., 2002b. Flexural folding of linear (paleomagnetic) data by non-coaxial axes of deformation: restoration and errors. Mitteilungen Naturwissenschaftlicher Verein für Steiermark, 132 , 35 – 38.

Pueyo, E.L., Larrasoaña, J.C., Mauritsch, H.J., Valero, B., González, P., Pocoví, A., Scholger, R., Millán, H., Laplana, C., 2002c. Preliminary paleomagnetic results from the filling of a Roman dam (Almonacid de la Cuba): archeomagnetic and environmental implications. New trends in Geo-, Paleo-, Rock- and Enviromental magnetism VIII Castle Meeting Proceedings, 49.

Pueyo, E.L., Parés J.M., Millán H., Pocoví A., 2003a. Conical folds and apparent rotations in paleomagnetism (A case study in the Pyrenees). Tectonophysics, 362 (1), 345 366.

Pueyo, E.L., Pocoví, A., Parés, J.M., Millán, H., Larrasoaña, J.C., 2003b. Thrust ramp geometry and spurious rotation of paleomagnetic vectors. Studia Geophysica Geodetica, 47, 331-357.

Pueyo, E.L., Pocoví, A., Millán, H., Sussman, A.J., 2004. Map view model to correct and calculate shortening in rotated thrust fronts using paleomagnetic data. In: Paleomagnetic and structural analyses of orogenic curvature (A. J. Sussman and A. B. Well, Eds.). Geological Society of America Spec., 383, 57-71.

Pueyo, E.L., Sussman, A.J., Oliva-Urcia, B., Larrasoaña, J.C., Beamud, B., Soto, R., Garcés, M., Gil-Peña, I., Almar, Y., Fernández, O., Vidal, O., 2005. The Pyrenean paleomagnetic database: towards better 3D restoration methods. 10th Scientific Assembly of the International Association of Geomagnetism and Aeronomy, IAGA-Abstracts 01319.

Pueyo, E.L., López, M.A., Oliva-Urcia, B., Sussman, A.J., Larrasoaña, J.C., Dinarés, J., Beamud, B., Soto, R., Garcés, M., Gil-Peña, I., Rodríguez, A., Almar, Y., Fernández, O., Villalaín, J.J., Calvo, M., Bógalo, M.F., Costa, E., Mochales, T., Vidal, O., Pueyo-Anchuela, O., Gil-Imaz, A., Román, M.T., Navas, J., 2006. A preliminary compilation of the Pyrenean paleomagnetic database. Proceedings MAGIBER IV, 73-76.

Pueyo, E.L., Ramón, M.J., Rodríguez-Pintó, A., Oliva-Urcia, B., Mochales, T., Sánchez, E., Pueyo-Anchuela, O., Oliván, C., López, M.A., San Miguel, G., 2013. High-resolution rotational kinematics in fold-and-thrust belts; what is new and what is left to do? The experience from the Southern Pyrenees. Geophysical Research Abstracts Vol. 15, EGU2013-5709-1.

Puigdefábregas, C., 1975. La sedimentación molásica en la cuenca de Jaca. Pirineos, 104, 1-188.

Puigdefàbregas, C. and Soler, M., 1973. Estructura de las Sierras Exteriores pirenaicas en el corte del río Gállego. (prov. de Huesca). Pirineos, 109, 5-15.

Ramberg, H. 1981. Gravity, Deformation, and the Earth's Crust in Theory, Experiments and Geological Applications. 2nd Edition Academic-Press, London, New York.

Ramón, M.J. and Pueyo, E.L., 2008. Cálculo de direcciones y planos virtuales paleomagnéticas: Ejemplos y comparación con otros métodos. Geotemas, 10, 1203-1206.

Ramón, M.J, Pueyo, E.L, Briz, J.L., Pocoví, A., Ciria, J.C., 2012. Flexural unfolding using paleomagnetic vectors. Journal of Structural Geology, 35, 28-39.

Ramón, M.J.; Pueyo, E. L.; Rodríguez-Pintó, A.; Ros, L. H.; Pocoví, A.; Briz, J. L.; Ciria, J. C. (2013) A computed tomography approach to understanding 3D deformation patterns in complex flexural folds. Tectonophysics. 593, 57–72 doi: 10.1016/j.tecto.2013.02.027 (8 May)

Ramón, M.J.; Pueyo, E. L.; Caumon, G.; Briz, J. L. (in review). Flexural unfolding of horizons using paleomagnetic vectors: a parametric approach. Am. Asoc. Petrol. Geol. Bulletin.

Ramón, M.J.; Fernandez, O.; Briz, J. L.; Pueyo, E. L. (in review). Sensitivity on flexural horizon restoration using 2D and 3D constraints: meshes and pin-element location. Mathematical Geosciences.

Ramsay, J G., 1967. Folding and fracturing of rocks. New York, McGraw Hill, 568 pp.

Ramsay, J.G., 1977. Plegamiento y fracturación de las rocas. Hermann Blume, pp. 361-390.

Ramsay, J.G., and Huber, M.I., 1983, The Techniques of Modern Structural Geology. Volume 1: Strain Analysis: London, Academic Press, 307 pp.

Reiter, K., Kukowski, N., Ratschbacher, L., 2011. The interaction of two indenters in analogue experiments and implications for curved fold-and-thrust belts. Earth and Planetary Science Letters, 302 (1-2), 132-146.

Robador, A., Samsó, J.M., Ramajo, J., Barnolas, A., Clariana, P., Martín, S., Gil-Peña, I., 2011. Mapa Geológico Digital continuo E. 1: 50.000, Zona Pirineos Vasco-Cantábrica (Zona-1600). GEODE. Mapa Geológico Digital contínuo de España. [on- line]. Sistema de Información Geológica Continua: SIGECO. IGME. Editor: J. Navas. http://cuarzo.igme.es/sigeco/default.htm

Rodríguez-Pintó, A., 2013. Magnetoestratigrafía del Eoceno inferior y medio en el frente Surpirenaico (Sierras Exteriores): Implicaciones cronoestratigráficas y cinemáticas.”. PhD University of Zaragoza 370 pp.

Rodríguez-Pintó, A., Pueyo, E.L., Pocoví , A., Barnolas, A., 2010. Paleomagnetic analysis in the Balzez anticline (Southern Pyrenees); Vertical-axis rotations and kinematic implications. Trabajos de Geologia , 30 (1), 169 -175.

Rodriguez-Pintó, A., Ramón, M.J., Oliva-Urcia, B., Pueyo, E.L., Pocoví, A., 2011. Errors in paleomagnetism: Structural control on overlapped vectors, mathematical models.Physics of the Earth and Planetary Interiors, 186, 11-22.

Rodriguez-Pintó, A., Pueyo, E.L., Serra-Kiel, J., Samsó, J.M., Barnolas, A., Pocoví, A., 2012a. Lutetian chronostratigraphic calibration based on magnetostratigraphy and shallow benthic zones biostratigraphy at the Isuela section (Southern Pyrenees). Palaeogeography, Palaeoclimatology, Palaeoecology doi: 10.1016/j.palaeo.2012.03.012.

Rodríguez-Pintó, A., Pueyo, E. L., Barnolas, A., Samsó, J. M., Pocoví, A., Gil-Peña, I., Mochales, T., Serra-Kiel, J., 2012b. Lutetian magnetostratigraphy in the Santa Marina section (Balzes anticline, Southwestern Pyrenees). Geotemas, 14.

Rodríguez-Pintó, A., Pueyo, E.L., Pocoví, A., Ramón, M. J., Oliva-Urcia, B., 2013a. Structural control on overlapped paleomagnetic vectors: A case study in the Balzes anticline (Southern Pyrenees). Physics of the Earth and Planetary Interiors, 215, 43–57. doi: 10.1016/j.pepi.2012.10.005.

Rodriguez-Pintó, A.. Pueyo, E.L.. Serra-Kiel, J.. Barnolas, A.. Samsó, J.M., Pocoví, A., 2013b. The Upper Ypresian-Lutetian in the San Pelegrín section (Southwestern Pyrenean Basin): magnetostratigraphy and larger foraminifera correlation. Palaeogeography, Palaeoclimatology, Palaeoecology, 370, 13–29. doi: 10.1016/j.palaeo.2012.10.029.

Rodríguez-Pintó, A., Pueyo, E.L., Sánchez, E., Calvin, P., Ramajo, J., Ramón, M.J., Pocoví, A., Barnolas, A., Casas, A.M., (2013c in review). Rotational kinematics of a curved fold: a structural and paleomagnetic study in the Balzes anticline (Southern Pyrenees). Tectonophysics.

Rouby D., Suppe J., Xiao H., 2000. 3D restoration of complexly faulted and folded surfaces using multiple unfolding mechanisms. Amer. Assoc. Petrol. Geol., 84, 805-829.

Rouby, D., Cobbold, P.R., Szatmari, P., Demercian, S., Coelho, D., Rici, J.A., 1993. Least- squares palinspastic restoration of regions of normal faulting. Application to the Campos Basin (Brazil).Tectonophysics, 221, 439-452.

Roure, F., Choukroune, P., Berástegui, X., Muñoz, J.A., Villien, A., Matheron, P., Bareyt, M., Séguret, M., Cámara, P. y Deramond, J., 1989. ECORS deep seismic data and balanced cross sections: geometric constraints to trace the evolution of the Pyrenees. Tectonics, 8, 41-50.

Rouvier, H., Henry, B., Macquar, J.C., Leach, D., Le Golf, M., Thibieroz, J., Lewchuck, M.T., 2001. Réaimantation régionale éocène, migration de fluides et minéralisations sur le bordure cévenole. Bulletin de la Societe Géologique de France, 172 (4), 503-516.

Rouvier, H., Henry, B., Le Gooff, M., 2012. Mise en évidence par le paléomagnétisme de rotations régionales dans la virgation des Corbières (France). Bull. Soc. géol. France, 183 (5), 409-424.

Roy, J.L. and Park, J.K., 1974. The magnetization process of certain redbeds: Vector analysis of chemi-cal and thermal results. Canadian Journal of Earth Sciences, 11, 437-471.

San Miguel, G., Hernández, R., Pueyo, E.L., 2010. Pyrenean Paleomagnetic Database; Concept, state-of-the-art, and web interface design. Proceedings MAGIBER VI, 50-53.

Santolaria, P., 2010. Estructura de las Sierras Marginales en el Sector Olvena Calasanz. Trabajo Academicamente dirigido. Dept. Ciencias de la Tierra. Universidad de Zaragoza 67 pp.

Scheepers, P.J.J. and Zijderveld, J.D.A., 1992. Stacking in Paleomagnetism: Application to marine sedi-ments with weak NRM. Geophysical Research. Letters, 1914, 1519-1522.

Scheidegger, A.M., 1965. On the statistics of the orientation of bedding planes, grain axes, and similar sedimentological data. US Geological Survey Professional Papers, 525C, 164–167.

Schmidt, P.W., 1982. Linearity spectrum analysis of multicomponent magnetizations and its application to some igneous rocks from south-eastern Australia. Geophysical Journal of the Royal Astronomical Society, 70, 647-665.

Schreurs, G., Hanni, R., Vock, P., 2001. 4-D Analysis of analog models: experiments on transfer zones in fold-and-thrust belts. In: Koyi, H.A. & Mancktelow, N.S. (eds) Tectonic Modeling. A Volume in Honor of Hans Ramberg. Geological Society of America Memoir, 193, 179-190.

Schreurs, G., Hänni, R., Panien, M., Vock, P., 2003. The analysis of analogue model experiments by helical X-ray computed tomography. In: Mees, F., Swennen, R., Van Geet, M. and Jacobs, P. (eds). Applications of X-ray computed tomography in the geosciences. Geological Society London, Special Publications, 215, 213-223.

Schreurs, G., Buiter, S.J.H., Boutelier, D., Corti, G., Costa, E., Cruden, A.R., Daniel, J.M., Hoth, S., Koyi, H.A., Kukowski, N., Lohrmann, J., Ravaglia, A., Schlische, R.W., Withjack, M.O., Yamada, Y., Cavozzi, C., Delventisette, C., Elder Brady, J.A., Hoffmann-Rothe, A., Mengus, J.M., Montanari, D., Nilforoushan, F., 2006. In: Buiter, S.J.H., Schreurs, G. (Eds.), Analogue and Numerical Modelling of Crustal-Scale Processes. Analogue benchmarks of shortening and extension experiments, 253. Geological Society, London, Special Publications, pp. 1e27.

Schwarz, E.J., 1962. Geology and paleomagnetism of the valley of the Río Aragón Subordan north and east of Oza. (PhD Thesis, University of Utrecht) Estudios Geológicos, 18, 193-240.

Schwerdtner, W.M., 1977. Geometric interpretation of regional strain analyses. Tectonophysics, 39 515-531.

Scott, G.D., 1984. Anomalous declinations from plunging structures. EOS Trans. AGU, 65, 866.

Séguret, M., 1972. Etude tectonique des nappes et series decollées de la partie centrale du versant sud des Pyrenées. Caractére sedymentaire, rôle de la compression et de la gravité. Thèse Fac. Sc. de Montpellier (1970). Publ. de l'Univ. des Sc. et Tec. du Languedoc (USTELA), Sér. Geol. Struct. nº 2. 155 pp.

Sellés-Martínez, J., 1988. Las correcciones estructural y tectónica en el tratamiento de los datos magnéticos. Geofísica Internacional, 27-3, 379-393 pp.

Setiabudidaya, D.J., Piper, D.A.,Shaw, J., 1994. Paleomagnetism of the (Early Devonian) Lower Old Red sandstones of South Wales: Implications to Variscan overprinting and differential rotations. Tectonophysics, 231, 257-280.

Soler, M., 1970. Etude Géologique du Haut Aragon Occidental, S.N.P.A. Documentación interna.

Soto, R., Casas, A.M., 2001. Geometría y cinemática de las estructuras Norte-Sur de la cuenca de Aínsa. Revista de la Sociedad Geológica de España, 14 (3-4), 199-211.

Soto, R., Casas, A.M., Storti, F., Faccenna, C., 2002. Role of lateral thickness variations on the development of oblique structures at the western end of the South Pyrenean Central Unit. Tectonophysics, 350 (3), 215-235.

Soto, R., Casas-Sainz, A.M., Pueyo, E.L., 2006. Along-strike variation of orogenic wedges associated with vertical axis rotations. Journal of Geophysical Research (Solid Earth), 111 (B10), B10402-B10423.

Stamatakos, J. and Kodama, K.P., 1991. Flexural flow folding and the paleomagnetic fold test; an example of strain reorientation of remanence in the Mauch Chunk Formation. Tectonics, 10 (4), 807-819.

Stamatakos, J. and Kodama, K.P., 1991. The effects of grain-scale deformation on the Bloomsburg formation pole, Jour. Geophys. Res., 96, 17919-17933.

Stewart, S.A., 1995. Paleomagnetic analysis of plunging fold structures: Errors and a simple fold test, Earth Planetary Science Letters, 130, 57-67.

Suppe J., 1985. Principles of Structural Geology: Prentice-Hall Inc., Englewood Cliffs, N.J., 537 pp.

Sussman, A.J., 2003. Thrust belt curvature: Structural and paleomagnetic analyses in the Catalunyan Pyrenees and Sevier orogen, unpublished Ph.D. Dissertation, The University of Arizona, 175 pp.

Sussman A.J., Butler, R.F., Dinarès-Turell, J., Vergés, J., 2004. Vertical axis rotation of a foreland fold and implications for the orogenic curvature: an example from the Southern Pyrenees, Spain. Earth and Planetary Science Letters, 6930, 1-15.

Sussman, A.J., Pueyo, E.L., Chase, C.G., Mitra, G., Weil, A.J., 2012. The impact of vertical-axis rotations on shortening estimates. Lithosphere, doi: 10.1130/L177.1

Taberner, C., Dinarès-Turell, J., Gimènez, J., Docherty, C., 1999. Basin infill architecture and evolution from magnetostratigraphic cross-basin correlations in the southeastern Pyrenean foreland basin. Geol. Soc. Am. Bull., 11, 8, 1155-1174.

Tauxe, L., 2002. Paleomagnetic principles and Practice. Kluwer Academis Publishers, 300 pp. ISBN 978-0-306-48128-4

Tauxe, L., 2005. Inclination flattening and the geocentric axial dipole hipótesis. Earth and Planetary Science Letters, 233 (3-4), 247-261.

Tauxe, L., 2009. Essentials of paleomagnetism. University of California Press, La Jolla, California. Web Edition 1.0, pp.512.

Tauxe, L., Kylstra, N., Constable C., 1991. Bootstrap statistics for paleomagnetic data. Journal of Geophysical Research, 96, 11723-11740.

Teixell, A., 1996. The Ansó transect of the Southern Pyrenees: Basement and cover thrust geometries. J. Geol. Soc. London, 153, 301-310.

Teixell, A., 1998. Crustal structure and orogenic material budget in the west central Pyrenees. Tectonics, 17 (3), 395-406.

Teixell, A. and García Sansegundo, J., 1995. Estructura del sector central de la Cuenca de Jaca (Pirineos me-ridionales). Rev. Soc. Geol. España, 8 (3), 215-228.

Thibert B., Gratier J.P., Morvan J.M., 2005. A direct method for modelling and unfolding developable surfaces and its application to the Ventura Basin (California). Journal of Structural Geology, 27, 303-316.

Van der Lingen, G.J., 1960. Geology of the Spanish Pyrenees, north of Canfranc, Huesca province. (PhD Thesis, University of Utrecht). Estudios Geológicos. Inst. Invest. Geol. ìLucas Malladaî, Madrid, 16, 205-242.

Van der Pluijm, B.A., 1987. Grain scale deformation and the fold test-evaluation of synfolding remagnetization, Geophysical Research Letters, 14, 155-157.

Van der Voo, R., 1990. The reliability of paleomagnetic data. Tectonophysics, 184, 1-9.

Van der Voo, R., Torsvik, T.H., 2001. Evidence for Late Paleozoic and Mesozoic nondipole fields provides an explanation for the Pangea reconstruction problems. Earth and Planetary Science Letters 187 (1–2), 71–81.

Weil, A.B., 2006. Kinematics of orocline tightening in the core of an arc; paleomagnetic analysis of the Ponga Unit, Cantabrian Arc, northern Spain. Tectonics, 25 (3), 23.

Weil, A.B., and Van der Voo, R., 2002. The evolution of the paleomagnetic fold test as applied to complex geologic situations, illustrated by a case study from northern Spain, Phys. Chem. Earth, 27, 1223-1235.

Weil, A.B. and Sussman, A., 2004. Classifying curved orogens based on timing relationships between structural development and vertical-axis rotations. Geological Society of America Special Paper 383, 1–17.

Weil, A.B., Gutiérrez-Alonso, G., Johnston, S.T., Pastor-Galán, D., 2013. Kinematic constraints on buckling a lithospheric-scale orocline along the northern margin of Gondwana: A geologic synthesis. Tectonophysics, 582, 25–49

Weinberger, R., Agnon, A., Ron, H., Garfunkel, Z., 1995. Rotation about an inclined axis: three dimensional matrices for reconstructing paleomagnetic and structural data. Journal of Structural Geology, 17 (6), 777-782.

Wickham, J., and Moeckel, G.P., 1997. Restoration of structural cross-sections. Journal of Structural Geology, 19 (7), 975-986.

Wilkerson, M.S., 1992, Differential transport and continuity of thrust sheets: Journal of Structural Geology, v. 14, no. 6, p. 749–751.

Wilkerson, M.C. and Dicken, C.L., 2001. Quick-look techniques for evaluating two-dimensional cross sections in detached contractional settings. AAPG Bulletin, 85 (10), 1759–1770.

Wilkerson, M.S.; Apotria, T.; Farid, T., 2002. Interpreting the geologic map expression of contractional fault-related fold terminations; lateral/oblique ramps versus displacement gradients. Journal of Structural Geology, vol.24, no.4, pp.593-607.

Williams, G.D., Kane, S., Buddin, T.S., Richards, A.J., 1997. Restoration and balance of complex fol-ded and faulted rock volumes; flexural flattening, jigsaw fitting and decompaction in three dimen-sions. Tectonophysics, 273 (3-4), 203-218.

Woodcock, N.H., 1977. Specification of fabric shapes using an eigenvalue method. Geological Society of America Bulletin, 99, 1231-1236.

Woodward, N.B., Boyer, S.E., Suppe, J., 1989. Balanced Geological Cross-Sections: An Essential Technique in Geological Research and Exploration. Short Courses in Geology, 6, 132.

Yonkee, A. and Weil, A.B., 2010. Quantifying vertical-axis rotation in curved orogens: integrating multiple data sets with a refined weighted least-squares strike test. Tectonics, 29.

Zijderveld, J.D.A., 1967. A.C. demagnetization of rocks: Analysis of results, in Methods in Paleomagnetism, Eds D.W. Collinson, K.M. Creen and S.K. Runcorn, Elsevier, Amsterdam.

Zingg, T., 1935. Beitrag zur Schotteranalyze. Schweizer Mineralogische und Petrographische Mitteilung, 15, 39-140.

Zotkevich, I.A., 1972. Reduction of the natural remanent magnetization of a plunging fold to the ancient coordinate system in paleomagnetic studies. Earth Physics, 2, 95-99.

I Appendix 1:

Achieving the optimal information from paleomagnetic analysis

We have been assuming the reliability of paleomagnetic data throughout the whole manuscript. Let us now focus on the acquisition of these paleomagnetic vectors from the rough initial data, known as *characteristic remanent magnetization* (ChRM). As we already mentioned (Section 2.2.1), the calculation of a ChRM is a key step during paleomagnetic data processing. In this line, we have developed the Virtual Paleomagnetic Directions (VPD) program based on the virtual directions (VD). We propose this multi task software because it is a global and rapid approach to evaluate all *natural remanent components* (NRM).

The VPD is designed as a global approach to tackle the demagnetization data of a site. This tool is especially useful and fast when dealing with large (i.e. u-channel data) or discrete and homogeneous (sites) datasets. Moreover, the VPD software also implements classic approaches (principal analysis components [PCA], stacking routine [SR], linearity spectrum analysis [LSA]) to allow comparing between them. The goal of the VPD software is not to substitute the expertise of paleomagnetic researchers, but to ease the identification and calculation of ChRM directions reducing the uncertainty, especially when dealing with large datasets.

I.1 Virtual directions in paleomagnetism: a global view on the NRM components

Virtual directions (VD) are all possible directions (or vectors) calculated among all possible demagnetization intervals for each specimen from a site (Pueyo, 2000; Ramón & Pueyo, 2008). In the same way, virtual circles (VC) are all possible demagnetization circles (or planes). Directions and circles are calculated without including the origin (*difference vectors*) and including it (*resultant vectors*). The rationale behind this calculus is that any stable direction of the natural remanent magnetization (NRM) will stand out above the scattered directions. Thus, if the ChRM can be defined in that site, it will necessarily be included in the VD data set. VD does not pretend to be a new method, but an auxiliary tool. The use of VD to help determining the NRM components is an approach that necessarily implies several assumptions, that are on the other hand applicable to all methods proposed for calculating ChRM directions, although only in exceptional cases are completely fulfilled:

- A ChRM can be isolated with the selected demagnetization routine.

- Directions are continuous, all valid steps within a given demagnetization interval are included to calculate any direction.

- The stepwise demagnetization process is expected to be homogeneous among the collection, demagnetization step increments are recommended to be similar.

- A magnetization component can be identified with a sufficient number of demagnetization steps.

- The site must be lithologically homogeneous (e.g., similar magnetic mineralogy) and must have the same structural attitude (i.e. belong to a set of beds with an equal bedding plane).

Let us suppose that there is a site with *m* specimens that are demagnetized following an homogeneous procedure of *n* steps. For each specimen all possible directions are calculated. Each direction is calculated using PCA (Kirschvink, 1980). The number of difference virtual directions (DVD) for one specimen is: $\sum_{i=1}^{n-1} i = (n^2 - n)/2$. To calculate the resultant virtual directions (RVD), the process is the same but includes the origin, being the number of RVD $\sum_{i=1}^{n} i = (n^2 + n)/2$. In this case there are *n* more possible directions because only one step is needed to form a direction that includes the origin. Therefore, a total of n^2 directions (difference + resultant) are automatically calculated for each sample, which results in $m * n^2$ total directions for that site (Fig. I.1).

The RVD data set mostly represents the directions that trend to the origin of the orthogonal demagnetization plot because the latter is included, although there is a background noise caused by demagnetization steps of other directions that are not directed to the origin. On the other hand the DVD data set will represent any direction contained in the studied site plus, again, the noise caused by directions obtained from mixed demagnetization windows. To characterize the VD data set, Fisher (1953) and Bingham (1974) statistics are calculated. The normalized eigenvalues (S_1, S_2, S_3) of the orientation matrix (Scheidegger, 1965; Bingham, 1974) will help identifying the anisotropy of the scatter caused by multi-component NRMs.

In the same way and with similar meaning, the virtual demagnetization circles can be calculated from two different sources of vectors (resultant and difference) which gives two new data sets: *difference virtual circles* (DVC) and *resultant virtual circles* (RVC). The expected result must be checked by observing the areas where denser intersections of circles are located and its anisotropy. The poles of demagnetization planes plotted in the stereographic projection tend to form a girdle whose pole, in turn, corresponds with the main intersection of all circles. The minimum eigenvector (e_3) of the Bingham (1974) statistics of this distribution of poles should be closer to the ChRM in this case.

Visualization of all virtual directions and calculation of its mean direction can be inappropriate for noisy data or for sites with more than one representative component. Therefore, post-processing becomes necessary to discriminate the components. With this aim, we propose the filtering of the data.

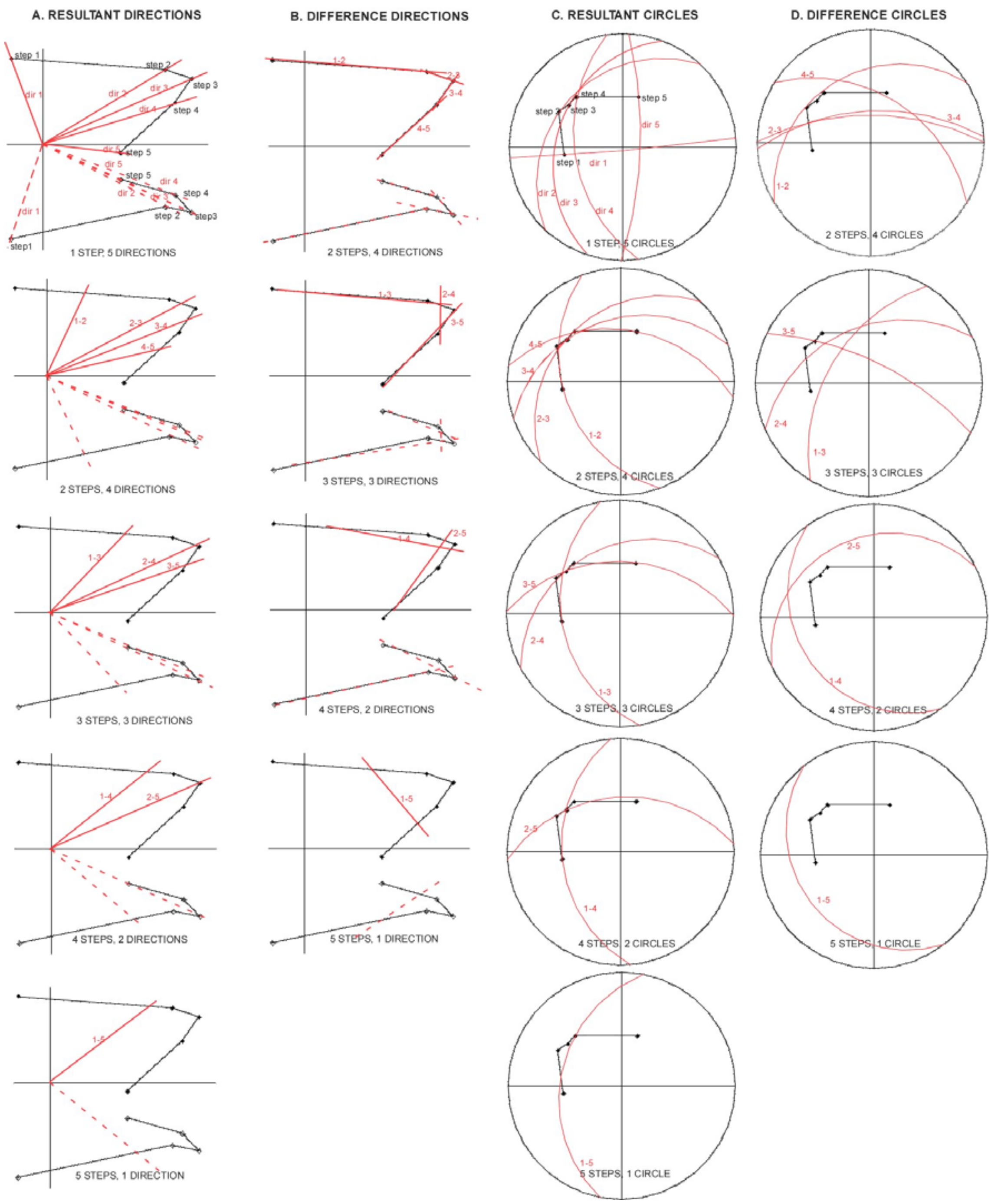

Figure I.1: Illustration of the virtual directions concept. Demagnetized sample with n=5 demagnetization steps. A) Resultant virtual directions (RVD). With only one step there are n directions, n-1 directions with 2 steps and so on until 1 direction with n steps. B) Difference virtual directions (DVD). The minimum number of steps required to calculate a direction is two. C) Resultant virtual circles (RVC). D) Difference virtual circles (DVC).

Several criteria can be used to filter the virtual directions and circles data sets (Fig. I.2): some can be considered more objective (number of steps, MAD, intensity) and some others are particularly based on the experience and expertise of the researcher (interval of demagnetization). This last criteria obviously lacks of objectivity but it can be very useful to automatically process very large homogeneous datasets. The criteria that we have used are as follows:

- Minimum number of steps. A difference direction can be defined in two steps and a resultant direction in only one step (including the origin of the demagnetization diagram). Nonetheless, a representative component should be defined using as many demagnetization steps as possible. However, a minimum number of steps can be established to extract only those directions that are stable and reliable.

- Maximum and minimum intensities. This filter is useful to remove instrumental noise (background intensities), laboratory errors, or anomalous samples (e.g., shock magnetized, lighting, etc). For example, the application of maximum threshold intensity could be very useful to differentiate bimodal distributions along u-channels (i.e. cyclic sequences).

- Minimum and maximum error (MAD). Low MAD values guarantee linearity for a direction ($lineMAD = a\tan\sqrt{(\lambda_3 + \lambda_2)/\lambda_1}$ where λ_i are the eigenvalues of the PCA) and planarity for a circle ($circleMAD = a\tan\sqrt{(\lambda_3 + \lambda_2)/(\lambda_3 + \lambda_1)}$), thus filtering with a maximum MAD is useful to remove poorly characterized directions and circles. Besides, the selection of a minimum MAD of 0.1º will avoid inclusion of resultant vectors characterized by only one step as well as difference vectors characterized by 2 steps (e.g., original demagnetization vectors).

- Interval of demagnetization / unblocking window. Although the most subjective, his approach is really meaningful when a fixed demagnetization interval is found for all specimens in the studied homogeneous site/profile/locality and particularly necessary if there is more than one component. Selection of minimum and maximum demagnetization steps can accurately constrain the virtual data set within the selected unblocking window. It could be very useful to quickly characterize the ChRM providing a clear definition of the demagnetization interval.

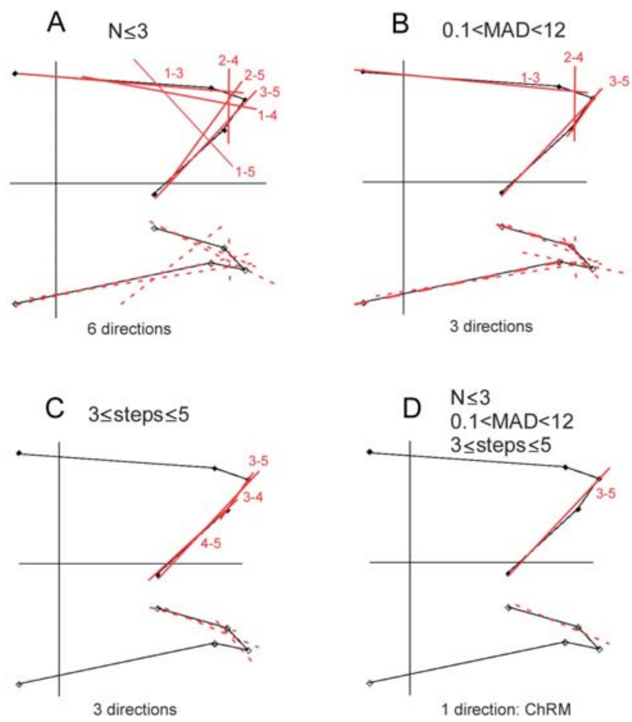

Figure I.2: Illustration of the filtering concept (example from sample of Fig. I.1). A) Minimum number of steps filter. B) MAD filter. C) Demagnetization interval / unblocking window filter. D) Final filter with multiple criteria.

I.1.1 Automatic calculation of demagnetization intervals

The selection of the demagnetization interval or unblocking window may be quite subjective. However, for an homogeneous dataset (homogeneity in terms of magnetic properties and tectonics between all specimens of a site) we want to facilitate this selection making it as objective as possible. In that sense, we want to use the virtual directions method to seek the most representative demagnetization interval. We will filter the VD data set with the calculated interval and determine the mean directions (ChRMs).

The idea is to find the interval that contains the group of most representative virtual directions. *Resultant* or *difference virtual directions* (RVD, DVD) can be considered if we assume that directions point toward the origin (complete demagnetization) or not (the general case). For further analysis, the initial VD data set (RVD or DVD) is objectively filtered selecting only reliable directions defined by a minimum number of steps (e.g. $n \geq 3$) and a maximum value of error (e.g. MAD < 15º).

We define groups of VD data sets filtered by each possible demagnetization interval. We consider that a well-represented group has an accurately determined direction (MAD < 15º) at least for half the specimens of the site. As the initial data set has already been objectively filtered, only groups with a minimum number of directions (the number of specimens divided by two) are used. The data quality or relevance for each group is measured with the precision parameter (k) of Fisher (1953). In order to gain resolution and better discern the results, we use it squared.

Each interval is defined by their initial and final demagnetization steps. The concurrent occurrence of these intervals in relevant groups leads to the selection of the proper interval or intervals. We plot weighted histograms for the initial and final steps: we count the numbers of times each step is the initial or final step of the groups but weighted by the squared precision parameter (k^2) of each group. Local maxima of the weighted histograms of initial and final steps may correspond with the unblocking windows for different natural remanent magnetization components (Fig. I.3). ChRM is the Fisher Mean of the VD filtered by the calculated interval (step max –min and # steps).

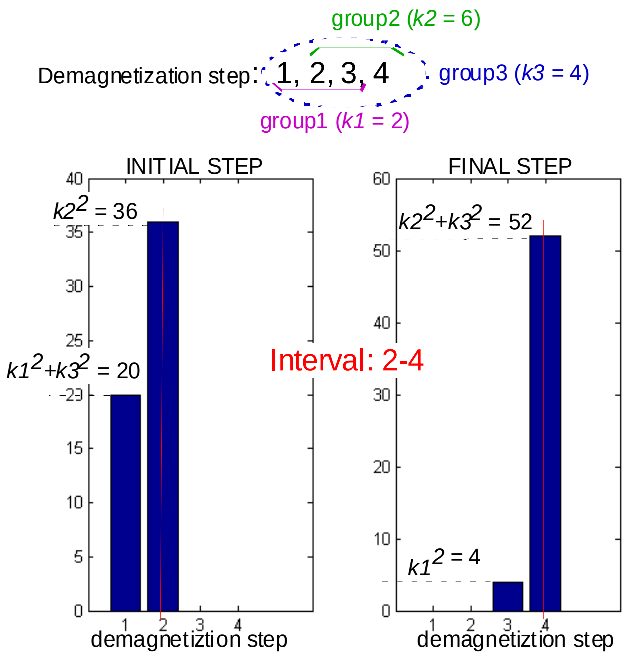

Figure I.3: Automatic determination of the demagnetization interval concept. Weighted histograms of initial and final steps. Example of a site with 4 demagnetization steps. There are three possible groups of VD filtered by interval. The group 2 (initial step 2 and final step 4) is the best represented (higher values of the histograms) and the one that defines the best characterized direction (k2=6); thus, it is the interval of the ChRM.

The VDP program includes a filtering menu with the weighted histograms and all filtering criteria. Additionally, there are some visualization windows including a display of the VD plotted in color maps corresponding with these filtering criteria. Moreover, some useful graphics, including separated stereographic projections from all subsets of the VD, the Woodcock (1977) diagram and a counter of directions before and after the filtering are displayed in this menu to help to decide the correct filtering parameters. The Woodcock (1977) diagram may be useful to discriminate the goodness of the filtering. This diagram is used to quantify the shape and anisotropy of the orientation matrix of any population of vectors in the spherical space (Scheidegger, 1965). Using the ratios of its normalized eigenvalues (S_1, S_2, S_3) in a way similar to the Flinn's diagram (Zingg, 1935 and Flinn, 1962) is helpful to determine anisotropies in the dataset. After an appropriate filtering, the S_1/S_2 clustering ratio and the total anisotropy of the orientation matrix (S_1/S_3) are expected to be increased for a well-defined ChRM direction. VC will show an enhancement of the girdling ratio (S_2/S_3) and the total eccentricity of the tensor (S_1/S_3).

I.2 Application to real data sets

In this section we show the potential of the VD approach when applied to two case studies involving real paleomagnetic data: a well-defined multi-component NRM in a site with tectonic purposes (ASN3 from Internal Sierras, Southern Pyrenees), and a large data set obtained from u-channels (Almonacid de La Cuba outcrop). Results are compared to those from three other techniques: visual inspection of demagnetization directions (PCA), the stacking routine (SR) and the linearity spectrum analysis (LSA). It is worth mentioning that we should not expect any consistent result in poor-quality sites after applying the VPD approach (or any other method).

I.2.1 Application to a site scale: multi-component NRM

Results for a paleomagnetic site (ASN3) from the Internal Sierras in the Southern Pyrenees with three components are presented here. This Cenomanian-Santonian site (10 standard demagnetized specimens) is affected by the Larra-Monte Perdido thrust system and the later Gavarnie thrust sheet. Apart from the primary Cretaceous direction, a post-folding (Eocene) reverse polarity remagnetization records the moderate CW rotation of the Guarga basement thrust which is the latest thrust affecting the area. The components have been isolated with standard *eye-ball* PCA fitting and using the stacking (SR), LSA and VD routines of the VPD software.

During PCA analysis one of the ten samples was rejected because of its inconsistency (n/N= 9/10, likely a core orientation error). Visualization of all VD with different colors for each sample gives us a global idea of the site and additionally helps us to reject this inhomogeneous specimen (Fig. I.4A). Results obtained with PCA for the intermediate and high unblocking temperature components were published by Oliva-Urcia and Pueyo (2007). Apart from a variable and low-temperature component, two stable components were defined during the thermal demagnetization procedure at the site scale: an intermediate temperature (between 250 and 460ºC; six or seven steps; D&I= 207º, -32º; α_{95}= 10º; k= 23) and a high temperature component (between 500 and 560ºC; three steps directed to the origin, D&I= 189º, 24º, α_{95}= 11º, k= 19). Different components can be distinguished visualizing the initial step of all VD (Fig. I.4B).

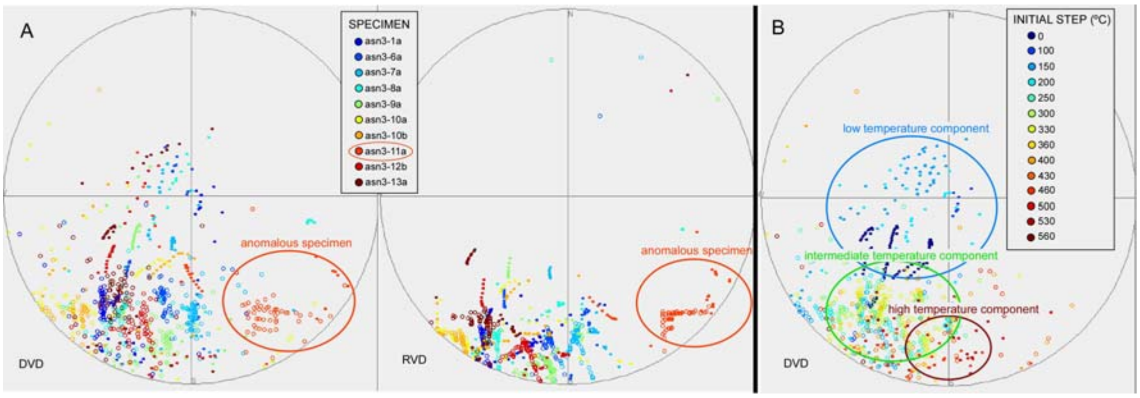

Figure I.4: Virtual Directions of ASN3 site. A) Color map: specimens or samples. B) Color map: initial step of each direction.

The ChRM direction for a stacked sample (SR, the mean of each step) is calculated rapidly after choosing the nine samples with demagnetization steps from 100 to 560ºC. A few obvious anomalous steps (mostly laboratory errors) were removed for further analysis. The stacked sample also helps to achieve a global idea of the paleomagnetic directions for the site. The unblocking windows for the three components are clearly recognizable (Fig. I.5A) and there is a good similarity with results from the PCA analysis of the stacking routine and the *eye-ball* fitting because of the good quality of the sample.

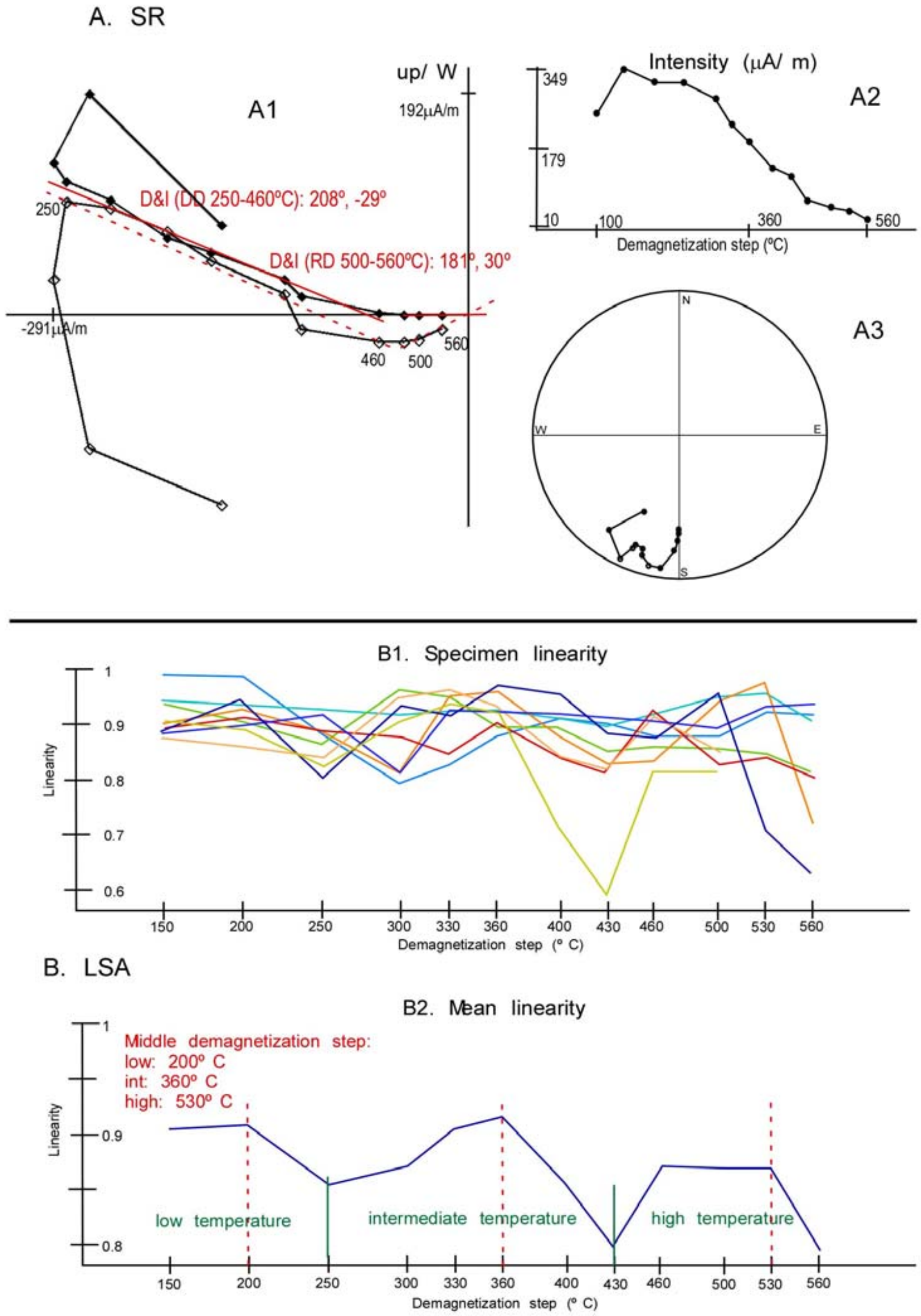

Figure I.5: A) Stacking routine (SR) for samples from site ASN3. The stacked sample calculates the mean direction for all samples from a site for each demagnetization step. A1) Orthogonal projection / Zijderveld (1967) diagram. A2) Equal area stereographic projection. A3) Intensity decay diagram. B) Determination of the demagnetization intervals for paleomagnetic data from site ASN3 using the spectrum of linearity (Schmidt, 1982). B1) Specimen linearity. B2) Mean linearity for all specimens of a site. Peaks of maximum linearity determine the middle demagnetization step of the intervals and minimum linearity ones are the extremes of the demagnetization windows.

The demagnetization intervals can also be calculated with the linearity spectrum analysis (LSA; Schmidt, 1982). LSA calculates the demagnetization interval in an automatic way looking for the best quality of directions. The term used to measure the quality is the linearity: *1-sin(MAD)*. The direction with longer demagnetization interval and maximum linearity is sought around the middle demagnetization steps for all specimens. The middle demagnetization step that determines the interval is the one with the maximum mean linearity of the site. Three intervals can be determined from the site mean-linearity diagram (Fig. I.5B); a low temperature component up to 250°C (around the middle step of 200ºC with maximum linearity), an intermediate unblocking temperature is defined between 250 – 430°C (middle step: 360ºC) and, finally, the high temperature component up to 560ºC (middle step: 530ºC). These ranges may slightly change within the individual samples but, as a rule, they are identical to those originally defined by Oliva and Pueyo (2007).

Moreover, we calculate the demagnetization interval leveraging the automatic technique described before (sub-section 1.1.1). We calculate the weighted histograms for the initial and final steps using the objectively filtered dataset (n≥3 and MAD<15º). Results are different for the difference and resultant virtual directions because there is more than one component and all intervals can only be observed using DVD. The weighted histograms for DVD show two local maxima that correspond with the demagnetization intervals of the two components (Fig. I.6). The high temperature interval is exactly the same and the intermediate temperature interval is defined by one step less but it is equivalent in meaning (from 300 to 460º).

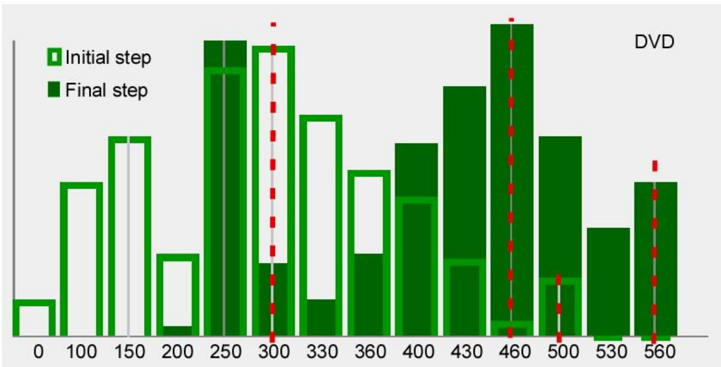

Figure I.6: Automatic determination of the demagnetization intervals using the weighted histograms technique for site ASN3. Only difference virtual directions objectively filtered (n≥3, MAD<15) are considered. Intervals are determined by local maximums of initial and final steps; interval 1: 300-460ºC, interval 2: 500-560ºC.

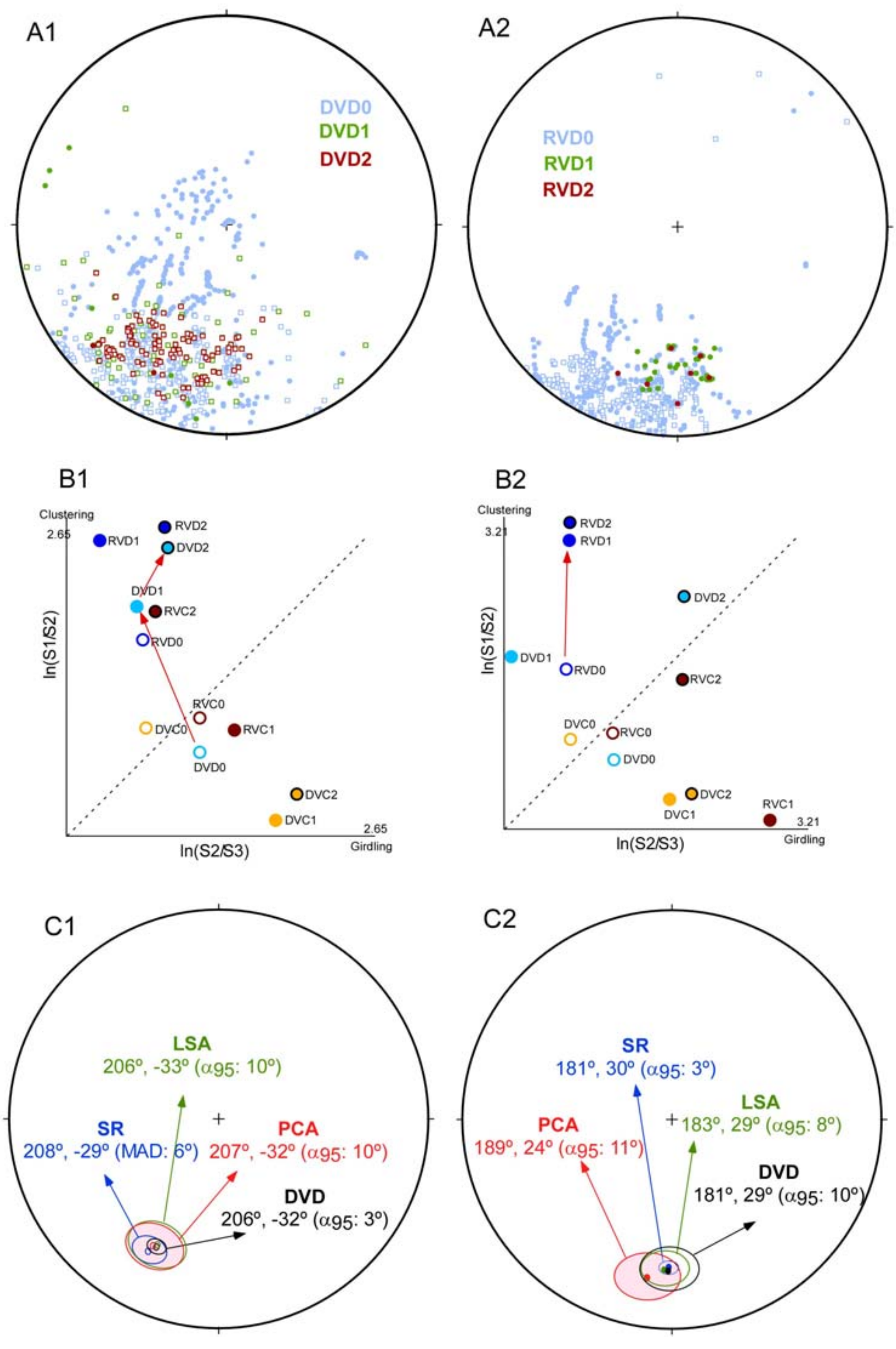

Figure I.7: A) VD from site ASN3 plotted on equal area stereographic projections. A1) DVD0: all difference virtual directions, DVD1: filtered by interval 250-460ºC (intermediate temperature component), DVD2: filtered by interval, number of steps (n ≥3) and MAD (<15). A2) RVD0: all resultant virtual directions, RVD1: filtered by interval 500-560ºC (high temperature component), RVD2: filtered by interval, number of steps (n≥3) and MAD (<15). B) Woodcock (1977) diagram. B1) Intermediate temperature component. B2) High temperature component. C) Means calculated with different methods. C1) Intermediate temperature component calculated with PCA, SR, LSA and DVD (n =7, MAD <15, interval: 250-460ºC). C1) High temperature component calculated with PCA, SR, LSA and RVD (n = 3, MAD <15, interval: 500-560ºC).

ASN3 (DD: 250-460ºC)	DEC (º)	INC (º)	α_{95}/MAD (º)	k	n/N
PCA	207	-32	10/-	23	9/10
SR	208	-29	-/6	-	9/10
DVD	206	-32	3/-	23	110/770
LSA (360)	206	-33	10/-	31	9/10

ASN3 (RD: 500-560ºC)	DEC (º)	INC (º)	α_{95}/MAD (º)	k	N
PCA	189	24	11/-	19	9/10
SR	181	30	-/3	-	9/10
RVD	181	29	10/-	43	7/892
LSA (530)	183	29	8/-	50	9/10

Table I.1: Paleomagnetic results for site ASN3 (intermediate and high temperature components). Virtual directions are filtered by the observed demagnetization intervals (250-460ºC and 500-560ºC) as well as the more objective filters (DVD2: n ≥3, MAD <15; DVD: n =7, MAD <15; RVD: n =3, MAD <15). Mean direction calculated with LSA is looked for around the middle demagnetization interval (intermediate component: 200ºC, high: 530ºC).

Using the particular procedure of this program, all virtual directions are calculated (RVD0: 892, DVD0: 770). For a multi-component NRM is essential to choose the correct demagnetization interval. The whole initial dataset is filtered by interval: the intermediate temperature component (250-460ºC) is calculated using difference directions and the high temperature component (500-560ºC) using resultant directions (Fig. I.7A). A second filter is applied trying to improve the quality of the selected directions: we select a minimum of three steps to define the direction as accurate as possible and we allow a maximum error (MAD) of 15º (110 DVD2 and 7 RVD2 remain). The application of filters in order to narrow both components increases the anisotropy of the orientation matrix (Fig. I.7B) as deduced from the Woodcock (1977) diagram.

However, after the filtering steps, the confidence angle of the intermediate direction is not comparable with the eyed-ball PCA fitting because the number of directions is different. Thus, in order to compare results, we filter the intermediate component with seven steps (Fig. I.7C, Table I.1). A common true mean direction (CTMD) in terms of McFadden and Lowes (1981) is found independently of the method used and the maximum deviation angle between means is 5º for the intermediate component. When the high unblocking temperature component is defined with fewer steps , PCA and the more automatic methods differ on an angle of 10º, although all of them share a CTMD (SR, LSA and RVD, really close between them, are included in the confidence angle of the PCA mean).

I.2.2 Application to automatic calculation to large data sets

To highlight the possibilities of the VD approach to a natural site with a large data set, we resort to an outcrop in Almonacid de la Cuba (Zaragoza, Spain). At the beginning of the 1st century AD, the largest dam (35 m) in the western world until the 16th century was built by the Romans in the vicinity of Cesaraugusta, now known as Zaragoza (NE Spain). The Almonacid de la Cuba reservoir completely overflowed at the end of the second century to give a total infill thickness of sediments of 25 m, 5 m of which are exposed by present-day river incision. Unfortunately, the exact dating of this uppermost exposure is not available.

Several standard paleomagnetic samples (both cores and plastic boxes) were taken (a sample every 5 cm) to search for a continuous record of secular variation throughout this period. Two u-channel samples (1.5 m length and 2x2 cm cross-section) were also collected from the studied outcrop (Fig. I.8) and were measured at 1cm stratigraphic intervals. IRM acquisition curves indicate the occurrence of low coercivity minerals, and thermomagnetic curves provide evidence for magnetite (dominant), iron sulfides (occasional) and hematite (rare) as magnetic remanence carriers (Pueyo et al., 2002). Results from stepwise demagnetization (both thermal and AF) of discrete samples allow us to differentiate two components: (1) an overprint due to the present geomagnetic field (PGF) and other viscous records (sampling, laboratory, etc.) that is identified up to 10 mT and (2) a stable ChRM that is identified from 100 to 350°C and from 20 to 60 mT. The SR run under the VPD of the lower u-channel sample confirms these intervals as the optimal demagnetization windows, that were helpful for design the filters to a large data set with a homogeneous demagnetization routine.

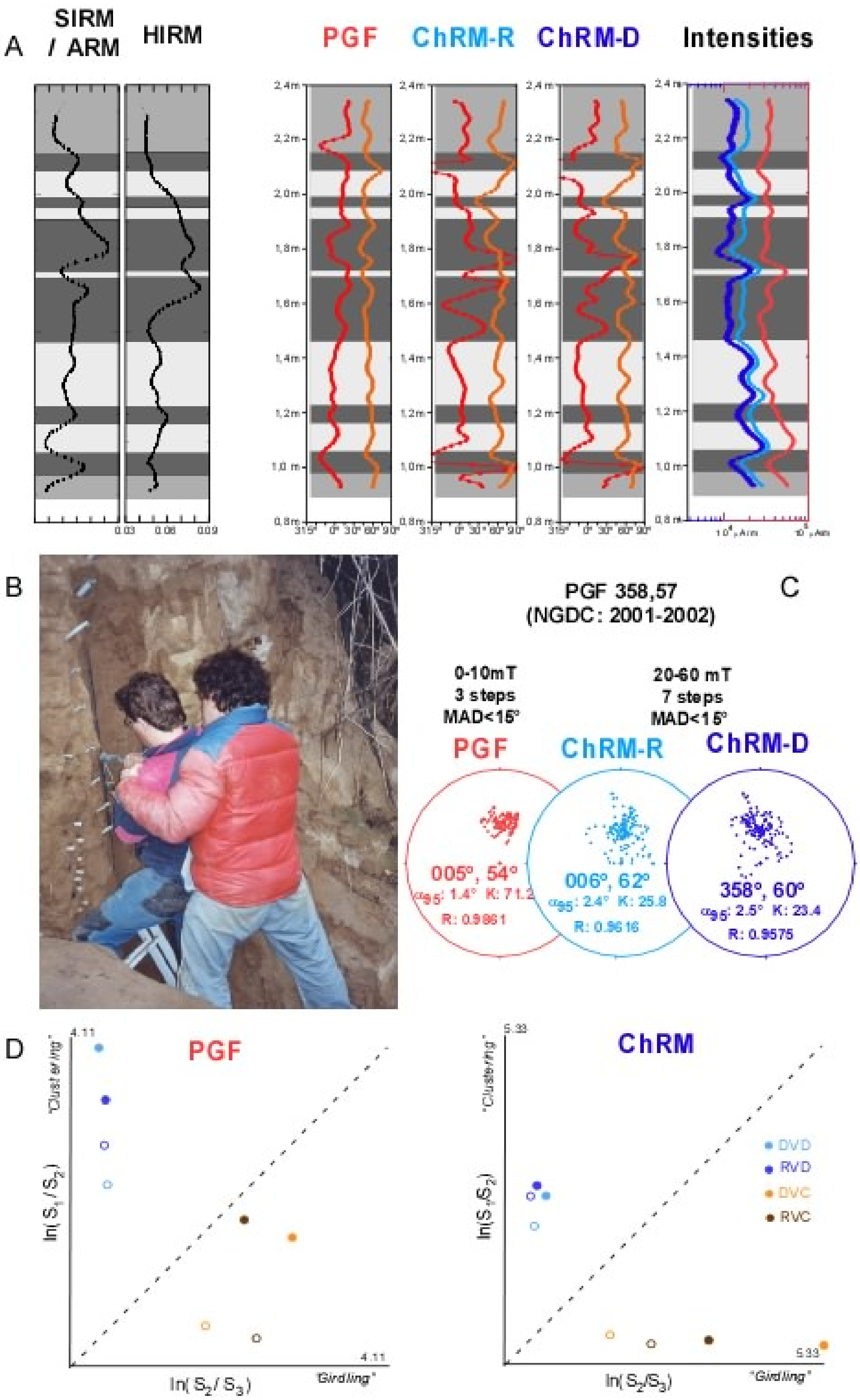

Figure I.8: Data from a u-channel sample from Almonacid de la Cuba sediments. A) Declination in red and inclination in orange. B) Sampling u-channels in a vertical outcrop. C) Equal area stereographic projection with the virtual directions for paleomagnetic data. Virtual directions filtered by interval: PGF from 0 to 10 mT (3 steps) and ChRM from 20 to 60 mT (7 steps) and MAD <15º. D) The Woodcock (1977) diagram for the PGF and ChRMs components. Open symbols: all data; solid symbols: filtered data.

In this case VPD helps to quickly estimate both components after applying the correct filters (Fig. I.8C). Only directions with MAD <15º are considered. The first component (PGF) is set between 0 and 10 mT; if we select three steps, only two directions (resultant and difference) per measured stratigraphic interval will result from the filtering. Since intermediate components are not necessarily directed toward the origin of the demagnetization plot, only the difference vectors have been considered. In any case, both VD sets show increases in the clustering ratios (Woodcock, 1977) (Fig. I.8D). The mean is well characterized (D&I= 005º, 54º; α_{95}= 1.4°; *k*= 71) and seems to be a slightly noisy record of the PGF, as deduced from the National Geophysical Data Center (NGDC) for the sampling site (D&I= 358º, 57º). The second filter between 20 and 60 mT includes seven demagnetization steps and gives a slightly different mean for the resultant and difference vectors (Fig. I.8C). This is likely caused by incomplete demagnetization that bias the resultant vectors. This ChRM drifts around the "expected" mean for the Roman period in the Iberian Peninsula (Pavón et al., 2009).

I.3 Availability and requirements

The program V*irtual Paleomagnetic Directions (VPD,* Fig. I.9*)* was developed to easily visualize the demagnetization data and to compare the results obtained with virtual directions (VD) and other classic methods: eye-ball inspection and fitting with principal components analysis (PCA), linearity spectrum analysis (LSA) and the stacking routine (SR). VPD was coded in Java to run the program in any operating system (*Linux, Mac, Windows*) on a Java Virtual Machine, as a single executable file with no special installation[1]. Principal Component Analysis (PCA) [Kirschvink, 1980] and part of the visualization menu have been inspired on the *Paldir* code developed by the University of Utrecht. The stacking algorithm [Scheepers and Zijderveld, 1992] is based on software *Gamsstack* [Pueyo et al., 2003] from Gams paleomagnetic laboratory (Montanuniversität Leoben, Austria) whereas LSA is detailed by Schmidt [1982].

[1] Java that can be easily downloaded and installed from the official site http://www.java.com/en/download. The Java SE 6 version is required. Software upgrades are available from http://www.igme.es/internet/zaragoza/aplicaInfor.htm.

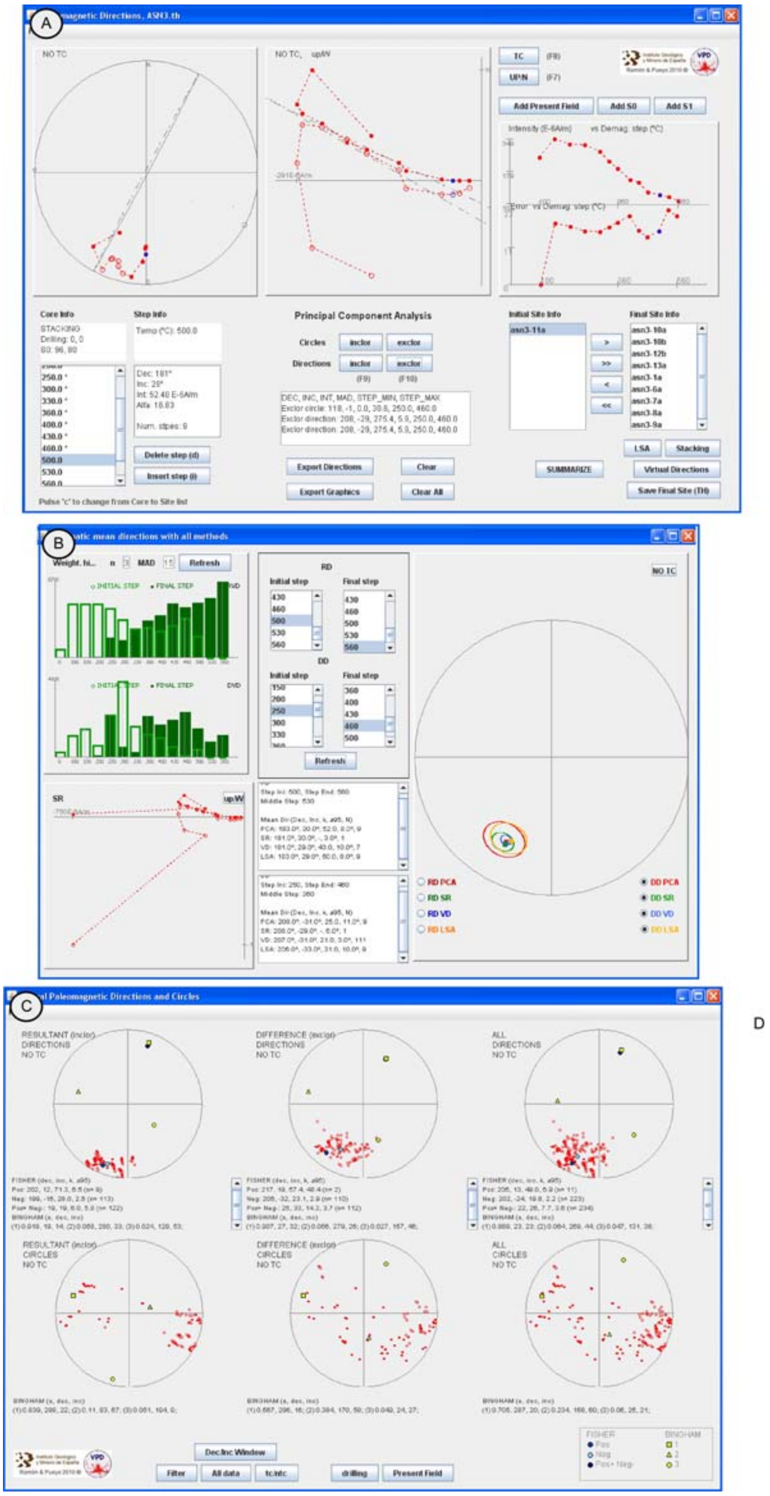

Figure I.9: VPD program. A) Main menu (sample level): stereographic projection, orthogonal projection, intensity decay graphic, visualization mode options, core/specimen/sample information, PCA menu, initial site and final site info-box, other methods buttons: LSA, SR, VD and summarize. B) Summarize window: weighted histograms, interval selection, SR orthogonal projection, ChRM calculated with all methods, stereographic projection of ChRM calculated with all methods (RD and DD). C) Virtual directions menu: stereographic projection with statistical information of resultant virtual directions (RVD), difference virtual directions (DVD), total virtual directions (VD), resultant virtual planes or circles (RVC), difference virtual circles (DVC) and total virtual circles (VC).

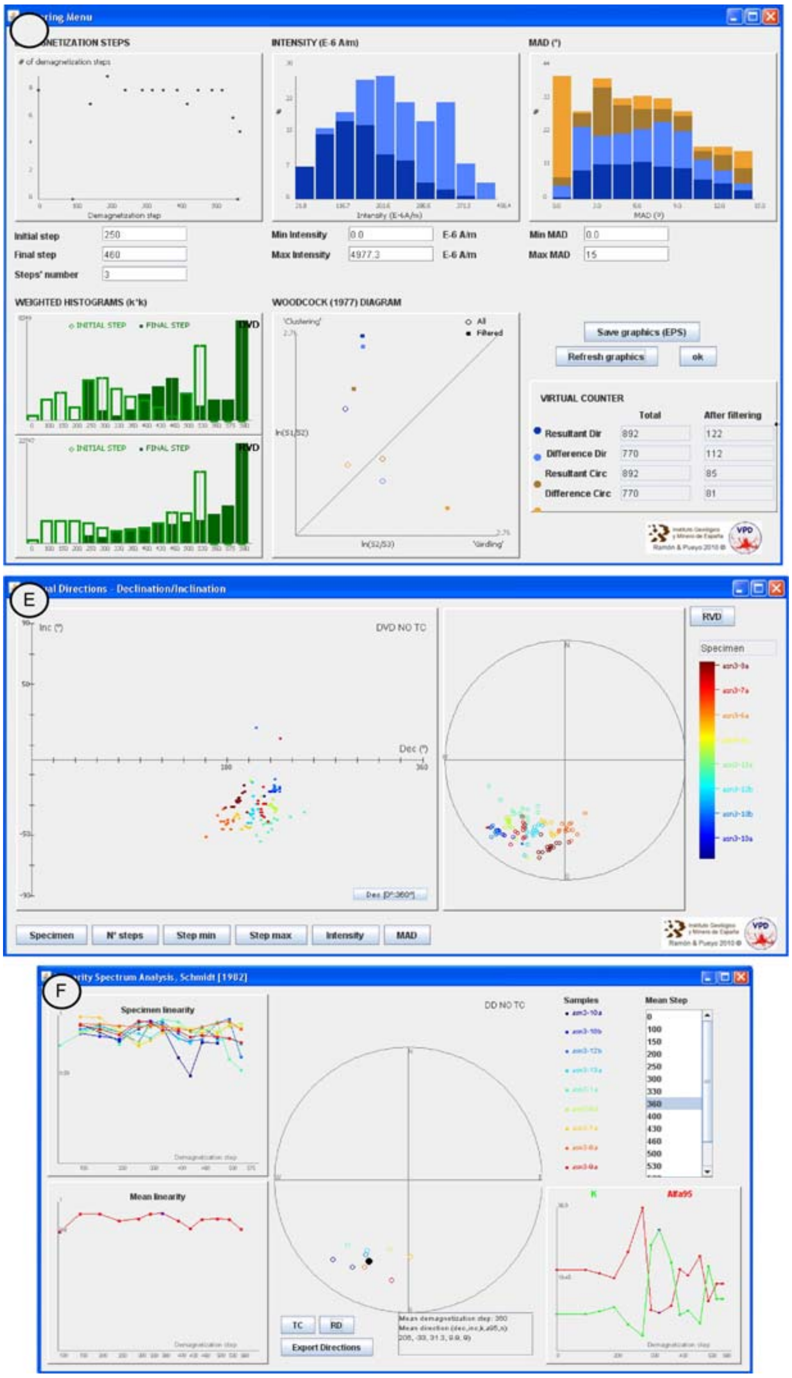

Figure I.9 (continued): D) Filtering window: number of demagnetization steps, frequency diagram of VD intensities, frequency diagram of VD MAD, filtering parameters (initial and final steps, number of steps, minimum and maximum intensity, minimum and maximum MAD), weighted histograms, orientation matrix control (Woodcock [1977] diagram), VD counter. E) Declination/inclination diagram with parameter selection to determine the color scale: specimen, number of steps, minimum step, maximum step, intensity and MAD. F) Linearity spectrum analysis window: specimen linearity, mean linearity of the site, stereographic projection of directions obtained with LSA with statistical information, mean demagnetization step selector. k and alfa95 of all mean directions calculated for each demagnetization step.

I.4 Conclusions

The virtual paleomagnetic directions (VPD) software is a useful tool for obtaining a global view of the paleomagnetic behavior of a site. The entire VD set allows researchers to obtain a rapid understanding of the magnetic behavior. Initial dataset can be filtered (minimum number of steps needed to define a direction, maximum error allowed, intensity and optimal demagnetization interval) to help estimating the NRM components. An automatic method is proposed to help determining the demagnetization intervals. Additionally, the program implements several existent methods to calculate the ChRM: principal component analysis (PCA by Kirschvink, 1980), stacking routine (SR by Scheepers and Zijderveld, 1992) and linearity spectrum analysis (LSA by Schmidt, 1982); which are really useful for checking the interval consistency of the data.

The VPD has been tested for a well defined multi-component character site and compared with other methods (PCA, SR, LSA) leading to similar and statistically indistinguishable results (all sharing a CTMD). Moreover, this tool is especially useful when dealing with homogeneous and large data sets. The ability to rapidly obtain large paleomagnetic data sets represents a growing problem for post-laboratory data processing. Large data sets (thousands of measurements), such as those derived from automatic instruments like the 2-G Enterprises SQUID magnetometer designed for u-channel samples, can be quickly generated. We apply this technique for a u-channel site with satisfactory results.

The VPD software allows a complete and friendly visualization of demagnetization data and allows conventional ChRM estimation approaches (eye-ball fitting by PCA of both directions and circles, stacking routine and linearity spectrum analysis) as well as the VD method with application of filters. The software package, with versatile output/input formats, allows fast and reliable processing of large data sets (see supplementary material).

II Appendix 2:

Paleomagnetic errors

Building on the idea of Appendix 1 about the reliability of paleomagnetic data, we want to control the errors caused by the geometry of folding from a theoretical point of view. With this work, we develop the mathematical modeling of several sources of error. In ideal conditions (perfect record of the paleomagnetic field direction and stable behavior in time) the paleomagnetic record could behave as an exact paleo-reference indicator. However paleomagnetic vectors are biased by numerous sources of scattering, like a low-quality primary record, natural scattering (e.g. secular variation), delaying time-gap during acquisition, poor magnetic stability over time, magnetic shallowing caused by sedimentary or tectonic load, several sources of instrumental limitations (incomplete cleaning, inability of isolation of components, creation of laboratory noise, etc.) and non-dipolar recordings of the magnetic field (Buttler, 1992; Voo and Torsuik, 2001; Tauxe, 2002; Kodano, 2012). Apart from these sources, some "structural" errors are controlled by the geometry of the deformation (Pueyo, 2010) and can be modeled and filtered. Controlling these errors we want to reduce the uncertainty.

An analysis of the implicit assumptions in paleomagnetic studies of fold and thrust belts reveals three possible sources of error with an intrinsic structural (geometric) control (Pueyo, 2010) (Fig. II.1):

Assumption 1) Laboratory procedures are able to completely isolate the original paleomagnetic vectors (Halls, 1978; Bailey and Halls, 1984; McFadden and McElhinny, 1988). When this fails, the subsequent overlapped paleomagnetic directions (e.g. primary record and the recent overprint) will display both the declination and the inclination errors, which will be controlled by the fold axis orientation, the degree of flank rotation (dip), the primary magnetic polarity as well as the degree of vector overlapping. In this case, the overlapped direction will be controlled by the structural position that will depend on the angular relationships between the original vector (including its polarity), the fold axis and the present field as well as the actual dip of the sampled bed and the intensity ratio between the primary and secondary (overlapped) intensities.

Some research has qualitatively focused this problem from an structural point of view (Dinarès and McClelland, 1991). More recently, an exhaustive and quantitative description of expected errors was devoted to this important issue (Rodríguez-Pintó et al., 2011, 2013). We assume that this important source of error has been finally understood and that it can be easily detected and corrected.

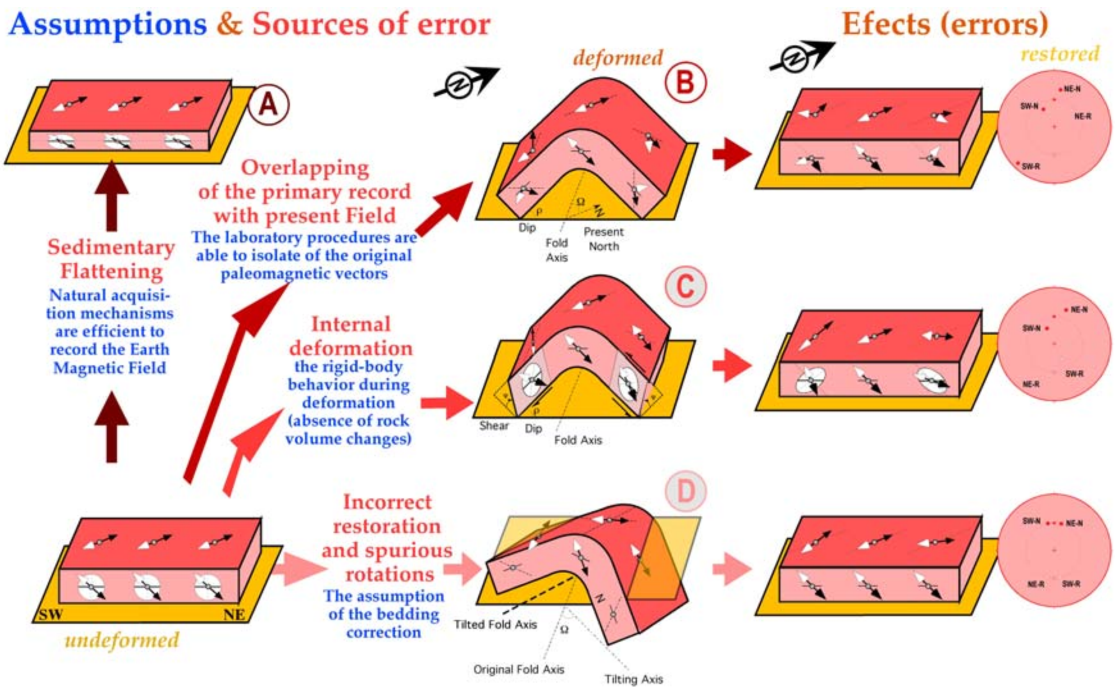

Figure II.1: Errors in paleomagnetic analysis (Pueyo A) Sedimentary flattening error. B) Structural control and modeled errors on overlapped paleomagnetic directions; the original vector has been overlapped with the present geomagnetic field, both vectors have the same intensity. D) Structural control on the magnitude of angular errors (declination) in incorrectly restored paleomagnetic directions. A plunging fold derived from an oblique tilting of a previous horizontal axis has been restored by the simple bedding correction.

Assumption 2) Rigid-body behavior during deformation and the absence of rock volume changes. When the rock volume undergoes active internal deformation during folding or shearing, the deformed paleomagnetic vectors will display again declination and inclination errors, but both polarities will behave similarly. In this case the errors will depend on the relation between the primary field orientation and the deformation tensor, which in fact, can be reduced to the orientation and magnitude of the shear in most cases.

This problem has been largely considered in paleomagnetic investigations (Cogné and Perroud, 1985; Lowrie et al., 1986; van der Pluijm, 1987; Kodama, 1988;

Stamatakos and Kodama, 1991). However a quantitative approach to the problem has still to be done. As it happens with overlapped directions, the final deformed vectors will depend upon the original vector, the fold axis and the magnitude of shear (strain tensor).

Assumption 3) Bedding correction is able to restore the bedding-vector couple to the ancient (paleo-) geographical reference system. This restoration may fail in complex deformation zones affected by non-coaxial or inclined axes of deformation (conical, plunging, forced folds, etc; see MacDonald, 1980 and Chan, 1988; spurious rotation by Pueyo et al., 2003a). In this case only the paleomagnetic declination will show deviations (spurious or apparent rotations). These deviations will be a function (non-coaxial case) of the obliquity (external rotation) of the deformation axes as well as of their magnitudes (e.g. degree of flank rotation for the original fold and amount of secondary tilting).

Much quantitative research has been done in this topic for the last years (Zotkevich, 1972; Scott, 1984; Sellés-Martínez, 1988; Setiabudidaya et al, 1994; Stewart, 1995; Weinberger et al., 1995; Weil et al., 2000; Pueyo et al., 2003a and 2003b; Weil, 2006 among others) but a numerical control is still necessary to rapidly evaluate this error when processing large datasets.

All these errors may cause severe problems in the so-called stability tests: all the three sources of error will change the result of the fold test (Weil and Van der Voo, 2002) following a false synfolding magnetization that may display also an artificial oroclinal bending of the dataset (Elredge et al., 1995). A fictitious negative reversal test may be derived from the overlapping of vectors (very severe) and the non-rigid-body behavior of the rock volume (internal deformation). Moreover, to detect these errors Pueyo (2010) also proposes the inclination-dip diagram (Fig. II.2 & Table II.1). All these sources of error reduce the reliability criteria established for paleomagnetic data (Van der Voo, 1990).

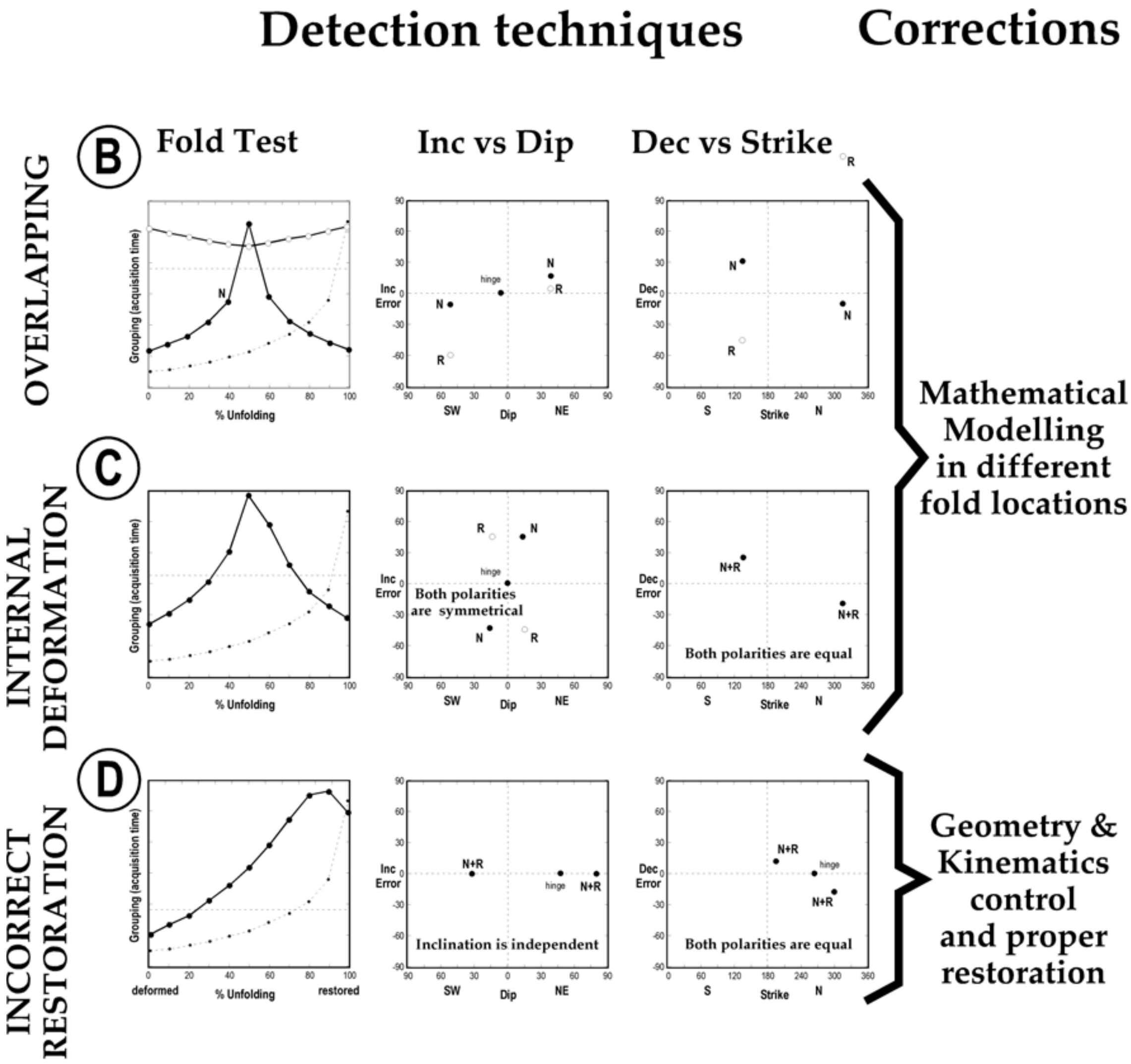

Figure II.2: Detection techniques of errors in paleomagnetic analysis (Pueyo, 2010).

	Error type	Source	Variables	Dec error	DEC *vs* Strike	Inc error	INC *vs* Dip	Fold test	Differential effect on Polarity	Polarity change	Reversal Test	Stereonet anisotropy
1	**Non-averaged secular variation**	insufficient sampling	n +/- sample distribution	YES (small)	NO	YES (small)	NO	NO	NO	NO	NO	YES
2	**Inclination flattening**	sedimentary load	original field (P), lithostatic load	NO	NO	YES	NO	NO	NO	NO	NO	YES
3	**Overlapping of components**	unefficient demagnetization	original field (P), fold axis orientation (α,β), secondary field (S), obliquity (Ω), int.P/int.S (r)	YES	YES	YES	YES	YES synfolding or non-significant	YES	YES (extreme cases)	YES	YES
4	**Internal deformation**	simple or pure shear during deformation	original field (P), fold axis orientation (α,β), obliquity (Ω), shear (γ) (strain tensor: D)	YES	YES	YES	YES	YES synfolding or non-significant	NO	NO	YES	YES
5	**Incorrect restoration** (complex structures)	non-commutative character of the deformation history	original field (P), fold axis orientation (α1,β1), secondary folding (α2,β2), obliquity (Ω)	YES	YES	NO	NO	YES synfolding or non-significant	NO	NO	NO	NO

Table II.1: Errors in paleomagnetic analysis (Pueyo, 2010).

II.1 Overlapping errors

We describe in this section the mathematical formulation needed to characterize the overlapping. A full description with a real example is presented by Rodriguez-Pintó et al. (2011 and 2013a). The mathematical modeling considers two paleomagnetic components overlapping in a cylindrical fold. To simplify the model, a horizontal flat bed and a primary magnetic vector (*P*) recorded in the rock are assumed. The rock pile is first folded (P_F). After a given time gap, a secondary component (*S*) overprints the primary signal and both components are overlapped (P_O). Bedding correction with respect to the primary component produces the paleomagnetic error that we want to characterize (declination and inclination error) (Fig. II.3 & II.4). We summarize the variables involved and describe the procedure step by step:

P→ Primary paleomagnetic vector. Vectors are characterized by its declination, inclination and intensity (P_{dec}, P_{inc}, $|P|$) or by its Cartesian coordinates (P_x, P_y, P_z) (see *Coordinates conversion).

P_F→ Folded paleomagnetic vector (before overlapping).

P_O→ Folded and overlapped paleomagnetic vector.

P_R→ Restored paleomagnetic vector.

S→ Secondary vector.

r→ P/S ratio, the degree of overlapping between the two components.

α,β→ Bedding plane, *α:* strike, *β:* dip. The fold axis orientation is equal to the strike and the plunge is considered null. The obliquity *Ω* is the angle between the primary declination (P_{dec}), and the fold axis trend $\phi = \alpha$.

*Coordinates conversion:

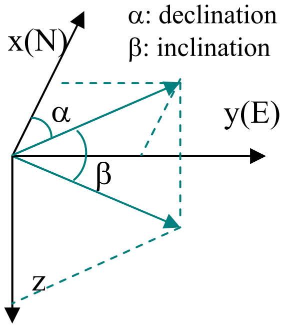

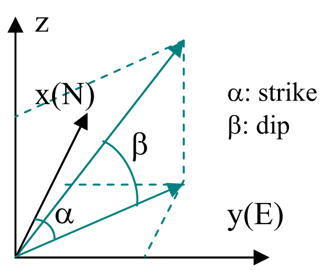

$$\alpha = a\tan(y/x)$$

$$\beta = a\tan(z/\sqrt{x^2+y^2}$$

(quadrant arcotangent)

$$x = \cos\alpha \cdot \cos\beta$$

$$y = \sin\alpha \cdot \cos\beta$$

$$z = \sin\beta$$

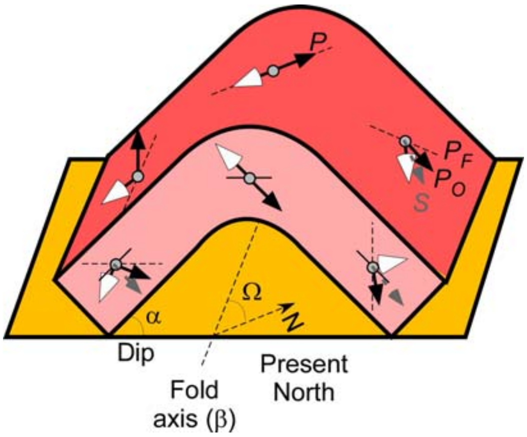

Figure II.3: Block diagram of overlapping error: the original vector has been overlapped with the present geomagnetic field; both vectors have the same intensity.

1) Rotation of the paleomagnetic vector during foliation:

$$P_F = R(\alpha, \beta) \cdot P$$

where *R* is the rotation matrix

$$R(\phi, \Psi) = \begin{pmatrix} (\cos\phi)^2 \cdot (1-\cos\Psi) + \cos\Psi & \cos\phi \cdot sen\phi \cdot (1-\cos\Psi) & sen\phi \cdot sen\Psi \\ \cos\phi \cdot sen\phi \cdot (1-\cos\Psi) & (sen\phi)^2 \cdot (1-\cos\Psi) + \cos\Psi & -\cos\phi \cdot sen\Psi \\ -sen\phi \cdot sen\Psi & \cos\phi \cdot sen\Psi & \cos\Psi \end{pmatrix}$$

being ϕ the trend of the horizontal axis rotation and Ψ the magnitude of rotation; since the plunge of the fold is negligible, the degree of limb rotation is equal to the dip of the limb (β).

2) Overlapping in the folded state:

$$P_O = P_F + S/r$$

3) Restoration of the overlapped paleomagnetic vector (without considering the secondary vector). The inverse rotation matrix is *R* with opposite magnitude of rotation:

$$P_R = R(\alpha, -\beta) \cdot P_O$$

4) Paleomagnetic error (ε_{dec}, ε_{inc}):

$$\varepsilon = P - P_R$$

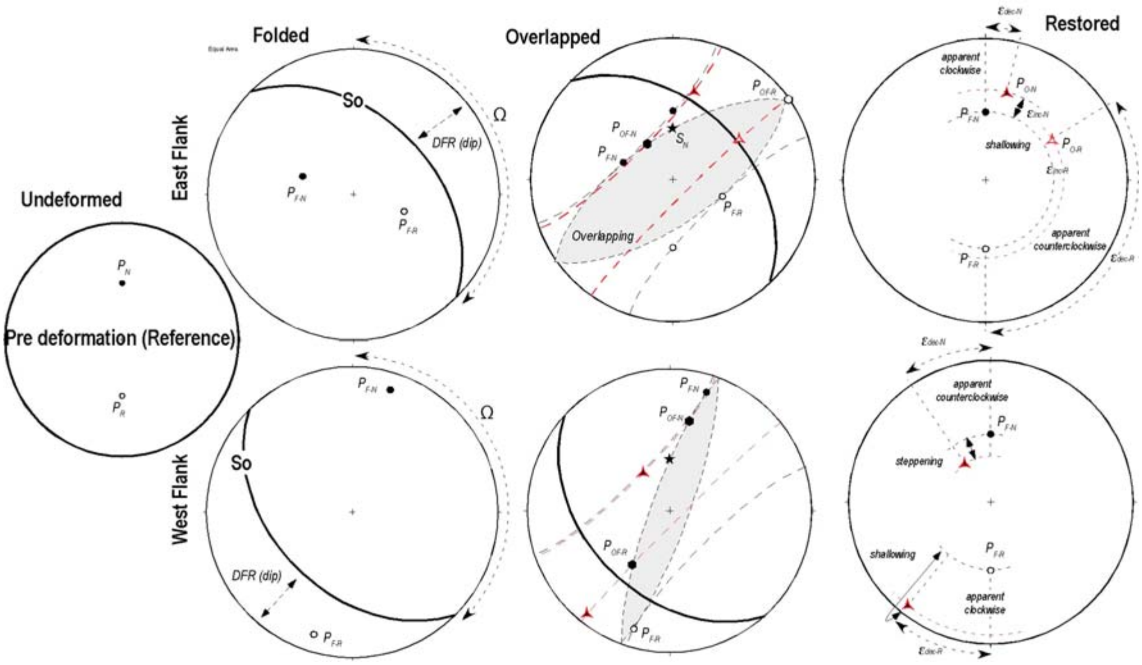

Figure II.4: Lower hemisphere stereographic projections showing different states of the magnetic record during folding, overlapping and restoration of Po. The block diagrams show four states. From left to right: 1) undeformed state (normal and reverse polarity), 2) folded position of the primary vectors, 3) folded and overlapped and 4) overlapped vectors restored to the horizontal. Note that the secondary component is assumed to be normal polarity.

Therefore, the scattering is basically controlled by the relationship between the primary and secondary magnitudes (*r* or *P/S* ratio), and the angular relationships of the paleomagnetic components respect to the fold geometry (fold axis orientation and dip of bedding planes). With this mathematical model and the excel macro developed (see supplementary material), we can calculate the declination and inclination errors caused by the overlapping of two components with a particular structural setting.

We simulate two examples (Fig. II.5) showing the paleomagnetic error caused by two similar overlapped vectors (P: 0º, 50º and S: 0º, 60º) and its scattering depending on the structural position. In this case, the error increases with the verticality of the limbs, and the parallel orientation of the primary vector with respect to the fold axis (obliquity(Ω)=0º) causes the highest declination errors while perpendicular orientation (Ω=90º) causes the highest inclination errors.

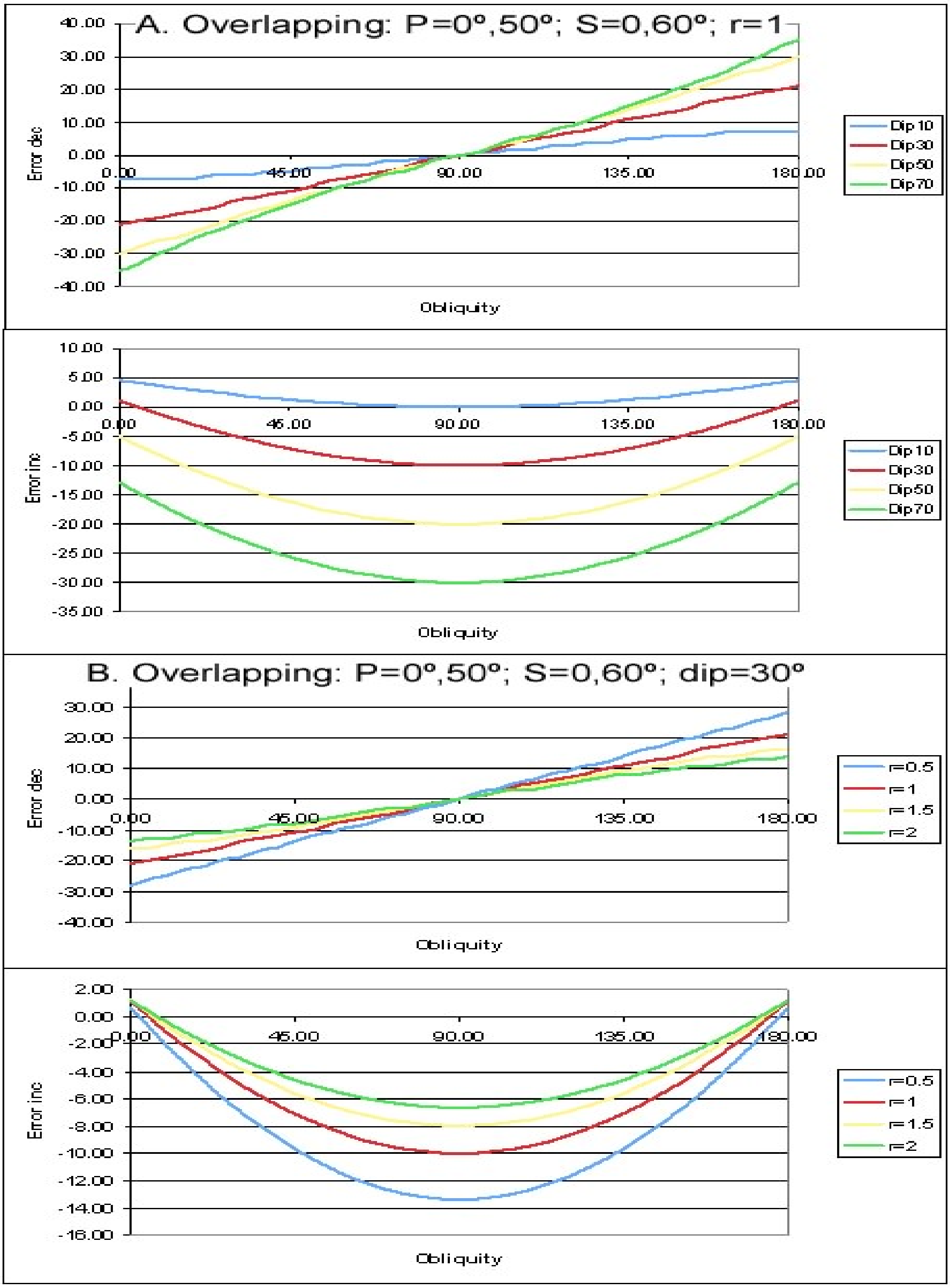

Figure II.5: A) Overlapping simulation with constant P/S ratio (r=1). Declination and inclination paleomagnetic error caused by the overlapping of a primary (P: 0º, 50º) with a secondary vector (S: 0º, 60º) in different structural areas (fold axis from 0º to 180º and dip of 10º, 30º, 50º and 70º). B) Overlapping simulation with constant dip (30º). Declination and inclination paleomagnetic error caused by the overlapping of a primary vector (P: 0º, 50º) with different proportions (r=0.5, 1, 1.5 and 2) of a secondary vector (S: 0º, 60º) in different structural areas (fold axis from 0º to 180º).

II.2 Shear errors

This is a preliminary model in which we describe a particular case of internal deformation: simple shear occurs in the flanks of a fold with flexural flow. Strain is only found in one direction, perpendicular to the fold axis. In that case, the paleomagnetic error depends on the structural position (fold axis and dip) and the magnitude of shear (Fig. II.6 & II.7). On the other hand, this error can be modeled for any kind of internal deformation provided that the strain tensor is known. Moreover, in this model there is another assumption: paleomagnetic vector behaves as a passive marker with lineal deformation. We now describe the variables and the mathematical equations step by step:

P→ Primary paleomagnetic vector.

P_F→ Folded paleomagnetic vector (before deformation).

P_D→ Folded and deformed (by simple shear) paleomagnetic vector.

P_R→ Restored paleomagnetic vector (without considering deformation).

α,β→ Bedding plane, α: strike, β: dip. α is the fold axis direction. The obliquity Ω is the angle between the primary declination (P_{dec}), and the fold axis trend (α).

γ→ Simple shear, elongation along the axis; ψ→ angle of simple shear ($\gamma = tg\psi$). The direction of simple shear is perpendicular to the bedding plane (α+90º, β)

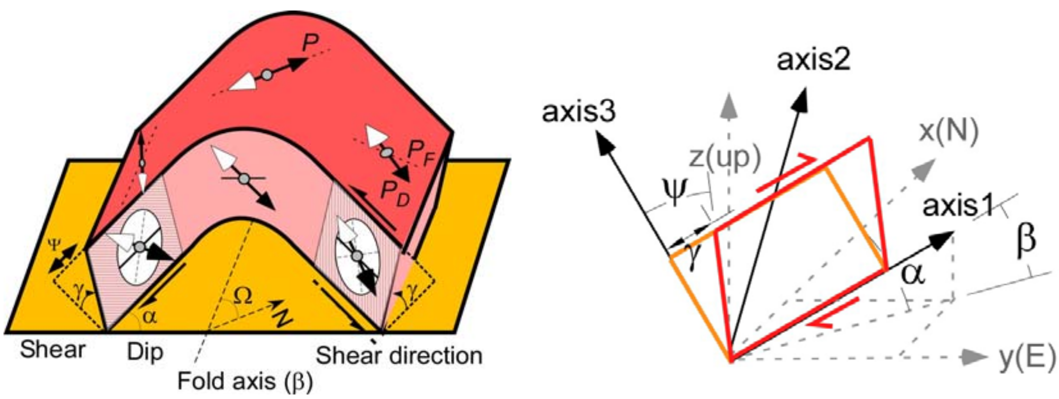

Figure II.6: Simple shear description. γ=tg(ψ) is the elongation and α, β the shear direction (axis1).

1) Rotation of the paleomagnetic vector during foliation. The rotation matrix is the same as in the previous section:

$$P_F = R(\alpha,\beta)\cdot P$$

2) Deformation by simple shear perpendicular to the fold axis. The paleomagnetic vector behaves as a passive marker:

$$D = A(\alpha + 90, \beta)' \cdot S(tg\psi) \cdot A(\alpha + 90, \beta)$$

$$P_D = D \cdot P_F$$

D is the symmetric strain tensor: $D = A' \cdot S \cdot A$ where the matrix A is the coordinate system defined by the eigenvectors and S is the matrix of the eigenvalues:

$$S(\gamma) = \begin{pmatrix} 1+\gamma & 0 & 0 \\ 0 & 1 & 0 \\ 0 & 0 & 1 \end{pmatrix}, \; A(\alpha, \beta) = \begin{pmatrix} axis1 \\ axis2 \\ axis3 \end{pmatrix}$$

$$axis1 = \begin{pmatrix} \cos\alpha \cdot \cos\beta \\ \sin\alpha \cdot \cos\beta \\ \sin\beta \end{pmatrix} \qquad axis2 = \begin{pmatrix} \sin\alpha \\ -\cos\alpha \\ 0 \end{pmatrix} \qquad axis3 = \begin{pmatrix} -\cos\alpha \cdot \sin\beta \\ -\sin\alpha \cdot \sin\beta \\ \cos\beta \end{pmatrix}$$

3) Restoration of the deformed paleomagnetic vector (without considering the deformation):

$$P_R = R(\alpha, -\beta) \cdot P_D$$

4) Paleomagnetic error:

$$\varepsilon = P - P_R$$

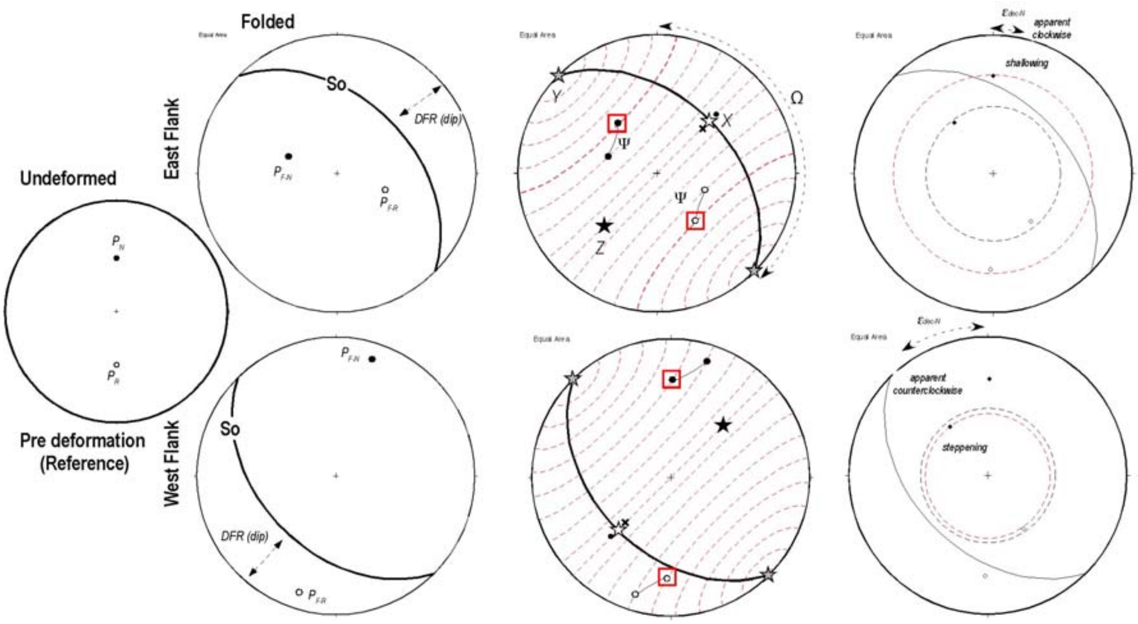

Figure II.7: Stereographic projections showing the different states of magnetic record during the folding, deformation and restoration processes.

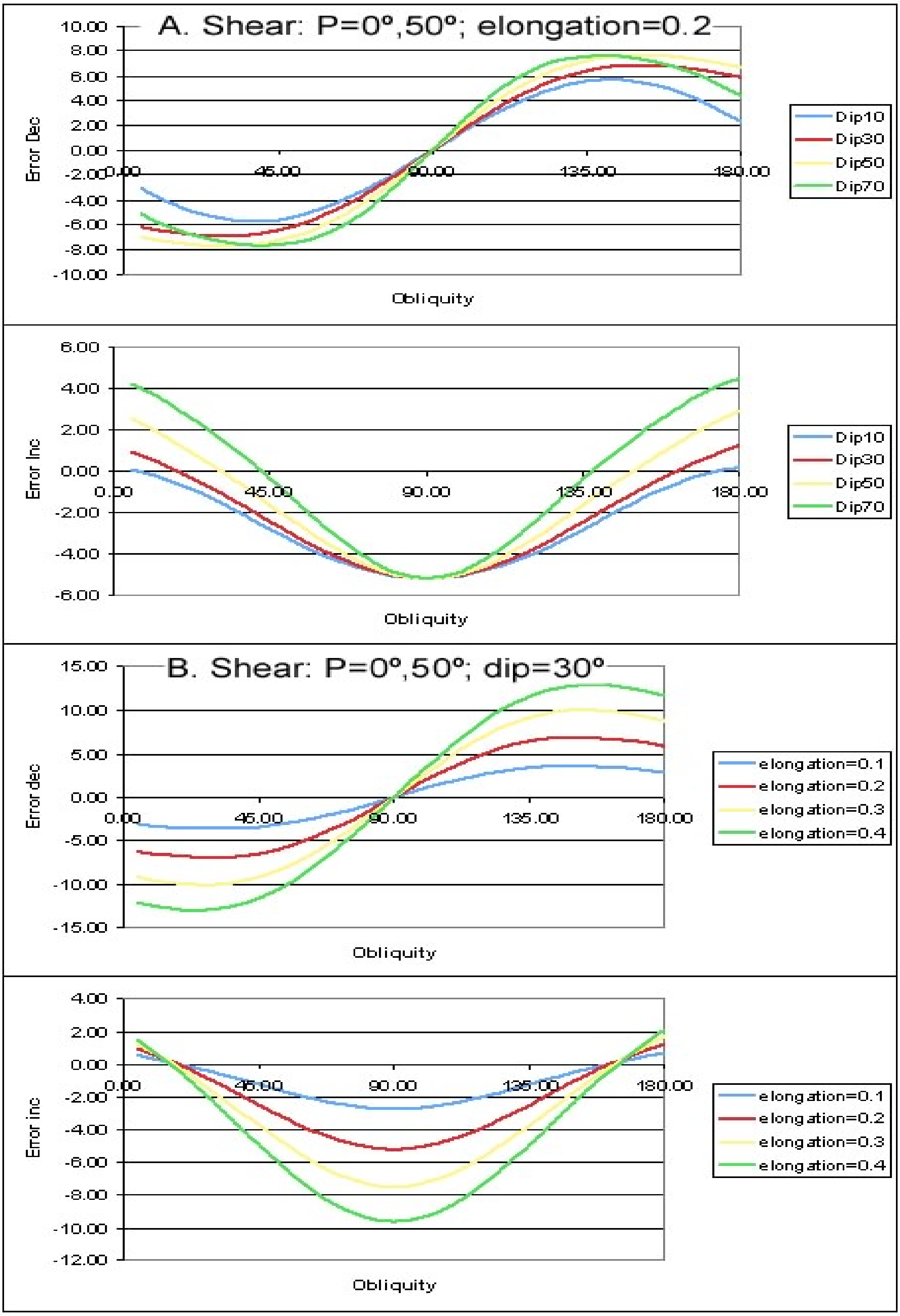

Figure II.8: A) Simple shear simulation with constant elongation (γ=0.2) for different structural areas (fold axis from 0º to 180º and dip of 10º, 30º, 50º and 70º). B) Simple shear simulation with constant dip (β=30º) for different magnitudes of deformation (γ=0.1, 0.2, 0.3 and 0.4) and structural areas (fold axis from 0º to 180º).

This error is basically controlled by the magnitude of deformation (γ) and the orientation of the shear (*Ω* and β). We simulate two examples (Fig. II.8) that show the paleomagnetic error caused by a simple shear perpendicular to the fold axis. As in the previous case for the same primary vector (P: 0º, 50º) the parallel orientation of this paleomagnetic vector with respect to the fold axis (Ω=0º) causes the highest declination errors while the perpendicular orientation (Ω=90º) causes the highest inclination errors. Definitively, large values of elongation cause higher paleomagnetic errors, in the same way that larger overlapping ratios caused higher errors in the previous case.

II.3 Superposed folding errors

We describe here a preliminary model of error produced by two steps of folding or tilting wrongly restored (bedding corrected) or after apparent fold axis correction (untilting of the perpendicular). After the two steps of folding we have a resultant plunging fold. The restoration procedure for a tilting fold is: 1) rotate with an axis perpendicular to the fold trend and a magnitude equal to the plunge and 2) rotate with the resultant bedding plane. Previous qualitative and quantitative analysis were performed on the 60's. Recently, Pueyo (2000) and Pueyo et al. (2002) have derived nomograms to quantify potential errors in paleomagnetic data. However, this is not valid in this case because the tilting is not from the original fold but caused by two steps of folding or tilting (Fig. II.9 & II.10). We here describe the variables and the mathematical equations step by step:

P→ Initial paleomagnetic vector.

P_F→ Folded paleomagnetic vector (after two steps of folding, with S_1 and S_2).

P_{AFAC}→ Paleomagnetic vector after apparent fold axis correction.

P_R→ Restored (fold axis correction + bedding correction) paleomagnetic vector.

α_1,β_1→ Tilting plane S_1 (strike and dip); $pole_1(\alpha_1\text{-}90, 90\text{-}\beta_1)$: pole of the plane. The first fold axis has null plunge and a trend equal to the strike (α_1). The magnitude of rotation is equal to the dip (β_1).

α_2,β_2→ Tilting plane S_2 (strike and dip). The second fold axis has null plunge and a trend equal to the strike (α_2). The magnitude of tilting is equal to the dip (β_2).

α_3,β_3→ Resultant bedding plane (strike and dip); *pole*$_3(\alpha_3$*-90, 90-*$\beta_3)$*:* pole of the plane.

fa$_3$(*trend*$_3$*,plunge*$_3$*)*→ Resultant fold axis.

$\alpha_{AFAC},\beta_{AFAC}$→ Bedding plane after apparent fold axis correction; *pole*$_{AFAC}$*:* pole.

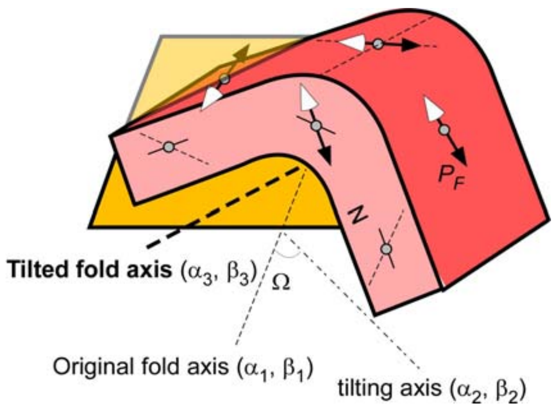

Figure II.9: Block diagram for a incorrectly restored tilted fold caused by two steps of foliation.

1) Double rotation of the paleomagnetic vector with steps of tilting S_1 and S_2:

$$P_F = R(\alpha_2,\beta_2)\cdot\left[R(\alpha_1,\beta_1)\cdot P\right]$$

2) Resultant bedding plane and fold axis after the second step of folding:

$$pole_3 = R(\alpha_2,\beta_2)\cdot pole_1 \rightarrow \alpha_3,\beta_3$$

$$fa_3 = R(\alpha_2,\beta_2)\cdot fa_1 \rightarrow trend_3, plunge_3$$

3) Apparent fold axis correction, to eliminate the plunge the resultant fold (fa_3):

$$P_{AFAC} = R(trend_3\text{–}90,-plunge_3)\cdot P_F$$

$$pole_{AFAC} = R(trend_3\text{–}90,-plunge_3)\cdot pole_3 \rightarrow \alpha_{AFAC},\beta_{AFAC}$$

4) Incorrect restoration of the folded paleomagnetic vector with the resultant bedding plane after apparent fold axis correction:

$$P_R = R(\alpha_{AFAC},-\beta_{AFAC})\cdot P_{AFAC}$$

5- Paleomagnetic error:

$$\varepsilon = P - P_R$$

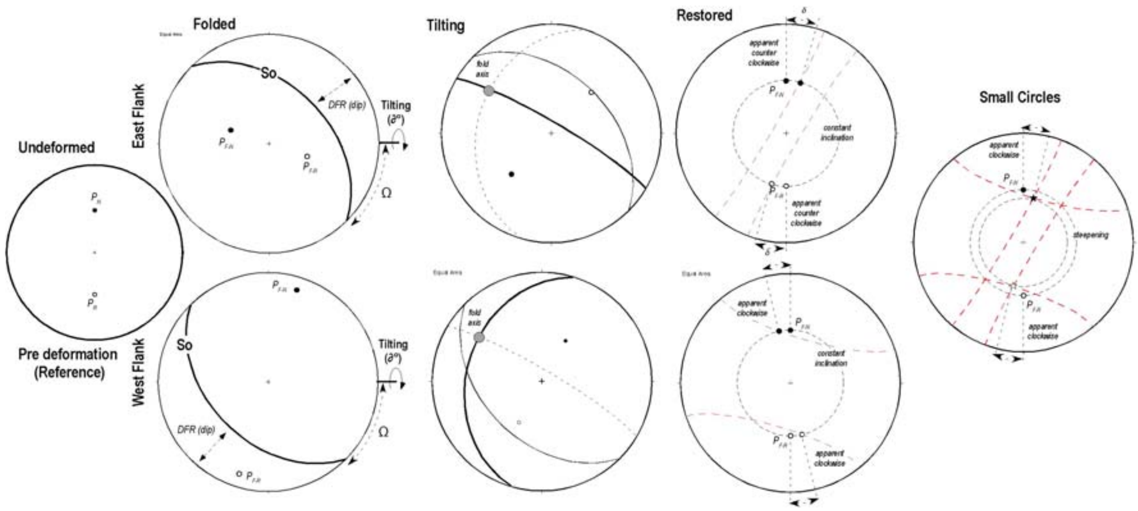

Figure II.10: Stereographic projections showing the different states of magnetic record during two steps of folding and later restoration.

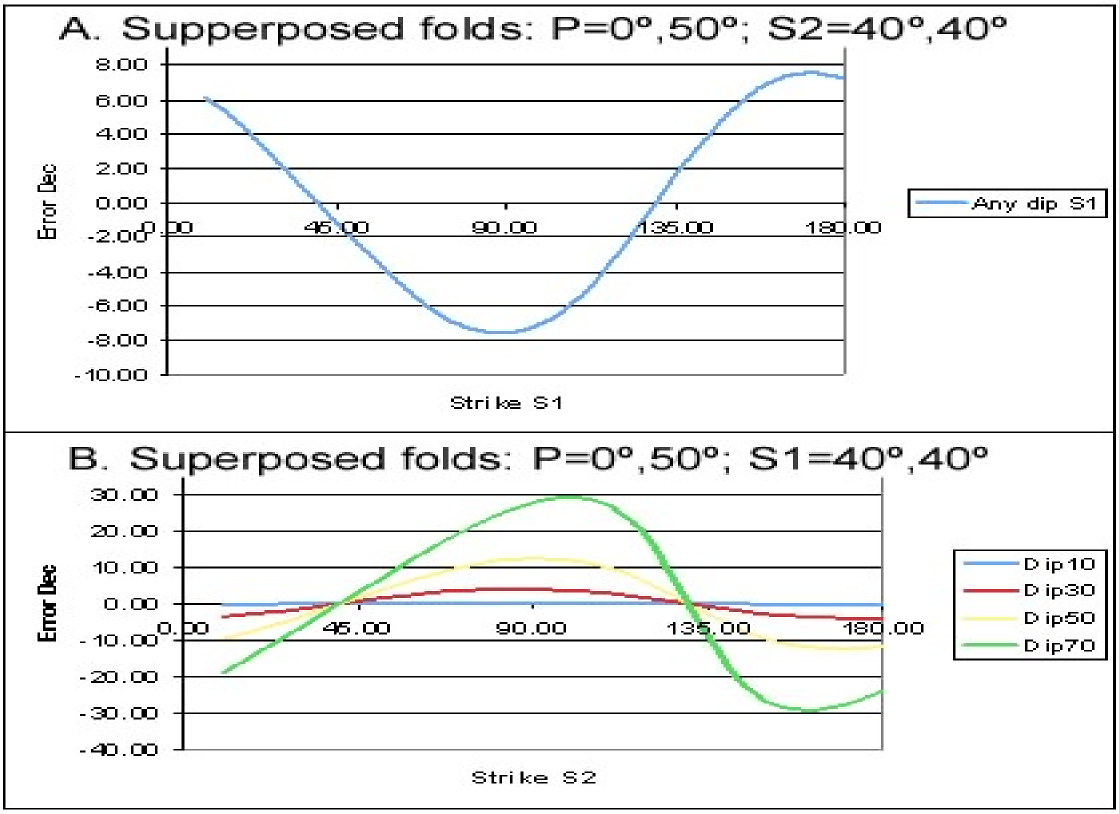

Figure II.9: A) Superposed folds simulation with constant S_2 (α_2=40º, β_2=40º) for different S_1. B) Superposed folds simulation with constant S_1 (α_1=40º, β_1=40º) for different S_2.

Superposed folds wrongly restored produce error only in the paleomagnetic declination and not in the inclination. The deviation is a function of the two bedding planes. We simulate two examples (Fig. II.11) which show the scattering error depending on S_1 and S_2. The magnitude of rotation of the first step of folding is well restored (β_1) but not the magnitude of rotation of the second step (β_2) that is proportional to the declination error.

Further analysis must be done, particularly in the shear and superposed folding error, but the characterization of these errors constitutes a great help for the identification of the source of error and its later correction.

Supplementary material

The work done with this thesis is an open door for further researches. Therefore, we pretend with the contents of the supplementary CD that methods and simulations can be reproduced and used as starting point for incoming studies. We detail the content of each folder.

Analog models

Files *marzal.ts* and *balzes.ts* are gOcad surface objects. They are the reconstruction of the analog models described in Sections 3.2.1 and 3.2.2 used to test the restoration methods. In order to restore the surface using the paleomagnetic constraint we need to select as “Default gu values” (in the Parameterizer2D window) the property with interpolated paleomagnetic vectors.

Piecewise restoration

The piecewise restoration code is programmed in *Matlab version 6.5* and needs to be run from Matlab. We include some simulations performed in this thesis (*simulation_sanMarzal.m, simulation_balzes.m and simulation_mapView.m*), the fold *restPmag* that contains the Matlab functions and the fold *ExampleData* with the files of initial surfaces to restore. To run the simulations we need to include this fold in the workpath. We detail the data and functions organization and flow:

Initial data:

1) Triangulated initial surface: nodes (*X,Y,Z*) and vertices of triangles (*tri*).

2) Polarity of triangles of initial surface (normal polarity: *pol* = 0).

3) Pin-element (starting point or line: *pin* = 1).

4) Paleomagnetism (no data value: *pmag0 (dec,inc)* = Inf, Inf) and its confidence angle (by default: where paleomagnetism is defined *alfa95* = 0 and where is undefined *alfa95* = 360). Reference unrotated data.

Restoration process:

1) Optional; extrapolation of scattered paleomagnetism:

[pmag_xyz,pmag_decInc]=extrapolatePmagB(tri,X,Y,Z,tri2,X2,Y2,pmag0,ref,pol);

pmagExtrap=mean(pmag_decInc);

decPmag=pmagExtrap(1,:,1); incPmag=pmagExtrap(1,:,2);

2) Flattening (initial paleomagnetic data is also flattened, only the resultant declination value is used in the fitting process):

[tri2,X2,Y2,azimuth,dip,pmag] = flattening3(tri,X,Y,Z,pol,decPmag,incPmag);

3) Fitting (with iterating process if paleomagnetism is not hard [α95 ≠ 0] and free rotation is allowed):

[tri3,X3,Y3,orderTri]= translationRotation(tri,tri2,X2,Y2,pmag,alfa95,ref,pin);

n =maximum number of iterations;

[X3,Y3]=iteratingB(tri,tri2,X3,Y3,alfa95,pmag,ref,n,orderTri,pin);

4) Welding:

[X4,Y4] = welding(tri,tri2,X3,Y3);

5) Calculus of dilation and deformation (relation between major and minor axis and direction of major axis):

d=dilation(tri2,X2,Y2,tri,X4,Y4);

[rel,ang]=deformation2(tri,X4,Y4,tri3,X3,Y3);

6) Visualization of results:

figure; trisurf(tri,X4,Y4,zeros(size(X4)),d); hold; axis equal; title('Dilation'); colormap(map1); caxis([-0.15 0.15]); view(2); triplot(tri(find(pin==1),:),X4,Y4,'r');

figure; trisurf(tri,X4,Y4,zeros(size(X4)),(rel)); hold; axis equal; title('Axis relation'); colormap(map2); caxis([1 1.3]); colorbar;

figure; trisurf(tri1,X4,Y4,zeros(size(X4)),(ang)); hold; axis equal; title('Maj. angle direction'); colormap(map1); caxis([0 180]); colorbar;

Parametric restoration

This fold contains the plugin *Restoration2D* for *gOcad version 2009.4*. This plugin is the restoration method based on the parametric approach in which we have incorporated the paleomagnetic constraint. We must set the paleomagnetic property as "Default gu value".

Map-view restoration

This simple *c* program (*restoredmap.exe*) plots the cartographic map in the restored state after the palinspastic (or map-view) restoration (Section 6.1). Two files are needed to run the program: 1) a text file with the vertices of texture and position (example: *vertices.txt*) and a 2) bitmap file with the raster image of the cartographic map (example: *carto.bmp*). The program is run from the command prompt adding two arguments corresponding with these two files (example: >*restoredmap vertices.txt carto.bmp*).

The vertices file contains the *x y* coordinates of texture and position. Vertices are sorted by triangles (three consecutive lines are the nodes of a triangle). Texture vertices are the points of the meshed initial map while position vertices are the points of the meshed restored map. Point range is from 0 to 1.

VPD

Virtual Paleomagnetic Directions program is fully described in Appendix1: Achieving the optimal information from paleomagnetic analysis. *VPD.jar* is the executable file whereas the *source* folder contains the code. We also include example files for each input format. *ASN3.th* and *Almonacid u-channels.txt* are the files used in

Section I.2 for the application to real data sets. We detail in the manual (*VDP Manual.pdf*) all routines of the program.

Paleomagnetic errors

These are the excel macros developed to compute the paleomagnetic errors described in Appendix 2:

1) Overlapping error

Input data: P (primary vector), S (secondary), r (P/S ratio), rotation matrix ($\alpha, 0, \beta$)

Output data: Error

2) Shear error

Input data: P (primary vector), bedding plane (α, β), simple shear (γ, ψ)

Output data: Error

3) Superposed folding error

Input data: P (primary vector), S1 (α_1,β_1), S2 (α_2,β_2)

Output data: Error